



Dunnill, Charles W. H. (2008) *Synthesis, characterisation and properties of tantalum based inorganic nanofibres*. PhD thesis.

<http://theses.gla.ac.uk/173/>

Copyright and moral rights for this thesis are retained by the author

A copy can be downloaded for personal non-commercial research or study, without prior permission or charge

This thesis cannot be reproduced or quoted extensively from without first obtaining permission in writing from the Author

The content must not be changed in any way or sold commercially in any format or medium without the formal permission of the Author

When referring to this work, full bibliographic details including the author, title, awarding institution and date of the thesis must be given

SYNTHESIS, CHARACTERISATION AND
PROPERTIES OF TANTALUM BASED
INORGANIC NANOFIBRES



UNIVERSITY
of
GLASGOW

A thesis submitted to the University of Glasgow for the degree of

Doctor of Philosophy

By

Charles W. H. Dunnill MSci

School of Chemistry

University of Glasgow

December 2007

Abstract

This thesis describes the synthesis and characterisation of 1-dimensional nanometric phases using simple preparative reactions and a variety of characterisation methods. Comparison of properties between the bulk and nanomorphology has played a large part and is a common theme throughout.

High aspect ratio tantalum disulfide, TaS_2 nanofibres were prepared from a 1:2 stoichiometric mixture of elemental powders in a one-step synthesis utilising silica ampoules. A surface assisted growth phenomena was investigated and found to significantly increase the yield, both in quality and quantity. The resulting nanofibres were seen to retain and indeed enhance some of the bulk properties, e.g. a 50 fold increase in observed superconducting transition temperature.

Changing the stoichiometry of the reactants to 1:3, produced tantalum trisulfide nanofibres. Tantalum trisulfide is of interest as it has pseudo 1-dimensional crystal structure and properties in the bulk. TEM and SAED have shown that the TaS_3 unit cell is oriented with the b direction parallel to the long axis of the nanofibres, indicating the potential for the transfer of the low dimensional properties of the bulk material into the nanophase morphology. (Low dimensional properties of bulk TaS_3 result from chains of tantalum atoms propagating along the b direction of the unit cell). Although the structure of the TaS_3 remains illusive the preliminary investigations show these nanofibres to be metallic along their lengths, potentially leading to many applications in nanoscale electrical devices.

The concept of pseudomorphic change from the disulfide nanomaterials into more functional materials such as Ta_3N_5 and Ta_2O_5 was investigated. Nanofibres were initially formed and can reversibly be inter-converted between the three different nanometric phases (TaS_2 , Ta_3N_5 and Ta_2O_5) using simple solid-gas reaction, without significant loss of nanofibrous morphology. Further this series of reactions shows potential for the formation of

other related and potentially applicable nanometric phases such as TaN, TaO₂ and TaON as well as opening the door to countless other analogous systems.

Quotes

“These nanotubes are so amazing that they may be useful to everybody”

Nobel laureate R. Smalley

Nanotechnology “will bring revolutionary changes to all branches of industry, beginning with the production of antibiotics and ending with new weapons”

E. Drexler

"Nanotechnology is the base technology of an industrial revolution in the 21st century. Those who control nanotechnology will lead the industry"

Michiharu Nakamura, Executive VP at Hitachi

Acknowledgements

Many people have been instrumental in the facilitation of the project. Firstly I'd like to thank Professor Duncan Gregory whose supervision has kept me on track throughout the project. Secondly I'd like to thank all the past and present lab members from both institutions; Nottingham and Glasgow, who have been there for support and made my time in the lab memorable. I would like to thank all the technical support, again from both institutions, be it workshop staff or technicians who have helped me find build or repair equipment.

I would also like to thank: Hannah Edwards and Paul Brown from the University of Nottingham and Ian MacLaren from the University of Glasgow, who have helped out with the TEM, as well as Nikki Weston from the University of Nottingham who has helped out with SEM and Jim Gallagher from the University of Glasgow who has been there for support with the primary SEM used in the project. A nanofibre based project like this is nothing without the ability to image the structures, so TEM and SEM have played an important role in the characterisation of some of the nanofibrous materials discussed.

Philip Moriarty and Andrew Stannard from the University of Nottingham are also thanked for their time in the attempts to gain understanding of the electrical behaviour of the nanowires.

Contents

Abstract.....	i
Quotes.....	iii
Acknowledgements.....	iv
Contents.....	v
Glossary of Abbreviations.....	ix
List of Tables.....	x
List of Figures.....	xii
 Chapter 1: General Introduction and Theory	1
1.1 Introduction.....	1
1.1.1 Current Uses of Nanotechnology	3
1.1.2 Inorganic Compounds Known to Form Nanofibres	6
1.1.3 Conventional Definitions for Inorganic Nanofibres	7
1.2 Basic Crystallography.....	7
1.2.1 Unit Cells, Crystal Systems and the Bravais Lattice	7
1.2.2 Point Groups.....	9
1.2.3 Space Groups.....	9
1.2.4 Miller Indices	10
1.2.5 Bragg's Law	12
1.3 Charge-Density-Waves	13
1.3.1 Formation of Charge-Density-Waves	14
1.3.2 Conduction in Charge-Density-Wave Systems	15
1.3.3 Measurable Properties of Charge-Density-Wave Systems	16
1.4 Magnetic Materials.....	16
1.4.1 Types of Magnetic Material	20
1.4.2 Paramagnetic Materials.....	20
1.4.3 Ferromagnetic Materials	22
1.4.4 Superconducting Materials.....	23
1.5 MX ₂ Compounds (Bulk).....	25
1.5.1 Tantalum Disulfide	26
1.5.2 Properties of TaS ₂	27
1.6 MX ₃ Compounds.....	30
1.6.1 Tantalum Trisulfide	30
1.7 Oxides.....	32
1.8 Tantalum Oxide.....	32
1.9 Nitrides	33
1.10 Tantalum Nitride	33
1.11 Inorganic Nanofibre Research.....	34
1.11.1 MX ₂ Compounds Nanofibres	35
1.11.1.1 Tungsten Disulfide Nanofibres.....	36
1.11.1.2 Molybdenum Disulfide Nanofibres	36
1.11.1.3 Niobium Disulfide Nanofibres	37
1.11.1.4 Tantalum Disulfide Nanofibres	38
1.11.1.5 Niobium Diselenide Nanofibres	39
1.11.1.6 Molibdenum Diselenide and Tungsten Diselenide Nanofibres	40
1.11.1.7 Other Disulfide Nanofibres	40
1.11.2 MX ₃ Compound Nanofibres.....	40
1.11.2.1 Tantalum Trisulfide Nanofibres	41
1.11.2.2 Niobium Triselenide Nanofibres	41

1.11.2.3	Titanium Trisulfide Nanofibres	42
1.11.3	Nitrides	42
1.11.3.1	Boron Nitride Nanofibres	42
1.11.3.2	Lithium Nitride Nanofibres	43
1.11.4	Oxides	43
1.11.4.1	Titanium Dioxide Nanofibres	43
1.11.4.2	Tantalum Oxide Nanofibres	44
Chapter 2:	Experimental	45
2.1	Introduction	45
2.2	Experimental Methods	45
2.2.1	Equipment and Techniques	45
2.2.2	Fume Hoods	45
2.2.3	Nitrogen Generator	46
2.2.4	Work Involving Glass	46
2.2.4.1	Silica Tubes	47
2.2.4.2	Glass Blowing Torch	47
2.2.4.3	Long Necked Powder Funnels	48
2.2.4.4	Ampoule Designs	49
2.2.4.5	Sealing Silica Ampoules Under Vacuum	50
2.2.4.6	Heating Silica Ampoules	52
2.2.4.7	Opening Silica Ampoules	53
2.2.4.8	Quenching Silica Ampoules	54
2.2.5	Furnaces	54
2.2.5.1	Elite Thermal Systems Muffle Furnace	54
2.2.5.2	Carbolite Three Zone Tube Furnace	54
2.2.5.3	Vecstar Furnaces Tube Furnace	55
2.2.5.4	Carbolite Tube Furnace	55
2.2.6	Sublimation of Excess Sulfur from Nanowires	55
2.3	Synthetic Preparations	56
2.3.1	Preparations Using Silica Ampoules	56
2.3.1.1	Preparations Using a Standard Silica Ampoule	56
2.3.1.2	Preparations Using a Surface Assisted Growth Ampoule	56
2.3.1.3	Long Tube Preparations	57
2.3.2	Flowing Gas Preparations	57
2.3.2.1	Preparations Using NH ₃	57
2.3.2.2	Preparations Using CS ₂	58
2.3.2.3	Preparations Using O ₂	59
2.4	Characterisation Techniques & Equipment Specifications	60
2.4.1	Powder X-ray Diffraction	60
2.4.1.1	Treatment of Powder Patterns	60
2.4.1.2	Powder X-ray Diffraction Sample Preparation	63
2.4.1.3	X-Ray Diffractometers	65
2.4.2	Scanning Electron Microscopy	67
2.4.2.1	Energy Dispersive X-ray Analysis	68
2.4.2.2	Sample Preparation for SEM	72
2.4.2.3	Scanning Electron Microscopes	72
2.4.3	Transmission Electron Microscopy	74
2.4.3.1	Bright Field Imaging	75
2.4.3.2	Selected Area Electron Diffraction	76
2.4.3.3	Nanobeam Diffraction Techniques	79
2.4.3.4	Dark Field Imaging	79

2.4.3.5	High Resolution Imaging	80
2.4.3.6	Sample Preparation for TEM.....	80
2.4.3.7	Transmission Electron Microscopes	82
2.4.4	Thermal Analysis.....	83
2.4.4.1	Thermo-Gravimetric Analysis.....	83
2.4.4.2	Differential Thermal Analysis and Differential Scanning Calorimetry	83
2.4.4.3	Sample Preparation for TG-DTA	84
2.4.4.4	Gravimetric Analysers	84
2.4.5	Magnetic Measurements	84
2.4.5.1	SQUID Magnetometry	84
2.4.5.2	Sample Preparation for SQUID	85
2.4.5.3	Centering the Sample	85
2.4.5.4	Working up SQUID data.....	86
2.4.5.5	SQUID Magnetometers.....	87
2.4.6	Diffuse Reflectance Spectroscopy.....	87
2.4.6.1	Sample Preparation for DRS	89
2.4.6.2	DRS Spectrometer	90
2.4.7	BET Isotherms for Surface Area Analysis.....	90
2.4.8	Atomic Force Microscopy.....	90
2.4.8.1	AFM Imaging	91
2.4.8.2	Electronic Measurements	92
2.4.8.3	Sample Preparation	93
2.4.8.4	Asylum Research Atomic Force Microscope.....	93
2.4.8.5	Collaboration	93
Chapter 3:	Tantalum Disulfide Nanofibres	94
3.1	Introduction.....	94
3.2	Experimental	95
3.2.1	Synthesis	95
3.2.1.1	Standard Preparation	96
3.2.1.2	Surface Assisted Growth Preparations.....	97
3.2.1.3	Effects of Temperature Regime on Nanowire Formation.....	98
3.2.1.4	Bulk Phase Syntheses.....	98
3.2.2	Characterisation	99
3.3	Results and Discussion	101
3.3.1	Preparation TaS ₂ 650_Std	101
3.3.1.1	Residual Powders.....	101
3.3.1.2	Fibrous Morphology	104
3.3.2	Preparation TaS ₂ 650_SAG.....	115
3.3.2.1	Residual Powders.....	116
3.3.2.2	Fibrous Morphology	118
3.3.3	Effects of Temperature on Nanowire Formation.....	126
3.3.3.1	TaS ₂ 1100_Std & TaS ₂ 1100_SAG	126
3.3.3.2	Preparations TaS ₂ 750 & TaS ₂ 900.....	128
3.3.3.3	Preparations TaS ₂ 600_SAG, TaS ₂ 500_SAG & TaS ₂ 400_SAG.....	129
3.3.4	Bulk Phase Syntheses	132
3.3.4.1	1T Polytype	132
3.3.4.2	2H Polytype.....	134
3.3.4.3	3R Polytype	135
3.4	Conclusions.....	136

Chapter 4: Tantalum Trisulfide Nanofibres	139
4.1 Introduction.....	139
4.2 Experimental	143
4.2.1 Synthesis	143
4.2.1.1 Standard Preparation	143
4.2.1.2 Surface Assisted Growth Preparation	144
4.2.1.3 Effects of Changing Temperature Regime on Nanofibrous Formation....	145
4.2.2 Characterisation	146
4.3 Results and Discussion	147
4.3.1 Preparations TaS ₃ 650_Std and TaS ₃ 650_SAG	147
4.3.1.1 Residual Powders.....	149
4.3.1.2 Fibrous Morphology	150
4.3.2 Effects of Temperature on Nanowire Formation.....	162
4.3.2.1 High Temperature Preparations.....	162
4.3.2.2 Preparation TaS ₃ 750	164
4.3.2.3 Low Temperature Preparations	166
4.3.3 Conclusions	169
Chapter 5: Tantalum Nitride and Tantalum Oxide Nanofibres	171
5.1 Introduction.....	171
5.1.1 Precedent for Reversible Pseudomorphic Reactions	172
5.1.1.1 Solid-Gas Exchange Reaction Involving Nanometric Phases.....	173
5.2 Experimental	175
5.2.1 Synthesis	175
5.2.1.1 Preparations by Ammonolysis Reactions.....	176
5.2.1.2 Preparations by Oxidation Reactions.....	178
5.2.1.3 Sulfidation Reactions	179
5.2.2 Characterisation	181
5.3 Results and Discussion	182
5.3.1 Ammonolysis Reactions	182
5.3.1.1 Preparation S-N950b_4h.....	182
5.3.1.2 Preparation O-N950b_4h	186
5.3.1.3 Preparation S-N950n_4h.....	189
5.3.1.4 Preparation S-N800n_4h.....	196
5.3.1.5 Preparation S-N650n_4h.....	200
5.3.1.6 Preparation O-N950n_4h	203
5.3.2 Preparations of Oxide Materials.....	205
5.3.2.1 Preparations S-O800b_4h	205
5.3.2.2 Preparation S-O400b_4h and S-O400b_16h.....	208
5.3.2.3 Preparation N-O400b_4h	211
5.3.2.4 Preparation S-O800n_4h.....	211
5.3.2.5 Preparation N-O800n_4h	215
5.3.2.6 Preparation S-O400n_4h.....	217
5.3.2.7 Preparation N-O400n_4h	219
5.3.3 Sulfidation Reactions	221
5.3.3.1 Preparations O-S1000b_14h.....	221
5.3.3.2 Preparation O-S850b_4h and Preparation N-S850b_4h	223
5.3.3.3 Preparation N-S850n_4h.....	224
5.3.3.4 Preparation O-S850n_4h.....	226
5.4 Conclusions.....	228
Chapter 6: References	232

Glossary of Abbreviations

1T-TaS₂ – 1T polytype of TaS₂
2H-TaS₂ – 2H Polytype of TaS₂
3R-TaS₂ – 3R polytype of TaS₂
AFM – Atomic Force Microscope
BET- Brunauer Emmett Teller (Theory used to calculate surface area)
BF – Bright Field (TEM imaging)
BFP – Back Focal Plane
CDW – Charge Density Wave
CNT – Carbon Nanotube
EDX – Energy Dispersive X-ray Analysis
DF – Dark Field (TEM imaging)
DRS – Diffuse Reflectance Spectroscopy
JEOL – Japanese Electron Optics Laboratory
m-TaS₃ – Monoclinic form of TaS₃
m_{hp}-TaS₃ – High pressure form of TaS₃
m_i-TaS₃ – Indexed form of TaS₃
PLD – Peierls Lattice Distortion (Periodic Lattice Distortion)
PMMA – Polymethyl Methacrylate
PXD – Powder X-Ray Diffraction
RT – Room Temperature
SAED – Selected Area Electron Diffraction
SAG – Surface Assisted Growth experimental setup
SEM – Scanning Electron Microscope
SQUID – Super Conducting Quantum Interference Device
STD – Standard experimental setup
TEM – Transmission Electron Microscope
TGA – Thermal Gravimetric Analysis

List of Tables

Table 1.1: A comprehensive list of many of the inorganic compounds known to form nanofibres, shown with respect to the 7 families. Taken and updated from Remškar. ²¹	6
Table 1.2: The 14 Bravais lattices for crystals.	8
Table 1.3: Table showing the interplanar spacings for the different crystal systems.	11
Table 1.4: Table showing different types of magnetic materials	17
Table 1.5: Units of magnetic measurements and their conversion table to SI.	18
Table 1.6: Table to show the different types of magnetism, their expected χ_M values and their characteristic behaviours and properties.	19
Table 1.7: Table to show the theoretical values of BM that correspond to the number of unpaired electrons.	22
Table 3.1: Experimental conditions for the changing temperature regime preparations.	98
Table 3.2: Unit cell parameters from the indexed powder pattern from TaS₂650_Std compared to the published values for 3R-TaS ₂ . ¹¹²	102
Table 3.3: Unit cell parameters from the indexed powder patterns from TaS₂650_Std compared to the published values for 3R-TaS ₂ . ¹¹²	117
Table 3.4: Unit cell parameters from the indexed powder patterns from TaS₂650_Std and TaS₂650_SAG compared to the published values for 2H-TaS ₂ . ¹¹²	119
Table 3.5: Unit cell parameters from the indexed powder pattern from TaS₂650_Std compared to the published values for 3R-TaS ₂ . ¹¹²	130
Table 3.6: Unit cell parameters from the indexed powder patterns of TaS₂1100_Std compared to the published values for 1T-TaS ₂ . ¹¹²	133
Table 3.7: Unit cell parameters from the indexed powder patterns of the 2H preparation compared to the published values for 2H-TaS ₂ . ¹¹²	135
Table 3.8: Unit cell parameters from the indexed powder patterns of the 3R preparation compared to the published values for 3R-TaS ₂ . ¹¹²	136
Table 4.1: Experimental conditions for the changing temperature regime preparations.	145
Table 4.2: Table to show the comparison between the two published monoclinic unit cells and the indexed solution for the nanofibres.	151
Table 4.3: Unit cell parameters from the indexed powder patterns of preparation TaS₃1100 compared to the published values for 1T-TaS ₂ . ¹¹²	163
Table 4.4: Unit cell parameters from the indexed powder patterns from TaS₃750 , compared to the published values for 1T-TaS ₂ . ¹¹²	165
Table 5.1: Table showing the experimental parameters for the preparations of tantalum nitride from bulk precursors.	177
Table 5.2: Table showing the experimental parameters for preparations of tantalum nitride from nanofibrous precursors.	178
Table 5.3: Table showing the experimental parameters for the preparations of tantalum oxide from bulk precursors.	178
Table 5.4: Table showing the experimental parameters for the preparations of tantalum oxide from nanofibrous precursors.	179
Table 5.5: Table showing the experimental parameters for the preparations of tantalum sulfide from bulk precursors.	180
Table 5.6: Table showing the experimental parameters for the preparations of tantalum sulfide from nanofibrous precursors.	180
Table 5.7: Unit cell parameters from the indexed powder patterns from S-N950b_4h , compared to the published values for Ta ₃ N ₅ . ¹⁴⁸	183
Table 5.8: Unit cell parameters from the indexed powder patterns from O-N950b_4h , compared to the published values for Ta ₃ N ₅ . ¹⁴⁸	187

Table 5.9: Unit cell parameters from the indexed powder patterns of S- N950b_4h and S-N950n_4h compared to the published values for Ta_3N_5 . ¹⁴⁸	189
Table 5.10: Unit cell parameters from the indexed powder patterns of S-N800n_4h and S-N950n_4h , compared to the published values for Ta_3N_5 . ¹⁴⁸	197
Table 5.11: Unit cell parameters from the indexed powder patterns of S-N650n_4h , S-N800n_4h and S-N950n_4h , compared to the published values for Ta_3N_5 . ¹⁴⁸	201
Table 5.12: Unit cell parameters from the indexed powder patterns of O-N950n_4h and O-N950b_4h , compared to the published values for Ta_3N_5 . ¹⁴⁸	204
Table 5.13: Unit cell parameters from the indexed powder patterns of S-O800b_4h , compared to the published values for Ta_2O_5 . ²²³	206
Table 5.14: Unit cell parameters from the indexed powder patterns of preparation S- O800n_4h , compared to the published values for Ta_2O_5 . ²²³	212
Table 5.15: Unit cell parameters from the indexed powder patterns of N-O800n_4h , compared to the published values for Ta_2O_5 . ²²³	215
Table 5.16: Unit cell parameters from the indexed powder patterns of O- S1000n_14h , compared to the published values for 3R-TaS_2 . ¹¹²	222
Table 5.17: Unit cell parameters from the indexed powder patterns of O-S850b_4h and O-S1000n_14h , compared to the published values for 3R-TaS_2 . ¹¹²	224

List of Figures

Figure 1.1: Images of (a) the TX Millennium brand building (Italcementi Group) and (b) a path in Japan. Both were made using TiO_2 coatings that photo-catalytically clean themselves and the surrounding air.....	5
Figure 1.1.2: Miller indices for a 2-dimensional lattice with unit cell (a,b)	10
Figure 1.3: Derivation of Bragg's law, showing parallel Rays, 1 and 2 incident on a surface consisting of semi transparent planes of atoms.	12
Figure 1.4: Diagram to show the origins of CDWs.	14
Figure 1.5: Schematic of a hysteresis curve.	23
Figure 1.6: Pictorial representation of the structure of the 1T, 2H and 3R polytypes of TaS_2 showing the origins of the ABC notation.....	27
Figure 1.7: Density of states diagram for the 1T and 2H polytype of TaS_2 . ¹²⁴	29
Figure 1.8: Crystal structure of TaS_3 (m- TaS_3) showing 4 unit cells stacked along the b direction of the unit cell. ¹²⁹	31
Figure 1.9: Crystal structure of Ta_2O_5 . ¹³⁸	33
Figure 1.10: Crystal structure of Ta_3N_5 . ¹⁴⁸	34
Figure 2.1: Schematic showing how a long necked powder funnel can deposit reactants at the bottom of the silica tubes without contaminating the inside walls of the silica tube to be sealed.	48
Figure 2.2: Schematic of the tubes used for the surface assisted growth experiments.....	50
Figure 2.3: Schematic of the glass blowing vacuum line.	51
Figure 2.4: Schematic of the two basic types of ampoule, (a) standard and (b) surface assisted growth experiments. The notation of the different Regions has been included to aid discussion.	52
Figure 2.5: Schematic for the sublimation reactions used for removing excess sulfur from bundles of nanowires.	56
Figure 2.6: Schematic of the ampoule design used in the surface assisted growth experiments, showing also the Regions from Figure 2.4 that will be used for discussion purposes.	57
Figure 2.7: Schematic of the experimental set up for the formation of nitride materials.	58
Figure 2.8: Schematic of the experimental set up for the formation of sulfide materials using the reaction of a suitable precursor and CS_2/Ar gas mixture.	59
Figure 2.9: Schematic of the experimental set up for the formation of oxide materials.....	59
Figure 2.10: Powder X-ray diffraction pattern showing diffracted intensity against 2θ for a blank carbon tab showing the background that may be associated with PXD patterns taken using this method of sample preparation.	65
Figure 2.11: Schematic of the workings of a generic Powder X-ray Diffractometer.....	66
Figure 2.12: Schematic diagram showing the interaction of an incident beam of electrons and a sample.....	68
Figure 2.13 Diagram to show the energy levels involved in EDAX.	69
Figure 2.14: Schematic of an EDX detector.....	71
Figure 2.15: Schematic of a TEM. ¹⁸⁵	75
Figure 2.16: Schematic diagram to show the electron beam path used in TEM.	75
Figure 2.17: Ray diagram showing how the electron beam magnifies the image from the specimen plane to the image plane. Different angled beams from the specimen can be focussed onto the image plane by altering the power of the lens.....	76
Figure 2.18: Ray diagram to show the basic concept behind electron diffraction.	77
Figure 2.19: Schematic showing Flemings right hand rule.....	78

Figure 2.20: Schematic of the encapsulation sample holder for TEM and the loading procedure.	81
Figure 2.21: Schematic showing the loaded sample holder.	81
Figure 2.22: Schematic of the encapsulated nanofibres TEM sample.	82
Figure 2.23: Colour spectrum of visible light showing the region of interest for UV-vis diffuse reflectance spectroscopy.	88
Figure 2.24: DRS spectrum of TiO_2 powder 99.99% rutile with a known onset at 3.0 eV used both as an example of the intended presentation of DRS data, and to show the calibration of the spectrometer.	89
Figure 2.25: Schematic representation of an Atomic Force Microscope.	91
Figure 2.26: Surface used for electronic measurements on the AFM.	92
Figure 3.1: Temperature profile used for the preparation of the TaS_2 nanofibres in TaS₂650_Std	97
Figure 3.2: PXD pattern showing the residual powder matching to the 3R- TaS_2 structure, (X-pert diffractometer).	102
Figure 3.3: SEM micrograph of the general morphology seen in the residual powders from TaS₂650_Std , (SEM #1).	103
Figure 3.4: TGA data showing the reaction profile of TaS_2 powder from TaS₂650_Std	104
Figure 3.5: PXD pattern showing a match between the fibrous materials from TaS₂650_Std both 2H- TaS_2 and 3R- TaS_2 , (D5000 diffractometer).	105
Figure 3.6: SEM micrographs of the fibrous material from TaS₂650_Std showing: (a) general morphology, (SEM #1); (b) diameter measurements of typical nanofibres, (SEM #1); (c) a bundle of nanowires separating, (SEM #2) and (d) the multiple ends of a single bundle, (SEM #2); (e) hexagonal crystal surrounded by thin nanofibres, (SEM #2); (f) hexagonal crystals and fibres, (SEM #2).	106
Figure 3.7: SEM micrograph of the general morphology from Figure 3.6(a) and the image of general morphology from the paper published by Rao and Nath. ⁴³ Showing the approximate measurements of the larger structures taken using ImageJ. ¹⁸⁶	107
Figure 3.8. TEM micrographs showing the basic morphology of the TaS_2 nanowires: (a) low magnification bright field TEM image of several TaS_2 nanowires; (b) bright field TEM image and corresponding inset SAED pattern of a single crystalline nanowire; (c) TEM image of a TaS_2 nanowire consisting of several individual filaments; (d) corresponding indexed SAED pattern of [0001] projection, (JEOL 2000FX microscope).	109
Figure 3.9: TEM micrographs showing: (a) a single TaS_2 nanowire composed of multiple filaments leading to a single crystal SAED pattern; (b) with splitting and streaking of spots perpendicular to the fibre long axis; (c) High resolution TEM image of 2H- TaS_2 (0001) planes, (JEOL 2000FX microscope).	111
Figure 3.10: TEM micrographs showing lateral splitting and longitudinal peeling, (JEOL 2000FX microscope).	112
Figure 3.11: TEM micrographs showing “nanorhubarb”, (JEOL 2000FX microscope).	113
Figure 3.12: SQUID results for a sample of TaS_2 nanowires from TaS₂650_Std	114
Figure 3.13: Optical microscope images of TaS_2 nanofibres: (a) internal coating of the walls of the adapted ampoules, (b) and (c) fibres growing off the tantalum foil surface and (d) a possible imperfection in the silica wall acting as a nucleating point for the growth of the fibres.	116
Figure 3.14: PXD analysis of the residual powders from TaS₂650_SAG . (D5000 diffractometer)	117
Figure 3.15: SEM micrograph showing the general morphology of the residual powder from TaS₂650_SAG , (SEM#1).	118

Figure 3.16: PXD for the nanofibres from TaS₂650_SAG , (D5000 diffractometer).....	118
Figure 3.17: SEM micrographs from TaS₂650_SAG showing: (a) general morphology of the fibrous material at low magnification; (b) higher magnification image of typical nanowires and (c) measurements demonstrating the diameters of the nanowires to be in the 100 – 600 nm range, (SEM #1).	120
Figure 3.18: SEM micrographs showing the fibres growing off the foil from TaS₂650_SAG , (SEM #1).	121
Figure 3.19: TEM micrograph and diffraction patterns of a TaS ₂ nanowire: (a) Bright field image; (b) SAED pattern at 0° tilt; (c) simulated [0001] diffraction pattern; (d) SAED pattern after 10° tilt about the wire axis; (e) simulated 10° tilt pattern; (f) SAED pattern after 20° tilt about the wire axis and (g) simulated 20° tilt pattern, (T20 microscope).....	123
Figure 3.20: (a) TEM micrograph showing the cross sectional area of a nanobelt; (b) square section and inset SAED pattern taken at 16 ° alpha tilt, (T20 electron microscope).....	124
Figure 3.21: SQUID magnetometry data showing a single superconducting T _c at 3.4 K for the bundles of superconducting TaS ₂ nanofibres observed in preparation TaS₂650_SAG . Measurements taken on the SQUID at Nottingham.	125
Figure 3.22: PXD pattern for the residual powder from TaS₂1100_Std , (D5000 diffractometer).	127
Figure 3.23: SEM micrographs from TaS₂1100 showing the morphology of the 1T-TaS ₂ , (SEM #1).	128
Figure 3.24: SEM micrograph of the fibrous material formed in TaS₂900_Std . (SEM #1).	129
Figure 3.25: PXD pattern showing the residual powder from TaS₂600_SAG matching 3R-TaS ₂ and 2H-TaS ₂ , (D5000 diffractometer).....	130
Figure 3.26: SEM micrographs from preparation TaS₂600_SAG (SEM #4).	130
Figure 3.27: (a) and (b) SEM micrographs showing nanoribbons of a 1:3 ratio Ta:S formed in TaS₂500_SAG , (SEM #4) and (c) PXD pattern indexing to the m _i -TaS ₃ structure discussed in Section 4.3.1.2, (D5000 diffractometer).	131
Figure 3.28: (a) PXD data showing the presence of 1T-TaS ₂ , (D5000 Diffractometer); (b) SEM micrograph showing typical morphology of 1T-TaS ₂ (SEM #4).	132
Figure 3.29: DSC data for the 1T polytype of TaS ₂ . Heated at 10 °Cmin ⁻¹ from room temp to 500 °C under argon.	133
Figure 3.30: PXD pattern of 1T-TaS ₂ after being annealed for 5 days at 400°C, showing a match to the 2H polytype, (D5000 diffractometer).	134
Figure 3.31: (a) PXD pattern (X-pert diffractometer) showing peaks matching the 3R-TaS ₂ phase; (b) SEM micrograph showing the general morphology of the crystals, (SEM #1).	136
Figure 4.1: Crystal structure of m-TaS ₃ ¹²⁹ showing 3 unit cells stacked in the <i>b</i> direction to illustrate the origin of the low dimensional behaviour.	140
Figure 4.2: Crystal structure of the sulfurs that surround the tantalum atoms in the chain structure of m-TaS ₃	141
Figure 4.3: Temperature profile used in TaS₃650_Std . This is given as an example of the temperature profile used throughout the preparations for TaS ₃ nanofibres.	144
Figure 4.4: Schematic of the results for (a) TaS₃650_Std and (b) TaS₃650_SAG . In each case three regions marked for discussion purposes.	148
Figure 4.5: PXD pattern showing the 36 indexed peaks from the powder pattern of the residual powders from Region I' of the ampoules of preparation TaS₃650_SAG , (X-pert diffractometer).	149
Figure 4.6: SEM analysis of the residual powders from TaS₃650 , (SEM #2).	150

Figure 4.7: PXD pattern for (a) typical nanowires from TaS₃650 and (b) typical residual powder from TaS₃650 , (D5000 diffractometer).....	151
Figure 4.8: Generated powder pattern for the two models of the TaS ₃ phases showing the similarities in the peak positions.	152
Figure 4.9: SEM micrographs of TaS ₃ nanofibres from TaS₃650_Std showing; (a) general morphology, (b) bundles of nanowires and ribbons / belts, (SEM #1).....	153
Figure 4.10: SEM micrographs from TaS₃650_SAG showing; (a) bundles of nanowires and (b) bales of aligned nanowires, (SEM #1).....	154
Figure 4.11: (a) TEM micrograph showing a single nanowire of diameter <75 nm; (b) corresponding diffraction pattern indexed to various spots in the 001 and the 010 directions of the m _i -TaS ₃ structure, (T20 microscope).	155
Figure 4.12: Schematic explaining how the SAED patterns were used to choose between the unit cell solutions from the PXD data towards the structure of the TaS ₃ nanofibres.	156
Figure 4.13: TEM images of TaS ₃ nanowires showing (a) the high tendency of the wires to split along lattice fringes and (b) a high-resolution TEM image showing the lattice fringes at ~9.9Å.....	157
Figure 4.14: AFM images and 3D plots of TaS ₃ nanowires on a SiO ₂ surface.....	159
Figure 4.15: (a) Single TaS ₃ nanowire connected to a gold electrode and the positions of the AFM IV curve measurements; (b) the IV trace from position 1 and 3 showing the potential vs. time and current vs. time plots that mirror each other and (c) IV trace showing the potential vs. time and current vs. time plots that show only background noise from position 3.....	160
Figure 4.16: Schematic showing a 5 electrode measurement setup for the resistivity measurement on a single nanowire.	162
Figure 4.17: PXD analysis showing the match between the products of TaS₃1100 and 1T-TaS ₂ . (D5000).....	163
Figure 4.18: SEM micrograph showing the general morphology of products from TaS₃1100 , (SEM #2).....	164
Figure 4.19: PXD pattern for TaS₃750 showing a match to both 1T-TaS ₂ and 3R-TaS ₂	165
Figure 4.20: SEM micrograph of a particle from the residual powders from TaS₃750 . (SEM #2)	165
Figure 4.21: Hexagonal plate-like structure of TaS ₂ from preparations TaS₃750 , (SEM #4).	166
Figure 4.22: PXD data for the preparation TaS₃500_SAG , (D5000 diffractometer and a carbon tab).....	167
Figure 4.23: SEM micrographs of TaS₃500_SAG , (SEM#4).....	168
Figure 4.24: SEM micrographs showing; (a) the formation of TaS ₃ nanofibres on a TaS ₂ surface coating from preparation TaS₃500_SAG and (b) a close up of the surface from which the nanofibres are growing and (c) Nanofibres peeling back off the surface with spots measured by EDX with the ratio of Ta:S given, (SEM #4).	169
Figure 5.1: Schematic of the proposed reactions for pseudomorphic transformation and inter-conversion of three nanometric phases.....	172
Figure 5.2: PXD pattern showing a match between the PXD peaks obtained from the products of preparation S-N950b_4h and those expected for the structure of Ta ₃ N ₅ , ¹⁴⁸ (D5000 diffractometer).	182
Figure 5.3: (a) SEM micrographs of typical Ta ₃ N ₅ particles from S-N950b_4h , (SEM #3) and (b) SEM Micrograph of TaS ₂ platelets, reproduced from Figure 3.3.....	183
Figure 5.4: TGA data from the products from S-N950b_4h	185

Figure 5.5: DRS spectra for the bulk Ta ₃ N ₅ sample, S-N950b_4h_a showing the band gap at 2.04 eV.	186
Figure 5.6: PXD data from O-N950b_4h showing a match to the peaks for both the Ta ₃ N ₅ and TaON contamination, (D5000 diffractometer).	187
Figure 5.7: SEM micrographs showing: (a) general morphology from O-N950b_4h and (b) general morphology from the commercial oxide material that was used as a precursor, (SEM #4)	188
Figure 5.8: UV-vis DRS spectrum for the products of O-N950b_4h and S-N950b_4h showing a band onset at 2.04 eV.	188
Figure 5.9: PXD pattern for the nanofibres from S-N950n_4h showing a match to the published structure of Ta ₃ N ₅ . ¹⁴⁸ Data collected using an adhesive carbon tab, (Section 2.4.1.2.3.3), (D5000 diffractometer).	189
Figure 5.10: SEM micrographs showing the general morphology of the products from S-N950n_4h , (SEM #4).	190
Figure 5.11: TEM micrographs showing a typical polycrystalline nanowire with SAED inset, (T20 microscope).	191
Figure 5.12: Typical SAED pattern for nanofibres from S-N950n_4h indexed to the published structure for Ta ₃ N ₅ . ¹⁴⁸	192
Figure 5.13: UV-vis DRS data for Ta ₃ N ₅ nanowires prepared in S-N950n_4h	195
Figure 5.14: SEM micrographs of the sonicated nanofibres, (SEM #4).	196
Figure 5.15: DRS spectrum comparing the results from S-N950n_4h , the sonicated particles and the bulk tantalum nitride from S-N950b_4h	196
Figure 5.16: PXD pattern showing the match between the products from S-N800n_4h and the crystal structure for Ta ₃ N ₅ . Data were collected from a sample adhered to an amorphous carbon tab (Section 2.4.1.2) using the D5000 diffractometer.	197
Figure 5.17: SEM micrographs showing the general morphology of fibres in the products of S-N800n_4h , (SEM #3).	198
Figure 5.18: TEM micrographs of Ta ₃ N ₅ nanowires from S-N800n_4h with inset diffraction patterns. The diffraction pattern in (b) was achieved by focussing the beam in on the individual crystal indicated and was indexed to the Ta ₃ N ₅ structure, (T20 microscope).	199
Figure 5.19: TEM micrographs showing: (a) Bright field image of the area in question with the indexed representative nanodiffraction pattern; (b-f) dark field images showing the different crystallographic orientations within the nanowire, (T20 microscope).	200
Figure 5.20: PXD showing the match to the crystal structure of Ta ₃ N ₅ for the nitride nanowires formed in S-N650n_4h . Data were collected using an adhesive carbon tab (D5000 diffractometer).	201
Figure 5.21: SEM micrographs showing the products of S-N650n_4h , (SEM #4).	202
Figure 5.22: TEM micrograph showing the Ta ₃ N ₅ nanowires from S-N650n_4h , (T20 microscope).	202
Figure 5.23: PXD data for O-N950n_4h	203
Figure 5.24: SEM micrographs showing the morphology of O-N950n_4h , (SEM #4).	204
Figure 5.25: TEM micrograph of the nitride nanowires from preparation O-N950n_4h , (T20 microscope).	205
Figure 5.26: PXD pattern for the products of S-O800b_4h , showing a match to the Ta ₂ O ₅ structure, (D5000 diffractometer).	206
Figure 5.27: TG-DTA data from the bulk powders of Ta ₂ O ₅ produced in S-O800b_4h	207
Figure 5.28: SEM micrographs showing the morphology from S-O800b_4h	207

Figure 5.29: UV-vis DRS data for the Ta ₂ O ₅ bulk powder produced in S-O800b_4h . The data show a band gap onset at 3.79 eV which is comparable to the 3.80 eV observed by other researchers. ¹³⁹⁻¹⁴³	208
Figure 5.30: PXD analysis of the products from S-O400b_4h	209
Figure 5.31: SEM micrographs from S-O400b_4h showing: (a) general morphology; (b) plate-like crystals, (SEM #4).....	209
Figure 5.32: TG-DTA trace for S-O400b_16h	210
Figure 5.33: PXD analysis for N-O400b_4h	211
Figure 5.34: PXD data for the nanowires from S-O800n_4h showing a match to the structure for Ta ₂ O ₅ , (D5000 diffractometer and double-sided adhesive carbon tab).....	212
Figure 5.35: SEM micrograph showing the Ta ₂ O ₅ ribbons from S-O800n_4h , (SEM #4).	213
Figure 5.36: TEM micrograph with SAED inset showing typical Ta ₂ O ₅ nanowires.	214
Figure 5.37: UV-vis DRS data collected for S-O800n_4h , showing a band gap onset at 3.81 eV for and S-O800b_4h , showing a band gap at 3.79 eV.....	214
Figure 5.38: PXD analysis of products from N-O800n_4h	215
Figure 5.39: SEM micrographs from N-O800n_4h , (SEM #4).....	216
Figure 5.40: Bright field and corresponding dark field images of the products of N- O800n_4h , (T20 Microscope).	217
Figure 5.41: (a) PXD pattern showing oxide nanowires of amorphous nature, (D5000 diffractometer); (b) TG analysis showing a 6 % increase in mass on heating in Ar/air mixture;	218
Figure 5.42: (a) SEM micrograph showing large ribbons, (S-O400n_4h); (b) SEM micrograph showing a fragmenting ribbon, (SEM #3) and (c) TEM micrograph showing a nanowire with the electron diffraction pattern inset, (S-O400n_4h), (T20 microscope).	219
Figure 5.43: (a) PXD pattern showing oxide nanowires of amorphous nature, (D5000 diffractometer); (b) TG analysis showing a 6% increase in mass on heating in Ar/air mixture;	220
Figure 5.44: SEM micrograph showing large ribbons, (SEM #4).....	220
Figure 5.45: PXD pattern from the residual powder corresponding to the 3R and 1T phases of TaS ₂ , (D5000).....	222
Figure 5.46: SEM micrographs showing the general morphology from O- S1000b_14h , (SEM #2)	223
Figure 5.47: PXD for the products of O-S850b_4h , (D5000 diffractometer).	223
Figure 5.48: SEM micrograph showing the general morphology of the powders from O-S850b_4h , (SEM #4).	224
Figure 5.49: SEM micrograph of the products from N-S850_4h , (SEM #4).	225
Figure 5.50: SEM micrographs showing the general morphology of : (a)TaS ₂ fibres (Figure 3.17); (b) Ta ₃ N ₅ nanofibres Figure 5.10 and (c) TaS ₂ nanofibres (Figure 5.49) (SEM #4).	226
Figure 5.51: PXD showing the match between the products of S-O850n_4h , (D5000 diffractometer)	226
Figure 5.52: SEM micrograph showing the nanofibres obtained from O-S850n_4h , (SEM #4).	227
Figure 5.53: SEM micrographs showing the general morphology of : (a)TaS ₂ fibres (Figure 3.17); (b) Ta ₂ O ₅ Fibres (Figure 5.35) and (c) TaS ₂ fibres (Figure 5.52), (SEM #4).	228
Figure 5.54: Diffuse reflectance data showing the superimposition of the 4 different phases described in this chapter on one set of axes.	230

Chapter 1: General Introduction and Theory

1.1 Introduction

Nanotechnology is widely thought to be the driving force behind the next revolution in technology, similar to the coal/steam relationship that drove the industrial revolution of the 1900's or the silicon chip that slowly changed the face of modern life from the 1950's. Increasingly nanotech is moving from the fiction books into the scientific papers and indeed more importantly from the scientific papers into the products that we the general public; see, choose to buy and use as we use to go about our daily lives.

Before long the concept of technology on the nanoscale will be so thoroughly incorporated into everyday things that we will be asking ourselves questions like, "How did we ever live without it?" Much like the itching feeling of being, "Not quite whole," that many people get these days when they leave their home without their mobile telephones, life without nanotechnology will soon be inconceivable.

As with many of these newfound technologies, much revolves around the definition. If you define nanomaterials and indeed nanotech as, "Materials or technology with typical dimensions in the nanometre region," then a few interesting observations can be made. Most notably, that nanotech has already been around in our lives for many years, the obvious example being cleaning products that contain colloidal suspensions of nano-sized particles, and in fact originates in science back in the days of Michael Faraday. It is becoming increasingly hard to find modern creams and ointments that contain no traces of "nano" sized additives. For instance it is the UV absorbing nanoparticles of zinc oxide that give sunscreens their sun screening properties.

Traditionally however we ignore the colloid side of nanoparticles research and concentrate more on new structures such as quantum dots, fibres, (tubes, rods, ribbons and wires), particles and films that have nanoscale dimensions. It is these nanoscale dimensions

that lead to interesting material properties that can vary drastically when compared to either the atomic or the bulk scale materials. An example of this is the size effect of elemental gold and silver. Both these metals are well known and indeed often used for their reluctance to be involved in any sort of chemistry. However as nanoparticles they become extremely reactive with application in many fields, such as catalysis.¹⁻⁴ The reason for the dramatic change in behaviour is the often considered to result from the changing ratio of surface area to total number of atoms; as the particle size decreases the proportion of the atoms that are on, or near to, the surface drastically increases.

The concept of “Nanoscience” was first mentioned publicly on December 29th 1959, by Richard Feynman in his talk at the Californian Institute of Technology entitled, “There’s Plenty of Room at the Bottom.” This was in many ways seen as the birth of “Nanoscience” or at least the first direction towards nanoscale research, but was delivered from a very physics based point of view.⁵ Nano-scale research in chemistry did not really take off until 1985 when Nobel Laureate Sir Harry Kroto discovered Buckminster Fullerene, the cage structure and 3rd allotrope of carbon.⁶ Nano-scale research became much more prevalent, however, in 1991 when Iijima discovered carbon nanotubes,⁷ and further still in 1992 when Tenne discovered the first “non-carbon” nanotubes of WS₂.⁸ The term “Nano” was now beginning to attract funding and consequentially appear in many research proposals thus delving further into the scientific domain. It is interesting to note however that the first reference to any sort of inorganic (Non-carbon) nanofibre in the scientific literature, was in 1979 when Chianelli describes “Rag like tubular structures” of MoS₂.⁹ These predate the discovery of carbon nanofibres and indeed Kroto’s “Bucky Balls”, making it the first reference to inorganic nanofibres as we now know them. The first reference to any sort of nanofibrous material was however in 1952 when a Russian scientist published SEM images in a paper detailing carbon nanotubes,¹⁰ predating even Feynman’s lecture. This could be seen as an example of the

unfairness of history as Iijima and Tenne are both widely recognised as having made the first discoveries.

1.1.1 Current Uses of Nanotechnology

The first use of nanotechnology is likely the incorporation of gold nanoparticles into glass. Medieval artisans made red stained glass by mixing gold chloride into molten glass creating tiny gold nanospheres, which absorb and reflect sunlight in a way that produces a rich ruby colour. This sort of glass has been widely used for the production of stained glass for more than 2000 years.¹¹

It was well known in the 1500's that Damascus steel was unlike any European steel and had extraordinary mechanical properties including an exceptional cutting edge. The secret recipe, however, was lost hundreds of years ago and the quality of the blades remained a mystery. Recent studies utilising TEM have shown the presence of carbon nanotubes in an ancient Damascus sabre,¹² suggesting that the probable source of the enhanced properties was the formation of carbon nanotubes within the steel during the forging process. This therefore is likely to be the first practical use of nanofibrous technology. It is also a fantastic example of how futuristic technology can be implemented and used to great effect, far in advance of its full scientific understanding.

More recently, a company based in Boston, (USA) is doing something similar, though with far more understanding of the mechanics of the process. Hyperion use carbon nanotubes called FIBRILS to enhance the conducting properties of polymers forming plastics that rival and indeed surpass the electrical properties of copper.¹³ These plastics have found many applications in the motor vehicle industry. Renault was the first car company to incorporate this technology into the "Megane" with a fuel tank that has the corrosion resistance and longevity of plastic with the earthing potential (spark prevention) of metal. The replacement of copper wires with conducting plastic reduces the weight significantly whilst improving the

lifetime and reliability leading to possible use in weight sensitive applications in fields such as aeronautics and F1 racing.

Other technologies are slowly emerging into all walks of life including medical surgery, space technology and household items. Not to mention the possible advances in computing.

Research and especially application is however still dominated by the carbon system, but increasingly the inorganic nanomaterials are catching up and indeed surpassing. The scope and range of different compounds with corresponding ability to tune the physical properties of the resultant products will inevitably push the balance in the favour of the inorganic compounds. As yet few examples exist of actual “real life” applications for inorganic nanosystems, however many applications are being proposed in the literature: Tenne *et al.* have shown fullerene structures of WS₂ being used as solid state lubricants,^{14, 15} overcoming the problems associated with the effects of moisture and vacuum. Graphite loses its ability to act as an effective lubricant in a vacuum because of the loss of adsorbed gas between the layers¹⁵ which aids the important sheering process necessary for lubrication. Bulk phase metal chalcogenide materials can act as good lubricating materials as a result of the inter-crystalline slip between the layers,¹⁵ however are not suitable for use in moist or oxygen rich atmospheres. The movement of the layers creates dangling bonds on the edges and indeed between the layers leading to the formation of oxides in the presence of water or oxygen, rendering the lubrication ineffective. The formation of closed cage like structures of WS₂ that can roll over each other and the surfaces as well as elastically deform to lubricate with good efficiency, overcomes both of these drawbacks and allows for use over a good temperature range.^{14, 15} Other proposed examples include nanoelectronics,¹⁶ catalysis¹⁷ and gas storage,¹⁸ to name just a few.

Perhaps the best-known current application for inorganic nanotechnology is the concept of self cleaning glass.¹⁹ Marketed by a number of leading glass manufacturing

companies, the application of a thin monolayer of anatase structure titanium oxide nanoparticles to the outer surface of a sheet of glass has allowed for “intelligent” self cleaning properties. The photo-catalytic TiO_2 breaks down carbon based deposits in the presence of UV light. It is these deposits that allow for the collection of dirt and residue along with water droplets that lead to the adhesion of dirt to the surface of the glass. The same can be applied to increase the wetability of glass and prevent condensation droplets from forming on mirror surface or to brickwork and paint leading to “ultra” white surfaces that self clean in the presence of UV light. In Japan for instance there is a street made of paving stones containing TiO_2 nanoparticles that is supposed to photo-catalytically clean itself and carbon based deposits from the air caused by motor vehicle pollution. Other examples of this sort of technology use are buildings that stay clean and in fact act as air cleaning agents (Figure 1.1).



Figure 1.1: Images of (a) the TX Millennium brand building (Italcementi Group) and (b) a path in Japan. Both were made using TiO_2 coatings that photo-catalytically clean themselves and the surrounding air.

Another current use of inorganic nanotubes is in measurement of the energy of protein folding using atomic force microscopy. WS_2 nanotubes can be used as tips in an atomic force microscope and used to grip the individual strands of protein in DNA. The energy required to unfold proteins can then be measured by manipulating the DNA using an atomic force microscope.²⁰

1.1.2 Inorganic Compounds Known to Form Nanofibres

Since the discovery of the first inorganic nanotubes, WS₂ by Tenne in 1992,⁸ a plethora of new inorganic systems have been announced in the scientific press. Remškar grouped the different inorganic compounds that are known to form nanofibres into 6 families in her review of inorganic nanosystems in 2004²¹ but it has since been prudent to reorganise this and add a 7th family along with updating with more recently discovered systems. Nitrides are a new and upcoming family of inorganic nanosystems, of relevance to this thesis with many examples appearing in the literature since Remškar's review. Table 1.1 shows a recent table of some of the presently existing inorganic nanofibrous systems divided into the 7 families as discussed above. In a continuing theme throughout the rest of the project, the term nanofibre is defined as any nanostructure with 1-dimensional characteristic, i.e. tube, rod, wire, ribbon etc.

Oxides	Chalcogenides	Halides	Nitrides	Mixed metal compounds	Metals	Others
SiO ₂ ²² TiO ₂ ²³ VO _x ²⁴ V ₂ O ₅ ²⁵ W ₁₈ O ₄₉ ²⁶ MoO ₃ ²⁷ RuO ₂ ²⁷ Al ₂ O ₃ ²⁸ In ₂ O ₃ ²⁹ Ga ₂ O ₃ ²⁹ ZnO ³⁰ BaTiO ₃ ³¹ PbTiO ₃ ³¹ Er, Tm, Yb, Lu Oxides ³² ZnO ³³ Ta ₂ O ₅ ³⁴ ZrO ₂ ³⁵ GaO, CuO ³⁶ CuOH ³⁶ SnO ₂ ³⁷ IrO ₂ ³⁸ CeO ₂ ³⁹ Ga ₂ O ₃ ⁴⁰	WS ₂ ⁸ MoS ₂ ⁴¹ NbSe ₂ ⁴² TaS ₂ ⁴³ CdS ⁴⁴ CdSe ⁴⁵ ZnS ⁴⁶ NiS ⁴⁷ NbS ₂ ⁴³ MoSe ₂ ⁴⁸ WSe ₂ ⁴⁸ TiS ₂ ⁴⁹ HfS ₂ ⁵⁰ ZrS ₂ ⁵⁰ ReS ₂ ⁵¹ Cu ₂ S ⁵² Bi ₂ Se ₃ ⁵³ CdTe ⁵⁴ NbSe ₃ ⁵⁵ Cu ₉ S ₈ ⁵⁶ PbSe ⁵⁷ Ag ₂ S ⁵⁸ TaS ₃ ⁵⁹ Cu _{2-x} Se ⁶⁰	NiCl ₂ ⁶¹ WO ₂ Cl ₂ ⁶²	BCN ⁶³ BN ⁶⁴ AlN ⁶⁵ GaN ⁶⁶ InN ⁶⁷ W(NO) ⁶⁸ SiN ⁶⁹ Li ₃ N TiN Ta ₃ N ₅	PbNb _n S _{n+1} ⁷⁰ W _x Mo _y C _z S _z ⁷¹ Au-MoS ₂ ⁷² Ag- WS ₂ ⁷² Ag-MoS ₂ ⁷² Nb-WS ₂ ⁷³ Cu _{5.5} FeS _{6.5} ⁷⁴ WS ₂ -carbon ⁷⁵ Mo _{1-x} WS ₂ ⁷⁶ NbS ₂ -carbon ⁷⁷ SrBi ₂ Ta ₂ O ₉ ⁷⁸ Co ₄₉ Pt ₅₁ ⁷⁹ Zn ₂ SnO ₄ ⁸⁰ AuCu ⁸¹ AuCu ₃ ⁸¹ CoPt ⁸² LiMo ₃ Se ₃ ⁸³ ZnGa ₂ O ₄ ⁸⁴ Mn ₃ GaN _{0.5} /GaN ⁸⁵ LaMnO ₃ ⁸⁶ BaTi _{0.5} Mn _{0.5} O ₃ InGaAs ⁸⁷	Au ⁸⁸ Co ⁸⁹ Fe ⁸⁹ Bi ⁹⁰ Cu ⁹¹ Ni ⁹¹ Te ⁹² Sb ⁹³	Si ⁹⁴ SiC ⁹⁵ LaB ₆ ⁹⁶ GaP ⁹⁷ WC ⁹⁸ MnP ⁹⁹ InP ¹⁰⁰

Table 1.1: A comprehensive list of many of the inorganic compounds known to form nanofibres, shown with respect to the 7 families. Taken and updated from Remškar.²¹

1.1.3 Conventional Definitions for Inorganic Nanofibres

Following an early publication by Thorne in 1989, the generally accepted definition for a nanoribbon is a nanoscale structure that has a width of at least 5 times the thickness.¹⁰¹ A nanobelt therefore is a “thick ribbon” or nanostructure with width less than 5 times the thickness,¹⁰² as used by Wu *et al.*⁵⁹ and Ma *et al.*¹⁰² Nanowires are a little controversial as the term seems to be used to describe long fibres that are close to round in cross sectional area regardless of whether they conduct electricity as would be expected from a macro-scale wire. Ideally however nanowires should conduct electricity and have higher aspect ratios than rod like formations. Nanorods tend to have low aspect ratios and straighter compositions, i.e. no bends and twist which are common in wires and ribbons, similar to those discussed by Zhu and Kroto.¹⁰³ As their name would suggest, nanotubes should be hollow. For the remainder of this thesis accurate representation of the fibres with respect to the definitions above will be attempted.

1.2 Basic Crystallography

Many of the properties of materials, including those described in this thesis are directly related to the crystal structures. Some understanding of basic crystallography is therefore required.

1.2.1 Unit Cells, Crystal Systems and the Bravais Lattice

Crystals are built up of repeating units of atoms in three dimensions. The repeating unit or motif is known as the unit cell and is defined by three lattice parameters; a , b and c , and three corresponding angles; α , β and γ . Unit cells fit together in three dimensions to give the crystal. There are 7 geometrical representations that can fit together in three dimensions to give a perfectly filled space and are known as the 7 crystal systems (Table 1.2). The 7 crystal systems are defined by symmetry and can only contain 4 specific lattices; primitive, (P), face

centred, (F), body centred, (I) or side centred, (C). Depending on the allowed lattices the combinations of the above leads to the 14 Bravais Lattices. The missing combinations are either not allowed, due to symmetry requirements or are represented by an alternative combination in a more simplified way. The lattices and essential symmetry are outlined in Table 1.2.

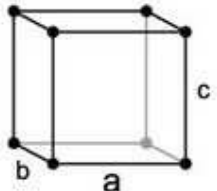
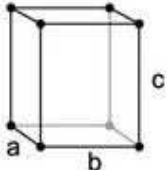
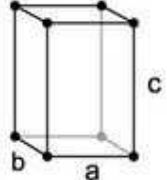
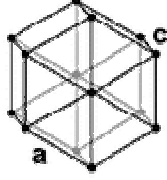
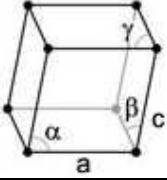
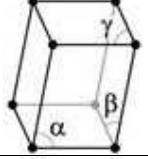
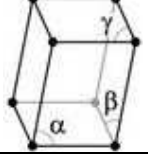
Crystal system	Example	Defining Parameters	Essential symmetry	Possible lattices
Cubic		$a = b = c$ $\alpha = \beta = \gamma = 90^\circ$	3 x 4 fold axes	P, F, I
Tetragonal		$a = b \neq c$ $\alpha = \beta = \gamma = 90^\circ$	1 x 4 fold axis	P, I
Orthorhombic		$a \neq b \neq c$ $\alpha = \beta = \gamma = 90^\circ$	3 x 2 fold axes	P, C, F, I,
Hexagonal		$a = b \neq c$ $\alpha = \beta = 90^\circ$ $\gamma = 120^\circ$	1 x 6 fold axis	P
Rhombohedral		$a = b = c$ $\alpha = \beta = \gamma \neq 90^\circ$	1 x 3 fold axis	P
Monoclinic		$a \neq b \neq c$ $\alpha = \gamma = 90^\circ$ $\beta \neq 90^\circ$	1 x 2 fold axis	P, C
Triclinic		$a \neq b \neq c$ $\alpha \neq \gamma \neq \beta \neq 90^\circ$	none	P

Table 1.2: The 14 Bravais lattices for crystals.

1.2.2 Point Groups

A crystallographic point group is a set of symmetry operations, like reflections or rotations, that leave a point fixed while moving each atom of the crystal to the position of an atom of the same kind. An infinite crystal would therefore look exactly the same before and after any of the operations in its point group. There are an infinite number of 3D point groups; however, they are restricted by having to be compatible with the discrete translational symmetries of the crystal lattice. This restriction results in 32 crystallographic point groups.

1.2.3 Space Groups

The space group of a crystal is a mathematical description of the symmetry inherent in the structure. The space groups in three dimensions are made from combinations of the 14 Bravais lattices (Section 1.2.1) with the 32 crystallographic point groups (Section 1.2.2) which belong to one of 7 crystal systems (Section 1.2.1). This results in a space group being some combination of the translational symmetry of a unit cell including lattice centering, and the point group symmetry operations: reflection, rotation, screw axes and glide planes. The combination of all these symmetry operations results in a total of 230 unique space groups describing all possible crystal symmetries.

Space groups can be defined using the international notation or Hermann-Mauguin notation by combining the point group identifier with the uppercase P, C (often noted as R), I, or F for primitive, side-centred, body-centred, or face-centred lattices. Translations within the lattice in the form of screw axes and glide planes are also noted, giving a complete crystallographic space group.

The screw axis is noted by a number, n , where the angle of rotation is $\frac{360^\circ}{n}$. The degree of translation is added as a subscript showing how far along the axis the translation is,

as a portion of the parallel lattice vector. E.g. $P2_1$ is a primitive lattice with a 180° (two-fold) rotation followed by a translation of $\frac{1}{2}$ of the lattice vector.

Glide planes are noted by a, b, or c depending on which axis the glide is along. There is also the n glide, which is a glide along the half of a diagonal of a face, and the d glide, which is along a quarter of either a face or space diagonal of the unit cell. The latter is often called the diamond glide plane as it features in the diamond structure.

1.2.4 Miller Indices

Lattice planes can be defined within the crystal such that the planes are equally spaced with all lattice points lying on members of the set. The planes cut the cell axes at fractions or infinity, if they are parallel to cell axes and the reciprocal of these are the Miller indices. In three dimensions these are defined by three indices; h, k and l. The space between the planes is the d_{hkl} spacing. An example of this in 2 dimensions is shown in Figure 1.1.2.

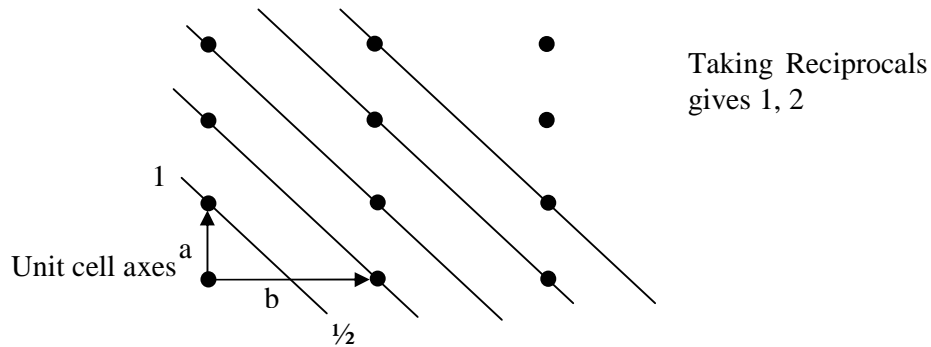


Figure 1.1.2: Miller indices for a 2-dimensional lattice with unit cell (a,b) .

The Miller indices are related to the d_{hkl} spacing using formulae that are specific to crystal types. For instance for orthogonal crystals (i.e. $\alpha = \beta = \gamma = 90^\circ$), the d spacing for any set of planes is given by Equation (1.1).

$$\frac{1}{d_{hkl}^2} = \frac{h^2}{a^2} + \frac{k^2}{b^2} + \frac{l^2}{c^2} \quad (1.1)$$

This is simplified in a cubic system as;

$$a = b = c \quad (1.2)$$

Therefore combining Equation (1.1) and Equation (1.2) gives:

$$\frac{1}{d_{hkl}^2} = \frac{h^2 + k^2 + l^2}{a^2} \quad (1.3)$$

In other systems the relationship is more complicated and shown in Table 1.3.

Crystal System	Interplanar spacing
Cubic	$\frac{1}{d_{hkl}^2} = \frac{h^2 + k^2 + l^2}{a^2} \quad (1.4)$
Tetragonal	$\frac{1}{d_{hkl}^2} = \frac{h^2 + k^2}{a^2} + \frac{l^2}{c^2} \quad (1.5)$
Orthorhombic	$\frac{1}{d_{hkl}^2} = \frac{h^2}{a^2} + \frac{k^2}{b^2} + \frac{l^2}{c^2} \quad (1.6)$
Hexagonal	$\frac{1}{d_{hkl}^2} = \frac{4}{3} \left(\frac{h^2 + hk + k^2}{a^2} \right) + \frac{l^2}{c^2} \quad (1.7)$
Monoclinic	$\frac{1}{d_{hkl}^2} = \frac{1}{\sin^2 \beta} \left(\frac{h^2}{a^2} + \frac{\sin^2 \beta}{a^2} + \frac{l^2}{c^2} - \frac{2hl \cos \beta}{ac} \right) \quad (1.8)$
Triclinic	$\frac{1}{d_{hkl}^2} = \frac{1}{V^2} \left[h^2 b^2 c^2 \sin^2 \alpha + k^2 a^2 c^2 \sin^2 \beta + l^2 a^2 b^2 \sin^2 \gamma \right.$ $+ 2hkabc^2 (\cos \alpha \cos \beta - \cos \gamma) + 2kla^2 bc (\cos \beta \cos \gamma - \cos \alpha)$ $\left. + 2hlab^2 c (\cos \alpha \cos \gamma - \cos \beta) \right]$ (1.9) $V = abc \left[1 - \cos^2 \alpha - \cos^2 \beta - \cos^2 \gamma + 2 \cos \alpha \cos \beta \cos \gamma \right]^{\frac{1}{2}}$

Table 1.3: Table showing the interplanar spacings for the different crystal systems.

Also of note is that in a hexagonal system it is often considered more practical to split the three indices into four as a result of the symmetry giving hki in the plane of the hexagon with angle 120 ° and l perpendicular to it. This notation is known as hexagonal indices notation and often given as [hkil]. With the use of hexagonal indices the d-spacing formulae given in Equation (1.7) can be represented by Equation (1.10).

$$d_{h,k,i,l} = \frac{\sqrt{\frac{3}{2}}a}{\sqrt{h^2 + k^2 + i^2 + \left(\frac{l}{\sqrt{\frac{2}{3}}\frac{c}{a}}\right)^2}} \quad (1.10)$$

Using the above formula, it is possible to assign h, k, (i,) and l values to d-spacings in a hexagonal system and vice versa. The d-spacings between atom layers can be seen using diffraction techniques. This project has utilised both powder X-ray diffraction (Section 2.4.1) and electron diffraction (Section 2.4.3.2).

1.2.5 Bragg's Law

When irradiated by radiation with frequency close to that of the atomic spacing, (X-rays) the hkl planes of atoms within the lattice can be considered semi transparent mirrors as shown in Figure 1.3.

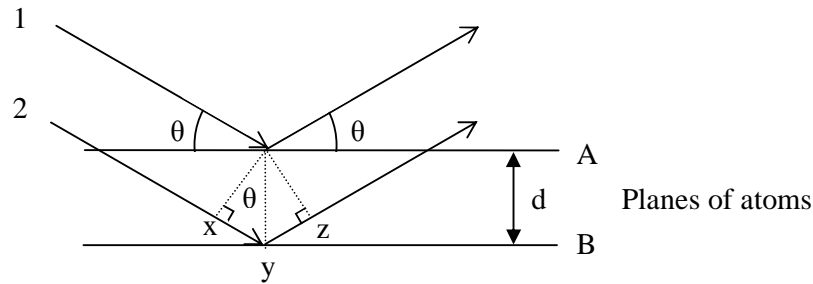


Figure 1.3: Derivation of Bragg's law, showing parallel Rays, 1 and 2 incident on a surface consisting of semi transparent planes of atoms.

Some of the X-rays are reflected off the atom planes with the angle of incidence equal to the angle of reflection whilst the majority are transmitted through, to be reflected off the lower planes. If two parallel rays are incident, 1 and 2, and reflect off adjacent planes, A and B, then the reflected rays will either constructively or destructively interfere depending on their phase. The conditions in which the two reflected planes will constructively interfere, with one and other, is when they reunite with the same phase. This can only occur when the extra distance travelled by Ray 2 is equal to an integral number of wavelengths. Hence:

$$xyz = n\lambda \quad (1.11)$$

From Figure 1.3 we can see, from basic trigonometry;

$$xyz = 2d \sin \theta \quad (1.12)$$

Combining Equations (1.11) and (1.12) gives:

$$2d \sin \theta = n\lambda \quad (1.13)$$

Strong reflections are therefore only observed for d-spacings that satisfy Equation (1.13). The diffractometer scans through angles of θ recording the intensity of the diffracted radiation as a measure of counts per unit time.

1.3 Charge-Density-Waves

When metals are cooled, they often undergo a phase transition leading to a different state with different types of order. These different types of order can have dramatic consequences on the electronic structures and thus the electronic and magnetic properties. For instance, metals such as lead, mercury and aluminium become superconductors at low temperatures as a result of electrons teaming up in Cooper pairs.¹⁰⁴ These pairs of opposite spin and momentum electrons can propagate through the new low temperature lattice order in a cooperative way with no loss of energy leading to superconducting properties. (See Section 1.4.4) Alternatively metals like iron and nickel become ferromagnetic as their unpaired electrons align leading to net magnetisation without the presence of a field. Resulting as a consequence of the temperature dependent phase transition, the underlying phase transition occurs at a specific temperature leading to critical values rather than general temperature trends.

In the mid 1970's a wide range of materials were discovered that showed quasi 1-dimensional properties. This class of materials are structurally unique and as such show unique physical properties. Examples of the unique properties are anisotropic electrical conduction, gigantic dielectric constants, unusual electronic properties and rich dynamical

behaviour. Perhaps the most striking of the unique properties is that of the formation of Charge-Density-Waves (CDW).¹⁰⁴

The simplest explanation for what a CDW is that a charge-density-wave is a modulation of the conduction electron density in a metal and an associated modulation of the lattice atom positions.¹⁰⁴ As with many interesting phenomena the ideas and theories needed to understand properties span many disciplines and indeed much of our understanding of condensed matter.

1.3.1 Formation of Charge-Density-Waves

In a metal the uniform separation of the periodic lattice with the atoms in their equilibrium positions leads to a highly uniform electron density as shown in Figure 1.4. This highly regular electron density is held in place by the high cost in coulomb energy for localised areas of high or low electron density. These local variations are highly suppressed resulting in a uniform electron density over the lattice. Some low dimensional materials at temperatures below a critical temperature T_P known as the Peierls temperature can under go a Peierls transition. This transition leads to a periodic distortion in the lattice (PLD) and results in a modulation of the electron density across the lattice. This is shown in the lower part of Figure 1.4. It is this periodic electron density that is known as a charge-density-wave.^{105, 106}

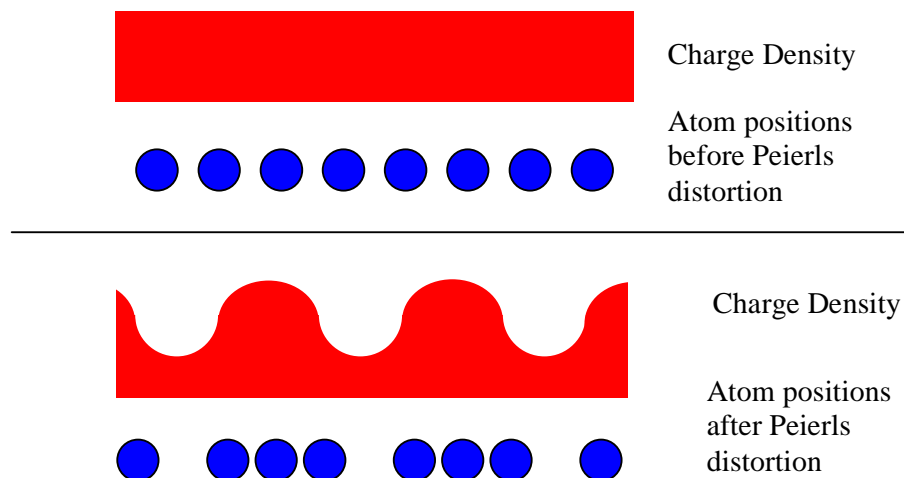


Figure 1.4: Diagram to show the origins of CDWs.

The periodic distortion of the ion lattice ($\sim 1\%$ of the inter-atomic spacing) creates a super-unit cell which through quantum mechanics slightly reduces the kinetic energy of the highest energy electrons. In a chicken and egg type situation, the reduction of kinetic energy can in certain circumstances compensate for the elastic energy needed for the lattice distortion that caused the change in kinetic energy in the first place. In quasi 1-dimensional metals at low temperatures, below T_P , the elastic energy cost to modulate the atomic positions is less than the gain in conduction energy associated with this loss in kinetic energy of the electrons. The CDW state is thus preferable as the ground state while at high temperatures, above T_P , the electronic energy gain is reduced by thermal excitation so the metallic undistorted state is most stable.¹⁰⁴⁻¹⁰⁶

1.3.2 Conduction in Charge-Density-Wave Systems

The mechanism of conduction is unlike that of semiconductors and metals (which conduct electricity by moving electrons through partially filled bands,) as it involves collective charge transfer. Since the trough of the wave (Figure 1.4) can be placed anywhere within the lattice without changing the total energy of the system, the CDW may slide freely thus allowing the conduction of charge in an electric field. The full band below the Fermi energy doesn't need any thermal excitation to promote electrons to the higher unoccupied band as the band itself can simply slide with respect to the lattice in the presence of an electric field. Lattice atoms oscillate back and forth producing a travelling potential. The conducting electrons then move with this potential to produce a current.¹⁰⁵

The CDW is pinned to the underlying lattice but free to move at the same time leading to two main characteristics. If the CDW's wavelength λ_c is an integral multiple of the lattice parameter "a" then the CDW is said to be "commensurate" as it has preferred positions relative to the lattice and its energy will oscillate with a period λ_c . In most cases however the CDW's wavelength is pinned weakly to the underlying lattice and strongly to impurities and

lattice dislocations. In the presence of a single impurity the system can lower the overall coulomb energy part of the Hamiltonian by positioning the trough or crest of a wave over the impurity in the lattice depending crudely on the electro-negativity of the impurity with respect to the lattice as a whole. In the presence of many impurities the CDW elastically deforms to optimise the impurity interaction energy. A similar thing happens with lattice distortions and dislocations. The wavelength of the CDW is now “incommensurate” with respect to the lattice. These interactions interfere with the free motion of the CDW and thus interfere with the conduction properties. In low fields both commensurate and incommensurate CDW will remain pinned to the lattice until the field exceeds the pinning strength of the interactions and will therefore exhibit a threshold field E_T below which no conduction will occur. CDW theories have for a while shaped the theories of superconductivity. In theory CDW materials should superconduct as the commensurate wave is free to move with no resistance; however, the impurities and lattice distortions prevent this at any temperature above absolute zero.^{101,}

104-106

1.3.3 Measurable Properties of Charge-Density-Wave Systems

Whilst the CDWs are particularly hard to actually “see,” given the equipment available, the effect they have are potentially noticeable. These effects include the pinning potential, the Peierls transition and the resistivity measurements. Atomic resolution STM can see the PLD, while variable temperature electronic measurements can observe the change in resistivity of the materials at low temperature.

1.4 Magnetic Materials

The magnetic properties of materials are controlled by the presence of unpaired electrons. If there are no unpaired electrons the material is said to be diamagnetic. If a material has unpaired electrons then it can be characterised in a number of ways. The major types of magnetic materials are as shown in Table 1.4.

Diamagnetic	No unpaired electrons.
Paramagnetic	Random orientation of electrons on different atoms.
Ferromagnetic	Alignment of electrons on all the atoms.
Antiferromagnetic	Antiparallel alignment of electrons on all the atoms.
Ferrimagnetism	Antiparallel arrangement with an unequal number of electrons in each direction.
Spin glass	Antiferromagnetic array, which is disrupted or frustrated by ferromagnetic coupling in localised domains.

Table 1.4: Table showing different types of magnetic materials

These different classifications lead to different properties and different traits. To understand the differences in these types of magnetic materials, an understanding of the interactions between the material and the magnetic field necessary.

Although convention dictates that SI units should be used; cm, gram, seconds (cgs) units are more convenient for these sorts of measurements and are used as standard in the literature and have therefore been used throughout this thesis. The difference in the two sets of units occurs as a result of different choices in the definition of the magnitude of the magnetic field, H , at a distance, r , from a magnetic monopole, q , (Equations (1.14) and (1.15)).

$$H = \frac{q}{4\pi r^2} \quad (SI) \quad (1.14)$$

$$H = \frac{q}{r^2} \quad (cgs) \quad (1.15)$$

H = Magnetic field

q = Magnetic monopole

r = Distance

There are four fundamental terms used to describe how a material is “magnetised.” These are; magnetic field, (H), magnetic induction, (B), magnetic polarisation or magnetisation (J), and magnetic moment per unit volume (M). Their roles and relationships are described below. The units for magnetic related measurements are shown in Table 1.5, along with their conversion factors from cgs to SI units.

<u>Quantity</u>	<u>cgs unit</u>	<u>Conversion cgs to SI</u>
Magnetic field H	Oe	$10^3/4\pi$
Magnetic induction B	Gauss	10^{-4}
Magnetisation M	Oe	10^3
Molar magnetisation J	Oe mol ⁻¹	10^3
Magnetic moment μ	emu	10^{-3}
Magnetic susceptibility χ	emu cm ⁻¹	4π
Molar susceptibility χ_m	emu mol ⁻¹	$4\pi \times 10^{-6}$
Gram Susceptibility χ_g	emu g ⁻¹	$4\pi \times 10^{-3}$
Magnetic flux ϕ	Gcm ²	10^{-8}
Magnetic moment Bohr Magnetons	9.274×10^{-27} emu	

Table 1.5: Units of magnetic measurements and their conversion table to SI.

If a substance is placed in a magnetic field H, the magnetic flux density, B will be related to the field by its permeability μ . This can be rewritten using the permeability of free space, μ_0 and the magnetisation, M.

$$B = \mu H \quad (1.16)$$

$$B = \mu_0 H + \mu_0 M \quad (1.17)$$

It follows from this that $\mu_0 H$ is the induction contribution generated by the field and $\mu_0 M$ is the induction generated by the material. The magnetic susceptibility of the material is defined as the ratio between the two contributions and is given as χ .

$$\chi = \frac{M}{H} \quad (1.18)$$

Substituting B Equation (1.16) into Equation (1.17) gives:

$$\begin{aligned} \mu H &= \mu_0 H + \mu_0 M \\ \mu &= \mu_0 (1 + \chi) \end{aligned} \quad (1.19)$$

The ratio of $\mu:\mu_0$ is known as the relative permeability μ_r

$$\mu_r = \frac{\mu}{\mu_0} = 1 + \chi \quad (1.20)$$

It is usual when looking at magnetic properties to consider the susceptibility. This is a measure of the response of a sample to an applied magnetic field. The susceptibility depends

on the amount of sample in the field, and is often rendered more useful by reference to the gram susceptibility, χ_g or molar susceptibility χ_M . These are measures of the total susceptibility given either per gram of substance or per mole respectively.

The different magnetic behaviours of materials can be characterised with respect to χ and μ_r values and their dependence on the applied field and temperature.

Diamagnetic materials have small negative values of χ , while paramagnetic materials have small positive values of χ . Hence, the flux density of diamagnetic materials decreases when in magnetic fields while the flux density of paramagnetic materials will increase. This leads to diamagnetic materials experiencing repulsion to the field while paramagnetic materials are attracted. Superconductors show in principle, perfect diamagnetism with a χ_M value of -1 emu mol^{-1} . Thus, the magnetic field is completely expelled.

In ferromagnetic materials χ is $\gg 1$ and hence there is a great attraction to the field, while in antiferromagnetic materials χ is positive but small.

<u>Material</u>	<u>Expected χ_M values</u>	<u>Reaction to a magnetic field</u>	<u>Dependence on a field H</u>	<u>Dependence on temperature</u>
Diamagnetic	Small -ve $-(1 \text{ to } 600) \times 10^{-5}$	Repelled	Independent	None
Perfect diamagnet, superconductor	-1	Entirely repelled		Dependent on T_C .
Paramagnet	Small +ive 0 to 0.1	Attracted	Independent	Decreases
Ferromagnet	1 to 10^7	Strongly attracted	Dependent	Decreases
Antiferromagnet	0 to 0.1	Attracted	May be Dependent	Increases
Pauli paramagnet	10^{-5}	Attracted	Independent	None

Table 1.6: Table to show the different types of magnetism, their expected χ_M values and their characteristic behaviours and properties.

1.4.1 Types of Magnetic Material

1.4.2 Paramagnetic Materials

Many paramagnetic materials obey Curie law behaviour, which states that the susceptibility is inversely proportional to the temperature, (Equation (1.21)).

$$\chi = \frac{C}{T} \quad (1.21)$$

χ = Susceptibility

C = Curie Constant

T = Temperature K

The relationship assumes no spontaneous interaction between adjacent unpaired electrons. If an interaction between adjacent electrons occurs then it is likely that ferromagnetic or antiferromagnetic behaviour is occurring at low temperature. The high temperature paramagnetic behaviour can be modelled using the Curie-Weiss law. θ is the Weiss constant.

$$\chi = \frac{C}{T - \theta} \quad (1.22)$$

θ = Ferromagnetic Curie temperature T_C . – Weiss constant

Ferromagnetic behaviour ($\theta = \text{-ive}$) moves the Curie fit to the right while antiferromagnetic behaviour ($\theta = \text{+ive}$) moves the Curie fit to the left. The temperature T_C obviously cannot be reached but the material departs from the Curie-Weiss (CW) behaviour at temperatures below the Neel temperature, T_N .

Ferromagnetic materials at low temperature have very high χ values, which fall off increasingly fast as the temperature rises. However, this only occurs below T_C . Above T_C the material displays CW behaviour so plots of χ^{-1}/T give straight lines with a curved section at temperatures below T_C . The cold region can be examined further by plotting relative magnetism against T/T_C . The effective magnetic moment can be calculated by the upper region of this plot where the fit to the CW law is best.

Antiferromagnetic materials have very small values of χ in well-ordered structures, which rises as the temperature increases as a result of thermally introduced disorder into the antiferromagnetic state. χ increases through a maximum at T_N and then decreases at higher temperature still, following the CW behaviour.

The effective magnetic moment μ_{eff} relates directly to the number of unpaired electrons and is only a valid measure if the unpaired electrons on the different atoms are isolated, as is the case when dealing with paramagnetic materials that show CW behaviour.

$$\chi_M = \frac{N_A \mu_0 \mu_B^2 \mu_{\text{eff}}^2}{3kT} \quad (1.23)$$

χ_M = Molar susceptibility. ($\text{M}^3 \text{mol}^{-1}$)

N_A = Avagadro's number 6.02×10^{23}

μ_0 = Permeability of free space, 1.62×10^{-6}

μ = Magnetic moment in JT^{-1}

k = Boltzmann constant $1.3806503 \times 10^{-23}$

μ_B = Bohr Magnetron = 9.274×10^{-24}

It therefore follows that the magnetic moment is given by:

$$\mu_{\text{eff}} = \sqrt{\frac{\chi_M 3kT}{N_A \mu_0 \mu_B^2}} \quad (\text{BM per formula unit}) \quad (1.24)$$

$$\mu_{\text{eff}} = 797.87 \sqrt{\chi_M^{\text{SI}} T} \quad (\text{BM}) \quad (1.25)$$

As
$$\sqrt{\frac{3k}{N_A \mu_0 \mu_B^2}} = 797.87 \quad (1.26)$$

Converting for cgs units we see that μ_{eff} is given by

$$\mu_{\text{eff}} = 2.827 \sqrt{\chi_M^{\text{cgs}} T} \quad (1.27)$$

By applying the Curie law to this χ_M value we obtain:

$$\mu_{\text{eff}} = \sqrt{C} \times 2.827 \quad \text{as } \chi_M = \frac{C}{T} \quad (1.28)$$

Linear regression of the χ_M^{-1} against T plots gives an accurate value for the μ_{eff} in specific regions of the graph, i.e. the high temperature region where the CW behaviour is most likely.

The linear regression gives the gradient which is $1/C$ allowing the use in Equation (1.28) for μ_{eff} calculation. As the magnetic moment relates to the number of unpaired electrons, (u_{pe}), it is possible to use the value of μ_{eff} as a measure of the number of unpaired electrons. Theoretical values of μ can be calculated from quantum theory.

$$\mu_s = g\sqrt{S(S+1)} \quad S = \frac{u_{pe}}{2} \quad (1.29)$$

μ_s is the spin only value for the magnetic moment

S is the total spin quantum number of the atoms

g is a gyromagnetic ratio that for a free electron has the value 2.00023 BM

Number of unpaired electrons	Magnetic moment μ_s BM
1	1.73
2	2.83
3	3.87
4	4.9
5	5.92

Table 1.7: Table to show the theoretical values of BM that correspond to the number of unpaired electrons.

Deviations from these values are caused by an orbital angular momentum contribution, which is dependent on the orbital angular momentum quantum number, L .

$$\mu_{S+L} = \sqrt{4S(S+1) + L(L+1)} \quad (1.30)$$

Both of these theoretical values are applicable to free electrons but the LS coupling tends to be less reliable unless heavy metal atoms are present like the lanthanides. In practice the latter is less reliable as the orbital angular momentum is partially or wholly quenched as electric fields on surrounding atoms restrict the orbital motion of the electrons. Hence these values overestimate the μ_{eff} .

1.4.3 Ferromagnetic Materials

Ferromagnetic materials show a cooperative interaction between the spins on the atoms, which align with an applied magnetic field. An increase in χ_g with temperature is observed, up to a specific temperature T_c , at which point the thermal energy is such that the alignment of

the spins is disrupted breaking down the ferromagnetism. Paramagnetic behaviour follows with a decrease in χ_g with temperature.

In ferromagnetic materials the magnetic moment is field dependent and it is often a useful way of characterising the material by way of a hysteresis curve at different temperatures. Here the temperature is set and the field scanned (Figure 1.5).

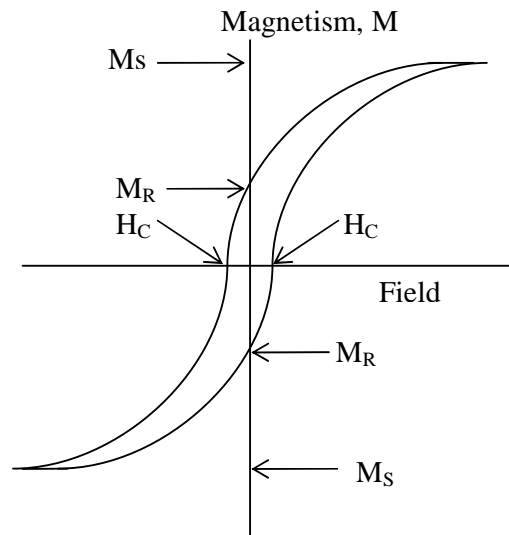


Figure 1.5: Schematic of a hysteresis curve.

M_S = Saturation magnetisation.

M_R = Remnant magnetisation.

H_C = Coercive Field.

Ferromagnetic materials can be characterised into two categories, hard and soft. This is referring to the cyclability in the hysteresis. A magnetically soft material has small M_S and H_C values, indicating that little energy is required to reach the saturation magnetism. A hard material has large M_S and H_C values, indicating that more energy is needed to reach saturation. The energy lost in the cycle is given by the area between the hysteresis curves.

1.4.4 Superconducting Materials

Superconductivity was first discovered by Heike Onnes, a Dutch scientist in 1911¹⁰⁷ when he noticed that there was a dramatic decrease in the resistance of mercury at liquid helium temperatures, 2 K. Since this discovery, superconductivity has been found in a number of

metals, alloys and compounds. So-called high temperature superconductivity was discovered in 1986 in the ceramic oxides $\text{La}_{2-x}\text{Ba}_x\text{CuO}_4$ ¹⁰⁸ and $\text{YBa}_2\text{Cu}_3\text{O}_7$.¹⁰⁹ The latter was the first example of superconducting state that was accessible by liquid nitrogen (above 77 K), and has brought superconductivity into the realms of possible application. Currently superconductors have applications in many fields: medical imaging; (MRI scanners), analytical science, (NMR characterisation and SQUID, see Section 2.4.5) transport; (Tokyo trains that hover), power storage; (superconducting magnetic energy storage mediums), and power production (superconducting alternators) to name but a few.¹¹⁰ Many of the current restrictions between theoretical possibilities and actual application involve limits of critical temperature T_C and critical field H_C . As yet, the highest temperature superconductor is still a far cry from the target of room temperature superconduction at around 300 K.

Superconductors have many characteristics; one of these is the concept of zero resistance in the superconducting state. Normal metals show a rise in resistance with temperature as a result of phonon scattering as the electrons pass through the material. Superconductors however experience a sudden decline in resistance as the temperature falls below a specific point. This is known as the T_C .

Traditionally superconductivity has been explained by the use of “Cooper pairs.” The theory is called BCS theory, named after Bardeen, Cooper and Schrieffer who were awarded the Nobel Prize in 1972 for their findings. Cooper pairs are pairs of electrons that couple together and travel through the material in a cooperative way as a superfluid, transferring charge as an exchange of phonons.¹¹¹

When a material has zero resistance below T_C it will expel a magnetic field up to a critical field strength, H_C (H_C is temperature dependant) and the material therefore becomes perfect diamagnet. This gives rise to the Meissner effect, as demonstrated when a superconductor levitates above a magnet. The unusual, rather uninteresting property of diamagnetism, which is experienced as a weak repulsion effect shown by all materials, now

becomes a major effect with enormous applicable properties, such as levitation. It is this perfect diamagnetism that allows us to characterise superconductors using SQUID magnetometry (Section 2.4.5.)

1.5 **MX₂ Compounds (Bulk)**

Much interest in this thesis concerns the layered chalcogenides that fit the formula MX₂, (M = Group IV, V, VI transition metal and X = S, Se, Te.) These materials have been studied over many years and much is known about their bulk structures. In general the structures consist of two types of three atom thick sandwiches or tri-layers, both involving a close packed array of chalcogen atoms with the metal ion either in an octahedral or trigonal prismatic coordination with the chalcogens. On the basis of these two coordination layers, many polytypes have so far been proposed mainly from the study of powdered samples. These polytypes depend on the compound under observation. For example, in TaS₂, F. Jellinek has proposed structure models for the 1T, 2H, 3R and 6R phases¹¹² from X-ray diffraction while F. J. DiSalvo has proposed an extra 4H_b-type structure.¹¹³

The majority of the MX₂ compounds have the fully octahedral structure as the high temperature phase, though MoS₂ has the trigonal prismatic phase.¹¹⁴

Formal oxidation states can be assigned to the ions in the structures with the metal having a 4⁺ charge and the chalcogen having a 2⁻ charge however there will be a degree of non stoichiometry and metal to metal bonding that will interfere with the formal oxidation states.

For the clarity of the text, the individual polytype of MX₂ structures will largely hereon be referred to in the noun form, with their “prefix” and “-TaS₂”, e.g. the 2H polytype of TaS₂ will be known simply as 2H-TaS₂.

1.5.1 Tantalum Disulfide

Tantalum disulfide is a typical member of the dichalcogenide group, and has been known for many years with the crystal structures first published by Jellinek in 1962.¹¹² Its initial discovery as one of the layered dichalcogenides has led to much interest in its electronic and physical properties including a wealth of research covering superconductivity and intercalation. It is known to have many polytypes, of these the conventionally labelled 1T,¹¹² 2H,^{112, 115} 3R^{112, 116} are the most common but there is also the presence of a 6R,^{112, 117} 4H_b¹¹³ structure as well as others that either do not carry the conventional labelling or are non stoichiometric. The difference between the polytype structures is due both to the coordination of the tantalum atoms with respect to the sulfur atoms within the try-layer sandwiches, and indeed the alignment of the sandwiches themselves. For example, the 1T polytype has octahedral coordination within the try layers, whilst the 2H and 3R polytypes both have trigonal prismatic coordination. The 4H_b and 6R polytypes consist of alternate octahedral and trigonal prismatic layers.¹¹⁸

For the sake of this thesis I will concentrate on the 1T, 2H and 3R structures as these are most relevant. The crystal structures are shown in Figure 1.6.

Of the three polytype structures the octahedrally coordinated 1T structure is the high temperature phase stable at temperatures above 1100 K but meta stable at temperatures below 550 K upon quench cooling¹¹⁹ and appears golden in colour. The stacking sequence can be related to the identical layers of atoms in terms of “ABC” notation where the corresponding letters align in phase with one and other. The 1T polytype structure can therefore be denoted as a simple ABC repeating unit see Figure 1.6. The 2H and 3R polytype structures both have trigonal prismatic coordination between the tantalum atoms and the sulfur atoms, and can be denoted by the ABACBC and ABACDCEFE stacking sequence respectively. Both the 2H and 3R structures appear as a fine blue / black powder, are stable at room temperature and are considered to be common phases. 2H-TaS₂ can be synthesised by annealing the 1T polytype

at 823 K,¹²⁰ though perfect crystallinity is rarely achieved, and is interesting as along with the 4H_b phase, displays superconductivity. The 3R structure can again be made by annealing at 800 K for longer periods of time.¹¹² The initial production of TaS₂ from elemental powders tends to produce a number of different polytypes and produce poor quality polytype phases with many lattice distortions, largely as a result of the energy of formation for the different phases being very similar.¹¹⁸ Some work in this thesis involved trying to reproduce reliable syntheses for the production of individual polytypes in the bulk phases, see Section 3.2.1.4.

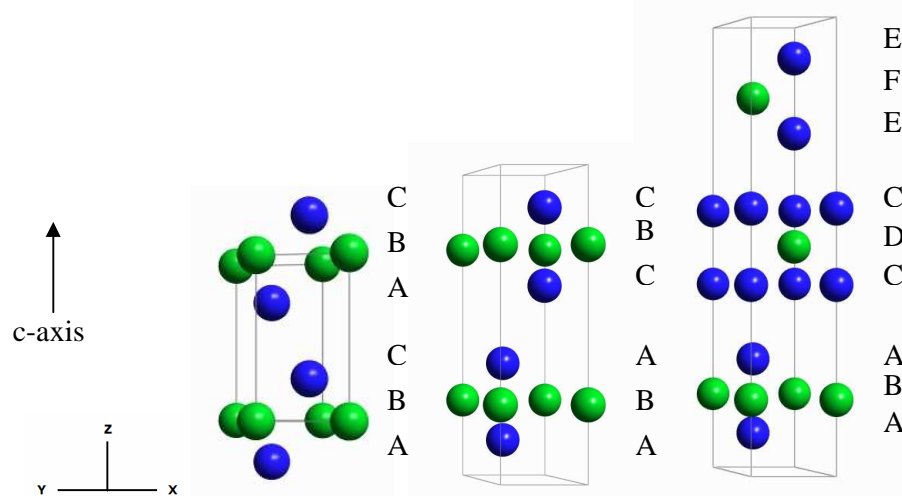


Figure 1.6: Pictorial representation of the structure of the 1T, 2H and 3R polytypes of TaS₂ showing the origins of the ABC notation.

1.5.2 Properties of TaS₂

The dichalcogenide materials of the group VI, V, VI elements are perfectly suited to intercalation given their layered structures. The weak van der Waals forces that hold the tri-layers together, allow the layers to separate creating space with which to accommodate the guest species within the host structure. A combination of the elongation of the c-axis and the changing of the band structure of the host species leads to in some cases dramatic changes in the properties of the host. These have been extensively investigated during the late 1980's and early 1990's.^{121, 122} Changes in physical properties can result from the intercalation of alkali metals, late transition metals and inorganic or organic molecules within the structure of

these layered dichalcogenides.^{121, 123} These intercalations can induce metal to semi-metal transitions, alter the charge-density-waves and change the superconducting properties as they change the structure of the host material.^{121, 123}

Tantalum disulfide undergoes extensive intercalation of many species, consequentially changing its physical and electrical properties in all three of the above mentioned polytypes as they all contain the layered structures with weak van der Waals forces between the tri-layers. An example of this is the intercalation of 2H-TaS₂ with organic molecules like methylene blue has been seen to raise the superconducting T_c from 0.6 K to between 2 and 5.5 K.¹²¹ The intercalation of Li and Sn into 2H-TaS₂ has also led to changes in crystal structure and to changes in electronic properties.¹²²

Of the three polytypes above, only the 2H structure is known to exhibit superconductivity,¹²¹ though the little known 6R and 4H_b also show a tendency towards superconductivity at low temperature. The density of states diagrams for the 1T and the 2H polytypes are shown in Figure 1.7 and leads to the conclusion that both 1T and 2H structures are metallic. The Fermi-surface in the 2H structure lies close to the boarder between metallic and semiconductor behaviour as it is very close to the top of a conducting band and near to a small band gap in the trigonal prismatic configuration and is believed to be the source of the superconductivity. There is likely an interaction between the electrons in the Fermi-surface and the top of the partially filled band. The formation of Cooper pairs can lower the overall energy of two electrons (with respect to two independent electrons) as they are constrained by the band gap in near proximity. Cooper pairs can cooperatively propagate through the structure leading to superconduction.

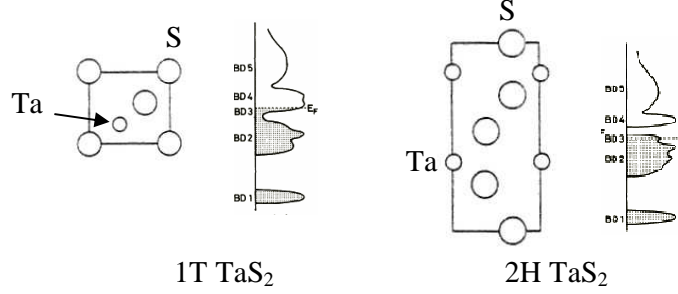


Figure 1.7: Density of states diagram for the 1T and 2H polytype of TaS_2 .¹²⁴

Bulk 2H- TaS_2 is known to superconduct at 0.6 K¹²⁵ or 0.8 K¹¹⁵ depending on the source. It has been found that the intercalation can lead to an increase in T_C from the 0.6 K / 0.8 K of the empty bulk material to between 2 and 5.5 K depending on the size of the intercalated species.¹²¹ The cause of this increase has been put down to either a suppression of structural instability¹²¹ or the formation of metal-metal bonds.¹²⁶ It is most likely due to both these factors and the formation of the commensurate CDWs.

The layered structure and atomic positioning of the tantalum atoms within the tri-layers of all three polytypes leads to metal-metal interactions and electrical conduction only along the planes of the layers. The sulfur atoms and the inter layer region lead to significant insulation between the layers giving quasi two-dimensional conduction or low dimensional behaviour.

All three of the polytypes of TaS_2 considered above can undergo a Peierls distortion and therefore exhibit CDWs. Section 1.3 outlines the theory behind what CDWs are and how they form. Much work has been done during the 90's concerning the phenomena of CDW in TaS_2 as significant similarities between CDWs and superconductivity theory exist. The two phenomena are closely related and dichalcogenide materials provided a suitable and convenient basis for the research in these fields.¹²⁷

1.6 MX₃ Compounds

Much interest in this thesis concerns the non layered, low dimensional chalcogenides that fit the formula MX₃, (M = Group IV, V, VI transition metal and X = S, Se, Te.) These materials have been studied over many years and much is known about their bulk structures. In general the structures consist of infinite chains of [MX₆] octohedra that extend parallel to the *b* axis and share upper and lower faces. The chains are separated by relatively large distances and weak interchain bonds.¹²⁸ It is these chains that give the MX₃ compounds their pseudo 1 dimensional properties. Formal oxidation states can be assigned though there is a high level of metal–metal interaction occurring. In the sulfide and selenide system it is possible to form X₂²⁻ species as well as X²⁻ species leading to the formal oxidation states of M⁴⁺ and X₂²⁻ + X²⁻.¹⁰²

1.6.1 Tantalum Trisulfide

Tantalum trisulfide (TaS₃) is a similar compound to the tantalum disulfide discussed in Section 1.5.1 with a few structural differences. It is highly significant in that the dimensionality has been lowered from a pseudo 2-dimensional system to a pseudo 1-dimensional system, now with infinite chains of tantalum atoms propagating throughout structure as shown in Figure 1.8 rather tantalum atoms extending through the 3 atom thick sheets in TaS₂. The monoclinic structure (m-TaS₃) was published in 1981 by Meerschaut *et al.*¹²⁹ with space group *P*2₁/*m* and unit cell parameters *a* = 9.515(2) Å, *b* = 3.3412(4) Å, *c* = 14.92(2) Å, and β = 109.99(2) °. The bonding shows 2 distinct S-S bond distances, (~2.05 Å and ~2.8 Å) in the base of the trigonal prism chains that make up the structure corresponding to the expected values of S-S bonds in the S₂²⁻ species and in compounds containing a pair of S²⁻ ions e.g. TaS₂. This indicates that the structure likely contains Ta⁴⁺, S₂²⁻ and S²⁻ species as shown in blue and yellow in Figure 1.8.

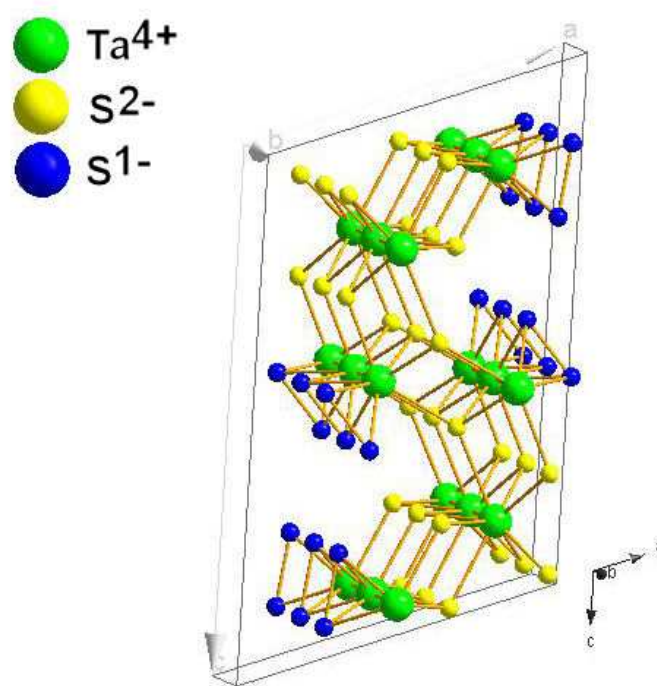


Figure 1.8: Crystal structure of TaS₃ (m-TaS₃) showing 4 unit cells stacked along the *b* direction of the unit cell.¹²⁹

First observed in 1938 by Blitz and Kocher¹³⁰ and then reconfirmed by Jellinek in 1962,¹¹² its presence and properties have interested physicists and chemists alike. There are two commonly referred to structures, the orthorhombic and the monoclinic. To differentiate between the different structures of TaS₃, the structures have been referred to with a prefix denoting whether the structure is monoclinic or orthorhombic followed by a subscript indicating the specific information about the phase where necessary. It is possible to prepare m-TaS₃ from elemental powders at 750 °C with a slight excess of sulfur over a 15 day period.¹³¹ The orthorhombic structure (o-TaS₃) with space group *C*222₁ has yet to have atom positions published. There is also a high pressure monoclinic form, of TaS₃ published by Kikkawa in 1981,¹³² hereon referred to as m_{hp}-TaS₃.

The properties of both m-TaS₃ and o-TaS₃ have subsequently been thoroughly investigated.¹³³⁻¹³⁶ Ambiguity about the crystal structure has caused many problems during the course of this project with PXD data not being of sufficient quality for the full refinement of the crystal structure.

The structure has an analogy of bundles of metallic chains, each with an insulating sheath,¹³⁶ leading to quasi 1-dimensional conduction through the Ta-Ta bonds in the chains along the “*b*” axis of the monoclinic unit cell, as shown in Figure 1.8.

At temperatures around 270 K the TaS₃ crystal structure undergoes a PLD leading to the formation of CDWs, (Section 1.3) as is apparent in the phase change between metallic above and semiconducting below at this temperature.¹³⁶ There is also another semiconducting phase transition at 160 K.¹²⁹ TaS₃ has been thoroughly studied along with NbS₃, as it was considered for a long time that that 1D materials may hold the key to high temperature superconductors, alas this was not the case.¹³⁷

TaS₃ is resistant to both hydrochloric acid and sodium hydroxide but oxidises readily under nitric acid. It decomposes when heated under vacuum at 650 °C into TaS₂ and sulfur.¹²⁸

1.7 Oxides

Oxide chemistry has been well established for centuries and has been the focus of the majority of traditional solid state chemistry research. Large numbers of compounds have been found to form as oxides principally due to their high stability and the ease of synthesis with applications covering many fields including: batteries, paints and catalysts to name but a few.

1.8 Tantalum Oxide

There are many forms of tantalum oxide including TaO₂ and Ta₂O₅, however the common and most stable form is tantalum (v) oxide or Ta₂O₅ sometimes known as tantite. The structure has been known since 1964 when published by Lehovc¹³⁸ and is orthorhombic with space group C222 and unit cell parameters *a* = 6.2000 Å, *b* = 3.6600 Å and *c* = 3.8900 Å as shown in Figure 1.9. Tantalum oxide is a white semiconducting solid with application including: hard scratch resistant surfaces, UV lasers and as gate insulators for multi-component circuits. Its melting point is about 1870 °C leading to high temperature applications too. It has a

bandgap in the UV-vis spectrum with estimated values of 3.80 eV.¹³⁹⁻¹⁴³ Thin films of Ta₂O₅ have shown potential applications in many electrical devices.¹⁴⁴

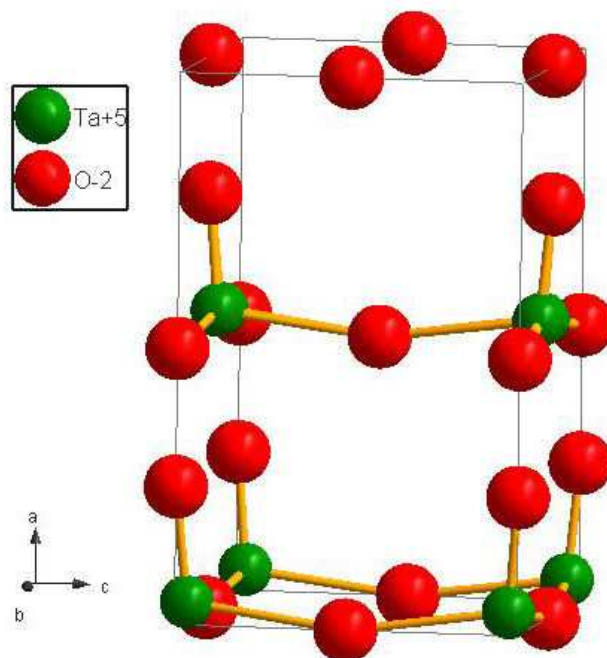


Figure 1.9: Crystal structure of Ta₂O₅.¹³⁸

1.9 Nitrides

Nitrides in general are a large group of materials that have been of much interest to many research groups world wide. In comparison to the oxides, there are relatively few compound reported but with many useful and interesting properties, nitrides continue to be of much interest. Much of the chemistry of nitrides is controlled by the reactivity of the N³⁻ species over the O²⁻ species leading to a plethora of different compounds and properties. However many of the compounds are air sensitive and involve complex reactions and chemistry requiring an inert atmosphere.

1.10 Tantalum Nitride

Tantalum nitride occurs with many different stiochiometry. E.g. TaN is a low temperature superconductor with properties that allow it to be used as high temperature coatings. The

cubic rocksalt structure was first published by Gatterer et.al.¹⁴⁵ and forms at high temperatures >1000 °C, below which it is meta-stable. Ta₃N₅ is a semi conductor with a band gap that is obtainable by sunlight and has been proposed as a potential photocatalyst in the splitting of water.^{140, 146, 147} There are also many other structures each of which have unique properties and potential for application. The structure of Ta₃N₅ has been known since 1973 when published by Straehle¹⁴⁸ and is shown in Figure 1.10 and has space group Cmc₂m and unit cell parameters $a = 3.8862(1) \text{ \AA}$, $b = 10.2118(2) \text{ \AA}$ and $c = 10.2624(3) \text{ \AA}$.

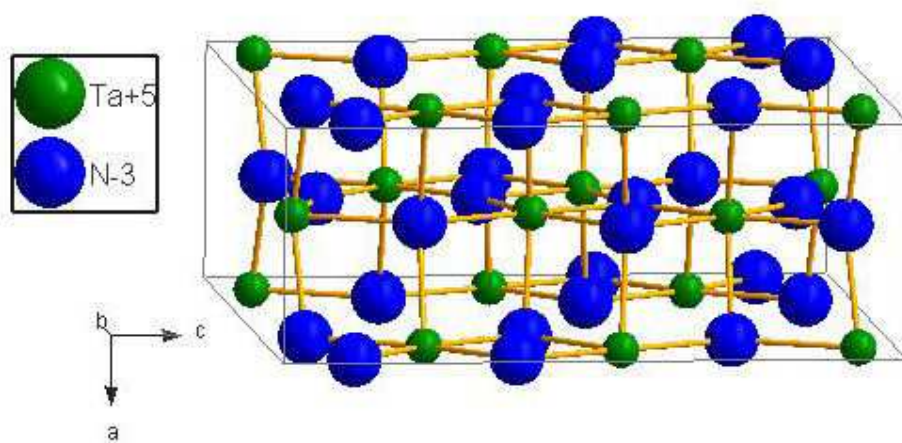


Figure 1.10: Crystal structure of Ta₃N₅.¹⁴⁸

1.11 Inorganic Nanofibre Research

The list of inorganic compounds that are known to form nanofibres is exhaustive and can be seen in Table 1.1, however a few structures are of specific importance to this thesis as they are either directly investigated or analogues to systems under investigation. There are now many different papers in the literature showing many different types of reaction that ultimately produces inorganic nanofibres of different compounds. The section below is incorporated so give a flavour of the current research from a mainly synthetic point of view and is by no means an all encompassing view of the subject, the subject is simply too large for that.

Information from other researchers is summarised here for reference from other chapters of this thesis.

1.11.1 MX₂ Compounds Nanofibres

MX₂ compounds have been important in the development of nanomaterials and nanoscience since a year after the first carbon nanotubes were discovered by Ijima.⁷ WS₂ was the first inorganic species to be seen in nanofibrous form⁸ and MoS₂ the second.⁴¹

The similarities in crystal structure between the layered chalcogenides and graphite has led to many analogous structures. (The 2H polytype has the same space group $P6_3/mmc$ as graphite¹⁴⁹) The tri-layer sandwiches are similar in nature to graphene sheets leading to similar structures; however some key differences exist resulting in fundamental alterations in the formation mechanisms. The inability of the MX₂ compounds to form odd membered rings within the structure is one such difference. This occurs because each metal atom must bond directly to chalcogen atoms and vice-versa. Carbon nanotubes achieve curvature of the end structures by incorporating odd membered rings within the 6 membered ring network that is the graphene sheet.⁷⁵ It was concluded that the MX₂ nanotubes, like WS₂, achieved end structures through lattice imperfections such as vacancies, discontinuous layers and dislocations.⁷⁵

The most common semiconductor materials, including III-V and II-IV semiconductors as well as silicon and germanium are unstable with respect to oxidation in air.¹⁵⁰ Nanostructures of these therefore need to be protected from oxidation, either from a native oxide of a covalently bonded species that acts as a passivation layer. Transition metal dichalcogenide materials have semiconductor properties often with useful band gaps and are readily accessible as nanofibres and are resistive to oxidation even in moist environments, making them a very attractive material for nanoscale semiconductor devices.¹⁵¹

1.11.1.1 Tungsten Disulfide Nanofibres

Remškar and Mrzel have shown that WS₂ nanotubes can be made in either single walled or multi walled bundles and ropes with low structural defects using a CVD reaction of bulk material and iodine as a transport agent.¹⁵²

WS₂ nanotubes were synthesised by Tenne *et al.* by the sulfidation of tungsten suboxide needle like nanoparticles in a horizontal box furnace at 840 °C.¹⁴⁹ The WO_{3-x} nanowhiskers were first produced in large quantities in a fluidised bed reactor at 1100 °C. Tenne and Rothschild also report the successful production of WS₂ nanotubes from tungsten sub-oxide produced in another fluidised bed reactor.¹⁵³ Tenne also has shown the production of WS₂ nanotubes by the reaction of H₂S with WO₂ nanowhiskers under mildly reducing conditions.¹⁵⁴ Kroto and Zhu have produced nanotubes from the sulfidation of WO_{2.7} nanorods again using H₂S.¹⁰³

Kroto and co-workers investigated WS₂ nanotubes produced in a templating reaction by coating carbon nanotubes with WO₃ before removing the template using a high temperature reducing atmosphere and H₂S in a similar reaction to that above with high resolution TEM.⁷⁵

1.11.1.2 Molybdenum Disulfide Nanofibres

Remškar and co workers have shown that MoS₂ nanotubes can be made in either single walled or multi walled bundles and ropes with low structural defects using a CVD reaction and iodine as a transport agent.^{72, 152} They also noted that the direction of propagation of the nanotubes is along the shortest unit cell parameter^{72, 152} and that the alloying of the MoS₂ with gold can stabilise the nanotubes leading to a non helical structure.¹⁵² The absence of an alloy always leads to a helical structure by their methods of synthesis. Nucleated growth led to “sea urchin” like structures similar to those seen in other systems, e.g. CdS.¹⁵⁵

Berntsen *et al.* produced MoS₂ nanostructures using a solvothermal method involving the decomposition of (NH₄)₂Mo₃S₁₃·H₂O in toluene.¹⁵⁶ The string like morphology resulted in large surface areas between 50 and 80 m²g⁻¹ and synthetic temperature of less than 400 °C make this one of the lowest temperature syntheses for nanofibrous structures so far seen.

Chen *et al.* have produced MoS₂ nanotubes by the sulfidation of MoO_{3-x} in similar reactions to those described above for the WS₂ nanotube formation.¹⁸ These nanotubes were investigated for electrochemical hydrogen storage. MoS₂ fullerene like structures as well as nanotubes were produced by Tenne *et al.* using a similar technique and a specific turbulent flow regime for the gases.⁴¹

Open ended MoS₂ nanotubes have been synthesised and their potential as a methanation catalyst investigated.¹⁷ The synthesis used was a three step gas-solid reaction involving the production of needles of tetrathiomolybdenum (NH₄)₂MoS₄, followed by ball milling and then a sintering process for 10 hours at 400°C. The research found that MoS₂ nanotubes provide an extremely effective methanation catalyst and can potentially have application in industry concerned with the removal of carbon oxides from gases and the prevention of “poisoning” of noble-metal catalysts in fuel cells.¹⁷

MoS₂ nanoribbons have been produced in a chemical synthesis by the reaction again of MoO₂ species with H₂S.¹⁵¹ The interesting thing here is that the MoO₂ nanowires were electrodeposited onto highly oriented pyrolytic graphite using the steps in the graphitic structure as a template.

1.11.1.3 Niobium Disulfide Nanofibres

Wu *et al.* have prepared long strands of NbS₂ nanowires by a CVD technique involving the use of both iodine and C₆₀ as transport and nucleating agents.¹⁵⁷ Their nanowires were seen to be brittle, long and likely consist of the 1T polytype. Kroto *et al.* have produced NbS₂ nanowires using silica tube reactions from elemental powders in the presence of iodine.¹⁵⁸

Remškar and Mrzel have shown that silver alloyed NbS₂ nanotubes can be made by the electron irradiation or microwave irradiation of NbS₂ nanoparticles. The particles appear to self assemble into nanotubes with the chains of Nb atoms appearing to act as nucleation sites for the formation.^{152, 159}

NbS₂ nanotubes have been made as described above using the reduction of NbS₃ in a hydrogen flow at 1000 °C.^{43, 160} This closely analogous system to TaS₂ is well studied and has been shown to display an elongation of the c-axis (~3%) on the formation of nanotubes.^{43, 160} It was noted that the [002] axis of the wire is perpendicular to the long axis. i.e. the direction of propagation of the tubes is along the shortest unit cell parameter.¹⁶⁰

Kroto *et al.* have produced NbS₂ nanotubes from a carbon nanotube templating reaction, similar to the production of WS₂. The nanotubes were formed by coating CNT with NbCl₄ and heating to 500 °C in air. The carbon nanotube was later removed by heating to 1100 °C under argon and H₂S.^{77, 161}

1.11.1.4 Tantalum Disulfide Nanofibres

So far there has been very little mention of TaS₂ nanofibres directly in the primary literature. Other than our publication there have been three papers outlining the production of TaS₂ nanofibres.

Rao *et al.* first proposed the synthesis of nanotubes of MS₂ compounds involving the reduction of MS₃ in a hydrogen stream as shown in Equation (1.31).⁴³



Whilst MoS₂ and WS₂ had by this time been studied and publicised, this was the first occurrence for both NbS₂ and TaS₂. The reason for this is that the trisulfides of W and Mo are amorphous while the trisulfides of Ta and Nb are crystalline. This leads to added constraints as the crystalline nature of the trisulfide has to be overcome in the reduction to the disulfide nanotubes.

Specifically for the TaS₂ system the reduction takes place with TaS₃ at 1000 °C for 30-60 minutes forming bundles of nanotubes and fullerene like structures. The Nanotubes have hollow cores and are reported to be between 20 and 40 nm in diameter. The ends are nearly rectangular which is not uncommon for the general group of dichalcogenide nanostructures. The PXD analysis showed a match to a structure of TaS₂ with a small elongation (~3%) along the c-axis of the unit cell. The nanotubes made in this manner were found to be sensitive to the electron beam leading to difficulties in obtaining high resolution data.

Rao *et al.* then proceeded to publish a further paper, again discussing general dichalcogenide systems of which TaS₂ was one where by the same synthesis the PXD analysis indicates a 2H polytype structure.¹⁶⁰

TaS₂ nanobelts have been prepared by Wu *et al.* in another two step process.⁵⁹ Here again a similar methodology of reducing TaS₃ has been used, but in this case the TaS₃ is used in the form of a nano-precursor. The first step of the synthesis was to form TaS₃ nanobelts from the direct combination of elemental powders. (See Section 1.11.2.1) The resultant TaS₃ nanobelts were washed in CS₂ and dried before being placed in another silica tube and reheated to 850 °C such that the sulfur was sublimed out of the crystal structure and crystallised on the cooler end of a temperature gradient leaving TaS₂ nanobelts.

1.11.1.5 Niobium Diselenide Nanofibres

It has been suggested that it should be possible to synthesise TaSe₂ and NbSe₂ nanowires by the reduction of TaSe₃ and NbSe₃ respectively in a hydrogen atmosphere.⁴³ However only the NbSe₂ nanofibres have so far been synthesised. TaSe₂ remains unique.

1-dimensional structures of NbSe₂ have been synthesised by a high dose of electron irradiation on a bulk phase of NbSe₂,⁴² thermal decomposition of NbSe₃ in a flow of argon at 700 °C,¹⁶² and have been removed from bulk powders prepared by chemical vapour transport with elemental Nb and Se in an evacuated silica ampoules at 800 °C.¹⁶³ They have also been

produced as nanowires and nanoribbons by the non-destructive removal of selenium from NbSe₃ structures.¹⁶⁴

1.11.1.6 Molibdenum Diselenide and Tungsten Diselenide Nanofibres

MoSe₂ and WSe₂ have been prepared by Rao *et al.* from the reaction of oxide materials in the bulk form with H₂Se, H₂ + N₂.⁴⁸

1.11.1.7 Other Disulfide Nanofibres

HfS₂ nanotubes were prepared by Rao and Nath by the reduction of the trisulfide prepared in bulk form by the reaction of elemental powders.^{50, 160} The tubes had hollow cores and rectangular closed ends. The 1T structure was found to be dominant with a slight ~1% expansion along the *c* axis of the unit cell (less than found for WS₂ and MoS₂ ~2-3 %). DRS measurements of the HfS₂ nanotubes show a slight blue shift with the band onset at ~2.1 eV.¹⁶⁰ The nanotubes were found to orientate with the *c* axis perpendicular to the long axis of the tube.⁵⁰

ZrS₂ nanotubes were prepared in the same way as the HfS₂ and were found to be extremely similar.¹⁶⁰

TiS₂ nanotubes have again been prepared by Rao and Nath from the reduction of the trisulfide.⁵⁰

Closed end multi-walled ReS₂ nanotubes have been produced by Brorson *et al.* by the impregnation of CNT with ReCl₅ before heating in H₂S at 1000 °C to remove the template and sulfidise the intermediate structure.⁵¹

1.11.2 MX₃ Compound Nanofibres

At the time of initial investigation there were relatively few non layered materials such as the MX₃ compounds that were known to form nanofibre like structures. Since then a few examples have arisen, many of which occur through indirect syntheses such as

grinding/milling or sonicating macro sized particles into nano-scale structures or using layered materials such as graphite as a precursor or templating agent.^{56, 165, 166} Few of the published methods for the formation of non layered materials consisted of direct syntheses by chemical reactions.

1.11.2.1 Tantalum Trisulfide Nanofibres

TaS₃ nano belts have been prepared by Wu *et al.* Elemental powders of tantalum and sulfur were mixed together in a 1:2 stoichiometry and sealed under vacuum in silica ampoules along with a small amount of iodine as a transport agent. The ampoule was heated to 760 °C for 48 hours over a small temperature gradient. The resulting products were nanobelts of TaS₃. These nanobelts were characterised by PXD where they were indexed to the orthorhombic structure for TaS₃. SEM shows belt like morphology and EDX gives a 1:3.5 ratio Ta:S.⁵⁹ These nanobelts were then converted into TaS₂ nanobelts.

1.11.2.2 Niobium Triselenide Nanofibres

Nanowires and nanoribbons of NbSe₃ have been extensively studied for their CDW properties and have provided a convenient platform for the physicists to perfect new techniques for the manipulation of nanofibres on surfaces for measurements.

NbSe₃ nanowires readily form from the bulk elemental powders when sealed in silica ampoules. Hor *et al.* used temperatures between 580 and 950 °C with slow heating (3 °C min⁻¹) and cooling (2 °C min⁻¹) with a 1 hour dwell time at maximum temperature.⁵⁵ They find that the morphology of the products changes dramatically with temperature of synthesis following a rough trend: powders at low temperature (600°C), wires and particulates (610 °C), wires and ribbons (630 °C), ribbons and particulates (750 °C) and just particulates at (850°C). The nanofibres formed in this process are single crystalline and have few defects. Further it is noted that at high temperature the crystal structure becomes the diselenide in particulate form with the triselenide forming nanofibres at lower temperature. Polytype

analysis of the high temperature powder was unsuccessful by PXD though a superconducting T_C of 7.2 K was obtained indicating the likelihood of the 2H polytype.

CDW measurements were taken though no information is given about the methods used to obtain the measurements other than to say that 4-terminal and 2-terminal measurements (Section 2.4.8.2) were taken. $NbSe_3$ is however known to undergo CDW transitions at about 58 and 154 K.¹⁶⁷

A similar paper by Slot *et al.*¹⁶⁸ shows that $NbSe_3$ nanowires can be made by the ultrasonic cleaving of particles in pyridine. The nanowires were loaded onto silica plates and e-beam lithography utilised to define a contact pattern. 4-terminal electrical measurements (Section 2.4.8.2) were then carried out.

1.11.2.3 Titanium Trisulfide Nanofibres

Nanobelts of TiS_3 have been synthesised by Ma *et al.* using methods that are extremely similar to those used in this project.¹⁰² These findings show that the belts are aligned with the 001 (Longest unit cell parameter) at $\sim 90^\circ$ to the long axis of the belt, they have the shortest unit cell parameter and the direction in which the chains of titanium atom propagate aligned with the long axis of the fibre. The synthesis consists of heating elemental powders of 1:3 stoichiometry within evacuated silica ampoules to 650 °C for 15 days using a temperature gradient of 80 to 100 °C along the 15 cm length. It is also noted that at high temperatures the trisulfide breaks down into the disulfide.

The formal oxidation states of the atoms have been assigned as Ti^{4+} and $S_2^{2-} + S^{2-}$.

1.11.3 Nitrides

1.11.3.1 Boron Nitride Nanofibres

BN is a closely analogous system to graphite and was originally a prime candidate for the formation of nanotubes by similar mechanisms to that of graphite. BN forms 6 atom rings

that are almost identical to those formed by the carbon atoms within graphite except using alternate boron nitrogen atoms in the 6 membered rings. Since its first appearance in nanofibrous form, in 1995 found by Chopra,⁶⁴ much research has been carried out in attempting to form BN nanostructures using similar techniques to those used for CNT production, (as explained here.)

Like the MX_2 compounds BN again has mechanistic differences with formation into nanotubes, when compared to carbon, as the 3+3 ring structure prohibits the formation of odd numbered rings and prevents curvature. This leads to highly strained ends involving dislocations and defects, much like that seen in the dichalcogenide systems.⁷⁵

BN nanotubes have been successfully produced by arc discharge reactions,^{64, 169, 170} laser ablation,^{171, 172} CVD techniques^{173, 174} and in large quantities by mechano-chemical methods.¹⁷⁵ Chen, Conway and Williams produced large quantities (<1 Kg) of multi-walled BN nanotubes by ball milling boron powder under an ammonia atmosphere, before annealing at 1200 °C.¹⁷⁵

1.11.3.2 Lithium Nitride Nanofibres

Li_3N has been known in our group for many years as a possible nanofibrous forming compound. Early research proved successful with different morphologies and crystallographic orientations possible and good kinetics for hydrogen uptake. The results have been discussed at various conferences including the world Hydrogen Energy conference in France 2006 but have yet to be officially published in a scientific journal.

1.11.4 Oxides

1.11.4.1 Titanium Dioxide Nanofibres

Hoyer produced TiO_2 nanowires using a moulded growth technique. Porous aluminium oxide was utilised to create the polymethyl methacrylate (PMMA) mould. The TiO_2 was then

electrochemically adhered to the PMMA mould creating the nano-tubular structures once the PMMA was removed.²³ This technique is similar to the templating methods used to form nanofibres around carbon nanotubes. Cottam and Shaffer have shown the production of TiO₂ nanorods / nanowires from the oxidation of similar morphology TiC structures.¹⁷⁶ In this multi-step synthesis easily produced carbon nanotubes were reacted with TiCl₄ to form titanium carbide nanowires before being oxidised to form TiO₂ nanotubes.

1.11.4.2 Tantalum Oxide Nanofibres

There have so far been two methods of producing Ta₂O₅ nanofibres. Both methods by Kobashi involve either a complicated hydrothermal synthesis that produced helical nanowire like structures³⁴ or in a very low yield of nanotubes produced by scrolling precursor sheets.¹⁷⁷

Chapter 2: Experimental

2.1 Introduction

This chapter aims to explain the different experimental preparations, the specialist equipment used and the specifications of the characterisation equipment and techniques. Any specific experimental procedures for individual experiments are explained in the results chapters for the systems in question but a general overview of the experimental techniques is given here.

As a result of the move from the University of Nottingham to the University of Glasgow, during the course of the project, different instruments have been used for similar purposes. Inevitably, the equipment specification has shown variance between institutions, however, all due care has been taken when comparing data received from different sources. The source of the data has been given where possible for comparison.

2.2 Experimental Methods

Much of the work described herein has been performed using evacuated silica ampoules and muffle furnaces. A standard preparation has been applied in addition to an alternative protocol for surface assisted growth and some flowing gas reactions. These are outlined in Section 2.3. First, however, it is important to consider the techniques and methods used in sample handling and manipulation.

2.2.1 Equipment and Techniques

2.2.2 Fume Hoods

The opening of the silica ampoules (Section 2.2.4.7) was performed in a ventilated fume hood to minimise contact with hazardous gasses that escaped upon opening. The possible formation of H_2S during the reaction, which has a low LD50 value was a possible contributors to the hazardous gas released upon opening. Preparations involving the use of NH_3 and CS_2

gases, (Section 2.3.2.1 and 2.3.2.2 respectively), were also carried out in tube furnaces that were confined within fume hoods so that toxic exhaust gas or leaking reagents didn't contaminate the laboratory.

2.2.3 Nitrogen Generator

The use of nitrogen at Glasgow was facilitated by a GeniSys nitrogen generator and a hard nitrogen gas ring. The nitrogen generator supplied 99.9 % nitrogen at a flow rate of 15 litres per minute from a 10 bar supply of compressed air from a Jun-Air compressor unit. The nitrogen generator works by passing the compressed air through carbon molecular sieves that absorb oxygen. A 200-litre ballast tank at a pressure of five bar provided the lab with 1000 litres of nitrogen at any one time. The nitrogen was primarily used to flush out apparatus before use.

2.2.4 Work Involving Glass

There are three main types of glass that are commonly used for scientific work, soda glass, borosilicate and pure silica (quartz):

Soda glass consists of silica (SiO_2) and soda (NaOH , which acts as a flux, lowering the softening temperature) and has a green tinge. It is cheap, soft and is the common glass found in most windows with a green tinge. Its low annealing temperature ($350\text{ }^\circ\text{C}$) and easy workability lends it to use in simple low temperature applications such as windows, wine bottles and basic chemical laboratory apparatus such as stirrer rods, beakers and measuring cylinders. Its soft nature allows easy etching for volumetric markings, though nowadays many of the markings are achieved by transfers. Cheap working costs allow for disposability making soda glass a useful material in the modern chemistry lab. Its low annealing temperature however prevents it from being used in high temperature applications.

Borosilicate (Pyrex) consists of silica with a boron flux and has a slight green tinge. This glass is much stronger and harder and has a higher flowing temperature ($\sim 560\text{ }^\circ\text{C}$) but is

still quite easy to work. These traits allow far more durability within the lab and applicability to higher temperature methods. Borosilicate tends to make up the majority of modern glassware in the lab (e.g. test tubes, boiling tubes, round bottomed flasks, Schlenk lines etc).

Silica or pure quartz (SiO_2) is the purest of silica-based glasses, not containing a flux. This glass has an annealing temperature of 1100 °C and is pure white when viewed along a length. Silica's high working temperature and brittleness limits application but the durability at high temperature makes it a useful material for synthetic techniques. At temperatures above 1200 °C silica begins to move under its own weight and deform with a cloudy appearance. This leads to an upper limit on the useable temperature for silica ampoules of 1100°C.

2.2.4.1 Silica Tubes

For many of the preparations performed over the course of this project, it has been necessary to seal reagents in silica ampoules under a vacuum. For these preparations, 12 mm diameter silica tubes with a wall thickness of 1mm and lengths of 1 m were obtained from Unilab (product number QU064808). These lengths can then be cut or worked to produce a range of ampoule size and shapes depending on experimental configuration, (Section 2.2.4.4).

2.2.4.2 Glass Blowing Torch

During the course of this work two different glass blowing torches have been used, both work in the same way but one is bench mounted and one is hand held. Both torches run off a gas (CH_4) supply and an oxygen supply at just over 1 Bar. By law both of these supplies have to be fitted with a non return valve and flash back arrestor as a premixed supply is being combusted. Different sizes and shapes of flame can be created by adjusting the gas and oxygen flow and are used for different applications. Of particular note, is a warming / cooling flame that is used to warm the glass prior to the work and cool the glass slowly after the work, preventing thermal shock and the cracking.

2.2.4.3 Long Necked Powder Funnels

For many of the reactions described in the thesis it has been necessary to redesign or custom build apparatus, one such example is the making of long necked powder funnels. It is important when filling the silica tubes, (Section 2.2.4.4), not to get contaminants on the inside wall of the tube. Contaminants here will infuse into the silica during the sealing process, (Section 2.2.4.5), as the silica flows inwards under vacuum causing weaknesses in the structure. This leads to ampoules that are unable to withstand the pressures of heating or the thermal shock of quenching. Long necked powder funnels are therefore used to place the elemental powders at the bottom of the silica tube without contaminating the internal surface.

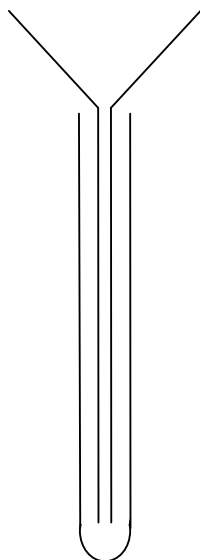


Figure 2.1: Schematic showing how a long necked powder funnel can deposit reactants at the bottom of the silica tubes without contaminating the inside walls of the silica tube to be sealed.

A standard powder funnel can be purchased from many suppliers and lengthened using a length of standard glass tube. The best method of joining the glass is to square the end of the funnel using a tungsten carbide glass knife so that it is a straight edge and inserting a bung in the base of the funnel. The newly cut square edge of tubing is heated in the warming flame of a glass blowing torch alongside the similar diameter glass tubing. Once warm, the flame is set to a medium sized roaring flame and both tubes are heated from their tips until glowing

red. The tubes are now pressed together out of the flame and set so that the overall tube is straight. Using a very small flame a hot spot is made along the seal and a small puff of air is blown into the end of the tube. This maintains the wall of the tube and brings the hotspot back out to the diameter of the original tubing, giving a seamless join. Rotating the tube by 180° and repeating the process with another small puff of air creates a second seamless join and then on the other two sides. The join should now be perfectly clear and of uniform dimensions with smooth internal and external faces all round its circumference. After cooling in the cooling flame and annealing for 2 hours at the annealing temperature, 550 °C for borosilicate, the funnel is ready for use.

2.2.4.4 Ampoule Designs

2.2.4.4.1 Ampoules for Standard Preparations

For a standard preparation ampoule, a 1 m length of silica tubing (Section 2.2.4.1) was bisected using a tungsten carbide glass knife and then each section drawn out and separated in the middle using a glass blowing torch with a large hot flame. This gives four equal length tubes, which are closed at one end and ~ 250 mm in length. The tubes can then be filled using a long powder funnel and sealed as described in Section 2.2.4.5 to give ampoules of ~ 150 mm in length.

2.2.4.4.2 Ampoules for Surface Assisted Growth Configuration Preparations

The ampoules used in reactions involving the investigation of surface assisted growth of inorganic nanowires were made from drawing two necks into a 500 mm section of silica tube, (Section 2.2.4.1) ~ 80 mm either side of the central position. The tube can then be drawn out and separated in the central position leading to two similar tubes with a neck approximately one third of the way along constraining the diameter of the tube as shown in Figure 2.2. Powder reactants can be placed in the lower section, using a long powder funnel, and a piece of metal foil in the upper section before being sealed under vacuum as described in Section

2.2.4.5 to give an ampoule of ~ 150 mm in length. The reduced diameter of the tube restricts the contact between the foil and the powders without hindering the gas phase reactions that likely occur.

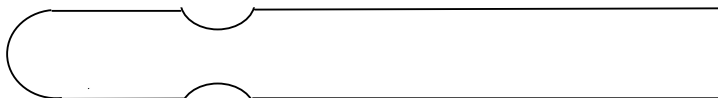


Figure 2.2: Schematic of the tubes used for the surface assisted growth experiments.

2.2.4.4.3 Long Silica Ampoules

Long tubes were made by drawing and sealing metre lengths of silica tube (Section 2.2.4.1) in the middle leading to two 500 mm long closed tubes. Adaptations for surface assisted growth (Section 2.3.1.2) can be built into the long tubes if required. The tubes can be filled using a long powder funnel and sealed as described in Section 2.2.4.5 to give ampoules of ~ 400 mm in length.

2.2.4.5 Sealing Silica Ampoules Under Vacuum

The powdered reagents were inserted into the tubes of desired size and design, before being attached to a specifically built vacuum line via a piece of thick rubber tubing and a jubilee clip. A schematic of the vacuum line is shown in Figure 2.3.

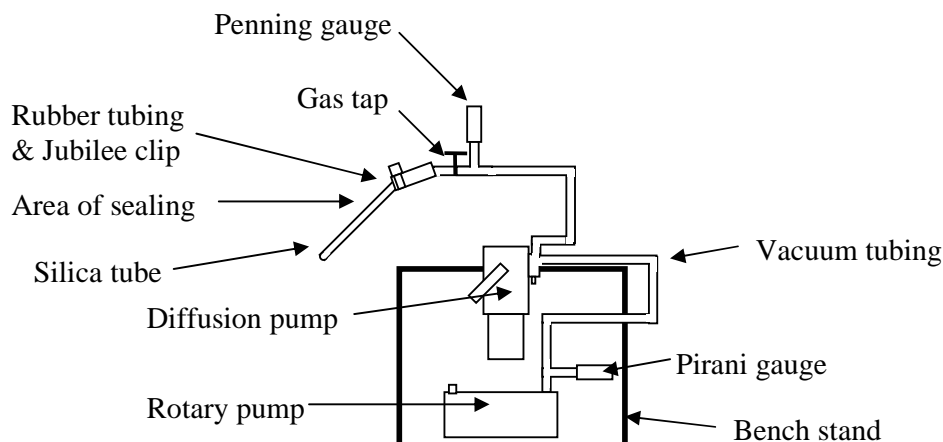


Figure 2.3: Schematic of the glass blowing vacuum line.

The vacuum line was attached to both a rotary pump and a diffusion pump, allowing the silica tube to be evacuated firstly to 10^{-1} Torr (rotary pump alone) and then to down to 10^{-5} Torr (diffusion pump). Once evacuated to the desired pressure as measured by the Penning gauge, the silica tube is sealed using a glass blowing torch to give an evacuated silica ampoule as shown in Figure 2.4.

The best method found for sealing the silica tubes under vacuum consists of making three small dimples, and then collapsing and the surrounding silica in upon itself. The advantage of this method over other methods is that the sealing process thickens the silica at the point of sealing retaining much of the original strength. Other methods of sealing silica tubes such as drawing the silica into a thin neck at the place where the seal is desired and then collapsing the thin silica in on itself is likely to produced very thin silica where the seal is situated and leaves the ampoules susceptible to breakage. Spreading the dimples evenly with the first dimple in a vertically downwards position allows the ridge on the right (if right handed) to be heated strongly while the other two ridges are simultaneously heated leading to easy separation of the ampoule from the unwanted section with an anti-clockwise rotation of the now sealed ampoule. For the sake of results and discussion the ampoules are each

divided up into three regions with ' to indicate whether the ampoule design was inclusive of the surface assisted designs, (Figure 2.4).

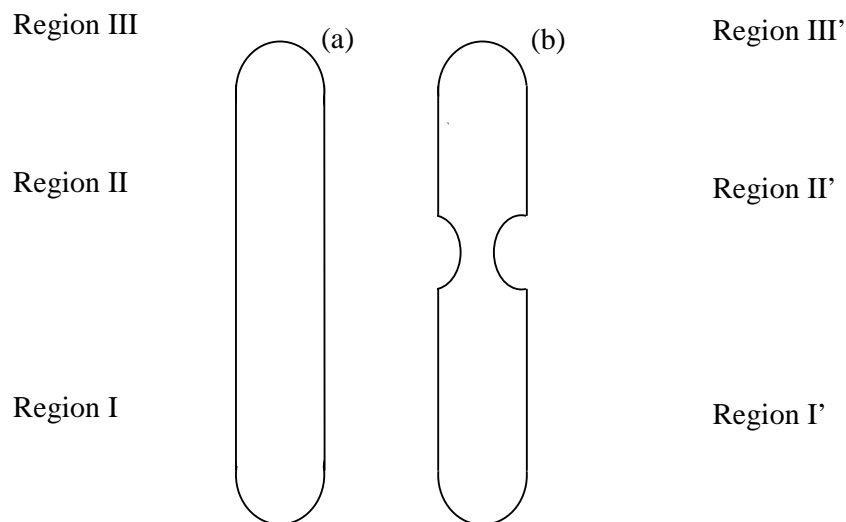


Figure 2.4: Schematic of the two basic types of ampoule, (a) standard and (b) surface assisted growth experiments. The notation of the different Regions has been included to aid discussion.

2.2.4.6 Heating Silica Ampoules

The silica ampoules can be heated using a variety of furnaces, with different programmable capabilities (Section 2.2.4.8) for details on the furnaces.

An initial step in the heating profile was often incorporated between the melting and boiling temperature of any volatile reactants to prevent the sudden evolution of gas within the ampoules at high temperature. Sudden changes in internal pressure could lead to exploding ampoules and should be avoided for safety considerations.

At temperatures above 1200 °C silica begins to move under its own weight and deform with a cloudy appearance. This leads to an upper limit on the useable temperature for silica ampoules of 1100°C. Higher temperature reactions would require significant changes to the experimental setup leading to incomparable results, so these have not been considered.

2.2.4.6.1 Pressures within the Silica Ampoules During Heating

As the silica ampoule is heated the more volatile phases present will evaporate, changing the internal pressure of the ampoule. The internal pressure can be estimated by using simple mole calculations and estimating the volume of the ampoule. The internal pressure of a silica ampoule can be modelled using ideal gas law behaviour as shown in Equation (2.1).

$$P \times V = n \times R \times T \quad (2.1)$$

P = Pressure (Bar)

V = Volume (L)

n = No. Moles

R = Gas constant ($8.31451 \times 10^{-2} \text{ LbarK}^{-1} \text{mol}^{-1}$)

T = Temperature (K)

A standard ampoule, ~15 cm in length and 1 cm in width, containing approximately 0.32 g of sulfur at 650 °C therefore has an internal pressure of about 65 bar as shown in Equation (2.2)

The volume of the ampoule is estimated as shown in Equation (2.3) and (2.4).

$$P = \frac{0.01 \times R \times 924}{0.0118} \approx 65 \text{ bar} \quad (2.2)$$

$$\text{Volume} = \pi r^2 \times \text{length} \quad (2.3)$$

$$\pi 0.5^2 \times 15 = 11.8 \text{ cm}^3 \quad (2.4)$$

The internal pressure will be critical to the synthetic process and will be highly susceptible to change if the quantities of starting reactants are altered. The pressure will drop drastically as the feedstock is used in the reaction but the silica must be able to withstand high pressures prior to reaction.

2.2.4.7 Opening Silica Ampoules

Silica ampoules can be opened by scoring the side with a tungsten carbide knife and snapping the ampoule in half. The ampoule cleaves easily with the inward rush of air disturbing the

lower density products. For safety reasons this is carried out in a fume hood as hazardous gasses may be released (Section 2.2.2).

2.2.4.8 Quenching Silica Ampoules

When quenching silica ampoules from temperatures above 500 °C there was a danger of exploding ampoules due to thermal shock. A full facemask, heatproof gloves and a long pair of tongs were used for these operations. Tubes were either removed from the furnace (Air quenched) or allowed to cool slowly inside the furnace. In some cases hot tubes were inserted into a bucket of 50 % water 50 % ice for faster cooling.

2.2.5 Furnaces

Elite Thermal Systems muffle furnaces, Vecstar tube furnaces and Carbolite tube furnaces have been used during the course of this research.

2.2.5.1 Elite Thermal Systems Muffle Furnace

The bulk of the silica work was carried out in one of the two Elite muffle furnaces, which have been available. These furnaces controlled by a Eurotherm 2416 temperature controller allow fully programmable temperature control over temperatures between room temperature and 1350 °C.

2.2.5.2 Carbolite Three Zone Tube Furnace

The Carbolite three zone furnaces allowed temperature gradients to be setup within the confines of the furnace work tube. There are three zones with a fully programmable temperature control (2416) in the centre. The edge zones shadow the central zone with a programmed temperature difference. The overall top temperature is 1200 °C.

2.2.5.3 Vecstar Furnaces Tube Furnace

The preparations using the CS₂ setup as described in Section 2.3.2.2 was carried out using a Vecstar tube furnace with a 32 mm work tube and flange fittings to allow gas to be passed down the tube during the heating cycle. The furnace has a top operating temperature of 1400 °C and a simple pin controlled time clock to engage and disengage the heating coils which are set using an analogue dial.

2.2.5.4 Carbolite Tube Furnace

The preparations using the NH₃ setup as described in Section 2.3.2.1 was carried out using a small Carbolite tube furnace with a 32 mm work tube and flange fittings to allow gas to be passed down the tube during the heating cycle. The furnace has a top operating temperature of 1600 °C and has no programmable features other than a digital temperature set point.

2.2.6 Sublimation of Excess Sulfur from Nanowires

A simple sublimation set up was used to sublime the excess sulfur off the sulfide nanowires once prepared as described in Section 2.3. A schematic of the setup is shown in Figure 2.5. The nanowires were placed in the bottom of the modified quickfit boiling tube and the apparatus evacuated using a rotary pump down to about 10⁻¹ Torr. The oil bath was then heated to 120 °C for a period of a few hours. The cold finger collected the sulfur and was cleaned periodically.

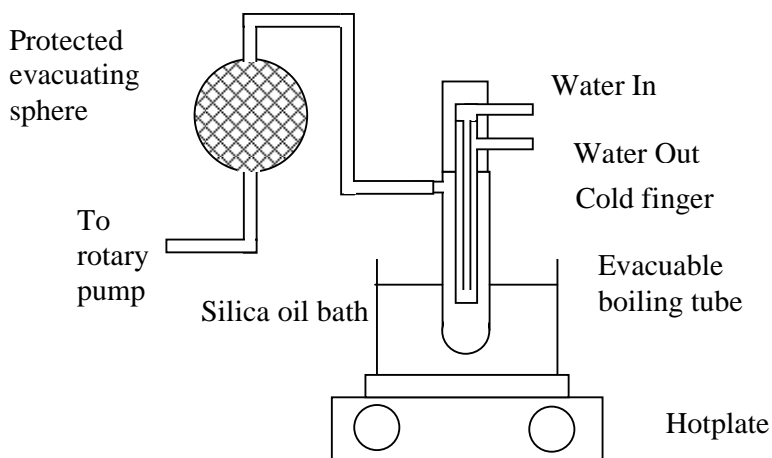


Figure 2.5: Schematic for the sublimation reactions used for removing excess sulfur from bundles of nanowires.

2.3 Synthetic Preparations

2.3.1 Preparations Using Silica Ampoules

2.3.1.1 Preparations Using a Standard Silica Ampoule

Silica ampoules were prepared (Section 2.2.4.4.1) and filled with a stoichiometric ratio of elemental powders before being sealed under vacuum (Section 2.2.4.5.) and heated over a heating profile using one of the furnaces given in Section 2.2.4.8.

2.3.1.2 Preparations Using a Surface Assisted Growth Ampoule

Silica ampoules were prepared (Section 2.2.4.4.2) and filled with a stoichiometric ratio of elemental powders and a piece of metal foil before being sealed under vacuum (Section 2.2.4.5.) and heated over a heating profile using one of the furnaces given in Section 2.2.4.8.

A schematic of this setup is shown in Figure 2.6.

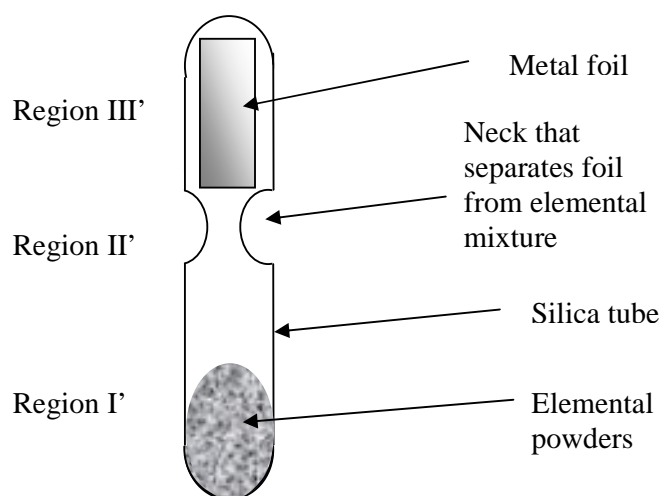


Figure 2.6: Schematic of the ampoule design used in the surface assisted growth experiments, showing also the Regions from Figure 2.4 that will be used for discussion purposes.

2.3.1.3 Long Tube Preparations

Long tubes, (Section 2.2.4.4.3), allowed temperature gradients to be setup within the zones of the three zone tube furnace, (Section 2.2.5.2). Surface assisted growth reactions could be incorporated, (Section 2.3.1.2).

2.3.2 Flowing Gas Preparations

2.3.2.1 Preparations Using NH_3

Nitride materials were prepared from suitable precursors using an ammonolysis reaction. Figure 2.7 shows a schematic of the experimental setup. In a typical preparation, ammonia, controlled by a flow meter attached to the cylinder, was passed through the work tube whilst the furnace controls the temperature or desired heating profile. The exhaust ammonia was passed through a water bath before being discharged through the fume hood. The water was replaced periodically to dispose of the ammonia solution formed. The experimental setup as well as the ammonia cylinder was housed inside the confines of a fume hood for safety considerations.

For reactions involving a non-oxide precursor, the work tube was purged with nitrogen for a period of up to an hour prior to the application of ammonia to prevent oxidation of the precursor prior to ammonolysis.

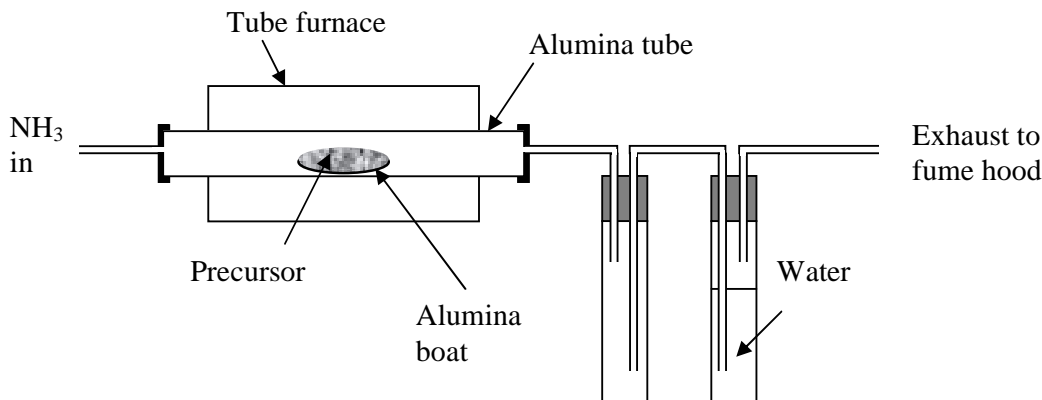


Figure 2.7: Schematic of the experimental set up for the formation of nitride materials.

2.3.2.2 Preparations Using CS_2

Sulfide materials were prepared by the reaction of CS_2 with suitable precursor. A schematic of the experimental setup is shown in Figure 2.8. The precursor was placed in an alumina boat and inserted into a central position within the work tube of a tube furnace. The end flanges were attached to the work tube and gas applied during the desired heating profile. To create a flow of effectively CS_2 gas, argon gas was bubbled through a Dreschel bottle containing liquid CS_2 . The volatile CS_2 evaporated and created an Ar/CS_2 gaseous mixture. The concentration of CS_2 could crudely be controlled by the temperature of the CS_2 liquid, controlled by the cooling tubes and the flow rate of the argon. The flow of Ar/CS_2 mixture was controlled by counting the rate of evolution of gas through the bubbler system. The experimental setup was housed inside the confines of a fume hood.

For reactions involving a non-oxide precursor, the work tube was purged with Ar for a period of up to an hour prior to the application of Ar/CS_2 to prevent oxidation of the precursor prior to sulfidation.

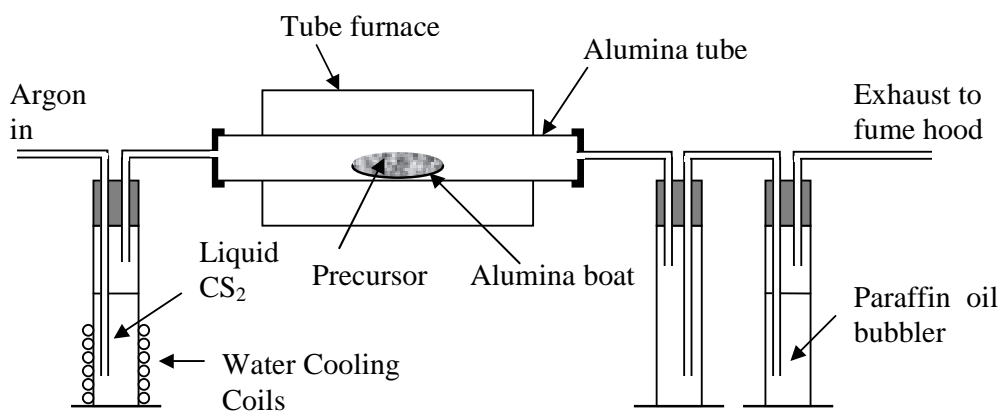


Figure 2.8: Schematic of the experimental set up for the formation of sulfide materials using the reaction of a suitable precursor and CS₂/Ar gas mixture.

2.3.2.3 Preparations Using O₂

Oxide materials were prepared from suitable precursors using a simple oxidation reaction. Figure 2.9 shows a schematic of the experimental setup. The furnace was heated over the desired heating profile under the flow of oxygen with the flow controlled by the evolution of gas through the protected bubbler system.

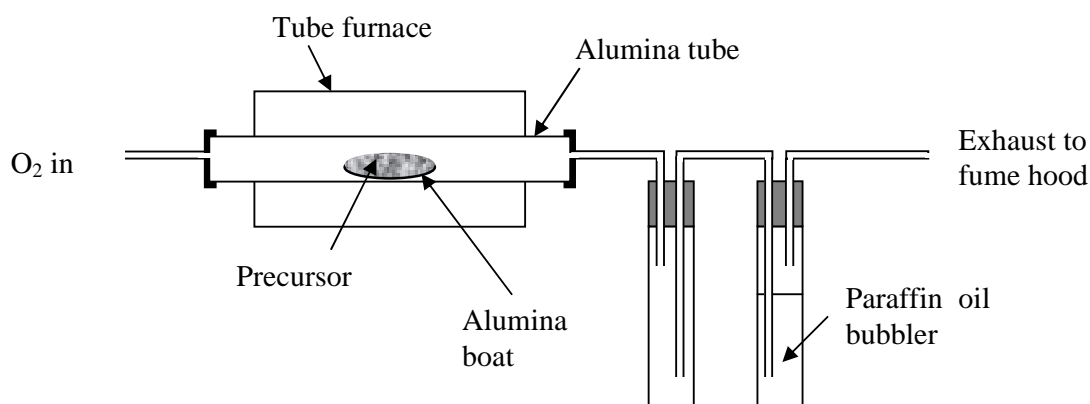


Figure 2.9: Schematic of the experimental set up for the formation of oxide materials.

2.4 Characterisation Techniques & Equipment Specifications

2.4.1 Powder X-ray Diffraction

Powder X-ray Diffraction (PXD) has been very important in this work as it allows rapid identification of known phases within a sample and can be used to identify structural features. PXD follows theory based around Bragg's Law and utilises the fact that the wavelength of X-ray radiation is comparable in length to the interplanar spacing of the atoms in a crystal, e.g. Cu K α = 1.5484 Å). A derivation of Bragg's Law is given in Section 1.2.5. Powder patterns consist of plots of intensity against diffraction angle. In this thesis all the powder patterns have $^{\circ}2\theta$ as the X axis. The peaks in a powder pattern represent the different d-spacings of the Miller indices (Section 1.2.4) and led to much useful information about the crystal structure.

2.4.1.1 Treatment of Powder Patterns

Different levels of information can be extracted from powder data. The different analysis options were largely dependant on the quality of data and the experimental requirements. In general, longer scans led to better data and higher-level analysis.

2.4.1.1.1 Phase identification

Known phases were identified by matching the diffraction patterns peak position and intensity to those of theoretical powder patterns, generated from crystal structures downloaded from the Inorganic Crystal Structure Database (ICSD)¹⁷⁸ or matched directly to the Powder Diffraction Files (PDF) for each phase. Once a match is made, the results can be plotted in software such as PowderCell 2.4,¹⁷⁹ which visually shows the observed data superimposed on a number of theoretically generated patterns from crystal structures.

2.4.1.1.2 Indexing

It is possible to relate the d-spacing of a crystal to particular Miller indices when the unit cell dimensions are known, (indexing). The relationships between the Miller indices and the d-spacings for different crystal systems are given in Section 1.2.4 and Table 1.3.

Indexing can be achieved using software like Dicvol 6,¹⁸⁰ which matches the input peaks with the probable peak positions for the known crystal systems. Software like CELREF¹⁸¹ can then refine the unit cell and match the best space group (Section 1.2.3).

2.4.1.1.3 Structure Refinement, “The Rietveld Method”

Hugo Rietveld as a Dutch mathematician took an early interest in the problems associated with neutron diffraction of powders back in 1964. The Rietveld Method has since become the basis of powder diffraction analysis worldwide.¹⁸²

Rietveld refinement was carried out using GSAS,¹⁸³ a full profile refinement software program. The Rietveld method fits experimentally obtained powder data to a refinable structural model allowing accurate measurement of unit cell dimensions, angles and atomic positions as well as information on the preferred orientation of the crystals.

The refinement uses the difference of squares method which is a standard mathematical method used for comparing two similar sets of data step by step. Each experimental data point is taken in turn and compared with the theoretical data point from the model, rather than comparing the shape of the pattern as a whole. The concept of refinement is to iteratively minimise S in Equation (2.5).

$$S = \sum_i w_i (y_i - y_{ci})^2 \quad (2.5)$$

S is the residual being minimised

w_i is the Weight factor $= \frac{1}{y_i}$

y_i is the Observed intensity

y_{ci} is the Calculated intensity

y_{ci} can be calculated from the crystal structure using Equation (2.6).

$$y_{ci} = s \sum_K L_K |F_K|^2 \phi(2\theta_i - 2\theta_K P_K A + y_{hi}) \quad (2.6)$$

s = scale factor.

K = Miller indices h, k, l , for the Bragg reflections.

L_K contains the Lorentz polarisation and multiplicity factors.

ϕ = reflection profile function.

P_K = preferred orientation function.

A = absorption factor.

F_K = structure factor for the K in the Bragg reflection.

y_{bi} = background intensity for the i^{th} step.

The accuracy of fit between the model and the data is then measured using a series of R factors. R_{wp} (Equation (2.7)) is considered the most useful of these as the numerator is the residual that is being minimised in the refinement.

$$R_{wp} = \sqrt{\left\{ \frac{\sum w_i (y_i(obs) - y_i(calc))^2}{\sum w_i (y_i(obs))^2} \right\}} \quad (2.7)$$

y_i = diffraction intensity,

$w_i = 1/y$

2.4.1.1.4 Broadening of the Peaks in Powder Patterns

Peak broadening is usually attributed to particle size and can lead to interesting information about the sample. The Scherrer equation gives an approximate relationship between the broadness of the peaks and the approximate particle size. The Scherrer equation is given in Equation (2.8) can be derived by differentiating the Bragg equation, (Equation (1.13)).

$$t = \frac{k\lambda}{B \cos \theta} \quad (2.8)$$

t = Thickness of crystals (particle size) nm

k = Particle shape correction best approximated to 0.9

B = Angular width, Full-Width at Half Maximum (corrected)

λ = Wavelength of X-rays in nm

θ = Angle of incidence of the X-rays

$$B = B_{obs} - B_0 \quad (2.9)$$

The angular width of the peaks is calculated as the Full Width at Half Maximum, (FWHM) from the most dominant peak and the mid point is taken to be the value of θ , both of which can be calculated by software that fit the peaks of the diffraction pattern. The corrected value for B is the difference between the peak width in the observed pattern and the peak width of a standard sample that has no broadening due to particle size, (Equation (2.9)).

The one drawback of the above simple method is that it works only if stress-related and instrument-related broadening is negligible in comparison to particle size effects. This condition is often met with particle sizes that are in the 10 - 100 nm range and perfectly spherical. Much of the work in this thesis involves particles that are larger in size than 100 nm and therefore the results for the Scherrer equation will carry some error.

2.4.1.2 Powder X-ray Diffraction Sample Preparation

Both flat plate and capillary mode Powder X-ray Diffraction (PXD) was utilised in this project.

2.4.1.2.1 Flat Plate Mode

A finely ground sample was placed in a 10 mm diameter circular depression within a glass slide or circular sample holder and smoothed over so that the surface of the sample was level with the sample holder, creating a flat surface with enough crystals of random orientation to produce a diffraction pattern according to the Bragg equation (Section 1.2.5). The slide was then carefully placed in a diffractometer.

2.4.1.2.2 Capillary Mode D8

Samples run on the D8 diffractometer were loaded into commercially available glass capillaries. Here the finely ground sample was placed in the opening of the capillary using a micro spatula and the capillary holder tapped against a hard surface till the powder migrated down to the bottom. The process was repeated until the capillary was nearly full and the capillary sealed using a cigarette lighter to melt the end closed. The capillary was mounted in bees wax, centred and then attached to the diffractometer for analysis.

2.4.1.2.3 Novel, Nanowire Sample Preparation

It was especially hard to obtain good PXD data for the nanofibres in this project. In general nanowires are difficult to analyse by PXD as a result of large anisotropy, small particle size and low densities making them generally susceptible to static and difficult to handle. The fibrous nature of the wires tended to block the fragile capillary leading to breakages. Many methods for loading flat plate slides for PXD data collection were investigated. These included:

2.4.1.2.3.1 Backfilling a slide

The depression in the slide was filled from behind against a smooth surface and then turned over to reveal the imaging surface.

2.4.1.2.3.2 Vacuum Grease Coated Slide

Sprinkling the wires over a slide coated in vacuum grease. This can overcome some of the anisotropy problems associated with nanofibrous PXD measurements though it is hard to achieve a good coverage without leading to problems with the height of the sample.

2.4.1.2.3.3 Amorphous Carbon SEM Tab

Sticking the fibres to a slide using adhesive tape or carbon tabs usually used in the preparation of SEM samples worked reasonably well, though there was often a residual

amorphous background observed. A PXD pattern for a blank carbon tab is shown in Figure 2.10. The peak at $22^\circ 2\theta$ was rarely observed and only on samples with a thin coverage of nanofibres.

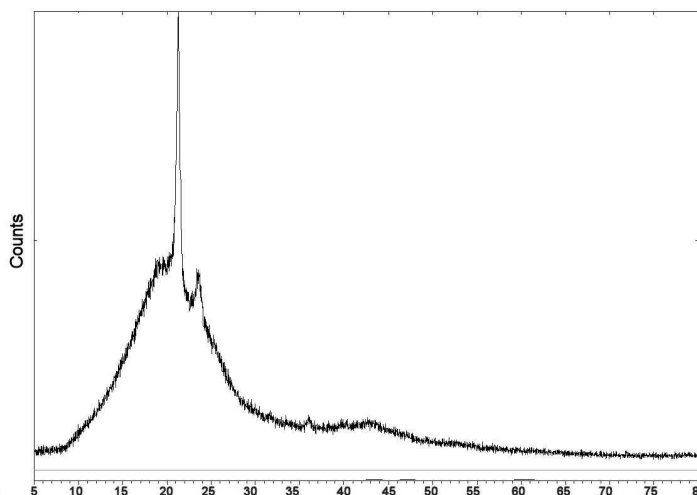


Figure 2.10: Powder X-ray diffraction pattern showing diffracted intensity against 2θ for a blank carbon tab showing the background that may be associated with PXD patterns taken using this method of sample preparation.

2.4.1.2.3.4 Filling a Hot Slide with a Nanowire Suspension

Nanowires were suspended in a volatile solvent (ethanol) and dropped into the circular depression of a glass slide where the solvent was encouraged to evaporate by the gentle application of heat $\sim 60^\circ\text{C}$.

2.4.1.3 X-Ray Diffractometers

PXD data is recorded as a diffraction pattern of intensity versus 2θ . In general, scans were run from 5 to $80^\circ 2\theta$ in step scan mode with a step of $0.02^\circ 2\theta$. The step time was varied between experiments resulting in scans of between 30 and 90 minutes. However, for refinement data the scans were left on overnight or longer leading to better statistics. A schematic of the working of a typical powder diffractometer is shown in Figure 2.11. The X-ray source is fixed while the sample and detector rotate to scan through the values of 2θ . Slits control the illumination of the sample and the detectors. It should be noted that the Siemens D5000

diffractometer utilises a different set up with the sample fixed and both the source and the detector moving around it.

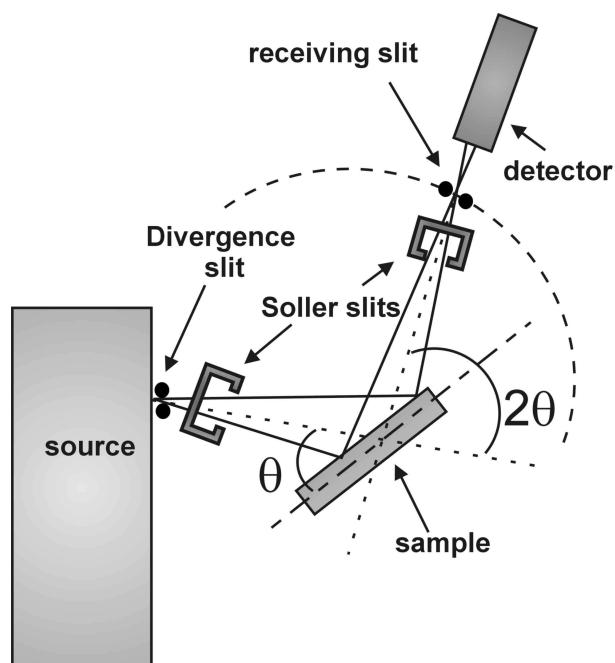


Figure 2.11: Schematic of the workings of a generic Powder X-ray Diffractometer.

Two different diffractometers were used in the work enclosed in this thesis so for comparison where data is shown an indication of which diffractometer was used is given with the data.

2.4.1.3.1 Phillips X-pert at the University of Nottingham

Data was collected using a Phillips X-pert system, fitted with a PW3710 diffractometer control unit. The system was operated at 40 KV and 40 mA, using Cu K_{α} radiation. Samples were loaded into glass slides with 10 mm depressions as described in Section 2.4.1.2.1.

2.4.1.3.2 Siemens D5000 at the University of Glasgow

Data was collected using a Siemens D5000 diffractometer operated in flat plate mode at 40 KV and 40 mA, using Cu K_{α} radiation. Samples were loaded into glass or (plastic slides of similar design) as described in Section 2.4.1.2.1 and rotated at 15 revolutions per minute during the acquisition of the data. A hot stage allowed in-situ XRD to be taken whilst heating

the sample up to 800 °C. The glass slides with carbon adhesive tabs (Section 2.4.1.2.3.3) were used with this diffractometer.

2.4.1.3.3 Bruker D8 at the University of Glasgow

Data was collected using a Bruker D8 operated in capillary mode at 40 KV and 40 mA, using Cu K α radiation. Samples were loaded into glass capillaries as described in Section 2.4.1.2.2.

2.4.2 Scanning Electron Microscopy

Scanning Electron Microscopy (SEM) is a very powerful tool that allowed the sample morphology to be imaged at the larger end of the nanoscale and has been utilised extensively during this project.

A beam of electrons is produced; often using a field emission gun (FEG) where by a powerful electric field removes electrons from a tungsten target and accelerates them towards the sample. The relatively low powered electrons interact with the surface and outgoing or scattered electrons are analysed. The surface of the sample is analysed for both primary and secondary electrons as they are scattered or emitted from the surface (Figure 2.12). The detector scans along the surface generating an image over a relatively large area. Primary electrons are the electrons emitted from the source and scattered off the surface while secondary electrons are emitted from the surface as they are knocked out of the valence orbitals of the surface atoms by the primary electrons. A three dimensional image of the surface can be achieved from computer processing of this data leading to very detailed images with good resolution down to about a hundred nanometres.

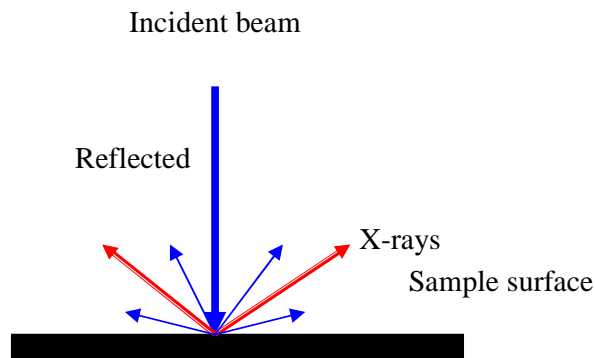


Figure 2.12: Schematic diagram showing the interaction of an incident beam of electrons and a sample.

2.4.2.1 Energy Dispersive X-ray Analysis

Energy Dispersive X-ray Analysis (EDX) allowed elemental analysis of a sample at the same time as the sample was imaged by the SEM. When a sample is bombarded with electrons some X-rays are emitted (Figure 2.12). Electrons knocked out of low-lying orbitals create holes that can be filled by electrons of higher energy, (Figure 2.13). Higher energy electrons then relax down into the holes emitting X-rays that are specific to the energy difference between the high and low energy state and therefore specific to the element that has emitted it, allowing elemental analysis. By reducing the size of the irradiated area, analysis on very small isolated parts of a sample is, in principle possible. The peak heights seen in the results are not directly related to the atomic ratio, as different atoms give a much stronger signal than others do, but the electronics can interpret them to give approximate atomic ratios.

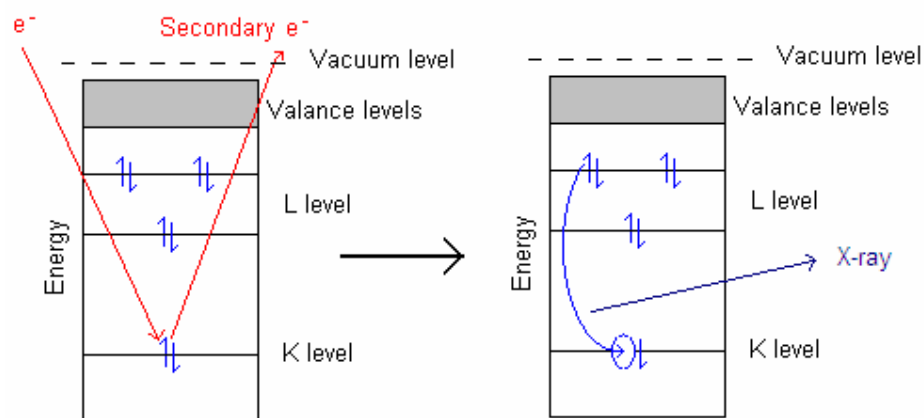


Figure 2.13 Diagram to show the energy levels involved in EDAX.

The results from the EDX analysis are given as a graph showing the intensities of the various signals detected by the machine. The peak positions are then assigned to the appropriate transition. Different atoms have different possible transitions depending on how low in energy the core electron shells (L, K and M) are with respect to the incident electrons. K lines are caused by X-rays emitted because of an electron dropping into a K level as shown by Figure 2.13, but L and M lines may also occur. The accuracy of this technique when working with low density, nano-sized objects is low because of the scattering obtained from the carbon tab on which the sample is loaded and the adhesive with which it is stuck. Measurements concerning carbon or oxygen are therefore particularly badly affected as these elements are used in the carbon tab and the adhesive. EDX is optimal for a uniform polished surface leading to possible errors with nanowire analysis. In general, similar calculations of atomic percentages performed using the sulfur K line and tantalum L line agree with those values originating from the sulfur K line and the tantalum M line to within a few percent, giving an indication of the accuracy of the technique. Elemental analysis results are given as a percentage ratio between the requested elements so where necessary the results have been published hereon as a percentage ratio with the error in the results given as a \pm figure after the result.

The resolution of the EDX spectrometer in general can be calculated using Equation (2.10) but is intimately linked to the method of detection of X-rays. X-ray energies can be detected in a number of ways. A simple system can involve a scintillation counter that counts the X-rays and a single crystal using Bragg reflections to individually select one wavelength at a time. This method however is slow and bulky. The common alternative is to use semiconductors to absorb the X-ray and produce electron-hole pairs. The electron-hole pairs are then separated from each other and stabilised before being detected by the electronics that counts the statistics. Stabilising the electron-hole pair is best done either by using a p-n junction in the same setup as a diode or by using an electric field across an intrinsic semiconductor. The diode setup allows the Fermi energy to be distorted across a “depletion” zone, which occurs between the two systems. Electron-hole pair formation within this depletion zone, results in electrons flowing down the potential gradient and the holes flowing up, thus preventing recombination and stabilising the higher energy state.

The alternative is simply to apply a charge to an intrinsic semiconductor thus separating the electron and hole at formation. The problems associated with both methods e.g. the small thickness of the depletion zone, can be overcome by combining the two methods in a p-i-n setup. Electrodes can then be attached at the back and front of the detector and a computer can interpret the information output. The favoured materials for the intrinsic part are Si and Ge, however ultra pure “intrinsic” Si is almost impossible to produce so Li is used as a dopant in small quantities to counteract the impurities and produce intrinsic behaviour. The result of this however, is that the detector has to operate at low temperature or Li diffusion occurs and the detector will malfunction, hence EDX detectors operate under liquid nitrogen conditions.

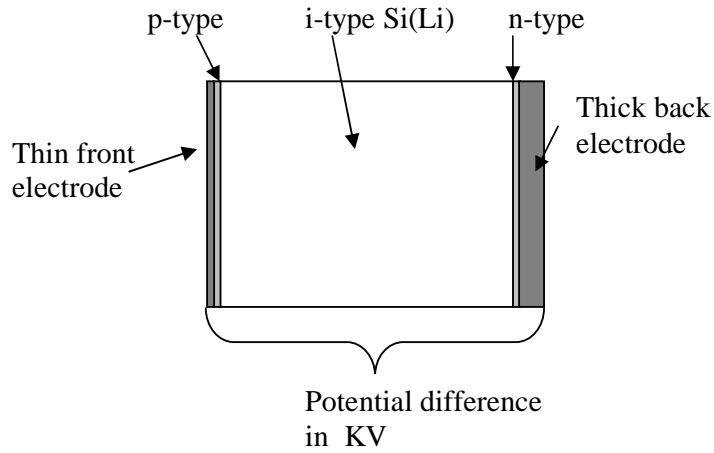


Figure 2.14: Schematic of an EDX detector.

The resolution can be calculated as follows.

$$R^2 = I^2 + P^2 + X^2 \quad (2.10)$$

R = resolution

I = intrinsic resolution of the sample set up (given in Equation (2.11))

P = intrinsic resolution of the electronics

X = intrinsic resolution of the detector setup

$$I = 2.35\sqrt{F\varepsilon E} \quad (2.11)$$

F = A statistical factor called the Fano factor

ε = Electron hole pair creation energy

E = X-ray energy.

As technological improvement leads to a reduction in the values of P and X in Equation (2.10), the resolution of the EDX analysis improves, however, the value of I is governed by physical constants and can therefore not be improved on by design. An ultimate resolution can therefore be obtained which for the standard Mn K α is ~111 eV, (P=X=0 in Equation (2.10)). It is also clear that as the X-ray energy decreases, resolution increases leading to data that are more accurate from the lower energy X-rays i.e. lighter atoms give better resolution.

During analysis, the X-ray enters the detector and is absorbed as it excites the electron-hole pairs. The electron-hole pairs are then separated and drawn to the edges of the

potential gradient and the signal amplified and processed by the electronics. During the processing time, the signal from further X-rays is ignored and the time is recorded as dead time. When recording it is important to monitor the dead time, which is given as a percentage of total time and should be less than 50 % depending on the analysis that is required. The dead time is controlled by the processing time and the count rate received from the sample. Scans were, in general taken over 60 seconds of live time and had approximately 5 – 10 % dead time.

2.4.2.2 Sample Preparation for SEM

The powdered or fibrous samples are scattered or wiped across a circular double-sided carbon adhesive tab and attached to an aluminium slug before being inserted into the SEM. In non-conducting samples, pre-treatment with an inert metallic layer, for example, gold is needed to reduce the build up of charge on the surface due to secondary electron loss. The samples in this project, however, were sufficiently conducting through the carbon tab to avoid the need for sample coating.

2.4.2.3 Scanning Electron Microscopes

2.4.2.3.1 Philips XL30 SEM, at The University of Nottingham

A Philips XL30 SEM-FEG has been used, operating at 20 KV in high vacuum mode with a working distance of 10 mm. An Oxford instruments EDX was attached to the side giving elemental analysis capability, of elements as light as carbon. A standard SED was used and the microscope was operated only in high vacuum mode.

2.4.2.3.2 Philips XL30 FEG ESEM, at the University of Nottingham

A Philips XL30 Environmental Scanning Electron Microscope – Field Emission Gun has been used at Nottingham. The ESEM has the potential to carry out imaging in a huge variety of modes or environments, including wet mode where an atmosphere of water vapour allows

the sample to be imaged whilst in a conducting environment. Controlled heating and cooling of the sample is also possible with real time monitoring. The ESEM was used in auxiliary mode with an X-ray secondary electron detector (SED) and a hook printed circuit board instead of the standard GSED (Gaseous Secondary Electron Detector) for EDX. This set-up was used to minimise the scattering from the sample allowing the working distance of 10 mm to have an effective distance of 2 mm and a working voltage of 20 KV. Mrs. N. Weston from the materials department at the University of Nottingham has been responsible as a SEM technician for the SEM work carried out on this machine.

2.4.2.3.3 Philips XL30 ESEM, at the University of Glasgow

A Philips XL30 SEM-FEG has been used in the geology department of Glasgow University, operating at 20 KV in high vacuum mode with a working distance of 10 mm. An Oxford instruments EDX was attached to the side giving elemental analysis capability. Again this microscope was only used in high vacuum work though it did have environmental mode capabilities. A standard SED was used to detect the electrons.

2.4.2.3.4 Philips XL30 ESEM, at the University of Glasgow

A Philips XL30 SEM-FEG was used in the chemistry department of Glasgow University, operating at 20 KV in high vacuum mode with a working distance of 10 mm. An Oxford instruments EDX was attached to the side giving elemental analysis capability, of elements as light as carbon. Again this microscope was only used in high vacuum work though it did have environmental mode capabilities. A standard SED was used to detect the electrons.

2.4.2.3.5 References to the XL30 ESEMs in this Thesis

As there are three different XL30 ESEM microscopes used throughout the project and one XL30 SEM all of which have achieved the same sorts of results, a simple numbering system has been adopted in reference to the different machines. These will hereon be referred to as SEM #1, SEM #2, SEM #3 and SEM #4 respectively as they appear in the text above.

2.4.3 Transmission Electron Microscopy

Transmission electron microscopy (TEM) has many similarities to optical microscopy with the main difference being the resolution achieved. This is because the resolution is inversely proportional to the wavelength of the imaging radiation.¹⁸⁴ Although the resolution of a TEM means different things depending on the function, the smallest distance that can be resolved δ can be approximated by Equation (2.12).

$$\delta = \frac{0.61\lambda}{\mu \sin \beta} \quad (2.12)$$

δ = smallest distance resolved

λ = Wavelength of light / electrons

μ = refractive index of material

β = semi-angle of collection

In Equation (2.12) $\mu \sin \beta$ (often referred to as the numerical aperture) can be approximated to unity giving the resolution of the microscope to be approximately half that of the wavelength of the radiation used. Electrons, having a smaller wavelength than optical light therefore give a higher resolution image. While glass can be used to focus photons of light, no material has yet been found to focus a beam of electrons so an electro-magnetic field is used for this purpose.¹⁸⁴ The inability to form a perfect lens for electrons has a massively detrimental effect on the resolution of a TEM however the achievable resolution is still far greater than that obtained from light or X-rays.

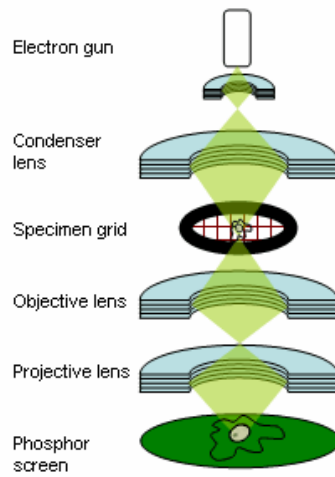


Figure 2.15: Schematic of a TEM.¹⁸⁵

Once produced, electrons can be accelerated to higher energies, (>200 kV,) giving them enough energy to pass through a sample. The electrons that pass through the sample ($<20000\text{\AA}$ thick) can then be focused down the TEM before being detected. Methods of detection include; photographic film, fluorescent screens, and CCD displays, depending on the age or cost of the microscope.

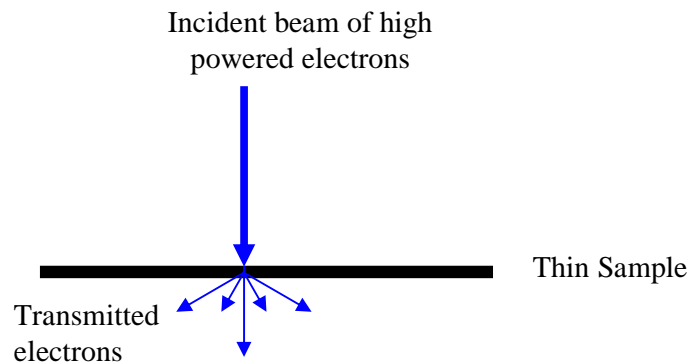


Figure 2.16: Schematic diagram to show the electron beam path used in TEM.

2.4.3.1 **Bright Field Imaging**

Bright field imaging is the standard type of imaging associated with TEM. The electron beam interacts with a thin sample as it passes through and is focused on a detection device. Fluorescent screens or CCD detectors can be used for the detection of electrons. Contrast

occurs because of the interaction between the electron beam and the material being analysed. Areas of low contrast (light) generally absorb or scatter the electrons the least and conversely the higher contrast areas (darker) generally absorb more electrons or scatter the most. Contrast can arise from many sources including; Bragg scattering, (diffraction contrast) as well as thickness of sample (absorption contrast). Figure 2.17 shows a ray diagram indicating how the magnification using a hypothetical one lens microscope is achieved. Different angled beams from the specimen can be focussed onto the image plane by altering the power of the lens which moved the focal point or back focal plane (BFP) forwards or backwards along the optic axis.

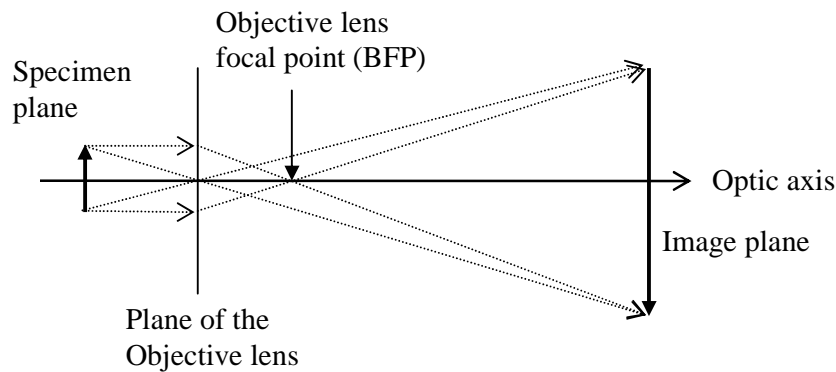


Figure 2.17: Ray diagram showing how the electron beam magnifies the image from the specimen plane to the image plane. Different angled beams from the specimen can be focussed onto the image plane by altering the power of the lens.

2.4.3.2 Selected Area Electron Diffraction

In Section 2.4.1 the diffraction of X-rays was considered. Electron diffraction is similar but using electrons. Diffraction of electrons can give a spot pattern from the transmission beam which can be imaged giving accurate information about the crystal structure as it is viewed in inverse space.

In Equation (1.13) it was shown that $n\lambda = 2d \sin \theta$ as a result of Bragg scattering of X-rays off a crystal lattice. The crystal lattice can scatter electrons as well and in fact better as they interact both with the nucleus and the electrons of the atoms within the lattice.

Parallel rays that have been diffracted off the same plane of atoms will be travelling parallel to each other and at the same angle from the optic axis. By changing the image plane and imaging at the point of the Back Focal Plane (BFP) the constructive interference observed by the Bragg scattering will appear as areas of high intensity. As each Bragg reflection will have a different angle with respect to the optic axis a series of spots will appear in the BFP forming a diffraction pattern. Large amounts of crystallographic information can be gleaned from the diffraction pattern as the spots are indexed or assigned to hkl values for the Bragg reflections to which they correspond.

A selected area aperture can be applied below the objective lens to isolate the rays (diffracted electron beams) that originate from one specific area of the sample. This allows detailed information about one specific region, hence Selected Area Electron Diffraction, (SAED).

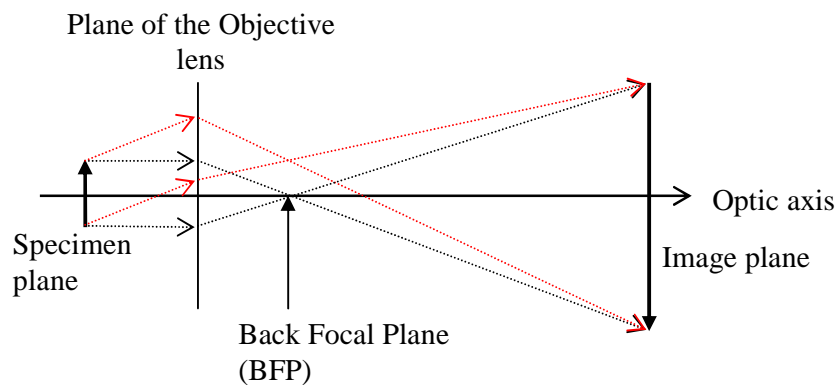


Figure 2.18: Ray diagram to show the basic concept behind electron diffraction.

When changing the microscope from imaging mode to diffraction mode it is necessary to move the focal plane from the image plane to the BFP. The simplest way of achieving this is to move the detector along the optic axis till it reaches the BFP; this however is unpractical in a microscope where the sample gun and detection positions are all fixed. The solution is to change the power of the objective lens so that the back focal plane extends down the column and appears in the physical position of the imaging plane. In changing the power of an

electromagnetic lens there will always be an associated rotation of the image projection arising as a result of the method in which the pole piece of the lens bends the beam of electrons. Flemings right hand rule (Figure 2.19) states that when a charged particle moves (current) through an applied field then there will be a force exerted on the particle (motion) with all three factors at right angles. This allows the beam to be controlled, however, there is also an inherent rotation associated with the use of opposing fields in the pole piece that makes the electromagnetic lens work.

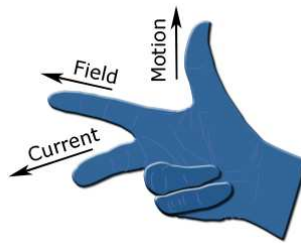


Figure 2.19: Schematic showing Flemings right hand rule.

The result is a rotational dependence between the orientation of the image and its diffraction pattern as it appears on the screen. There are methods of overcoming the problem of rotational alignment between the image and the diffraction pattern that can be built into the microscopes. JEOL microscopes for instance, including the JEOL 2000FX (Section 2.4.3.7.1), have no rotation (or very little) between the image and the diffraction pattern as a result of effectively using two objective lenses with reverse polarities so as to get the same magnification and focussing but with one lens rotating clockwise and the other lens rotating counter-clockwise. FEI microscopes, (including the T20, Section 2.4.3.7.3) over come this in a different way but have a 90° rotational constant. The consequence on this work is that the alignment between the images and the diffraction patterns will vary depending on the microscope used.

In electron diffraction the spots occur in inverse space (K-space) while the lattice exists in real space. It is therefore necessary to be able to interconvert between the two. This is done using Equation (2.13).

$$Dd = 2\lambda l \quad (2.13)$$

D = measured distance between spots on diffraction pattern. (mm)

d = d spacing (nm)

λ = camera constant

l = camera length (cm)

The camera constant λ can be calculated from comparing measurements with spacings from a known standard as shown by Equation (2.14). Once calculated the camera constant can be used to evaluate other diffraction patterns as this is constant to the microscope. The diffraction patterns are evaluated on a light box using a pair of Vernier callipers if on photographic film or using Image J¹⁸⁶ if electronic, with measurements averaged over a number of spots in all three directions. The units used in the measurements are irrelevant as long as they are constant in all calculations.

$$\lambda = \frac{Dd}{2l} \quad (2.14)$$

2.4.3.3 Nanobeam Diffraction Techniques

By condensing the beam down with a small spot size and a small condenser aperture it is possible to acquire an electron diffraction pattern without the selected area aperture. These electron diffraction patterns look similar to a standard SAED but have larger more diffuse spots. The focusing of the beam can occur on a very small scale and effectively only illuminate the area of interest.

2.4.3.4 Dark Field Imaging

In dark field imaging a diffraction pattern is achieved and the electron source moved so as to interact with the sample at an angle. If the angle corresponds with that of a specific Bragg condition from the electron diffraction pattern then a dark field image is achieved. The dark field image shows contrast from the areas of the sample from which the intensity of the diffraction spot originates. In imaging a perfect single crystal the DF image should be the

reverse contrast to the BF image as all the crystal will be responsible for all the diffraction spots. In a polycrystalline or semi-polycrystalline material, different crystals will have a different contribution to the spots in the pattern. Different contrast will therefore be observed.

2.4.3.5 High Resolution Imaging

By combining all the beams from all the diffraction occurrences High Resolution TEM can be achieved. A very high magnification is used and given the correct sample conditions, resolution down to atomic planes is possible. The main difficulties with this technique are the need for atomically stable instrumentation and really high quality samples. Few samples are of sufficient quality for HRTEM as you need areas of very thin regions containing ordered atomic planes.

2.4.3.6 Sample Preparation for TEM

2.4.3.6.1 Dispersion of Nanofibres onto a Carbon Holey Grid

Small quantities of material were placed in a small agar mortar with a few drops of propan-2-ol and agitated using the pestle. The solution was then dropped through a holey carbon grid (300 mesh Ni) into a clean piece of filter using a Pasteur pipette, leaving the nanowires dispersed on the surface of the grid.

2.4.3.6.2 Cross Section Encapsulation Using Silica Wafers

In an attempt to take images and diffraction patterns down the length of the nanowires, an encapsulation preparation was performed. Small sheets of silica, 10 x 5 x 0.6 mm were cut from a sheet and cleaned by sonicating in ethanol (1 minute). Epoxy resin was mixed and infused with nanowires on a glass slide before being applied to the top surface of a silica wafer and roughly aligned before being transferred to a hot plate at 150 °C for setting. After setting, the second piece of silica was applied with clean epoxy to give a sandwich like structure (Figure 2.20). The sandwiches were ground down, by attaching to a glass slide and

sanding with wet and dry paper, so that they fitted vertically into the central hole of titanium encapsulation holders with the fibres running vertically (Figure 2.20).

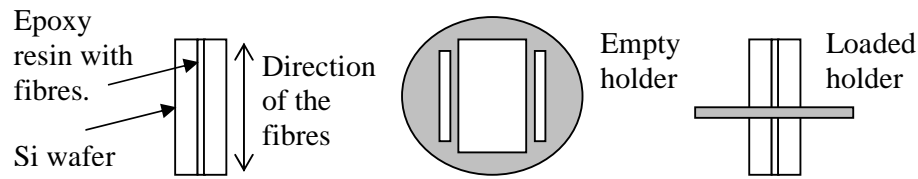


Figure 2.20: Schematic of the encapsulation sample holder for TEM and the loading procedure.

Once vertical in the holder, more epoxy was applied, holding the wafer sandwich in place. The samples were then ground vertically until just the sample holder and wafer cross section remained and a thickness of about 80 μm (Figure 2.21).

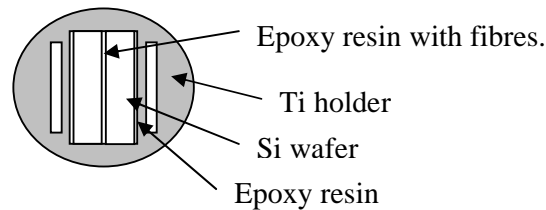


Figure 2.21: Schematic showing the loaded sample holder.

The samples were thinned to an electron transparent thickness using a Gatan dimple grinder with 4 μm diamond paste and a precision ion polishing system, (PIPS). Dimpling from both sides to a depth of 35 μm , gave a central region of about 10 μm thickness, indicated by the beginnings of the transmission of light through the silicon. The samples were milled using the pips until the smallest hole appeared in the centre of the wafer. At this point, the samples were ready to be loaded into the TEM and the electron transparent region examined (Figure 2.22).

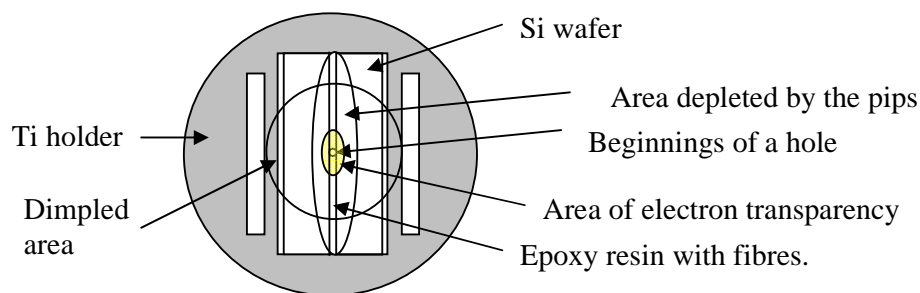


Figure 2.22: Schematic of the encapsulated nanofibres TEM sample.

2.4.3.7 Transmission Electron Microscopes

2.4.3.7.1 JEOL 2000FX TEM, at the University of Nottingham

Operated at 200 KV, with SAED achieved at a camera length of 100 cm. Photographic plates used for the recording of images with auto selected exposure times. The photographic images were then scanned into digital images for analysis and presentation. The collection of the TEM data at the University of Nottingham was performed by Hannah Edwards and Paul Brown from the department of Materials, Mining and Mechanical Engineering. (See Acknowledgements on Page iv).

2.4.3.7.2 JEOL 1200 TEM, at the University of Glasgow

The JEOL 1200 is a very simple low resolution TEM that has been in the department for many years. Operating at 80 KV it utilises photographic plates for bright field imaging. The diffraction constants were calculated, but the inability to set the eucentric height leads to unreliable values with large errors so reliable diffraction data wasn't collected on this microscope.

2.4.3.7.3 FEI Techni T20 TEM, at the University of Glasgow

Bright field imaging, selected area electron diffraction (SAED), and nanobeam diffraction data were collected on this sophisticated electron microscope made by FEI Company, Eindhoven, Netherlands. It was operated at 200 kV with Images and diffraction patterns recorded using a SIS Megaview III CCD camera (Olympus Soft Imaging Solutions GmbH,

Münster, Germany). High-resolution imaging was achieved using a GIF digital recording device. The collection of much of the TEM data at the University of Glasgow was performed by or with the help of Ian MacLaren from the department of Physics. (See Acknowledgements on Page iv).

2.4.4 Thermal Analysis

Thermal analysis is a powerful technique when characterising materials and has been used in this project in the search for phase changes and as a basis for the experimental parameters for the inter-conversion of polytypes and compounds. There are many aspects to thermal analysis but only a few have been utilised:

2.4.4.1 Thermo-Gravimetric Analysis

Thermo Gravimetric Analysis, (TGA) traces the minute changes in mass associated with heating small quantities of material to high temperature under a great number of experimental conditions, allowing the observation of reactions and decompositions. TGA can be used to identify an unknown phase or stoichiometry by comparing the actual mass change with the predicted mass change for the hypothetical system. However, some knowledge of the likely starting and final phases is necessary.

2.4.4.2 Differential Thermal Analysis and Differential Scanning Calorimetry

Differential Thermal Analysis (DTA) and Differential Scanning Calorimetry (DSC) allows measurement of heat flows during the TGA run to trace the differing endothermic and exothermic properties of the material / reaction as it is heated. When materials change phase or rearrange their atoms to change from one polytype to another, energy is absorbed but there will be no associated mass change. These should show up on the DTA and DSC trace.

2.4.4.3 Sample Preparation for TG-DTA

The TG-DTA was first calibrated with an empty crucible over the entire range of the experimental parameters. This was performed as a crucible buoyancy correction and determined the parameters of the experiment. Powdered samples (~100 mg) were placed in an alumina crucible and inserted into the TG-DTA. The machine already set up from the buoyancy correction then performs the desired scan for the sample. In general TG-DTA scans were performed from RT to 1000 °C or 1400 °C at a heating rate of 10 °C per minute, in flowing argon, (20 mlmin⁻¹) and air, (60 mlmin⁻¹).

2.4.4.4 Gravimetric Analysers

2.4.4.4.1 TA Instruments DSC

The DSC measurement was carried out using a Thermal Analysis DSC operated between room temperature and 500 °C at 10 °C min⁻¹ in an aluminium sample pan.

2.4.4.4.2 Netzsch STA

Measurements were run using a TG-DTA produced by Netzsch. The instrument was housed within the confines of a glove box to allow air sensitive sample loading which was unnecessary for this project. Scans were typically run on 100 mg samples from room temperature to 1000 °C at 10 °C min⁻¹.

2.4.5 Magnetic Measurements

Some theory behind magnetism in materials is given in Section 1.4. The experimental use and measurements for magnetic materials is given here.

2.4.5.1 SQUID Magnetometry

A Superconducting Quantum Interference Device (SQUID) is in basic terms a very sensitive voltage and current meter. A sample is placed inside a superconducting coil where any

magnetic moment will induce a current within the superconducting coils. The induced current within the coils can be measured to a very high level of accuracy, even with a very small mass of sample, and relates directly to the magnetic moment of the sample, which can be calculated.

The results were obtained using the SQUID in Reciprocal Sample Option (RSO) mode as this improves the sensitivity of the instrument.

2.4.5.2 Sample Preparation for SQUID

SQUID samples were prepared by placing small amounts of experimental samples into a gelatine capsule and inserting them into the centre of a drinking straw. The gelatine capsule was held shut using a small piece of special magnetically inert tape which doubled as a restraint by wedging the sample in the drinking straw. Care was taken at every stage not to touch the sample, gelatine capsule or drinking straw with anything that may have a magnetic moment or cause transfer of water. All handling was performed using gloves, plastic tweezers and Teflon coated spatulas. The straw was pierced using a hypodermic needle to allow gas flow and prevent pressure differences before the being attached to the end of the sample holder. The sample holder was inserted into the machine through an air lock, having been thoroughly cleaned and dried to prevent moisture accessing the cold areas of the machine where it will solidify. The SQUID magnetometer was set at room temperature during the loading and unloading.

2.4.5.3 Centering the Sample

Once loaded, the sample was centred at 2 cm using a full range scan at 1000 Oe field at room temperature. The RSO settings were optimised so that the standard deviation was at least 4 orders of magnitude lower than the machine moment recorded. This was done essentially through trial and error, performing scans with different RSO settings. Of the 4 RSO variables, the number of cycles is usually set at 5 and the number of measurements per cycle

to 4. The other two being the RSO distance and the frequency were varied. It was found that the RSO distance was usually between 1 and 3 cm and the frequency was between 0.5 and 3 Hz. The SQUID was generally set to do a T_C scan where it scanned through the temperature range (2 – 300 K) taking magnetic susceptibility readings at short intervals. This showed up the superconducting transitions and could be repeated over a smaller range with more accuracy once initial data had been collected.

2.4.5.4 Working up SQUID data

Once the data was collected, the values for χ_g , χ_M , $1/\chi_M$ and μ_{eff} were extracted through various calculations.

The machine moment (MM) needed to be corrected firstly for the effect of the gelatine capsule. This was calculated from running an empty gelatine capsule and working out its magnetic moment, which is dependant on both the temperature and the field.

$$GC = (-1.8 + \frac{1.83}{T} \times 10^8) \times H \frac{GCW}{0.0434} \quad (2.15)$$

GC = Gel cap correction (emu)

T = Temperature (K)

H= Field (Oe)

GCW= Gel cap weight (g)

The sample machine moment (SMM) was then calculated by subtracting this value from the raw data (MM) recorded by the SQUID, leaving the magnetic moment that has been due solely to the sample.

$$SMM = MM - GC \quad (2.16)$$

SMM = Sample machine moment (emu)

MM = Machine Moment (emu)

This sample machine moment then led to the Observed Gram Susceptibility (OXG) of the sample, and indeed the observed molar susceptibility (OXM) by multiplying OXG by the

relative formula mass of the sample, (Equation (2.18)), giving the susceptibility per mole of substance while taking into account the gel cap.

$$OXG = \frac{SMM}{H \times SW} \quad (2.17)$$

OXG = Observed Gram Susceptibility (emu g⁻¹)

SW = Sample weight (g)

$$OXM = OXG \times RFM \quad (2.18)$$

The OXG and OXM were further corrected for the diamagnetic contributions to the susceptibility of the ions present. These are found in the primary literature and are given as + or – values at 10⁻⁶ emu/mol. The sum of these corrections can be subtracted from the observed χ_M (OXM) values to give sample χ_M values for the material. Sample χ_M values allow the calculation of μ_{eff} which is the effective magnetic moment of the material as shown in Equation (1.27).

2.4.5.5 SQUID Magnetometers

Both departments at Nottingham and Glasgow had the same make and model of SQUID magnetometer. The SQUID was a Quantum Design MPMS-XL.

2.4.6 Diffuse Reflectance Spectroscopy

Diffuse Reflectance Spectroscopy (DRS) is a technique that collects and analyzes the diffuse light, (scattered at all angles) from the sample when irradiated at different wavelengths. This is in contrast to other techniques that measure the specula light that is scattered with a dominant angle. The difference between diffuse and specula light is best described by reference to matt and gloss paint. Matt paint has diffuse reflectance while gloss has a much higher degree of specula reflectance. The sample was irradiated by UV-vis light and the reflected beams are focussed on a detector using a spherical mirror. The focussed light

having passed through the sample now carries information about the sample that can be interpreted.

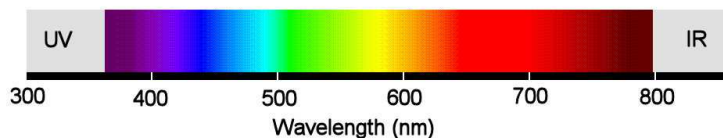


Figure 2.23: Colour spectrum of visible light showing the region of interest for UV-vis diffuse reflectance spectroscopy.

DRS data can be displayed in a large number of ways, depending on the information required. In line with many of the DRS publications considered, observed data presented herein will be presented as a plot of absorption against wavelength in nm running from blue to red along the x-axis and arbitrary units of absorption up the y axis. The data once collected was reordered so the x-axis ran blue→red (Figure 2.23) and converted into a percentage of the total absorption using the formula given in Equation (2.19). Onset values were calculated by extrapolation of the steepest part of the curve towards the baseline, reading off at 0 % in nm and converting to eV using Equation (2.20). Converting into percentage absorption allows all plots to be super imposed within the same range of values on the y axis clearly showing the different onset positions. The spectrometer was calibrated using a commercial sample of TiO₂ (99.99 % rutile, Aldrich chemicals) with known band gap onset at 3.00 eV. The calibration curve is shown as an example of a diffuse reflectance spectrum in Figure 2.24.

$$A = ((y - a) / (z - a)) \times 100 \quad (2.19)$$

A = % value

y = value for absorption in data set

a = smallest value in data set

z = largest value in data set

$$\lambda = \frac{hc}{E} \quad (2.20)$$

λ = wavelength (M)

h = Planks constant 6.6208×10^{-34}

c = Speed of light = $3.814 \times 10^8 \text{ ms}^{-1}$

E = Energy of the light with said wavelength λ (J)

As

$$\frac{E}{e} = \text{energy eV} \quad (2.21)$$

e = Charge on an electron

E now in units of eV is given by Equation (2.22)

$$E = \frac{hc}{\lambda e} \quad (2.22)$$

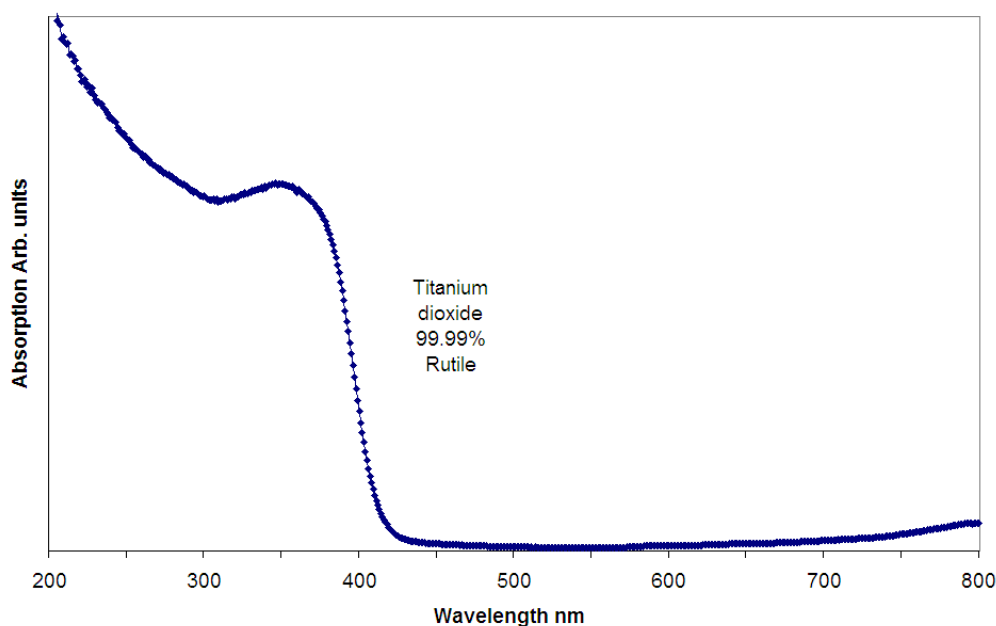


Figure 2.24: DRS spectrum of TiO_2 powder 99.99% rutile with a known onset at 3.0 eV used both as an example of the intended presentation of DRS data, and to show the calibration of the spectrometer.

2.4.6.1 Sample Preparation for Diffuse Reflectance Spectroscopy

Powdered samples were placed in the sample holder and inserted into the DR spectrometer.

The praying mantis mirror was placed over the top of the sample and the sample compartment sealed for light.

2.4.6.2 Diffuse Reflectance Spectrometer

The DRS spectrometer used was a Varian, Cary 500 scan UV-vis-NIR spectrophotometer with a praying mantis mirror attachment. Scans were run in absorption mode from $800 \leq \text{nm} \leq 200$ after calibration at a scan speed of 300 nm min^{-1} .

2.4.7 BET Isotherms for Surface Area Analysis

BET analysis was carried out using a Gemini Micrometrics, Surface Area Analyser with samples dried overnight by heating to 110°C in a flow of nitrogen gas using a Gemini Micrometrics flow prep 060.

2.4.8 Atomic Force Microscopy

Atomic Force Microscopy, (AFM) belongs to a family of microscopy techniques known as probe microscopy. Probe microscopy included the better known techniques of Scanning Tunnelling Microscopy, (STM). The principle of probe microscopy is that when a sharp tip comes into close proximity with a surface (few angstroms) it will experience some form of interaction which can be measured to give information about the surface of the sample. With the use of piezo-electric crystals, the arm holding the tip can be manipulated on a minutely small and accurate scale to maintain a constant interaction and therefore a constant distance between the tip and the surface giving an accurate height map. The different forms of probe microscopy utilise the different interactions that are possible and thus give different information about the surface

AFM utilises the physical interactions between the surface and the tip when in close proximity, as shown in Figure 2.25. Different tips can be used for different effects, e.g. a hydrophobic tip will have a different reaction to a hydrophilic surface than a hydrophilic tip. The surface is placed on a table that has two-dimensional controls and allows the tip to scan across it while the cantilever has 1-dimensional control to maintain the constant height above the sample. A laser is projected onto the cantilever, which allows accurate measurement of

the minute changes in height and angle of the cantilever. By scanning across the sample, an accurate map of the surface is achieved with high resolution.

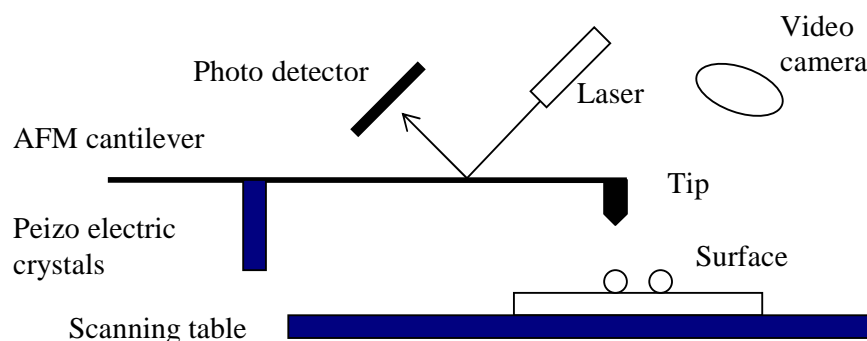


Figure 2.25: Schematic representation of an Atomic Force Microscope.

2.4.8.1 AFM Imaging

A fine tip was inserted into the tip holder on the AFM and then positioned on top of the prepared sample, placed on a glass slide with 2 dimensional control situated on a “Stable Table” to dampen out vibrations. The tip was aligned with the laser which is achieved with the help firstly of a camera and secondly using the software to maximise the output signal. Once aligned the tip was tuned for the best resonant frequency by the software. The feedback mechanism was engaged and the tip lowered to $0.8\ \mu\text{m}$ above the surface. At this point, the feedback loop controls the altitude of the tip maintaining the constant distance while the tip was lowered further until it is in the middle of the feedback mechanism’s range of movement.

Scans can be run up to an area of $90\ \mu\text{m}$ by $90\ \mu\text{m}$ with a range of speeds and resolutions. The camera was used to align the larger bundles of nanowires within the $90\ \mu\text{m}$ by $90\ \mu\text{m}$ region viewed by the AFM and a low resolution quick scan is taken. Higher resolution slower images can then be taken from within this region. The AFM was controlled by Igor Pro software.

2.4.8.2 Electronic Measurements

Typically in IV curves a voltage is supplied across an object and the current that flows is measured, however it is equally possible to supply the current and measure the voltage, thus obtaining information on the resistance using Ohm's Law. There are 2 standard types of electrical connection when taking IV curves. These are 2-terminal connections and 4-terminal connections. The concept is the same but in the 2-terminal measurements the current and voltage are supplied and recorded using the same terminals. In 4-terminal measurements the current / voltage is supplied by 2 of the terminals and the current / voltage is measured across the other two. This cuts out the interference from contact resistance.

The AFM setup at Nottingham (Section 2.4.8.4) allowed for 2-terminal electronic measurements of samples on a surface. Nanowire samples were spin coated (Section 2.4.8.3) onto prepared polished silica surfaces that contain a gold grid. The grids were formed by evaporating gold through a blanking setup with 200 μm thick wire and 200 nm spaces between the wires. The application of silver paint to the edge of the silica plate once the nanowires are in place connects the grid lines and allows electronic measurements on the nanowires using a special AFM tip, (Figure 2.26). The camera was again used for the alignment of the nanowires within the AFM and positioning of the AFM tip at intervals along the wire to complete the circuit allowed length dependant electronic measurements to be taken.

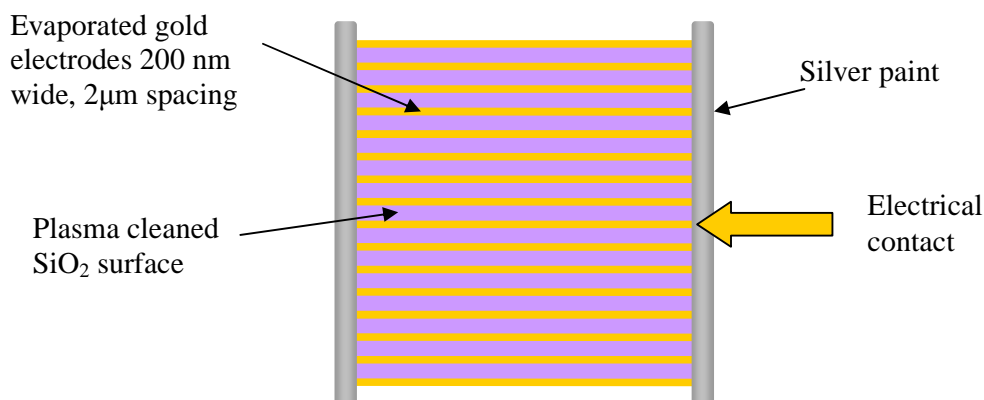


Figure 2.26: Surface used for electronic measurements on the AFM.

2.4.8.3 Sample Preparation

A typical silicon surface was cut from a silicon sheet into squares of side 9 mm having been sheared along the 111 unit cell direction. The surface was polished before being cleaned by sonicating in a number of different solvents, (ethanol, toluene and water), to remove all likely contaminants prior to plasma cleaning and rinsing in water of extreme high purity (80 m Ω resistance).

The samples were dispersed in a volatile solvent, (toluene), and placed drop wise onto the cleaned polished surface which is held in place inside the spin coating machine by a vacuum. Once in place the surface disk is spun at 3000 rpm for 30 seconds, momentarily increasing the wettability of the surface before the solvent evaporates. This process was carried out in a clean room using high purity solvents to avoid any contamination from dust or solvents.

2.4.8.4 Asylum Research Atomic Force Microscope

The AFM used in this project was a custom-built AFM by Asylum Research

2.4.8.5 Collaboration

AFM was achieved in collaboration with Prof. P. Moriarty and Mr. A. Stannard from the University of Nottingham. Spin coating was carried out in the clean room at Nottingham with Mr. A. Stannard. The images and readings were taken by myself, having been trained on the basic use of the Nottingham equipment, again supervised by Mr. A. Stannard. (See Acknowledgements on Page iv).

Chapter 3: Tantalum Disulfide Nanofibres

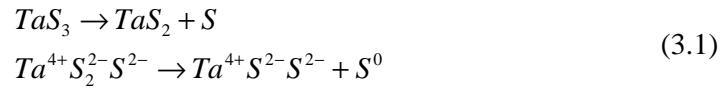
3.1 Introduction

To date much of the research concerning inorganic nanostructures has involved the investigation of transition metal dichalcogenide materials, MX_2 ($\text{M}=\text{GIV to VI}$ and $\text{X} = \text{S, Se, Te}$). MX_2 compounds have a layered structure, (Section 1.5), with many structural similarities to that of graphite¹⁴⁹ and are therefore likely candidates for the formation of nanofibres with many examples in the literature (Table 1.1). Most interest has so far been directed towards WS_2 and MoS_2 with very little work conducted concerning the analogous Ta system, TaS_2 , which was considered an appropriate starting point for this project. Prior to the commencement of this project, there was only one report of the formation of TaS_2 nanotubes,⁴³ with little actually understood about their mechanism of formation and the intricate details of their structures. The possibility of preparing nanofibrous structures of TaS_2 and comparing the interesting physical properties of the nanomorphology with those of the bulk material was intriguing.

When trying to prepare TaS_2 nanofibres, there are many analogous systems that can be considered in the literature. These materials however are also relevant to the synthesis of other materials are outlined in this thesis so to avoid unnecessary repetition have been incorporated into Section 1.11.1 but will form the basis of discussion.

There are currently 3 preparations for nanofibres of TaS_2 in the literature. The first consists of heating tantalum trisulfide in the bulk phase in a reducing atmosphere of hydrogen and produces small amounts of TaS_2 nanotubes.¹⁸⁷ This method is both a multi step method, as it involves the formation of a tantalum trisulfide precursor prior to the formation of the nanotubes, and has very low yields. The second method involved the formation of trisulfide nanobelts directly from elemental powders using iodine as a transport agent and then decomposing the nanobelts with little alteration of morphology into TaS_2 by heating to 850

°C, using a temperature gradient to separate the residual sulfur.⁵⁹ This method is again a multi-step process with low yields. Both preparations involve the conversion of TaS₃ into TaS₂ as shown by Equation (3.1). The Ta remains in the 4+ oxidation state with the sulfur S_2^{2-} species being disproportionated into S^{2-} and S^0 . Interestingly this process seems to occur spontaneously at temperatures above 650 °C (under vacuum)^{59, 136} though the use of a reducing agent seems to promote a reduction in the size morphology and the formation of nanotubes across a wide range of MX₂ compounds.^{43, 50, 160}



The final preparation currently in the literature is our paper and covers much of what is to follow in this chapter.¹⁸⁸ The concept of forming nanofibres of TaS₂ from the direct heating of elemental powders in a single step synthesis remains unique with respect to the first two preparation methods and has been investigated hereon.

3.2 Experimental

3.2.1 Synthesis

There have been two major synthetic preparations that have been investigated at different temperatures, along with some minor preparations for the bulk phases. These are explained in this section with general principles and experimental setups outlined in Section 2.3. It is prudent at this point to introduce a preparation naming system which has subsequently been used throughout the thesis.

The preparation names consist of a list of reactants and their relative quantities in the reaction mixture followed by a temperature before the unique preparation conditions. Preparation names will be highlighted in bold to distinguish them from the main text. E.g. the preparation involving a 1:2 ratio Ta:S, heated at 650°C under the standard conditions,

(Section 3.2.1.1) will be referred to as **TaS₂650_Std**. If the unique preparation conditions (**Std** or **SAG**) are irrelevant, then this section of the reference will be omitted, e.g. **TaS₂650** will refer to all the reactions at 650 °C with a 1:2 ratio Ta:S.

3.2.1.1 Standard Preparation

In a typical reaction, elemental powders of Ta (99.9% -325 mesh, Aldrich) and S (99.5% Fisher Chemicals) were ground together in stoichiometric mixtures and sealed under vacuum ($\sim 4 \times 10^{-5}$ Torr) in silica tubes, to form ampoules (Section 2.2.4.5). Once sealed, the silica ampoules were held upright with all the powder at one end before being placed horizontally in the centre of a box furnace (Section 2.2.4.8) on a ceramic brick and heated over a specific temperature profile. The temperature profile used in the standard preparation (**TaS₂650_Std**) is shown Figure 3.1. As explained in Section 2.2.4.6, Step ii in the heating profile, at 115 °C is important as it allows the sulfur to liquefy and to an extent vaporise under the evacuated conditions, preventing sudden changes in internal pressure. Once heated to 650 °C for a period of 60 hours (Step iv) the ampoules were removed from the furnace and allowed to cool to room temperature, (Step v). The results generally showed < 20 mg of low density fibrous material attached to the sides of the ampoules, extending down the length of the ampoule with a residual powder at the bottom. The resultant nano-products were mechanically separated from the residual powders using tweezers once the silica tubes had been opened (Section 2.2.4.7) and were characterised (Section 2.4) with results are discussed in Section 3.3.1.

The synthesis was tuned to find the best synthetic conditions for the formation of nanowires. It was found that the best yields occurred with vacuums $> 1 \times 10^{-2}$ Torr and ~ 1 -2 g of starting material in a 12 mm diameter silica tube with ampoules ~ 120 -150 mm in length. This corresponds to 0.9 g (0.005 moles) Ta and 0.32 g (0.01 moles) S according to Equation (3.2). Three Regions have been defined within the ampoules as shown in Figure 2.4 which will be used for discussion purposes.

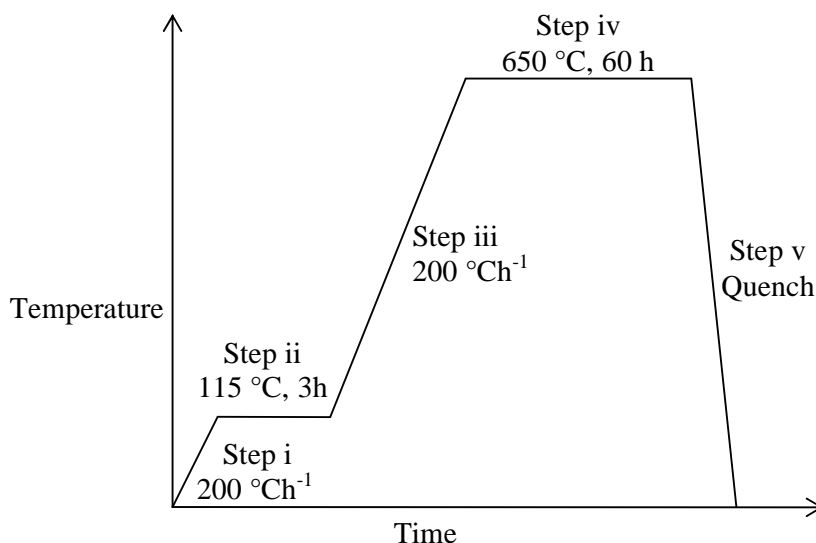


Figure 3.1: Temperature profile used for the preparation of the TaS₂ nanofibres in **TaS₂650_Std.**

3.2.1.2 Surface Assisted Growth Preparations

In other reactions specially designed silica ampoules with a width restriction or neck half way along the length have been made as described in Section 2.3.1.2 and shown in Figure 2.6. Stoichiometric mixtures of elemental powders, 0.9 g (0.005 moles) Ta and 0.32 g (0.01 moles) S, as seen in Equation (3.2), were loaded into the lower section and a piece of tantalum foil; 30mm x 10mm x 0.25mm (99.9%, Aldrich) placed in the upper section. These tubes were heated over the same temperature profile (Figure 3.1) as used for the **TaS₂650_Std**, (Section 3.2.1.1). The results generally showed < 40 mg of low density fibrous material attached to the sides of the ampoules, extending down the length of the ampoule and growing on the foil, with a residual powder at the bottom. The products were again separated by mechanical methods and characterised, with the results discussed in Section 3.3.2.

TaS₂650_SAG was run against 2 different controls. In the controls, similar tube configurations and conditions were used but the upper region of the ampoules contained either iron foil; 30mm x 10mm x 0.25mm (99.9%, Aldrich Chemicals), (**TaS₂650_SAG_Fe**) or

remained empty (**TaS₂650_SAG_Empty**). Iron is known to have catalytic effects on the formation of various nanowires so was an obvious choice for comparison.¹⁸⁹⁻¹⁹¹

3.2.1.3 Effects of Temperature Regime on Nanowire Formation

Different temperature profiles were utilised to see how they affect the formation of the nano-structures. Experimental parameters were kept constant with only the upper temperature limit (Step iv in Figure 3.1) changing. Preparations were carried out with both standard synthesis and surface assisted growth configurations.

High temperature preparations (**TaS₂1100**) were attempted with an upper temperature of 1100 °C. The choice of this temperature was governed by the upper temperature limit of the silica ampoules (Section 2.2.4.6) that have been used throughout this project. Higher temperature capability would require significant changes to the experimental setup leading to incomparable results. Lower temperature preparations were also carried out; the experimental conditions are given in Table 3.1.

Preparation Reference	Annealing Temperature °C
TaS₂1100_Std	1100
TaS₂1100_SAG	1100
TaS₂900_Std	900
TaS₂900_SAG	900
TaS₂750_Std	750
TaS₂750_SAG	750
TaS₂600_SAG	600
TaS₂500_SAG	500
TaS₂400_SAG	400

Table 3.1: Experimental conditions for the changing temperature regime preparations.

3.2.1.4 Bulk Phase Syntheses

The ability to reproducibly form individual polytypes of TaS₂ in single phase samples has for many years been unclear in the literature. There are a number of different syntheses that allegedly provide single phase products for different uses however no one paper really

reviews this aspect of research. Individual syntheses for the 1T, 2H and 3R polytypes were investigated and are outlined below with the results discussed in Section 3.3.4.

3.2.1.4.1 1T Polytype

Mixtures of poly-phase TaS₂ were sealed under vacuum ($\sim 4 \times 10^{-5}$ Torr) in silica tubes, to form ampoules (Section 2.2.4.5). Once sealed, the silica ampoules were held upright with all the powder at one end before being placed horizontally in the centre of a box furnace (Section 2.2.4.8) on a ceramic brick and heated at $200\text{ }^{\circ}\text{Cmin}^{-1}$ to $1100\text{ }^{\circ}\text{C}$ for a period of ~ 3 hours. The ampoules were removed from the furnace and quenched in bucket of water, (50%), ice, (50 %) (Section 2.2.4.8). The results are discussed in Section 3.3.4.1.

3.2.1.4.2 2H Polytype

1T-TaS₂ was sealed in an evacuated (1×10^{-4} Torr) silica ampoule and heated at $400\text{ }^{\circ}\text{C}$ for 5 days. The resulting blue / black flowing powder was characterised and discussed in Section 3.3.4.2.

3.2.1.4.3 3R Polytype

The 3R polytype can be made by heating a 1:2 Ta:S mixture of elemental powders over the heating profile shown in Figure 3.1 and allowing to cool slowly from $650\text{ }^{\circ}\text{C}$, as is been shown in the Section 3.3.1.

3.2.2 Characterisation

PXD was carried out with typical analysis running as a step scan $5 - 80\text{ }^{\circ} 2\theta$, with a step size of 0.02 ° utilising a step rate that gave ~ 3 h scans in flat plate mode. Different diffractometers have been used for the analysis as explained in Section 2.4.1.3. PXD slides were prepared for powders by smoothing the powder products over the indentation in the PXD slide to provide a flat uniform surface. Different methods of loading the PXD slide with nanofibres were attempted, as outlined in Section 2.4.1.2. The best results came from either adhering the

nanofibres to the glass slide using a carbon tab, (Section 2.4.1.2.3.3) or dispersing the nanofibres in ethanol and dropping them into a hot glass slide (Section 2.4.1.2.3.4).

SEM was performed at 20 KV, in high vacuum mode, with a typical working distance of 10 mm and spot size 3 or 4. Samples were loaded onto aluminium slugs using a double-sided adhesive carbon tabs which provided enough conduction to prevent the need for a coating procedure. EDX was used in conjunction with the SEM to ascertain approximate elemental ratios. Different SEMs have been used for the SEM analysis as explained in Section 2.4.2.3.

TEM and electron diffraction was carried out using two different microscopes (Section 2.4.3.7), with typical samples loaded by dispersion of nanofibres onto a carbon holey grid (300 mesh Ni) using propan-2-ol. To gain cross section analysis the nanowires were aligned vertically in a sandwich of silicon wafer and epoxy resin and ground down vertically till electron transparent. The full method for the encapsulation of nanofibres in silicon wafer sandwiches is given in Section 2.4.3.6.2.

TGA was achieved using a Netzsch STA. Powdered samples ~100 mg or nanofibrous samples ~10 mg were loaded into alumina crucibles and heated at a rate of $10\text{ }^{\circ}\text{C min}^{-1}$ over a temperature range of either RT-1000 $^{\circ}\text{C}$ or RT-1400 $^{\circ}\text{C}$ under a flow of air (60 mlmin^{-1}) and argon (20 mlmin^{-1}).

DSC was achieved using a Thermal Analysis DSC with scans run in the range of 20-500 $^{\circ}\text{C}$ with a heating rate of $10\text{ }^{\circ}\text{C per minute}$ on samples ~30 mg.

SQUID analysis was carried out using a Quantum Design MPMS-XL. Samples were loaded into gelatine capsules and inserted into SQUID sample holders before being loaded into SQUID. Scans were run from 2.8-300 K with field strength 10 Oe with both zero field cooling and field cooling data recorded. The raw data was then worked up as explained in Section 2.4.5.4 to give meaningful values.

3.3 Results and Discussion

3.3.1 Preparation TaS₂650 Std

Upon quenching in air, a low density fibrous material was observed in the ampoules, along with a residual powder in Region I. The fibrous material was observed on the powder and along the length of the silica coating the internal surface of the ampoules, Region II. This coating became free over time as the ampoules were moved and manipulated leaving a fibrous mass not dissimilar to fine cotton wool or spiders silk. The residual powder observed in the lower region of the ampoule below the fibrous material was black in colour and could be poured from the ampoules once the fibrous material was removed. Care was taken to maintain an upright positioning of the ampoule to prevent cross contamination of the nanofibres with the residual powder.

3.3.1.1 Residual Powders

3.3.1.1.1 Powder X-ray Diffraction

PXD data of the black residual powders from **TaS₂650_Std**, (Figure 3.2) shows peaks that correspond to the peaks expected from 3R-TaS₂ when cooled slowly. On quenching in air some 2H-TaS₂ contamination was observed. Peak broadening in X-ray diffraction data can be associated with particle size (Section 2.4.1.1.4). The use of the Scherrer equation (Section 2.4.1.1.4) on the data in Figure 3.2, yields values of ~1.8 µm for the particle size.

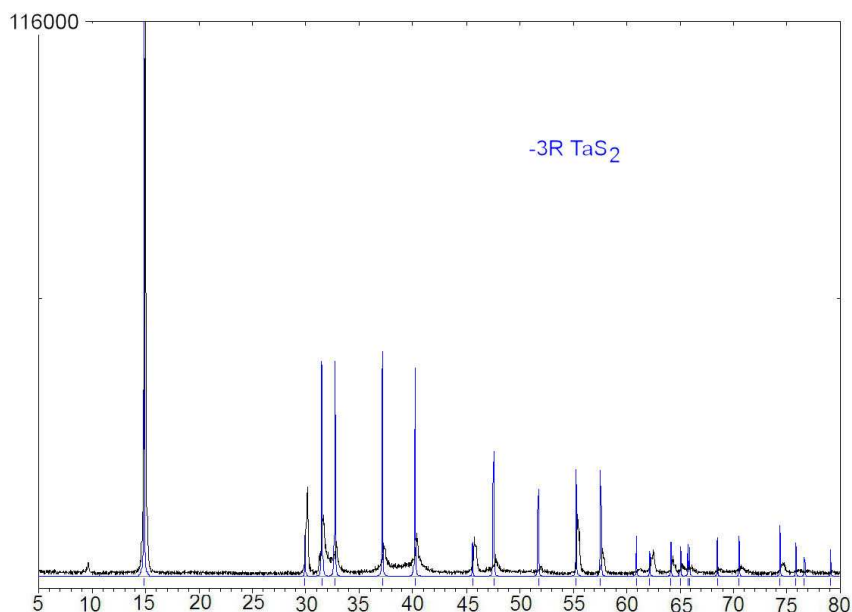


Figure 3.2: PXD pattern showing the residual powder matching to the 3R-TaS₂ structure, (X-pert diffractometer).

The peaks in the PXD pattern from the slow cooling, shown in Figure 3.2 were indexed and refined to a hexagonal unit cell of cell parameters as shown in Table 3.2. The published values for the unit cell positions of 3R-TaS₂ are also shown indicating that the phase is a good match, though there is a small contraction of the c parameter with respect to the published values. Errors were not given in Jellinek paper¹¹² so the accuracy of the unit cell parameters is hard to ascertain.

Phase	a	c
TaS₂650_Std	3.312(1) Å	17.8248(4) Å
3R-TaS ₂	3.320 Å	17.90 Å

Table 3.2: Unit cell parameters from the indexed powder pattern from **TaS₂650_Std** compared to the published values for 3R-TaS₂.¹¹²

3.3.1.1.2 Scanning Electron Microscopy

The residual powder showed a uniform morphology of round particle platelets (Figure 3.2(a)). The platelets were seen to be $\sim 47 \mu\text{m}$ in diameter and $\sim 6 \mu\text{m}$ thicknesses (Averaged over 10 measurements using ImageJ¹⁸⁶). The particle thickness measurements are in contrast to the calculated values for the average particle size by the Scherrer equation, $6 \mu\text{m}$ vs. $1.8 \mu\text{m}$,

indicating that the Scherrer equation may be under estimating the values for particle size. The smaller particles will lower the average thickness calculated by the Scherrer equation, accounting for some of the difference but likely not all. The platelets have an elemental ratio of ~40:60 Ta:S, by EDX, (± 2). This was averaged across many samples and corresponds to a ~1:1.5 stoichiometry, suggesting that the platelets are slightly tantalum rich, i.e. $Ta_{1+x}S_2$. The error in this may be due to the intricacies of the EDX system as explained in Section 2.4.2.1.

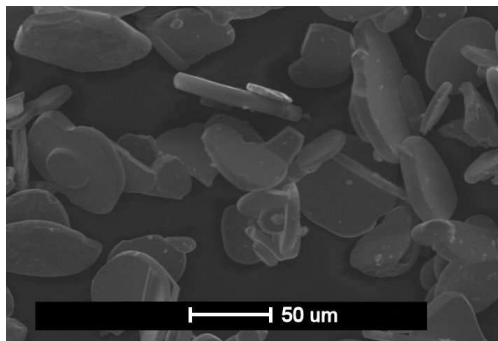
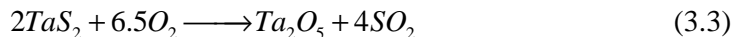


Figure 3.3: SEM micrograph of the general morphology seen in the residual powders from **TaS₂650_Std**, (SEM #1).

3.3.1.1.3 Thermo-Gravimetric Analysis

TGA was utilised to see how accurate the EDX results were for the readings on the particles and nanomorphologies. The results shown in Figure 3.4 show a mass drop of 9.84 % which is comparable with the 9.85 % that would be expected from the oxidation of TaS_2 to Ta_2O_5 , as shown by Equation (3.3).



The initial change in mass suggests that the reaction goes through a half-way intermediate that could, by the drop in mass, (3.36 %), involve the loss of one of the sulfur atoms and the gain of one and a half oxygen atoms per formula unit, for which the theoretical change in mass would be 3.29 %. The oxidation therefore occurs in two steps from Ta^{4+} to Ta^{5+} via a $Ta^{4.5+}$ intermediate, i.e. Equation (3.4). These results are indicating that as explained in Section

2.4.2.1, the accuracy of the EDX cannot be relied upon. It is however still useful as a guide as to the approximate stoichiometry of the product $\pm 2-3\%$.

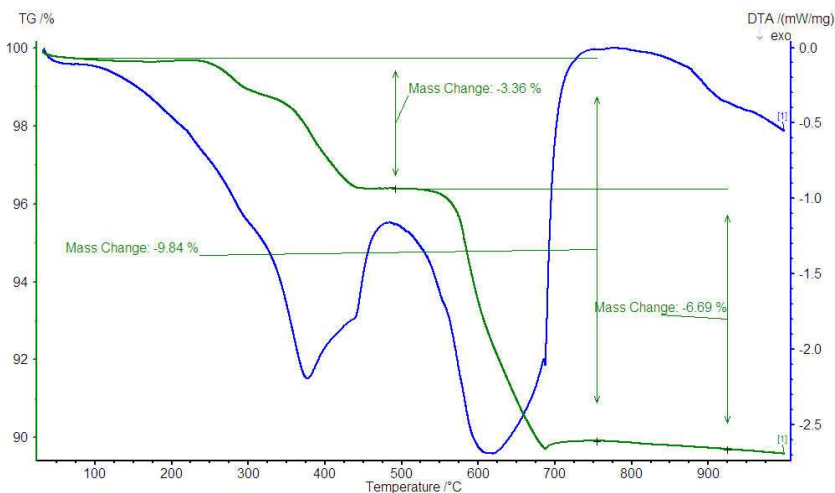
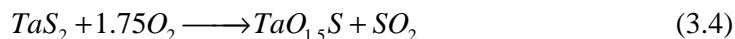


Figure 3.4: TGA data showing the reaction profile of TaS_2 powder from **TaS₂650_Std**.

3.3.1.2 Fibrous Morphology

3.3.1.2.1 Powder X-ray Diffraction

PXD analysis on the fibrous material (Figure 3.5) and shows peaks that match those expected for both 2H-TaS₂ and 3R-TaS₂ but an absence of 1T-TaS₂. Obtaining good PXD data for nanofibres is especially difficult as explained in Section 2.4.1.2. There is significant preferred orientation in the 001 direction in the powder pattern which is typical of the anisotropy of the disulfide structures and also some peak broadening indicating the small size of the structures under examination. The particle sizes calculated by the Scherrer equation from the dominant peak was ~ 39 nm, which is in agreement with the TEM analysis for the thickness of the fibres at the lower range of values. The peaks that correspond to 2H-TaS₂ were indexed and refined to give a hexagonal unit cell of cell parameters of $a = 3.32(1) \text{ \AA}$, $b = 12.165(1) \text{ \AA}$ which corresponds to 2H-TaS₂ as discussed further in Section 3.3.2.2.1.

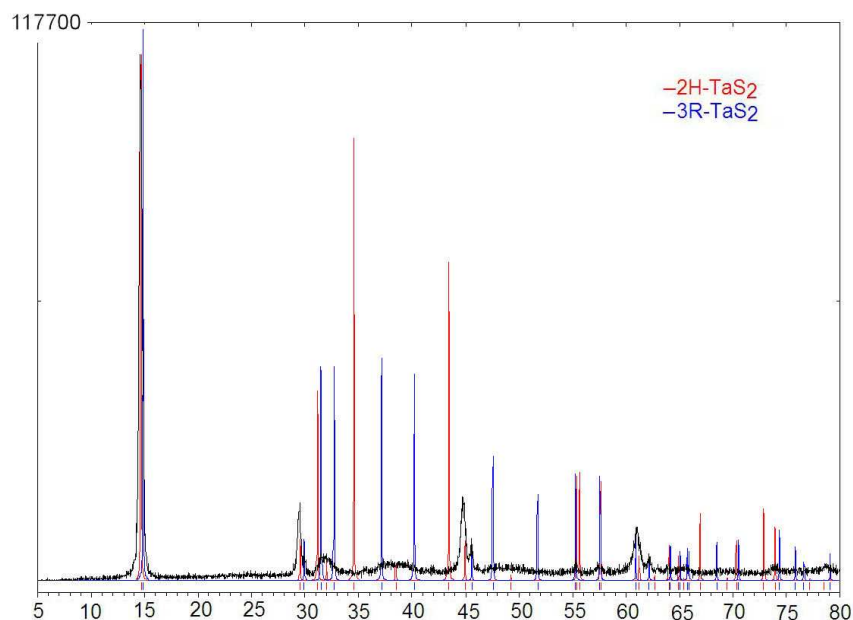


Figure 3.5: PXD pattern showing a match between the fibrous materials from **TaS₂650_Std** both 2H- TaS₂ and 3R-TaS₂, (D5000 diffractometer).

3.3.1.2.2 Scanning Electron Microscopy

The morphology of the wires is shown in Figure 3.6(a), and consists of long thin fibres and larger, thicker bundles of fibres. Figure 3.6(b) shows the widths of the wires to be in the range of 1.5 μm to 100 nm and lengths in excess of 1.2 mm leading to high aspect ratios of up to 12,000, (1.2 mm/100 nm). Figure 3.6(c) and (d) show fibres to be bundles of thinner fibrils. Figure 3.6(e) and (f) shows hexagonal structures observed in and around the nanofibrous formations. The hexagonal structures were rarely perfect hexagons and often distorted with one length (edge to edge) longer than the other two, (Figure 3.6(e)) and a thickness that is $\sim 6 \mu\text{m}$ as with the particles in the residual powder, Figure 3.2(a).

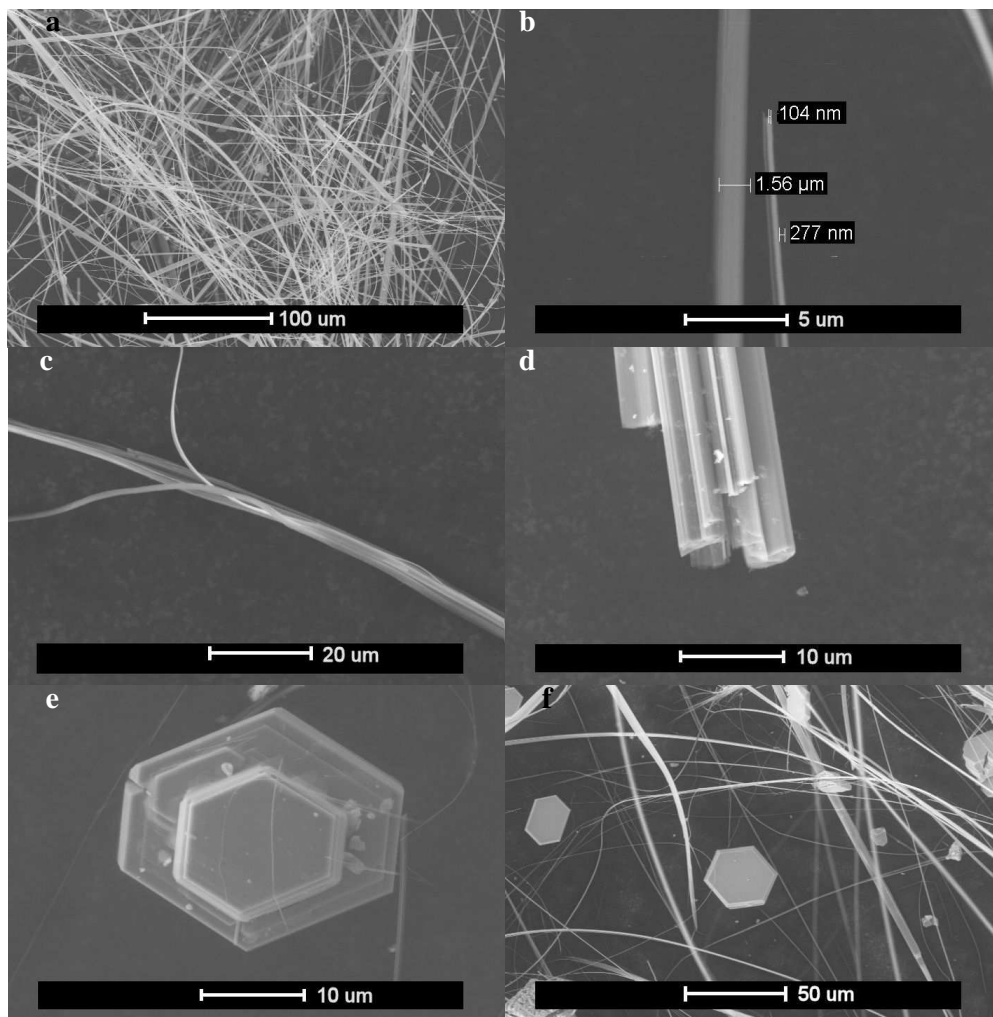


Figure 3.6: SEM micrographs of the fibrous material from **TaS₂650_Std** showing: (a) general morphology, (SEM #1); (b) diameter measurements of typical nanofibres, (SEM #1); (c) a bundle of nanowires separating, (SEM #2) and (d) the multiple ends of a single bundle, (SEM #2); (e) hexagonal crystal surrounded by thin nanofibres, (SEM #2);(f) hexagonal crystals and fibres, (SEM #2).

The fibres in Figure 3.6(a) can be compared to the nanotubes observed by Rao and Nath in their initial publication of the discovery of TaS₂ nanofibres.⁴³ These nanofibres were described as nanotubes and were made by the reduction of TaS₃ by H₂. The image from this paper is copied and placed beside Figure 3.6(a) in Figure 3.7 with some added measurements marked using ImageJ.¹⁸⁶ When taking these measurements, care was taken to maximise the pixel numbers thus reducing the errors by zooming in on the image the errors are likely ± 0.05

μm . The general morphologies are seen to be very similar with the size of the larger structures in both images $\sim 2 - 8 \mu\text{m}$ in diameter. The structures from **TaS₂650_Std** show the higher diameter range by about $4 \mu\text{m}$ but the wires tend to be neater with cleaner structures and longer lengths. Both sets appear to be made up of bundles of smaller fibrils and appear to contain ribbon-like formations and belts as defined in Section 1.1.2.

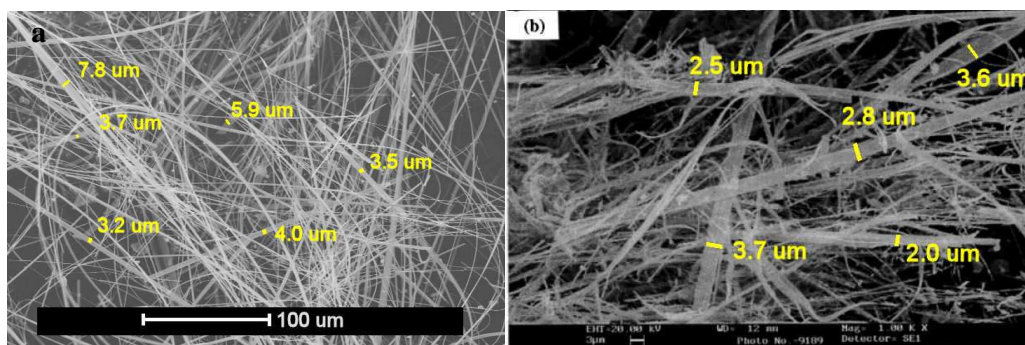


Figure 3.7: SEM micrograph of the general morphology from Figure 3.6(a) and the image of general morphology from the paper published by Rao and Nath.⁴³ Showing the approximate measurements of the larger structures taken using ImageJ.¹⁸⁶

3.3.1.2.3 Transmission Electron Microscopy

The collection of the TEM data for the TaS₂ nanowires at The University of Nottingham was performed by Miss H. Edwards and Prof. P. D. Brown from the department of Materials, Mining and Mechanical Engineering.

Characterisation by TEM showed the presence of a bundled morphology where one wire was composed of several smaller fibrils, in agreement with the SEM. Individual fibrils consist of straight, clean edged, uniform diameter nanowires with a broad distribution of diameters from 20-550 nm and an average diameter of 450 nm, (23 Measurements), while the diameters of the bundles ranged from 50 nm to $2.5 \mu\text{m}$ and had an average diameter of $\sim 700 \text{ nm}$ (19 measurements). Lengths up to 1.2 mm for the bundles and 1 mm for the individual nanowires lead to aspect ratios up to 20000 for the bundles and 50000 for the individual wires; (1.2 mm/60 nm) and (1 mm/20 nm) respectively.

The wires were very straight with constant diameters along their length, until fragmentation occurs at the tips, (Figure 3.8(a) and (b)). Although some thinner wires, (Figure 3.8(c)) appeared to be flexible and ribbon-like, the higher diameter wires were very brittle, leading to fracture of the bundles into smaller segments during sonication which may be due to the clustered filamentary structure of the nanowires.

Despite often consisting of several crystallites, the nanofibres displayed single crystalline SAED patterns, as illustrated in the inset of Figure 3.8(b). The filamentary morphology of the nanowires suggests a cooperative growth mechanism, whereby a number of nanowires are nucleated and simultaneously propagate according to one crystallographic direction, sharing a single orientation of the TaS₂ crystal structure. As variation in the crystal structures of the 1T, 2H and 3R polytypes of TaS₂ are in the *(00l)* stacking of the planes of TaS₂, leading to differences in the *c*- lattice parameter, the [0001] projection SAEDs of the three polytypes are highly similar and hence the diffraction pattern in Figure 3.8(d) can be indexed to give a close match to any of the three structures. However careful analysis of this and further nanowire SAED patterns at other projections yield a more precise match to 2H-TaS₂ than 1T-TaS₂. Other crystal structures examined included 3R-TaS₂ and a less common structure of TaS₂ recorded by Heagg and Schoenberg¹⁹² with a *c*- lattice parameter of 35.94 Å and space group $R\bar{3}m\ hr$. Neither of these crystal structures provided an acceptable match to the measured SAED data.

The nanowire and diffraction pattern relationship is further illustrated by the bright field TEM image and corresponding SAED pattern of Figure 3.8(b). Figure 3.8(c) shows a thin, flexible nanowire and a larger nanowire composed of at least five TaS₂ crystallites, leading to the varied contrast across the wire. The nanowire appears to have fractured during sample preparation, hence taking on an uneven terminal edge. The corresponding SAED pattern of Figure 3.8(d) is characteristic of those produced by the nanowires. The pattern

consists of single crystalline spots in an equally spaced hexagonal arrangement and has been indexed to the [0001] projection of TaS₂.

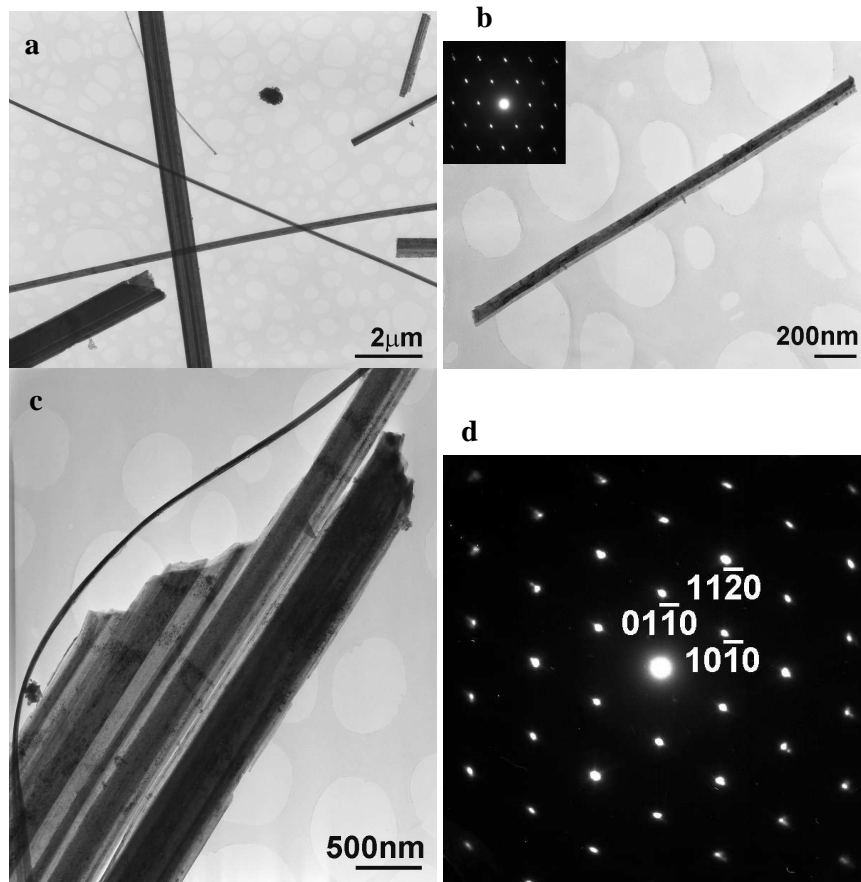


Figure 3.8. TEM micrographs showing the basic morphology of the TaS₂ nanowires: (a) low magnification bright field TEM image of several TaS₂ nanowires; (b) bright field TEM image and corresponding inset SAED pattern of a single crystalline nanowire; (c) TEM image of a TaS₂ nanowire consisting of several individual filaments; (d) corresponding indexed SAED pattern of [0001] projection, (JEOL 2000FX microscope).

The principle spots of the SAED pattern in Figure 3.8(d) have been labelled to convey, along with the corresponding image, the orientation relationship between the nanowires and the TaS₂ crystal structure. (The SAED was acquired using the JEOL 2000FX there is no rotational constant between the SAED and the image, Section 2.4.3.2) Analysis of electron diffraction patterns obtained for the nanowires found that the $11\bar{2}0$ spots and hence $11\bar{2}0$ direction were in-line with the long axis of the nanowires, indicating the $11\bar{2}0$ direction to be the growth direction of the TaS₂ corresponding with the shortest distance between the origin

and the unit cell edge. The hexagonal unit cell can therefore be considered to be growing fastest and most preferentially along the shortest unit cell direction as has been noted in other systems.^{55, 72, 152, 160, 193} Four of the six equivalent $10\bar{1}0$ directions were found to be oriented at $\pm 30^\circ$ to the fibre axis, with the remaining two $10\bar{1}0$ directions at 90° to the fibre axis. The relationship between these planes and the corresponding d-spacings were consistent with a hexagonal system and in particular the structure of 2H-TaS₂. Therefore, the $10\bar{1}0$ planes of TaS₂ lie at $\pm 60^\circ$ and parallel to the nanowire axis, while $11\bar{2}0$ planes are perpendicular to it. On tilting the nanowires during TEM analysis, some were observed to display SAED patterns with streaking and splitting of the single crystal spots in a direction perpendicular to the long axis of the wire. Figure 3.9(a) is a bright field TEM image of one such nanowire, composed of multiple filaments and so yielding a streaked selected area electron diffraction pattern, as displayed in Figure 3.9(b). The streaking of spots is most likely due to 2-dimensional planar defects lying across the diameter of the nanowire; the splitting of spots suggests the presence of multiple phases. Diffraction spots aligned with the $11\bar{2}0$ growth direction exhibit little splitting, but those spots perpendicular to the $11\bar{2}0$ exhibit an increasing degree of separation distance from the centre of the SAED pattern, indicating that a second phase with a shorter lattice parameter than the main phase may be incorporated into the nanowire. Therefore, despite the majority of data being consistent with the crystal structure of 2H-TaS₂, it is conceivable that some of the wires are composed of a mixture of polytypes.

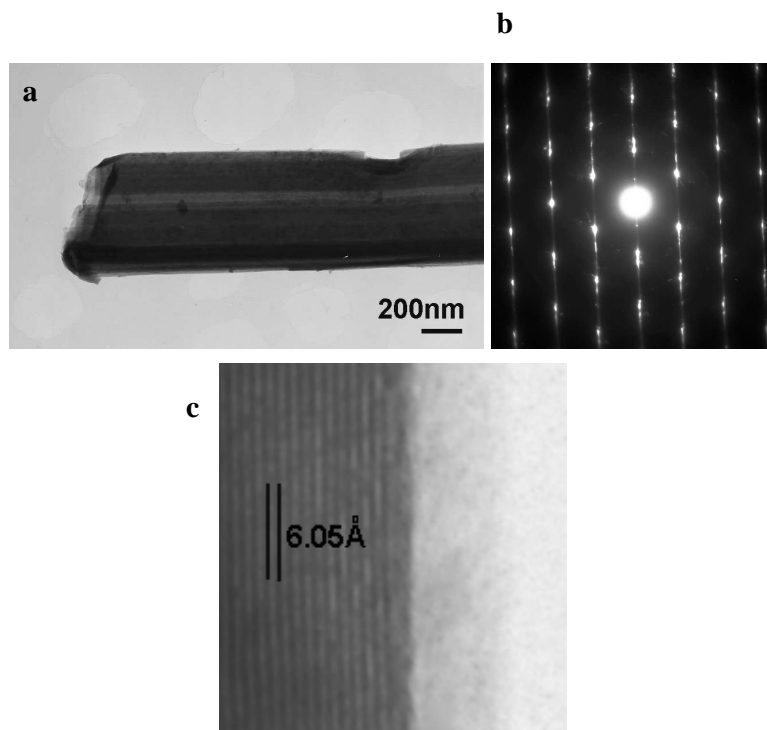


Figure 3.9: TEM micrographs showing: (a) a single TaS₂ nanowire composed of multiple filaments leading to a single crystal SAED pattern; (b) with splitting and streaking of spots perpendicular to the fibre long axis; (c) High resolution TEM image of 2H-TaS₂ (0001) planes, (JEOL 2000FX microscope).

The assignment of the major phase of these nanowires to 2H-TaS₂ is supported by the work of Nath and Rao,¹⁶⁰ which describes TaS₂ nanostructures produced through the reduction of TaS₃ under flowing H₂. The nanostructures, which had predominantly tubular morphology, were identified as being 2H-TaS₂ through the analysis of PXD data. Wu *et al.*⁵⁹ describe the synthesis of TaS₂ nanobelts by the conversion of TaS₃ under vacuum at 850 °C. These nanobelts have been assigned to the Haegg *et al.* $R\bar{3}m$ *hr* crystal structure¹⁹² of TaS₂ with *c* parameter of 35.94 Å.

By tilting the nanowires within the TEM away from the [0001] projection, atomic lattice fringes were observed parallel to the nanowire surface. Figure 3.9 is a bright field TEM image of the edge of a nanowire, displaying such lattice fringes. On measurement of the fringes, the atomic plane spacing was determined to be 6.05 ± 0.08 Å. This spacing coincides

with the (0002) plane spacing of 2H-TaS₂ at 6.0485 Å. The equivalent (0001) plane spacing of the 1T-TaS₂ polytype structure is similar to that of the 2H, but at 5.8971 Å, was found to exceed the error associated with the plane spacing measurement of 0.08 Å, further corroborating the premise that the nanowires measured were of the 2H polymorph. Along with the crystalline lattice planes an amorphous film could also be observed on the surface of the wires, most likely due to the post-synthesis oxidation of the TaS₂ nanowire surface to one of the tantalum oxides on exposure to the atmosphere. This film is also visible in Figure 3.9, as a layer of contrast, approximately 5nm thick, between the crystalline part of the wire and the amorphous carbon film of the TEM grid.

As mentioned earlier the larger fibres appear brittle in nature leading with a high tendency to split along the longitudinal weaknesses as shown in Figure 3.10. This is again indicative of cooperative growth mechanism of formation.



Figure 3.10: TEM micrographs showing lateral splitting and longitudinal peeling, (JEOL 2000FX microscope).

Interesting structures have also been observed in the course of the TEM analysis. Strange rhubarb-like structures appeared in one sample which could be attributed to the longitudinal splitting of large hollow tubes. (A hollow tube split along its long axis will produce two rhubarb-like curved structures) These are shown in Figure 3.11.

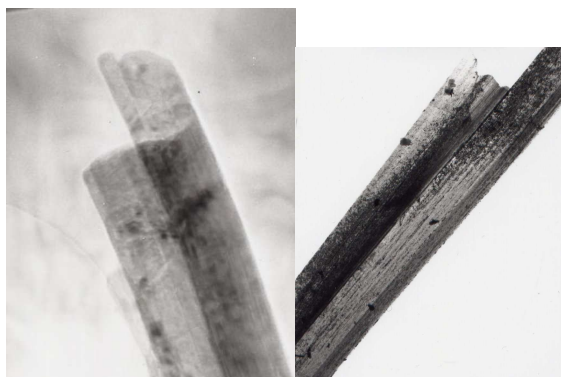


Figure 3.11: TEM micrographs showing “nanorhubarb”, (JEOL 2000FX microscope).

3.3.1.2.4 Magnetic Measurements

The results from SQUID analysis, (Figure 3.12) show a superconducting transition at ~ 4.25 K. This is in relation to the known 2H-TaS_2 T_C at 0.6 K^{123} or 0.8 K^{115} depending on the information source. This T_C would be masked by the phase that is superconducting at 4.5 K should the SQUID magnetometer used in the experiments be able to achieve temperatures below 1.8 K and observe the superconducting state at $< 0.8 \text{ K}$.

The shape of the zero field cooling trace also shows a minima change in gradient at $\sim 3.5 \text{ K}$ indicating the possibility of a second superconducting phase below the 4.5 K . The superconducting transition expected from bulk tantalum is around 4.75 K^{192} hinting at the possibility that microscopic quantities of tantalum around the wires, due to cross contamination are responsible for the underlying superconductivity observed at $\sim 4.25 \text{ K}$ and is masking the superconducting transition from the nanofibres. SEM and PXD fail to show the presence of the tantalum but the EDX did show a slight increase in the tantalum content of the wires. The PXD results are unsurprising as the peaks expected for tantalum correspond with those of 2H-TaS_2 so a microscopic quantity of tantalum contamination would therefore be unnoticeable by PXD. There are also many ways in which the tantalum can be hidden in the SEM micrographs. A thin film of tantalum metal can coat the nanowires and appear invisible as can particles of too small a size for the resolution of the SEM used for the analysis.

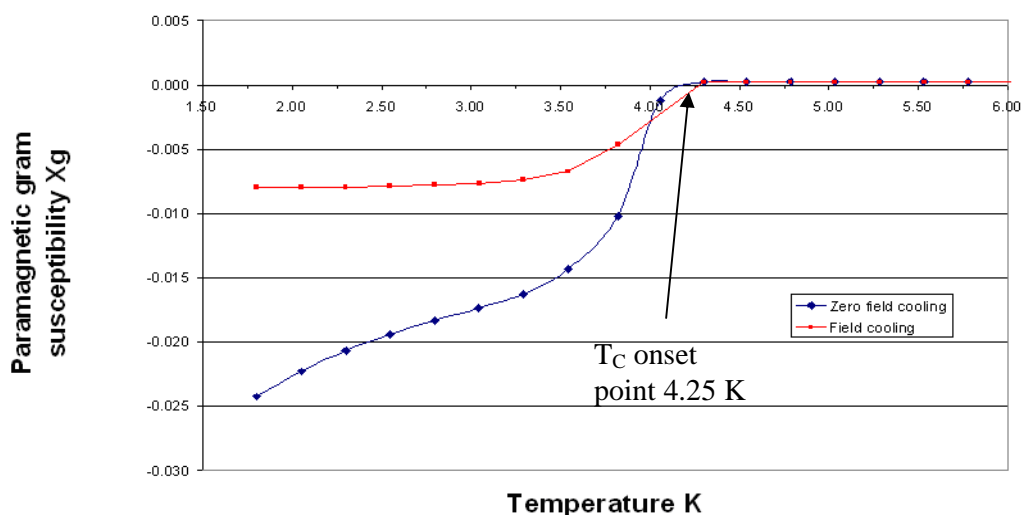


Figure 3.12: SQUID results for a sample of TaS₂ nanowires from **TaS₂650_Std**.

The Ta-S system has many constraints when characterising by the use of SQUID. The first and most important is that all results have to be held in direct comparison with those for tantalum metal, which exhibits superconducting properties just above the range expected for TaS₂. Tantalum metal is itself hard to characterise by SQUID as it has a variable T_c due to phase purity and gas adsorption, most notably oxygen.^{194, 195} The second constraint is that the formation of a microscopically pure sample of 2H-TaS₂ from elemental powdered reactants is difficult as the differences in energy of formation between the different polytypes is extremely small.¹¹⁸ Excess sulfur leads to inconsistent stoichiometry in the products and possible material contamination from the other phases. Many residual powder samples were observed to show a T_c at 4.75 K and hints of peaks in the PXD pattern at 38.5, 55.5 and 70 ° 2 θ . These correspond to the $Im\bar{3}m$ structure of tantalum that is used as a reactant in the reaction mixtures (Section 3.2.1.1). It is therefore likely that if tantalum is present in the residual powder, then it will also be present on or in the nanowires due to cross contamination and will as such show up in the SQUID results.

3.3.2 Preparation TaS₂650_SAG

In the series of experiments designed to investigate a possible surface assisted growth process we observed a similar yield of low density fibrous material to that seen in the standard synthesis, on the walls of the silica ampoule, creating an outer coating of low density fibrous material on the inside of the silica ampoule as shown in Figure 3.13(a). An extra substantial mass of fibres was also observed to form on and around the tantalum foil, shown in Figure 3.13(b) and (c). Thus the yield appears to increase in the presence of the tantalum surface, (< 40 mg). The extra fibrous material (~ 20 mg) consists of long needle like structures growing approximately perpendicular to the surfaces of the foil, Figure 3.13(b) and (c). Figure 3.13(d) shows how the nanowire formations in the inside of the ampoule appear to nucleate around and grow from a possible imperfection within the wall of the silica. This observation is in agreement with the observations from the standard synthesis without the presence of Ta foil.

In the control reactions, described in Section 3.2.1.2, contrasting results are observed. Preparation **TaS₂650_SAG_Empty** showed no sign of nanostructure formation in Region III' and a decreased yield of nanowires on and around the residual powder (Region I') with respect to the standard synthesis. The neck is therefore seen to impede the formation of the nanostructures, possibly due to the constriction of vapour flow within the silica ampoule. **TaS₂650_SAG_Fe** showed only limited formation of fibrous material in Region I' and no nanowire formation in the Region III', on the iron surface. There was however evidence of surface reaction on the iron foil which was coated in a brittle silvery layer that was easily removed. This shiny layer on the iron foil was analysed using PXD, SEM and EDX. The results show that this material is iron sulfide (FeS). PXD showed a match to the $P\bar{6}2c$ structure (ICDD PDF: 00-051-0001). SEM showed smooth crystalline platelets of a few μm in diameter and EDX suggested a Fe:S elemental ratio of ~1:1, in agreement with the PXD results.

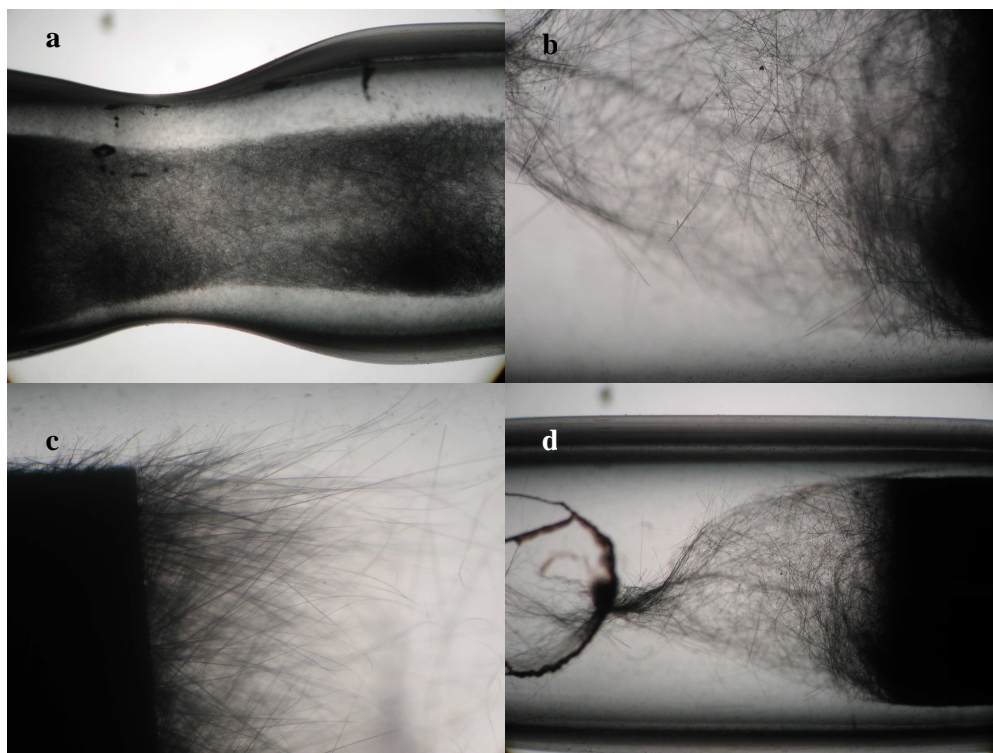


Figure 3.13: Optical microscope images of TaS₂ nanofibres: (a) internal coating of the walls of the adapted ampoules, (b) and (c) fibres growing off the tantalum foil surface and (d) a possible imperfection in the silica wall acting as a nucleating point for the growth of the fibres.

Collectively these results are suggesting that the sulfur is preferentially reacting with the more reactive iron rather than the less reactive tantalum powder that is present. The lack of nanowire formation on the iron surface leads to the conclusion that the iron does not play a catalytic role in this reaction under these conditions. It also indicates that the high yield of nanowires on the tantalum foil is occurring as a result of the tantalum's presence in Region III', rather than simply the presence of a surface. The preference to react with the iron at the other end of the ampoule rather than the tantalum around the sulfur is indicating that the reaction takes place from the gaseous sulfur reagent rather than a liquid phase.

3.3.2.1 Residual Powders

The residual powders were black in colour. PXD analysis showed them to be the 3R-TaS₂ (Figure 3.14) polytype with the 2H-TaS₂ contaminating some samples. The peaks were

indexed to a hexagonal unit cell with cell parameters given in Table 3.3. The unit cell parameters match those for 3R-TaS₂ with minimal contraction of the unit cell parameters.

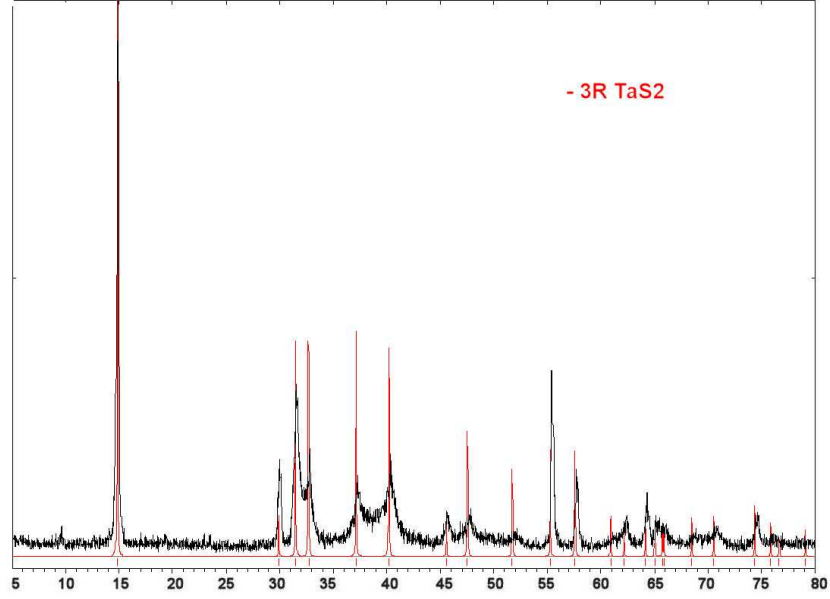


Figure 3.14: PXD analysis of the residual powders from **TaS₂650_SAG**. (D5000 diffractometer).

Phase	<i>a</i>	<i>c</i>
TaS₂650_Std	3.310(1) Å	17.8228(5) Å
3R-TaS ₂	3.320 Å	17.900 Å

Table 3.3: Unit cell parameters from the indexed powder patterns from **TaS₂650_Std** compared to the published values for 3R-TaS₂.¹¹²

SEM analysis was achieved showing the general morphology to be similar to that of **TaS₂650_Std**. Flat plat-like particles are observed with typical diameters ~ 50 μm, and ~ 5 μm thick. These plate-like structures are typical of the layered dichalcogenide materials. And similar to those observed in **TaS₂650_Std**.

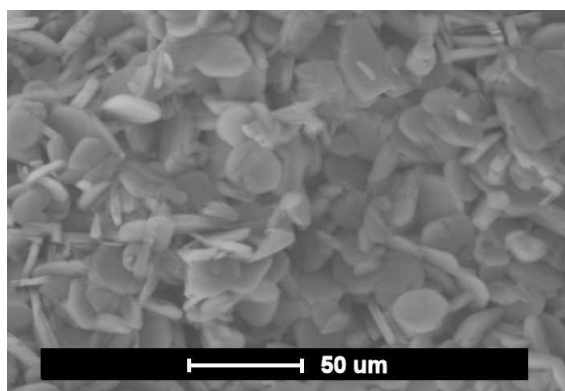


Figure 3.15: SEM micrograph showing the general morphology of the residual powder from **TaS₂650_SAG**, (SEM#1).

3.3.2.2 Fibrous Morphology

3.3.2.2.1 Powder X-ray Diffraction

PXD was carried out on the nanowires from **TaS₂650_SAG**. The pattern showed very similar peaks to those observed in **TaS₂650_Std** as shown in Figure 3.16. The Scherrer equation again gives particle size measurements of ~35 nm, similar to the 39 nm observed in **TaS₂650_Std**. This corresponds well with the thickness of the fibres from the TEM micrographs.

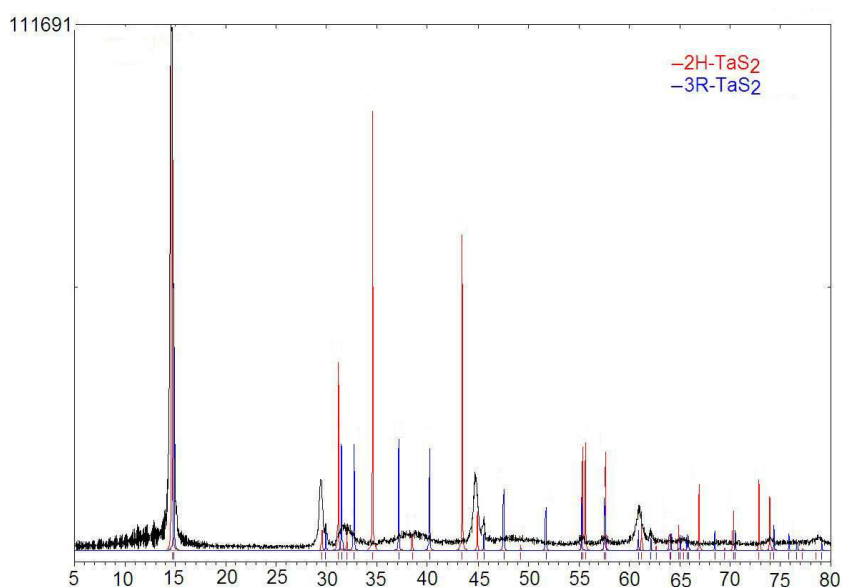


Figure 3.16: PXD for the nanofibres from **TaS₂650_SAG**, (D5000 diffractometer).

The peaks that correspond to 2H-TaS₂, shown in red in Figure 3.5 and Figure 3.16, were indexed and refined using CELFEF¹⁸¹ to a hexagonal unit cell with parameters shown in Table 3.4. The results from the standard configuration preparation have also been shown for reference. It appears that there is a degree of expansion of the *c*-parameter (~0.5 %) as is common with the formation of inorganic nanofibres from MX₂ compounds, e.g. Rao and Nath have seen a ~3% increase in the *c* parameter in the formation of WS₂ nanotubes.⁵⁰

Phase	a	c
TaS₂650_Std	3.32(1) Å	12.165(1) Å
TaS₂650_SAG	3.32(2) Å	12.159(2) Å
2H-TaS ₂	3.314 Å	12.097 Å

Table 3.4: Unit cell parameters from the indexed powder patterns from **TaS₂650_Std** and **TaS₂650_SAG** compared to the published values for 2H-TaS₂.¹¹²

3.3.2.2.2 Scanning Electron Microscopy

SEM performed on the nanowires from **TaS₂650_SAG** showed bundles of nanofibres (Figure 3.17(a)), similar to those seen from **TaS₂650_Std**, though with aspect ratios up to nearly twice those seen in the standard preparation, with lengths now in excess of 2.5 mm. Diameter measurements shown in Figure 3.17(b) showed the fibres to be in the approximate range of 100 – 600 nm with the larger microfibrils again seen to be wrapped bundles of smaller fibrils.

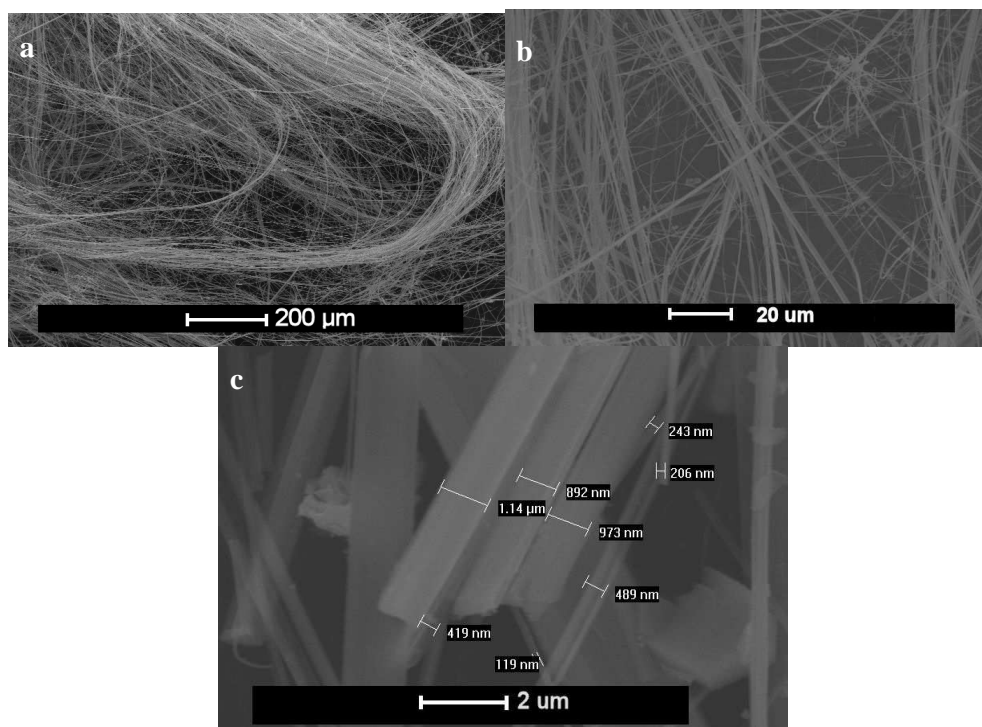


Figure 3.17: SEM micrographs from **TaS₂650_SAG** showing: (a) general morphology of the fibrous material at low magnification; (b) higher magnification image of typical nanowires and (c) measurements demonstrating the diameters of the nanowires to be in the 100 – 600 nm range, (SEM #1).

No hexagonal crystals (Figure 3.6(f)) were observed in products from Region III' of the surface assisted preparations indicating that the foil somehow inhibits the formation of the hexagonal crystals, possibly preferentially forming the nanofibres. Detailed searches for the hexagonal crystals in the products from Region I' however were not carried out.

Detailed SEM images of the fibres growing off the surface of the tantalum foil were taken as shown in Figure 3.18. The nanofibres are clearly seen growing out of a coating on the Ta foil. Both the foil coating and the fibres were shown by EDX to have a ~1:2 ratio Ta:S indicating TaS₂. This is in contrast to the findings in Section 4.3.2.3.1 where the products of **TaS₃500_SAG** show a clear stoichiometry of 1:3 in the fibres and 1:2 in the surface coating the Ta foil. Also in contrast is the brittleness of the surface coating which in **TaS₃500_SAG** was seen to peel off the surface revealing the Ta metal underneath. In these micrographs the surface appears more stable than observed in the **TaS₃500_SAG**.

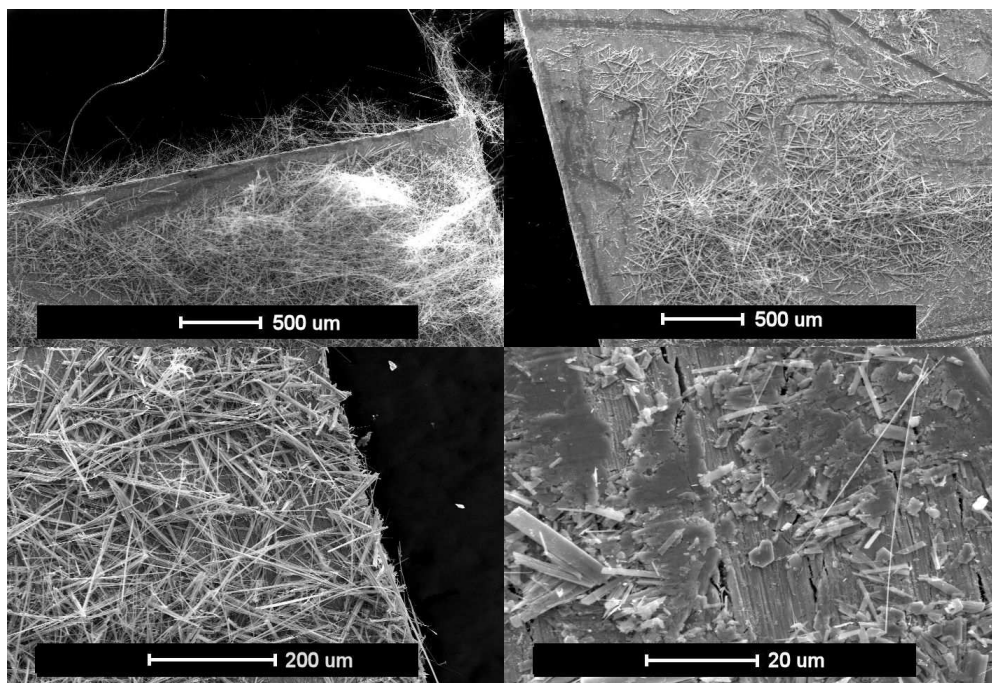


Figure 3.18: SEM micrographs showing the fibres growing off the foil from **TaS₂650_SAG**, (SEM #1).

3.3.2.2.3 Transmission Electron Microscopy

Much of the TEM work at the University of Glasgow has been achieved by or with help from Dr. I. MacLaren in the Physics department.

The TaS₂ nanofibres from **TaS₂650_SAG** grow along one of the $\frac{1}{3}\langle 2\bar{1}\bar{1}0 \rangle$ directions of the crystal structure just like those analysed from **TaS₂650_Std**. This is shown in the SAED patterns in Figure 3.19(b) which have been corrected for the rotation of the microscope and are comparable to the wire shown in Figure 3.19(a). The fibres were often found to lie with basal plane parallel to the holey carbon film and thus [0001] diffraction patterns were easy to obtain. Unfortunately, the [0001] diffraction pattern is identical for the 1T, 2H and 3R structures, so an alternative orientation is needed to make an unambiguous structure determination possible. The ideal solution would be to have the crystal oriented along a direction in the basal plane, since then the periodicity in the *c* direction could be directly determined from the diffraction patterns, but this orientation could never be achieved in the samples mounted on carbon films, except possibly in some cases where the wire was

too thick to remain electron transparent, hence work aimed at encapsulating the fibres vertically in a TEM sample holder, (Section 2.4.3.6.2) An alternative was to tilt the wire shown in Figure 3.19(a) in a controlled manner about its axis. After 10° tilt, a pronounced spot splitting is observed in the direction perpendicular to the wire axis (arrowed in Figure 3.19(d); careful measurements, and comparisons with the simulated diffraction pattern of Figure 3.19(e) confirm the split spots to have the indices $02\bar{2}1$ and $02\bar{2}2$ in one direction and $0\bar{2}2\bar{1}$ and $0\bar{2}2\bar{2}$ in the other (as indexed to the 2H structure). The $02\bar{2}1$ and $0\bar{2}2\bar{1}$ spots can only exist with the 2H structure as they would index as $02\bar{2}\frac{1}{2}$ / $0\bar{2}2\frac{1}{2}$ for 1T and as $02\bar{2}\frac{3}{2}$ / $0\bar{2}2\frac{3}{2}$ for 3R. Similarly, after 20° tilt, a more pronounced spot splitting is observed between $01\bar{1}1$ and $01\bar{1}2$, as can be seen in Figure 3.19(f) and the simulated diffraction pattern of Figure 3.19(g). As above, the $01\bar{1}1$ spot is only explicable for the 2H structure as it will give fractional indices for the other structures in the *c* direction. Thus, electron diffraction in the transmission electron microscope confirms that the wires are formed in the 2H structure. The formation of nanofibres out of MX₂ compounds appears to favour the 2H polytype with both TaS₂¹⁶⁰ nanotubes and examples of analogous systems observed to favour the 2H polytype, e.g. NbSe₂⁵⁵ and MoS₂.¹⁵¹

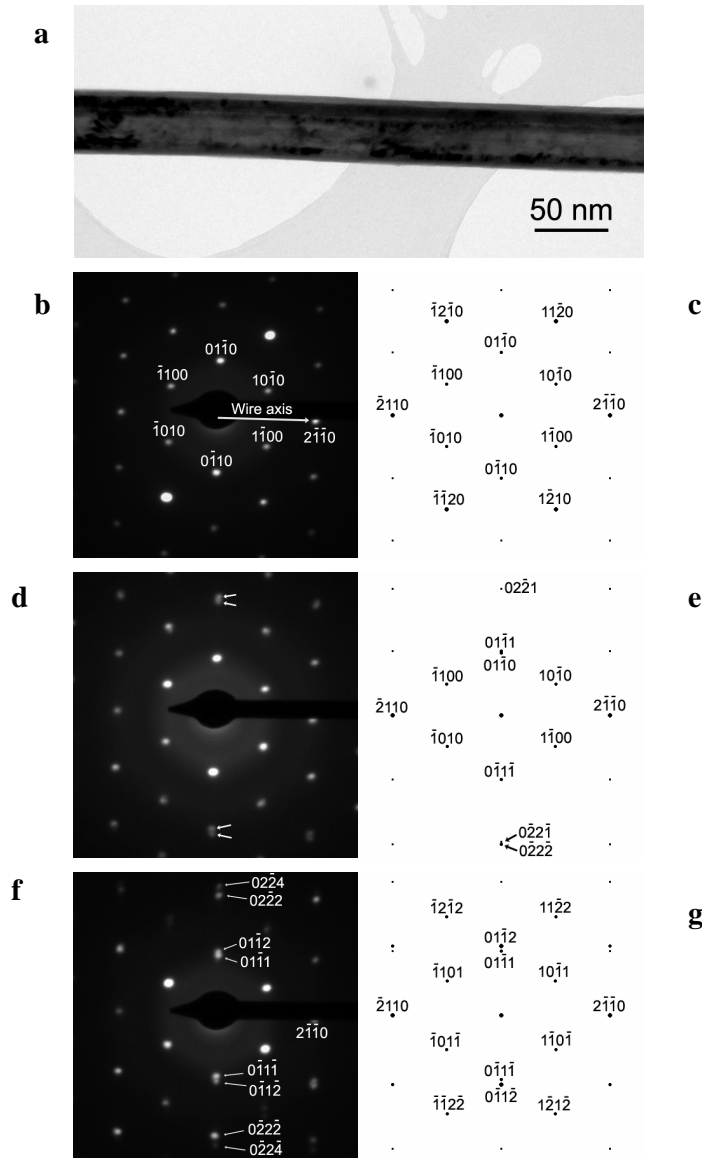


Figure 3.19: TEM micrograph and diffraction patterns of a TaS₂ nanowire: (a) Bright field image; (b) SAED pattern at 0° tilt; (c) simulated [0001] diffraction pattern; (d) SAED pattern after 10° tilt about the wire axis; (e) simulated 10° tilt pattern; (f) SAED pattern after 20° tilt about the wire axis and (g) simulated 20° tilt pattern, (T20 microscope).

Although the TEM has conclusively shown that the nanofibres are of the 2H structure without the need for encapsulating samples, the encapsulated samples did prove interesting. Figure 3.20(a) shows a cross section of a nanofibre. The rectangular shape is clearly observed and noted that the general width is about 3 times that of the breadth. According to the definitions given in Section 1.1.3, this concludes a nanobelt like morphology. However, Figure 3.20(b) shows a square section nanofibre with an inset diffraction pattern. It was necessary to tilt this

to 16° in order to achieve a zone axis indicating that the nanowire was not vertical with respect to the optical axis of the microscope. It is possible therefore that the image in Figure 3.20(a) could be a lot thinner than it appears as it may be inclined with respect to the optical axis of the microscope leading to a more nanoribbon-like morphology.

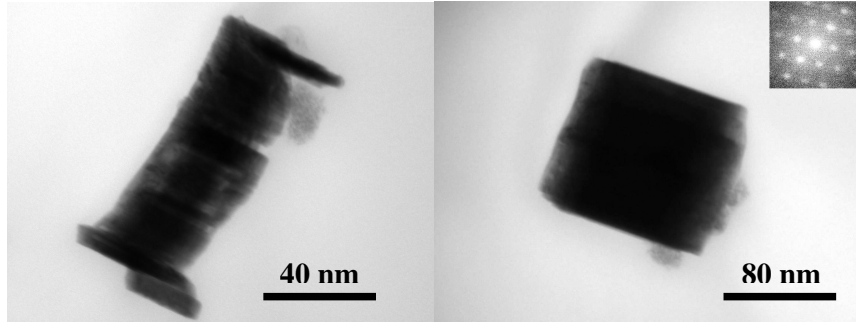


Figure 3.20: (a) TEM micrograph showing the cross sectional area of a nanobelt; (b) square section and inset SAED pattern taken at 16° alpha tilt, (T20 electron microscope).

3.3.2.2.4 Magnetic Measurements

SQUID results show superconductivity at low temperature. A superconducting transition is observed at 3.4 K, shown in Figure 3.21. This is in contrast to the superconducting transition observed previously of 4.5 K. It is believed that the 4.5 K reading originated from particles of tantalum metal present in and around the nanowires giving a T_C at a value associated with that of Ta metal. This leaves the possible second superconducting phase seen in the SQUID results of **TaS₂650_Std** at around 3.5 K (Section 3.3.1.2.4), to be due to the same superconducting phase as observed here in **TaS₂650_SAG**, i.e. the TaS₂ nanofibres.

It is known that in bulk 2H-TaS₂ a T_C of 0.6 K¹²³ or 0.8 K¹¹⁵ depending on the information source. Friend *et al.* have shown how this can be raised to between 2-5.5 K as a result of intercalating various species with in the layers causing suppression of structural instability.¹²¹ Wu *et al.* have shown that for TaS₂ nanobelts a T_C of 2.7 K⁵⁹ can be recorded which falls within the range of cited temperatures for the intercalation of TaS₂ by Friend *et al.*. Indeed Wu *et al.* suggested that structural instability was the cause of their high T_C .⁵⁹ This suppression of structural stability is actually a suppression of the CDW state that arises as the

electronic state changes with the lattice, whose parameters are constrained by the intercalating species. Likewise Tian *et al.* have shown how nanowires of bismuth can exhibit a T_C of 7.2 and 8.3 K, corresponding well with the bulk material in a high pressure phase rather than sub 50 mK in the standard phase.¹⁹⁶

The high T_C observed in the TaS₂ nanofibres could also be a result of a bundling effect. It has been shown by Pokropivnyi that when nanowires are ordered in bundles a “Conductivity strengthening effect” occurs.¹⁹⁷ E.g. semi-conducting BN nanotubes become metallic^{198, 199} and metallic single walled carbon nanotubes become superconducting,¹⁹⁹ suggesting that an increase in T_C might occur when TaS₂ nanofibres form bundles, and could help to explain the increase in T_C from the nanobelts to the bundles of nanofibres. From the limited data available there seems to be a trend towards an increase in T_C as a result of constraining crystal structure either by morphology, pressure or intercalation. SQUID measurements on single nanowires of 2H-NbSe₂ have however shown no increase in superconducting T_C between the bulk and the nanowire phase morphology though a 6 fold increase in the critical field required to change the resistance by CDW effects along the c parameter of the unit cell.¹⁶⁴ This could be indicating the preference for NbSe₂ to form low temperature CDW states rather than superconducting states as is the case for the triselenide.²⁰⁰

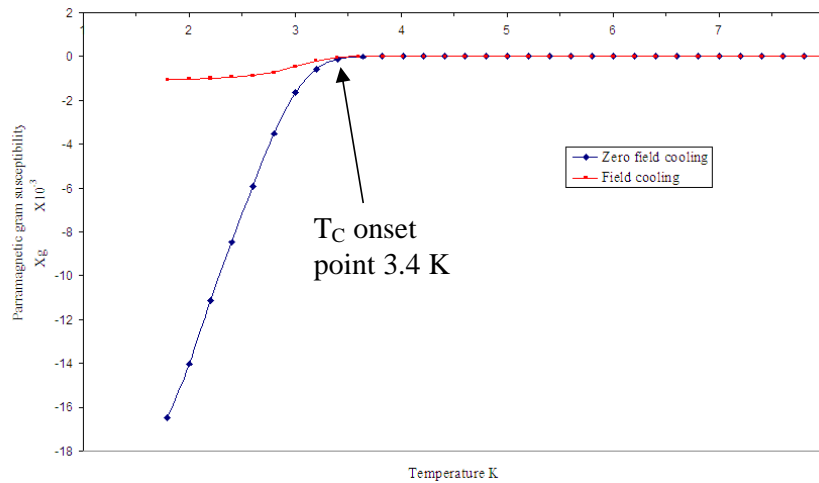


Figure 3.21: SQUID magnetometry data showing a single superconducting T_C at 3.4 K for the bundles of superconducting TaS₂ nanofibres observed in **TaS₂650_SAG**. Measurements taken on the SQUID at Nottingham.

Given the contrast between the numbers of superconducting phases within the samples, more than one for **TaS₂650_Std**, only one for **TaS₂650_SAG**, it is reasonable to conclude that residual tantalum is responsible for the higher T_C in the samples from **TaS₂650_Std**. The possible second superconducting phase in **TaS₂650_Std** is TaS₂ superconducting at around 3.4 K. It is this phase that is uniquely isolated in **TaS₂650_SAG**. The bundles of TaS₂ nanofibres therefore have a superconducting T_C at 3.4 K.

SEM and TEM have shown that the nanofibres break easily and shear along their longitudinal weaknesses (Figure 3.10(a)). The brittle nature of the nanofibres suggests that the separation from the foil is likely to involve nanofibres breaking close to their ends rather than retaining bits of tantalum metal or lumps of tantalum disulfide from the surface as they are separated. The tantalum metal surface also appears to be protected by the layer of TaS₂ that covers it in Figure 3.18. SEM and TEM confirm this assumption as no evidence of tantalum particles is seen on the ends of the nanofibres. Indeed in Figure 3.18 it is possible to notice the ends of the nanofibres still adhered to the surface coating of the foil rather than holes where the tantalum once was. This leads to the conclusion the control exerted on the system by the foil and the neck in the ampoule enabling the constant separation of the nanowires from the residual powder in **TaS₂650_SAG** allowed for the harvesting of an uncontaminated yield of nanofibres and should therefore give a more reliable result from SQUID, thus a single value for T_C .

3.3.3 Effects of Temperature on Nanowire Formation

3.3.3.1 TaS₂1100 Std & TaS₂1100 SAG

If the temperature of the upper dwell, (Step iv in Figure 3.1) is raised from 650 °C to 1100 °C for the final stage of the heating profile, then the yield of nanowires drops to zero. Quenching in air from this temperature leads to a crystalline powder with a golden tinge. Both

TaS₂1100_Std and **TaS₂1100_SAG** gave similar results, though in the case of **TaS₂1100_SAG** the metal foil was particularly corroded though no excess of tantalum was observed in the PXD patterns. The foil should have disrupted the overall stoichiometry of the system leading to either an excess of tantalum or a higher order tantalum sulfide species, e.g. TaS, Ta₂S, or Ta₃S₂.

PXD analysis of these golden tinged crystals showed a clear match to the 1T polytype, (Figure 3.22), indicating that the high temperature, 1T bulk phase is more stable than the nanowires at high temperature. The ease and reliability of 1T formation led to its use in the attempted formation of other bulk polytypes of TaS₂ (Section 3.3.4).

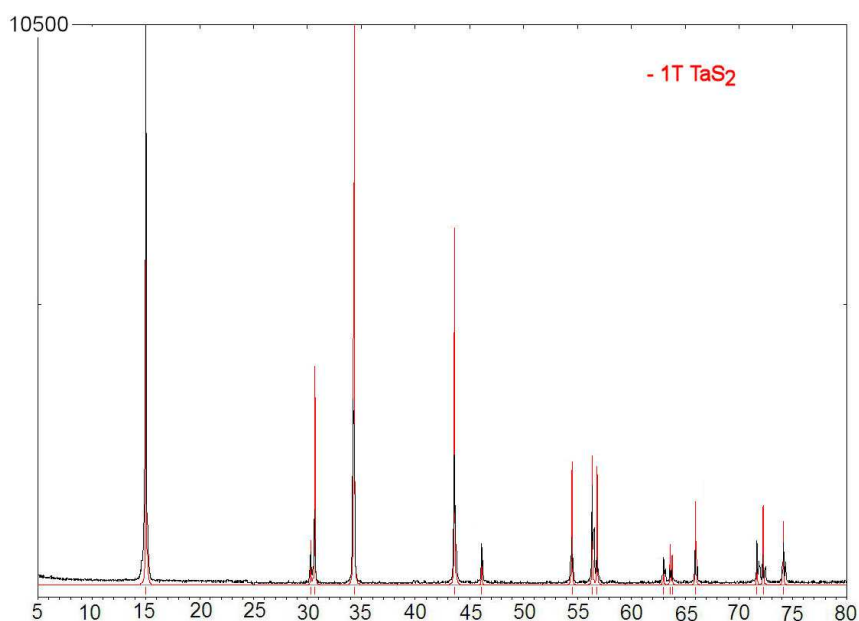


Figure 3.22: PXD pattern for the residual powder from **TaS₂1100_Std**, (D5000 diffractometer).

The 1T polytype formed in **TaS₂1100** show a round plate-like morphology as seen in Figure 3.23. These platelets are very like those seen in the general morphology that is shown in Figure 3.3(a) which was seen to be the 3R polytype by PXD. The morphology is almost identical, indicating that the morphology of the residual particles may not be intricately connected to the polytype in question, in the bulk powders. All the polytypes of TaS₂ are layered with varying layer stacking sequences and therefore likely to exhibit flat plate-like

morphologies. EDX showed a ~40:60 ratio, Ta:S, (± 2) from **TaS₂1100** indicating that the errors mentioned in Section 2.4.2.1 may be due to systematic errors in the SEM rather than non-stoichiometry in the products. The non-stoichiometric tantalum from the foil in **TaS₂1100_SAG** was strangely absent from the EDX findings.

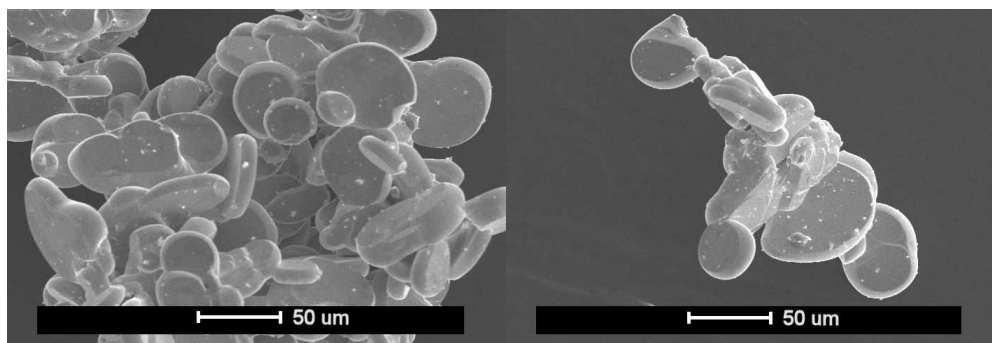


Figure 3.23: SEM micrographs from **TaS₂1100** showing the morphology of the 1T-TaS₂, (SEM #1).

3.3.3.2 Preparations TaS₂750 & TaS₂900

At 750 °C we see a reduction in yield of low density fibrous material with respect to **TaS₂650** and the residual powder has the beginnings of a gold tinge to its colour, indicating the beginnings of the formation of the 1T polytype. As the temperature of the synthesis increases further we see a continued lowering of the yield and an increase in the formation of the 1T polytype. **TaS₂900_Std** formed a minute amount of very low density fibrous material in Region I of the ampoule while **TaS₂900_SAG** just formed the black residual powder. The fibrous material was black in colour and has a very different morphology to that observed in the other preparations. This is shown in Figure 3.24. The morphology was far smaller in dimensions, (with widths that can no longer be fully resolved by the SEM) when compared to the wires observed in **TaS₂650_Std** and **TaS₂650_SAG**. These feather-like fibres seem to grow out of the centre of a clump indicating some form of nucleated growth mechanism. The quantities of material were too small for PXD analysis and TEM was never achieved so polytype analysis is unavailable.

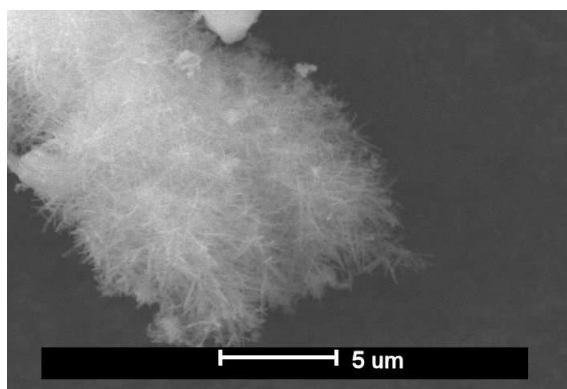


Figure 3.24: SEM micrograph of the fibrous material formed in **TaS₂900_Std.** (SEM #1).

3.3.3.3 Preparations TaS₂600 SAG, TaS₂500 SAG & TaS₂400 SAG

Nanofibrous formation was observed at temperatures below the 650 °C. In these preparations only the surface assisted setup was utilised as the results so far suggested that the formations would be similar, with superior yields and lower contaminants arising from the surface assisted configurations.

In **TaS₂600_SAG** and **TaS₂500_SAG** nanofibrous products are observed. These products are however different in both morphology and structure. **TaS₂600_SAG** produced nanowires of long straight morphology with a ~ 1:2 ratio by EDX, (Figure 3.26) and very similar to those produced in **TaS₂650_Std** and **_SAG**. PXD analysis showed a match in peak positions to the 2H and 3R structure. There is also the presence of another phase responsible for the peak at 26,45 ° 2θ the best matching possible phase is that of TaO₂ where a peak is expected at 26.86 ° 2θ. There therefore may be some oxide contamination.

The peak positions from the data in Figure 3.25 were indexed to a hexagonal unit cell that corresponds to the 2H-TaS₂ structure, and to the hexagonal unit cell of 3R-TaS₂. A good match was received to both structures; however there appears to be minimal enlargement of the *c* parameter in both cases. The energy of formation of the polytypes is particularly close leading to difficulties in obtaining pure phases.¹¹⁸ The 3R structure seems to be favoured at slightly higher temperature however preparations of the two different polytypes in the literature differ by as little as 23 °C. 2H-TaS₂ can reportedly be synthesised by annealing the

1T polytype at 823 K,¹²⁰ though perfect crystallinity is rarely achieved, while the 3R structure can again be synthesised by annealing the 1T polytype at 800 K for longer periods of time.¹¹² The difference in temperature is almost insignificant, but does explain the likelihood of forming mixed polytype products.

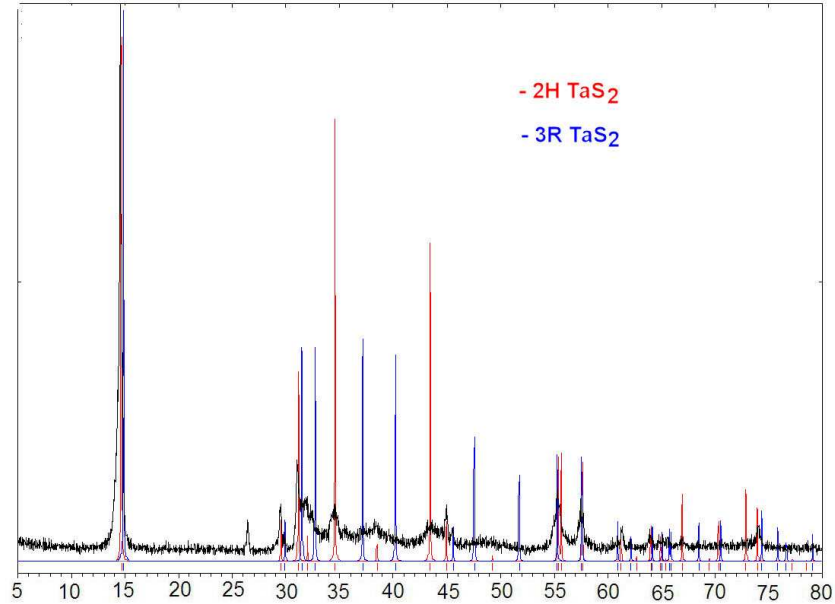


Figure 3.25: PXD pattern showing the residual powder from **TaS₂600_SAG** matching 3R-TaS₂ and 2H-TaS₂, (D5000 diffractometer).

Phase	<i>a</i>	<i>c</i>		<i>a</i>	<i>C</i>
TaS₂650_Std	3.318(5) Å	12.102(2) Å		3.322(4) Å	18.169(1) Å
2H-TaS ₂	3.314 Å	12.0970 Å	3R-TaS ₂	3.320 Å	17.90 Å

Table 3.5: Unit cell parameters from the indexed powder pattern from **TaS₂650_Std** compared to the published values for 3R-TaS₂.¹¹²

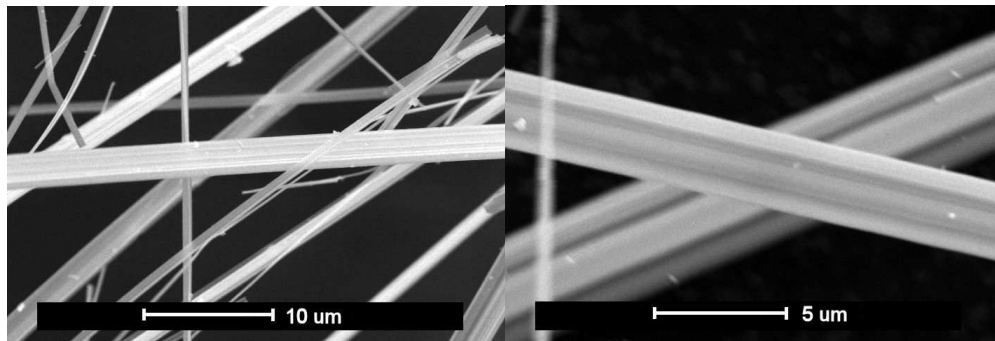


Figure 3.26: SEM micrographs from preparation **TaS₂600_SAG** (SEM #4).

In contrast to **TaS₂600_SAG**, **TaS₂500_SAG** produced curly ribbons of 1:3 ratio Ta:S by EDX (Figure 3.27). The PXD pattern for **TaS₂500_SAG** matched that observed for the indexed structure of TaS₃ (m_i-TaS₃) discussed in Chapter 4.

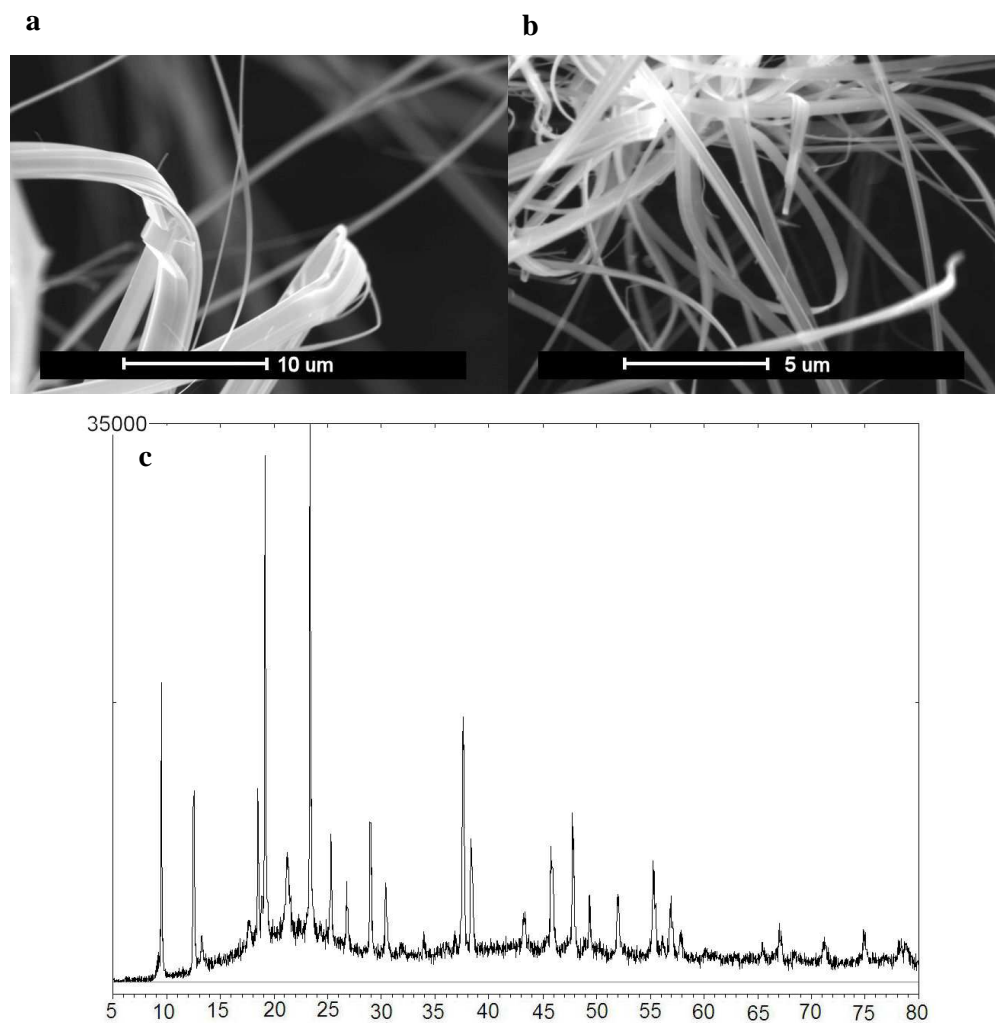


Figure 3.27: (a) and (b) SEM micrographs showing nanoribbons of a 1:3 ratio Ta:S formed in **TaS₂500_SAG**, (SEM #4) and (c) PXD pattern indexing to the m_i-TaS₃ structure discussed in Section 4.3.1.2, (D5000 diffractometer).

TaS₂400_SAG produced no nanofibrous products indicating that the reaction to nanofibres only progresses at temperatures above 400°C however, a black residual powder is still formed in Region I and I' (Figure 2.4) and shown to be multiphase TaS₂ along with much starting material contamination by PXD.

3.3.4 Bulk Phase Syntheses

During the course of the investigation into the different polytypes of TaS₂, preparations of the different polytypes as single phases were attempted. There are many different published routes to the different polytypes, of which some have been successfully reproduced. The selective control of polytype as well as morphology of TaS₂ structures would be highly desirable.

3.3.4.1 1T Polytype

As noted with **TaS₂1100**, the 1T polytype can be synthesised easily by heating the stoichiometric ratio of elemental powders up to 1100 °C for 60 hours and allowing to cool slowly, as described in Section 3.2.1.4.1. The 1T polytype is golden, in colour and consists of large crystals. PXD analysis shows the presence of a single phase 1T-TaS₂ and was indexed to a unit cell of space group $P\bar{3}m1$ and lattice parameters as shown in Table 3.6 using dicvol,¹⁸⁰ which are comparable with 1T-TaS₂. Similar products were obtained by the heating of residual powders from other preparations to 1100 °C in silica ampoules for at least 3 hours and quenching in 50 % ice 50 % water mix.

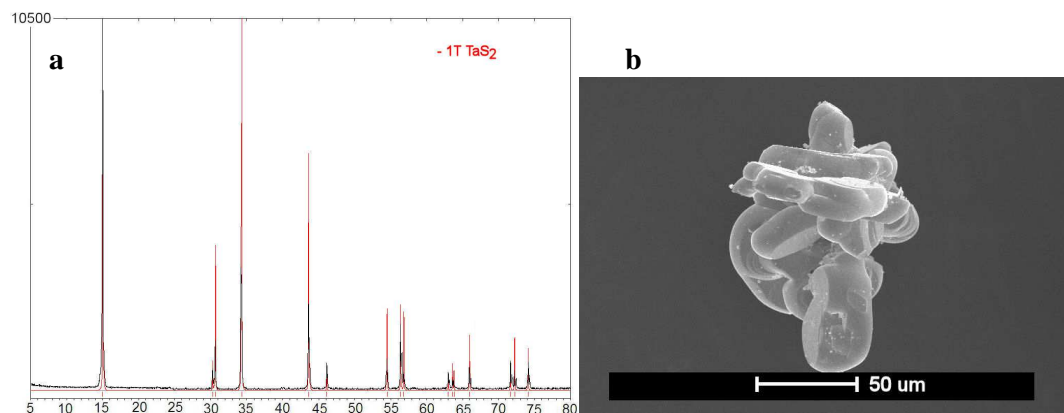


Figure 3.28: (a) PXD data showing the presence of 1T-TaS₂, (D5000 Diffractometer); (b) SEM micrograph showing typical morphology of 1T-TaS₂ (SEM #4).

Phase	<i>a</i>	<i>c</i>
TaS₂1100_Std	3.359(6)	5.8878(6)
1T-TaS ₂	3.3649	5.8971

Table 3.6: Unit cell parameters from the indexed powder patterns of **TaS₂1100_Std** compared to the published values for 1T-TaS₂.¹¹²

The ease of formation of the 1T polytype by heating at 1100 °C for a period of time see section 3.3.4.1, led the 1T polytype to be used as a convenient starting point for the preparations of the other phases. Indeed many preparations in the literature for the individual polytypes involve a heating step > 900 °C at which temperature the 1T polytype is likely dominant.

To investigate the stability of the 1T polytype and see if it could be converted into the other polytypes easily, DSC was utilised. Three significant features are observed in the DSC experiments (Figure 3.29). The first is the large peak at around 75 °C which is due to the melting of the residual sulfur that is present in and around the 1T particles. Sublimation of excess sulfur (Section 2.3.6) failed to remove enough sulfur given the sensitivity of the DSC. The second region is very small and at 260 °C and the final broad phase change seen in the region of 400 °C. These were investigated and are explained in the sections relevant to the polytypes formed.

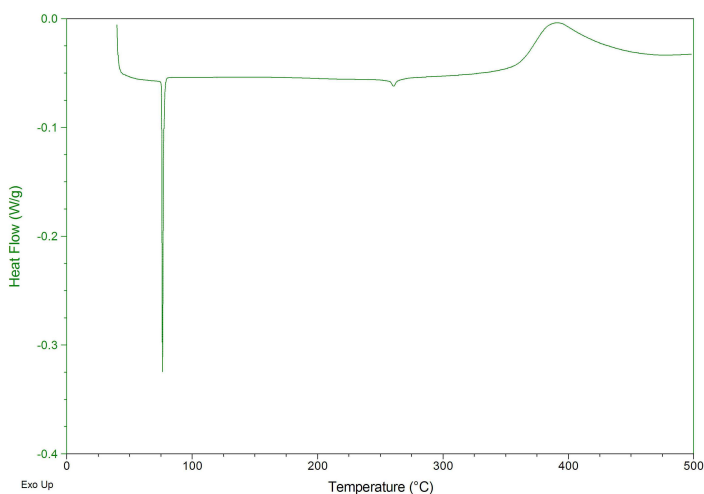


Figure 3.29: DSC data for the 1T polytype of TaS₂. Heated at 10 °Cmin⁻¹ from room temp to 500 °C under argon.

3.3.4.2 2H Polytype

The annealing of 1T-TaS₂ at 400 °C for 5 days produced a powder that was blue/black in colour with PXD analysis (Figure 3.30) showing peaks that match those expected for the 2H polytype. The peak in the DSC trace (Figure 3.29) at 400 °C was therefore due to a phase transition into 2H-TaS₂. The use of the Scherrer equation showed particle thicknesses of ~3.2 µm and the morphology was seen in SEM to be plate-like with thicknesses of a few µm and diameters of 20 – 40 µm. The exact stoichiometry of the TaS₂ is uncertain as TaS₂ especially in the 2H polytype suffers from many lattice distortions and the PXD data was not of sufficient quality to refine out the atom positions. Annealing over night produced a mixture of the 1T and the 6R and for 2 days produced the 6R in pure form, indicating the similarities in thermodynamics between the two trigonal prismatic forms of TaS₂; 2H and 6R. The peaks were indexed to a unit cell of space group *P63/mmc* and unit cell parameters as shown in Table 3.7 and are a good match to the 2H structure.

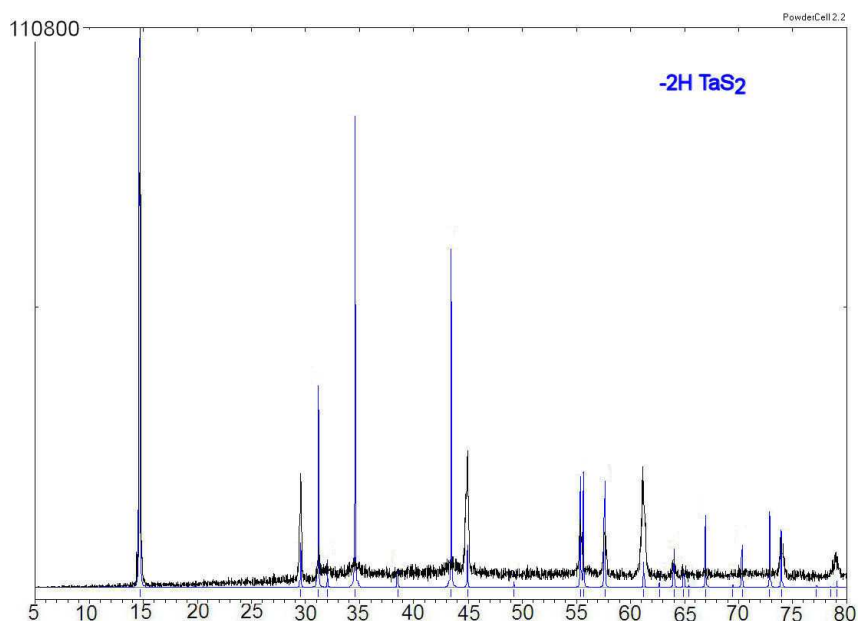


Figure 3.30: PXD pattern of 1T-TaS₂ after being annealed for 5 days at 400°C, showing a match to the 2H polytype, (D5000 diffractometer).

Phase	<i>a</i>	<i>C</i>
Preparation	3.317(4)	12.1084(4)
2H-TaS ₂	3.314	12.097

Table 3.7: Unit cell parameters from the indexed powder patterns of the 2H preparation compared to the published values for 2H-TaS₂.¹¹²

A synthesis for 2H-TaS₂ proposed by Figueroa *et al.*¹¹⁷ involves the heating of a stoichiometric mixture of Ta foil and S to 1220 K for 8 days and then annealing at 920 K for 4 days in silica ampoules. A powdered tantalum starting material produces the 6R polytype, again showing the similarity between the two trigonal prismatic forms. This synthesis is significantly 200 °C higher in temperature and taking approximately 5 days longer than the synthesis described above and starting from a foil based starting material which is less convenient than the powdered precursor. At 1220 K the 1T polytype will likely dominate, certainly by raising the temperature from 922 °C (1220 K) to 1100°C (upper limit of silica ampoules) the 8 days should be significantly reduced to ~3 days. 2H-TaS₂ is described as a flowing blue black powder which is consistent with these findings.

3.3.4.3 3R Polytype

Particles from the residual powder from many preparations were seen to be the 3R phase by PXD and were shown by EDX to have an average a 33:67 ratio, Ta:S (± 2) Both PXD pattern and SEM micrograph of the general morphology are given in Figure 3.31. Some of the PXD patterns showed a striking preferred orientation towards the 001 direction, indicating that the structures have large anisotropy. This is further backed up in the SEM micrographs where we see large plate-like particles. It is likely that when the XRD slide was smoothed over the platelets aligned so that the upper layers were flat and smooth with all the crystals orientated in the same vertical direction, i.e. the 001 plane of the crystal structure. The peaks were

indexed to a unit cell of space group $R3m$ and unit cell parameters as shown in Table 3.7 and are a good match to the 3R structure.

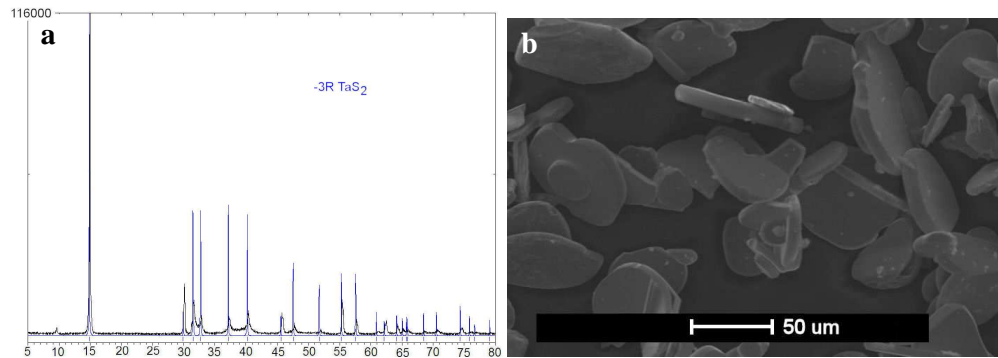


Figure 3.31: (a) PXD pattern (X-pert diffractometer) showing peaks matching the 3R-TaS₂ phase; (b) SEM micrograph showing the general morphology of the crystals, (SEM #1).

Phase	a	C
Preparation	3.312(1)	17.8248(4)
3R-TaS ₂	3.3200	17.900

Table 3.8: Unit cell parameters from the indexed powder patterns of the 3R preparation compared to the published values for 3R-TaS₂.¹¹²

3.4 Conclusions

It is clear from the work in this chapter that nanofibres of TaS₂ can be produced using a simple one-step synthesis. This is in contrast to the multi step syntheses so far published.^{43, 59, 187} Further, a high level of control over the morphology and structure of the product can be maintained throughout the process. As the synthesis temperature decreases, a change in morphology is observed from particles of 1T-TaS₂ produced at high temperature (**TaS₂1100**), “nanofeathers” of TaS₂, produced at slightly lower temperatures, (**TaS₂900**), followed by belts (**TaS₂700**) and ribbons of TaS₂ (**TaS₂600**) and then ribbons of TaS₃ (**TaS₂500**). At temperatures below 400 °C, no nanofibrous formation is observed.

At 650 °C the nanowires produced are of the 2H structure as shown by PXD, SQUID and TEM analysis.

The morphology of the majority of the fibrous material from both TEM and SEM observations would appear to be a belt-like morphology, though some control as a result of temperature exists. Conventional definitions are given in Section 1.1.3. These fibres closest resemble a belt-like morphology as found by Wu *et al.*⁵⁹ The thinnest dimension of the belts is that parallel to the long c -axis, or in other words, the slowest growth occurs perpendicular to the basal plane layers of the 2H structure. This has also been noted in nanoribbons of the 2H polytype of MoS₂.¹⁵¹ The long axis of the needles is along $\frac{1}{3}\langle 2\bar{1}\bar{1}0 \rangle$, and the wider dimension of the wires is along $\langle 0\bar{1}10 \rangle$. It is interesting to note that the nanowires have such a radically different symmetry to that of the 2H unit cell, although it may be noted that smaller hexagonal platelets have been observed in SEM images as a by-product to the nanowire production. It seems likely that the formation of elongated wires rather than hexagonal platelets is therefore driven by kinetic or materials supply factors in the synthesis and does not represent a thermodynamically preferred state.

SQUID analysis on the samples from the standard preparations (**TaS₂650_Std**) were not single phase as they had two superconducting phases, of which one is believed to be TaS₂ nanofibres ($T_C \sim 3.4$ K) and the other Ta metal ($T_C \sim 4.5$ K). The tantalum metal is not present in the surface assisted preparations (**TaS₂650_SAG**) measurements due to the unique method of growing the fibres away from the feedstock of tantalum and the brittle nature of the wires that break away from the surface. Numerous efforts have been made to synthesise superconducting nanomaterials for nanodevices and electrical connections²⁰¹⁻²⁰⁹ with extra potential predicted for 1-dimensional nanoscale superconductors as the confinement of Cooper pairs and supercurrent flows could provide phenomena such as quantum phase slips^{210, 211} and quantum switching effects²¹² which have important applications in quantum computing. TaS₂ in the form of 1-dimensional superconducting nanostructures are therefore highly relevant and show much promise for applications even though the T_C is relatively low.

The exact mechanism of how the surface is affecting the growth of the nanofibres is unclear, however its advantageous role is apparent. The yield is increased as a result of the surface assisted growth phenomena with similar morphology products to those grown in the absence of a tantalum surface. The cleanliness of the yields is markedly improved by utilising the surface assisted growth setup as shown by the SQUID data, and the lengths of the fibres is improved as shown by the SEM data.

At temperatures below 900 °C the foil is relatively uncorroded leading to the belief that the tantalum in the foil is not involved in the stoichiometry of the reactants at 650 °C. How therefore are the tantalum and sulfur reactants transporting up the tube to form preferentially on the foil? At temperatures in excess of 1000 °C below the boiling point of Ta, it is safe to assume that the mechanism does not involve gaseous elemental constituents. TaS₂ is also solid to temperatures well above 1000 °C (~1800 °C) leading to suggestion that the transporting phase is not TaS₂ either. Although not isolated in this work there is a likelihood of a volatile phase of tantalum sulfide that is acting as a transport agent. It has been noted that I₂, S₂Cl₂ and S can all successfully act as transport agents in CVT reactions with TaS₃ at 550 to 500 °C.¹³⁶ No further information was given about the sulfur containing species and its identity other than the fact that a large 30 % excess of sulfur was required.

Chapter 4: Tantalum Trisulfide Nanofibres

4.1 Introduction

Following the initial discoveries of nanofibrous materials,^{7, 8} research has concentrated largely on layered inorganic materials that mimic the ability of graphite to form anisotropic nanostructures as a result of their layered 2-dimensional structures.¹⁴⁹ These materials include boron nitride⁶⁴ and other layered dichalcogenides, MX_2 ($\text{X}=\text{S}, \text{Se}$) such as WS_2 ,⁸ MoS_2 ⁹ and NbS_2 .²¹³ Recently inorganic nanoscale research has expanded into materials that do not possess layered structures and significantly differ from the pseudo-graphitic layers seen in the dichalcogenides.^{55, 166, 193, 214} These unique non layered materials often have different and desirable electronic, photonic and mechanical properties in bulk form, so possible reproduction and modification or enhancement of these properties on the nanoscale is of interest.

The formation of nanomaterials from non-layered materials has been achieved in many ways, some of which were outlined by Xiong *et al.* and involve concepts like templating using carbon nanotubes, concentration depletion and electrospinning.¹⁶⁶ Very few of these or other synthetic methods for nanowire production involve a single-step synthesis; i.e. removal of either a templating step, sonication of macroscale precursors, or a chemical change of a previously prepared nano-precursor. A simple single-step synthesis route is therefore advantageous.

TaS_3 was first reported by Blitz and Kocher in 1938¹³⁰ and again by Jellinek in 1962,¹¹² however, the crystal chemistry of TaS_3 remains ambiguous. There are two commonly referred to structures, a monoclinic phase (m- TaS_3) and an orthorhombic phase (o- TaS_3). The full structure of m- TaS_3 was published in 1981 by Meerschaut *et al.* with space group $P2_1/m$ and lattice parameters $a = 9.515(2) \text{ \AA}$, $b = 3.3412(4) \text{ \AA}$, $c = 14.912(2) \text{ \AA}$ and $\beta = 109.99^\circ$,¹²⁹

while o-TaS₃ forms in the space group $C222_1$ and lattice parameters $a = 36.804 \text{ \AA}$, $b = 15.173 \text{ \AA}$, $c = 3.340 \text{ \AA}$ but has yet to be fully refined for atom positions.¹³³ The properties of m-TaS₃ and o-TaS₃ have subsequently been thoroughly investigated.¹³³⁻¹³⁵ There is also a high-pressure phase of the m-TaS₃ published by Kikkawa *et al.* in 1982 with the same space group as m-TaS₃ and lattice parameters $a = 9.52 \text{ \AA}$, $b = 3.35 \text{ \AA}$, $c = 14.6996 \text{ \AA}$ and $\beta = 107.487^\circ$ which has again been fully refined.¹³² For discussion purposes, and to keep with the nomenclature used above, this structure will hereon be referred to as m_{hp}-TaS₃. The main difference between m-TaS₃ and m_{hp}-TaS₃ is that under high pressure the β angle reduces by nearly 3° .

Monoclinic tantalum trisulfide (m-TaS₃) is a low dimensional conductor with infinite chains of tantalum atoms running parallel to the crystallographic “*b*” axis of the unit cell. Conduction has been shown to occur along the chains of tantalum atoms, with larger sulfur atoms forming an insulating matrix in the remaining volume between the tantalum chains (Figure 4.1), leading to pseudo 1-dimensional conduction.

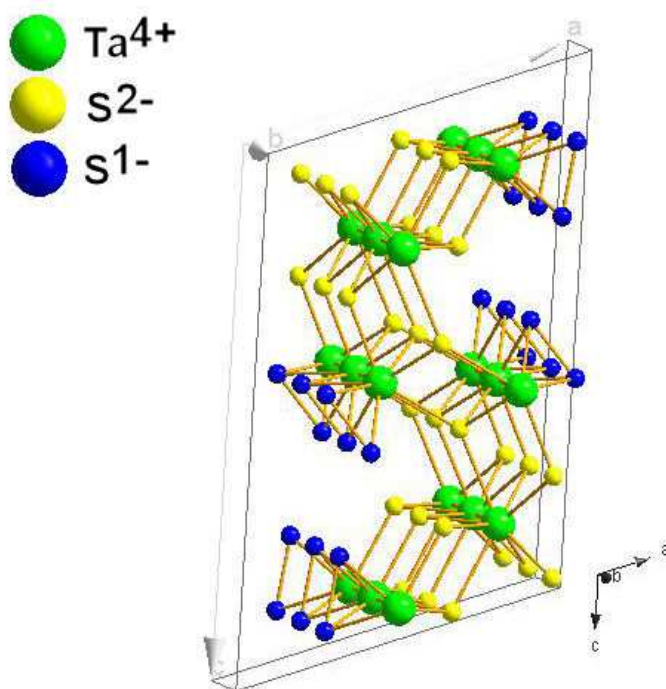


Figure 4.1: Crystal structure of m-TaS₃¹²⁹ showing 3 unit cells stacked in the *b* direction to illustrate the origin of the low dimensional behaviour.

The chains of tantalum atoms propagate through the structure as trigonal prisms with 6 sulfurs surrounding each tantalum atom, (Figure 4.2). There are also two other sulfurs that are further away from the tantalum than the other sulfurs (2.747 Å and 2.870 Å) but not so far as to exclude the possibility of bonding marked in red. These chain bridging sulfurs have been linked to the formation of slabs or ribbon-like structures.¹²⁹

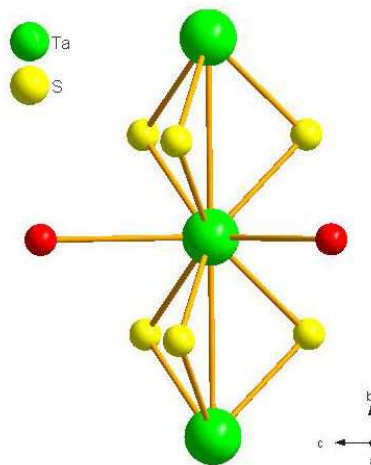


Figure 4.2: Crystal structure of the sulfurs that surround the tantalum atoms in the chain structure of $m\text{-TaS}_3$.

The change in stoichiometry from TaS_2 to TaS_3 shows a notable change in crystal structure and dimensionality. As discussed in Section 1.5.1, TaS_2 has pseudo 2-dimensional properties with the chemistry and behaviour dominated by the layered structure.²¹⁵ Likewise the interesting properties of bulk TaS_3 are directly related to the crystal structure, specifically the relation between the chains of tantalum atoms and the b direction of the unit cell, leading to pseudo 1-dimensional properties. Chapter 3 and indeed much other research have shown that the formation of nanofibres tends to occur with a specific crystallographic direction controlling the growth, leading to crystallographic texture. Texture is in this case observed as an alignment of the long axis of the nanofibre with a specific crystallographic direction, often noted as the shortest unit cell parameter in layered materials.^{55, 72, 152, 160, 193} Should the formation of nanofibrous morphology be possible from a crystal structure with a such as

TaS₃, with its chains of tantalum atoms running parallel to the *b* direction of the unit cell, then it is likely that the chains will direct the growth leading to texture and may result in the transfer of low dimensional properties from bulk to nanofibres morphology. This outcome could lead to potential application within nanoscale devices, e.g. should the chains of Ta propagate in the direction of the fibres then the fibres should be metallic, as has been observed in a similar material Nb₃Te₄.^{193, 214}

Currently the only paper in the literature, concerning the formation of nanofibres of TaS₃ is by Wu *et al.* who describe the formation of “nanobelts” that were found to be of the o-TaS₃ structure.⁵⁹ TaS₃ nanobelts were formed in silica ampoules with iodine as a transport agent at 760 °C (for conventional definitions of nano-scale morphology see Section 1.1.2). The TaS₃ nanobelts had an orthorhombic structure with lattice parameters *a* = 36.80 Å, *b* = 15.15 Å and *c* = 3.340 Å, matching the structure of o-TaS₃.¹³³ The cross section of the belts was seen to be rectangular with widths in the range of 40-900 nm, heights in the range 20-50 nm and lengths of several centimetres. The crystal structure was aligned with the long axis of the belts by the [031] direction. High resolution TEM showed lattice fringes of 30.8 and 15.21 Å corresponding to the [1200] (hexagonal indices) and [010] spacing of the o-TaS₃ phase and therefore support the XRD results for o-TaS₃.¹³³

The o-TaS₃ nanobelts prepared by Wu *et al.* were used as a nano-precursor for the formation of TaS₂ nanobelts by the removal of sulfur in a thermolysis reaction at 850 °C,⁵⁹ indicating the instability of the TaS₃ nanobelts at high temperature. Interestingly the decomposition of the TaS₃ nanobelts to TaS₂ results largely in the retention of morphology and the formation of nanobelts of TaS₂. Further work is carried out related to this concept in Chapter 5.

An analogous system to TaS₃ is NbSe₃ (Section 1.11.2.2) and indeed TiS₃ (Section 1.11.2.3), both of which have been successfully synthesised as nanofibrous materials in much

the same way as described above by Wu. A similar method was used in this chapter for the formation of TaS₃ nanofibres.

4.2 Experimental

4.2.1 Synthesis

Many synthesis procedures were performed in an attempt to try to understand the TaS₃ nanofibrous system. These are outlined in this section with the results discussed in Section 4.3.

In keeping with previous notation, the preparation names will consist of a list of reactants and their relative quantities in the reaction mixture followed by a temperature before the unique preparation conditions. Preparation names will be highlighted in bold to distinguish them from the main text, e.g. the preparation involving a 1:3 ratio Ta:S, heated at 650°C under the standard conditions, (Section 4.2.1.1) will be referred to as **TaS₃650_Std**. If the unique preparation conditions (**Std** or **SAG**) are irrelevant then this section of the reference will be omitted, e.g. **TaS₃650** refers to all 1:3 ratio preparations performed at 650 °C.

4.2.1.1 Standard Preparation

In a typical standard preparation, a stoichiometric quantity (1:3) of tantalum (99.9% -325 mesh, Aldrich) and sulfur (99.5% Fisher Chemicals) were ground together using a mortar and pestle and sealed in silica tubes to form ampoules under a vacuum of *ca.* 4×10^{-4} Torr. In all cases 1-2 g of starting material was used leading to the use of 0.9 g (0.02 mol.) tantalum and 0.48 g (0.06 mol.) sulfur. The silica tubes were prepared, filled and sealed into ampoules, as described in Section 2.3.1.1. Once sealed, the silica ampoules remained vertical with all the powder at one end before being placed horizontally on a ceramic brick in the centre of an Elite muffle furnace, (Section 2.2.5.1) and heated over a temperature profile that was similar

to that used in the TaS₂ nanofibre preparations, (Section 3.2.1.1). Step i was for safety considerations, as outlined in Section 2.2.4.6. Once heated for a period of up to 60 hours, (Step iv), the ampoules were quenched in air to room temperature (Step v) as described in Section 2.2.4.8. The resultant nanofibres were physically separated from the residual powders using tweezers once the ampoules had been opened and characterised. The three regions within the ampoule, as introduced in Figure 2.4, will be used for discussion purposes when the results from **TaS₃650_Std** are discussed in Section 4.3.1.

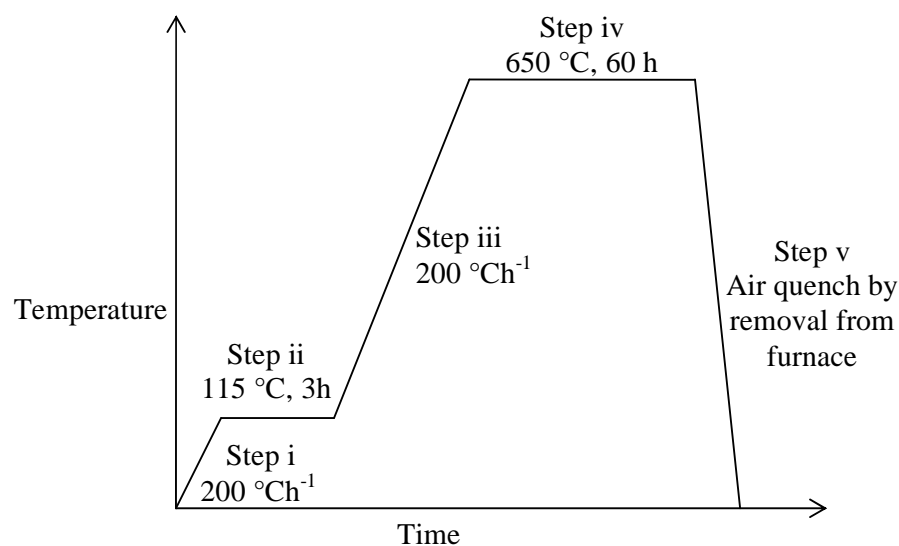


Figure 4.3: Temperature profile used in **TaS₃650_Std**. This is given as an example of the temperature profile used throughout the preparations for TaS₃ nanofibres.

4.2.1.2 Surface Assisted Growth Preparation

Following the success of the surface assisted growth experiments with the tantalum disulfide system, (Section 3.2.1.2 and Section 3.3.2), similar experiments were carried out with the tantalum trisulfide system. In these reactions 0.9 g (0.005 mol) tantalum (99.9% -325 mesh, Aldrich) and 0.48 g (0.015 mol) sulfur (99.5% Fisher Chemicals) were mixed using a mortar and pestle and placed in the lower section of a specially adapted silica tube, (Section 2.2.4.4.2) using a long powder funnel. A piece of tantalum foil; 30 mm x 8 mm x 0.1 mm, (99.9%, Aldrich Chemicals), was inserted into the upper region of the adapted silica tube

before it was evacuated and sealed to form an ampoule (Section 2.2.4.5). The result was an ampoule with two volumes separated by a constriction; lower volume containing a mixture of elemental powders, and the upper volume containing a piece of tantalum foil as shown by Figure 2.6. The ampoules, once sealed were transported to an Elite muffle furnace, (Section 2.2.5.1), in an upright position to maintain the physical separation of the reactants. The ampoules were heated horizontally over a temperature profile as shown in Figure 4.3 and the resultant nanofibre formation removed by mechanical methods. The results from preparation **TaS₃650_SAG** are discussed in Section 4.3.1, using the three regions as introduced in Figure 2.4.

4.2.1.3 Effects of Changing Temperature Regime on Nanofibrous Formation

Different temperature profiles were utilised to see how they affect the formation of the nano-structures. Experimental parameters were kept constant with the exception of the maximum reaction temperature (Step iv). Preparations were carried out in both standard and surface assisted growth configurations.

High temperature preparations (**TaS₃1100**) were attempted with a maximum temperature (Step iv) of 1100 °C. The choice of this temperature was governed by the upper temperature limit of the silica ampoules that have been used throughout this project (Section 2.2.4.6). Lower temperature preparations were also carried out; the experimental conditions are given in Table 4.1.

Preparation Label	Annealing Temperature °C
TaS₃1100_Std	1100
TaS₃750_Std	750
TaS₃500_Std	500
TaS₃400_Std	400
TaS₃1100_SAG	1100
TaS₃750_SAG	750
TaS₃500_SAG	500
TaS₃400_SAG	400

Table 4.1: Experimental conditions for the changing temperature regime preparations.

4.2.2 Characterisation

PXD was carried out with typical analysis running as a step scan between 5 and $80^\circ 2\theta$, with a step size of 0.02° utilising a speed that gave ~ 3 hour scans. For the scans that were required for higher level analysis longer scans were carried out again over the same range but lasting for 15 hours. Different diffractometers have been used for the analysis as explained in Section 2.4.1.3. PXD slides were prepared for powders by smoothing the powdered products over the indentation to provide a flat uniform surface. Many different methods of loading the PXD slide with nanofibres were attempted, as outlined in Section 2.4.1.2 as the nanofibres proved reluctant to yield a PXD pattern of sufficient resolution for quantitative X-ray analysis, indexing or refinement. The best results came from either adhering the nanofibres to the glass slide using a carbon tab, (Section 2.4.1.2.3.3) or dispersing the nanofibres in ethanol and dropping them into a hot glass slide (Section 2.4.1.2.3.4).

SEM was performed at 20 KV, in high vacuum mode, with a typical working distance of 10 mm and spot size 3 or 4. Samples were loaded onto aluminium slugs using a double-sided adhesive carbon tabs which provided enough conduction to prevent the need for a coating procedure. EDX was used in conjunction with the SEM to ascertain approximate elemental ratios. Different SEMs have been used for the SEM analysis as explained in Section 2.4.2.3.

TEM and electron diffraction was carried out using two different microscopes (Section 2.4.3.7), with typical samples loaded by dispersion of nanofibres onto a carbon holey grid (300 mesh Ni) using propan-2-ol.

AFM measurements were performed using a custom built Asylum Research AFM. Nanowires from **TaS₃650_SAG** were spin coated onto a silicon dioxide surface as described in Section 2.4.8.3 and placed in the AFM. To take electronic measurements, SiO₂ surfaces striped with gold 200 nm wide were prepared (Section 2.4.8.2) and coated as described in Section 2.4.8.3.

4.3 Results and Discussion

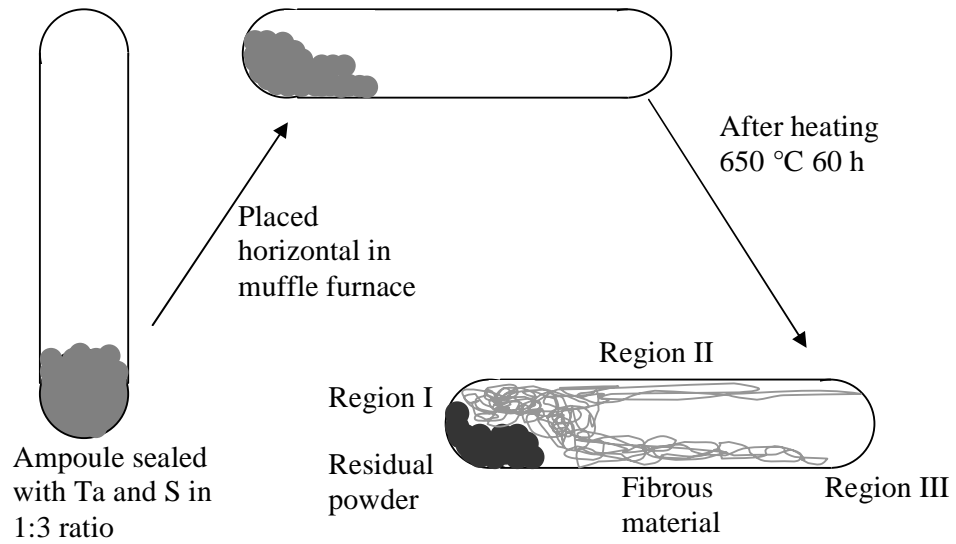
4.3.1 Preparations TaS₃650 Std and TaS₃650 SAG

Upon quenching in air, nanowire formation was observed along the edges of the ampoules in Region II and II', and on the residual powder that remained in Region I and I'. Figure 4.4 show schematics of the reaction results along with the Regions that will be used for discussion purposes, initially introduced in Figure 2.4. Defects in the walls of the ampoules again appeared to act as nucleating points for the nanowire formation as seen in the TaS₂ system in Figure 3.13(d).

TaS₃650_SAG showed similar yields in fibrous material in Region I' to that found in Region I of **TaS₃650_Std** with an additional yield growing from the surface of the tantalum foil in Region III' as shown in Figure 4.4(b). Thus the yield appears to have increased when compared with preparation **TaS₃650_Std** as was found in the TaS₂ system Section 3.3.2.

The products of the standard and surface assisted growth preparation were indistinguishable in terms of morphology, composition and structure and have therefore been combined as one section. Where specific differences occur between the two configurations, they have been outlined in the relevant sections.

(a) **TaS₃650_Std**



(b) **TaS₃650_SAG**

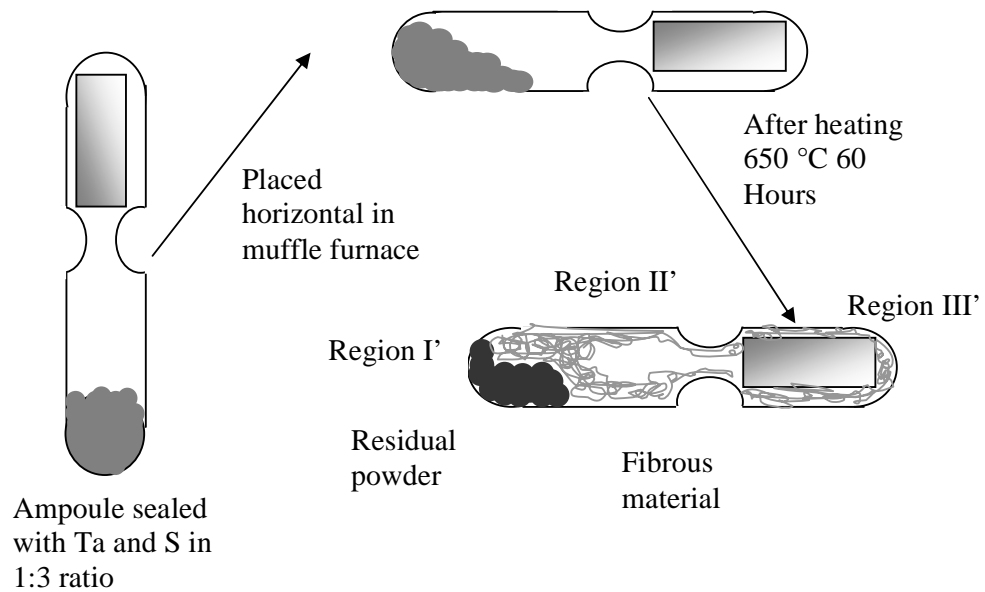


Figure 4.4: Schematic of the results for (a) **TaS₃650_Std** and (b) **TaS₃650_SAG**. In each case three regions marked for discussion purposes.

4.3.1.1 Residual Powders

The residual powder from Region I & I' of the ampoules from preparations **TaS₃650** gave a PXD pattern that could be indexed to the o-TaS₃¹³³ unit cell and not to any of the published monoclinic phases of TaS₃. The powder pattern was indexed using 36 different peaks and has an orthorhombic unit cell with lattice parameters $a = 36.75(3) \text{ \AA}$, $b = 15.164(6) \text{ \AA}$ and $c = 3.344(2) \text{ \AA}$ and fits the space group $C222_1$. The PXD pattern from preparation **TaS₃650_SAG** and the peaks that have been used for the indexing are shown in Figure 4.5. o-TaS₃ is the phase identified by Wu *et al.* for TaS₃ nanobelts.⁵⁹ Unfortunately, there is no refined structure for this phase in the literature. Attempts to determine the full structure from the powder data through direct methods (and refine the structure using least squares refinement) proved futile as the PXD data appeared not to be sufficiently resolved. The structure could perhaps be obtained using a Synchrotron X-ray source.

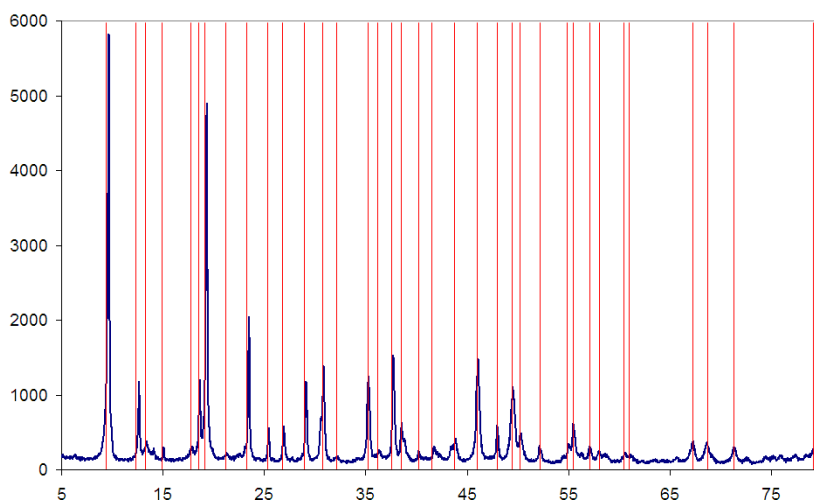


Figure 4.5: PXD pattern showing the 36 indexed peaks from the powder pattern of the residual powders from Region I' of the ampoules of preparation **TaS₃650_SAG**, (X-pert diffractometer).

SEM analysis (Figure 4.6 showed the residual powder to consist of sharp angular particles with a broad range of dimensions $\sim 100 \mu\text{m}$. The general morphology is not plate-like as

would be expected from a material that does not possess a layered crystal structure and EDX confirmed a 25:75 ratio Ta:S (± 1) indicating TaS₃.

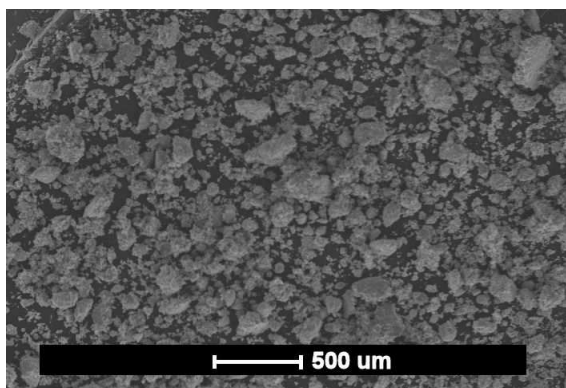


Figure 4.6: SEM analysis of the residual powders from **TaS₃650**, (SEM #2)

4.3.1.2 Fibrous Morphology

4.3.1.2.1 Powder X-ray Diffraction

Figure 4.7 shows 2 PXD patterns; one from the nanofibres, (a) recovered from Region III' and the other from the residual powders, (b) recovered from Region I' of an ampoule from preparation **TaS₃650_SAG**. It is clear from this comparison that there are inherent differences between the phases and indeed that the nanofibres are not of the same structure as the residual powders. The nanofibre powder pattern fails to index to either of the known phases of TaS₃.

Many of the PXD patterns that were taken of the nanofibres were plotted on the same axes and the 10 best resolved peaks extracted. These peaks were run through Dicvol,¹⁸⁰ an indexing program that indexes the pattern to unit cells in all the possible crystallographic systems (Section 1.2.1). A number of solutions were obtained and these were matched against the most representative PXD pattern and compared to the possible space groups for that solution, before the unit cells were refined in CELREF¹⁸¹ using the 20 most resolved peaks in that pattern. The most likely 3 solutions were then used to index the SAED data, (Section 4.3.1.2.3 and one final solution was selected as the solution with the best fit to all the data.

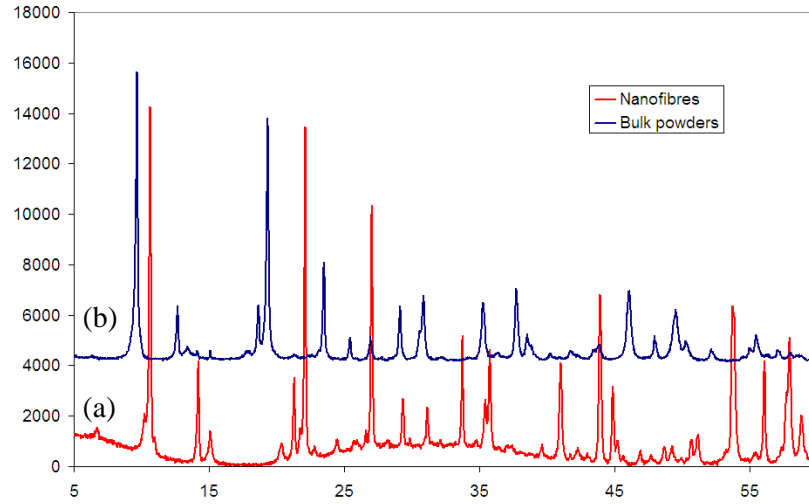


Figure 4.7: PXD pattern for (a) typical nanowires from **TaS₃650** and (b) typical residual powder from **TaS₃650**, (D5000 diffractometer).

The final indexed unit cell solution was monoclinic with cell parameters $a = 9.966(1) \text{ \AA}$, $b = 3.4698(1) \text{ \AA}$ and $c = 14.631(3) \text{ \AA}$ and $\beta = 106.49(1)^\circ$ with space group $P12_1/m1$. In keeping with the notation first introduced in Section 1.6.1, the indexed form of TaS₃ is hereon referred to as m_i -TaS₃. The unit cell for m_i -TaS₃ is similar to both the published, m -TaS₃¹²⁹ and m_{hp} -TaS₃¹³² but has a significantly reduced β angle when compared to m -TaS₃. The unit cell is a closer match to the m_{hp} -TaS₃ than m -TaS₃ indicating that there may be some analogy between constraining the structure into a nanofibrous form and applying pressure. The unit cell parameters of all three phases are given in Table 4.2. A comparison of the two theoretical powder patterns is given Figure 4.8. Theoretical powder patterns for the model of both the published monoclinic forms are very similar with almost identical peak positions and different peak heights, yet quite different to the observed pattern.

Label	a	b	c	β
m -TaS ₃ ¹²⁹	9.515(2) \AA	3.3412(4) \AA	14.912(2) \AA	109.99 $^\circ$
m_{hp} -TaS ₃ ¹³²	9.52 \AA	3.35 \AA	14.6996 \AA	107.487 $^\circ$
m_i -TaS ₃	9.966(1) \AA	3.4698(1) \AA	14.631(3) \AA	106.49(1) $^\circ$

Table 4.2: Table to show the comparison between the two published monoclinic unit cells and the indexed solution for the nanofibres.

The indexed unit cell for m_i -TaS₃ is also similar to the unit cell given for the analogous NbSe₃ nanowires found by Slot *et al.* which have unit cell parameters $a = 10.0$ Å, $b = 3.5$ Å, $c = 15.6$ Å and $\beta = 109.5^\circ$.¹⁶⁸ The nanowires of NbSe₃ are however in this case more likely to closer resemble the crystal structure of the bulk as a result of the synthetic procedure when compared to TaS₃ nanofibres formed in the methods above. The NbSe₃ nanofibres were formed by ultrasonically cleaving bulk NbSe₃ crystals rather than a chemical reaction. The crystal structure of the resultant nanofibres would be expected to be highly controlled by the original bulk crystal structure. The NbSe₃ was noted as being similar to and indeed the starting point for the crystal structure determinations for the high pressure phases of TaS₃, NbS₃ and TaSe₃ by Kikkawa *et al.*¹³²

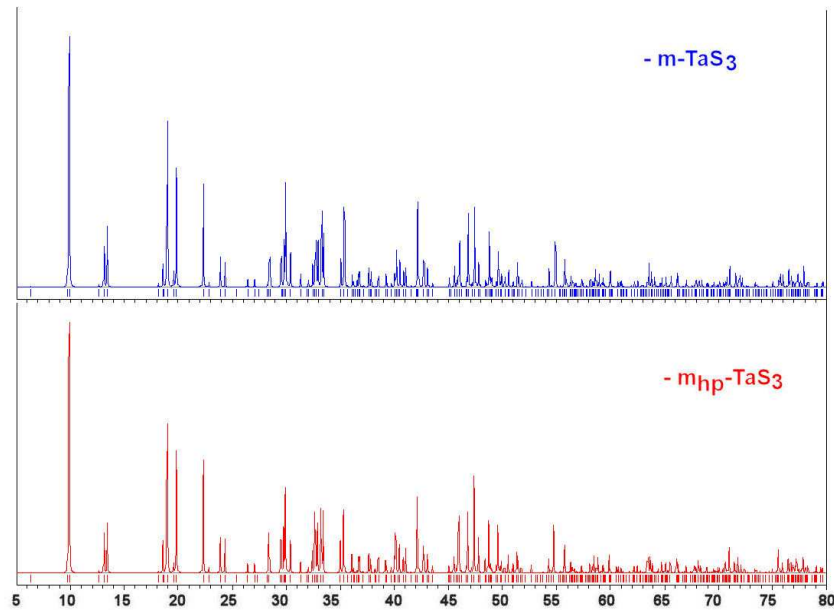


Figure 4.8: Generated powder pattern for the two models of the TaS₃ phases showing the similarities in the peak positions.

The inability to refine the structure for atom positions from the X-ray data has been a large hindrance to this project. The unit cell parameters are in agreement with PXD and SAED data but it has not been possible to acquire a sufficiently close starting model for Rietveld refinement of the structure. The best results were obtained using m_{hp} -TaS₃ as a starting model with the indexed unit cell parameters, but a reasonable refined structure was unobtainable. χ^2

values of ~ 5 were the best that was achieved. Attempts were made to form bulk scale materials with crystals of $m_i\text{-TaS}_3$ but to no avail the X-ray data not sufficiently resolved for refinement to the model. Synchrotron experiments would help to determine the structure by providing high resolution data, though there may be problems associated with sample purity. It is possible that $m\text{-TaS}_3$ or $o\text{-TaS}_3$ is interfering with the intensities of expected peaks leading to the complications encountered in the structure determination.

4.3.1.2.2 Scanning Electron Microscopy

The fibrous material from Region III & III' was seen to be of 1-dimensional morphology with aspect ratios of $\sim 20,000$ (lengths in excess of 4 mm and widths up to 200 nm), (Figure 4.10). This is in contrast to the aspect ratio of 12,000 recorded for **TaS₂650_Std** discussed in Chapter 3. The nanofibres of TaS_3 are similar in terms of appearance to those observed by Wu *et al.* in the form of nanobelts and have comparable aspect ratios.⁵⁹ Lengths of up to 4 mm is extremely long for nanofibres however comparable lengths have been observed in analogous systems e.g. TiS_3 .¹⁰²

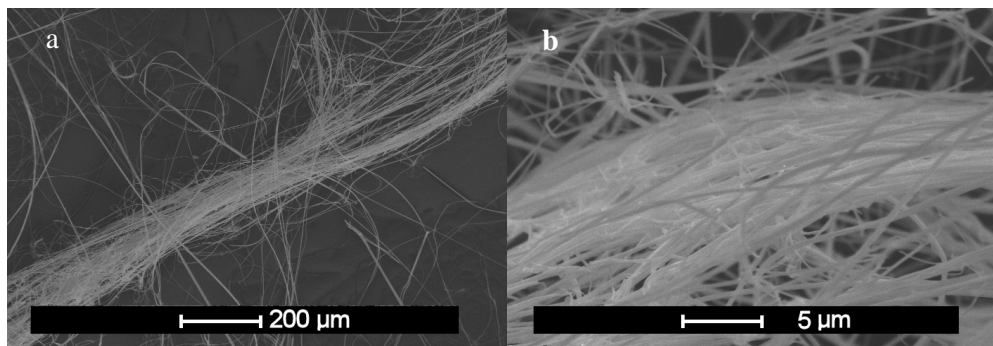


Figure 4.9: SEM micrographs of TaS_3 nanofibres from **TaS₃650_Std** showing; (a) general morphology, (b) bundles of nanowires and ribbons / belts, (SEM #1).

EDX showed an average ratio of 25:75 Ta:S, (± 1) indicating a 1:3 ratio and suggesting a TaS_3 stoichiometry. Bundles and mats / bales of aligned nanowires were seen from the surface assisted preparations (Figure 4.10). The bales were comprised of fibres of similar dimensions to those described above, except shorter in length. The bales were $\sim 40\text{ }\mu\text{m} \times 60$

μm and 5-10 μm thick and seen in the fibres close to the tantalum foil surface, indicating that they may have originated on the surface and broken away during the opening of the ampoules. This was one of the few areas where the results from **TaS₃650_SAG** differed in any way to those from **TaS₃650_Std**. No notable increase in length was observed, though the fibres from both syntheses were in general longer than in the TaS₂ preparations, the lengths of the TaS₃ nanofibres were < 4 mm while TaS₂ < 1.2 mm. Also no hexagonal crystals were observed while using a 1:3 ratio of starting materials, as would be expected with the formation of TaS₂.

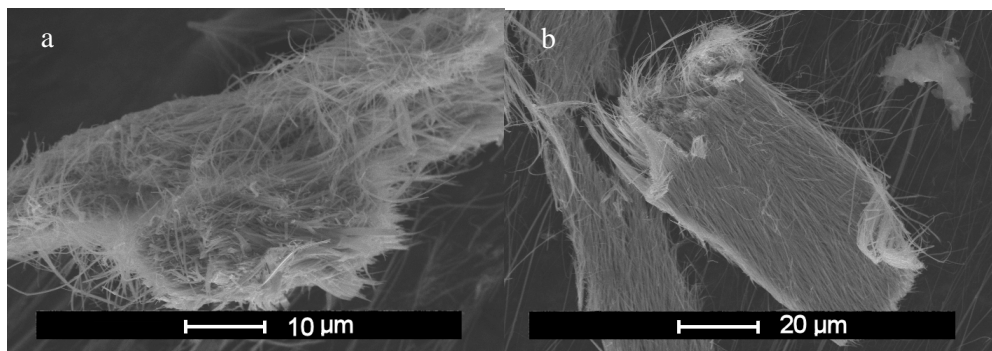


Figure 4.10: SEM micrographs from **TaS₃650_SAG** showing; (a) bundles of nanowires and (b) bales of aligned nanowires, (SEM #1).

4.3.1.2.3 Transmission Electron Microscopy

TEM on the trisulfides was performed with both Prof. P. D Brown from University of Nottingham and Dr. I. MacLaren from University of Glasgow.

TEM from **TaS₃650_Std** and **TaS₃650_SAG** shows the presence of nanofibres with diameters in the range 50 – 100 nm (Figure 4.11). SAED data were used to differentiate accurately between the three possible solutions gained from the PXD data by Dicvol in Section 4.3.1.2. The method used for indexing is best described with a schematic (Figure 4.12). Essentially a number of SAED patterns were indexed to each of the structures and the errors calculated between the actual positions and the theoretical positions for the diffraction spots.

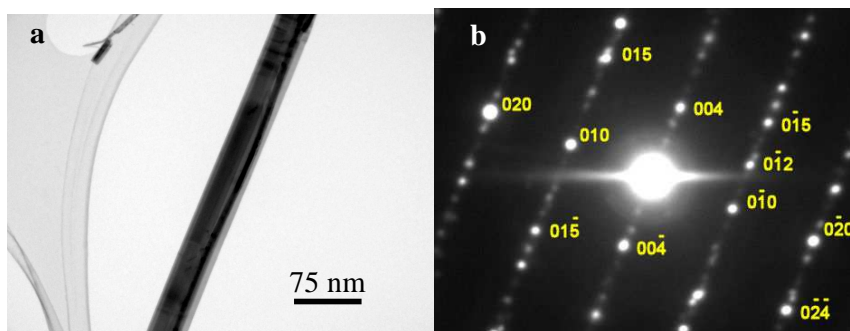


Figure 4.11: (a) TEM micrograph showing a single nanowire of diameter <75 nm; (b) corresponding diffraction pattern indexed to various spots in the 001 and the 010 directions of the m_i -TaS₃ structure, (T20 microscope).

Starting with the first SAED pattern and the first structure (to avoid confusion the m_i -TaS₃ structure will be used); the spots were assumed to be a zone axis meaning that the largest spot spacing was representative of the shortest unit cell parameter which for m_i -TaS₃ would be the “ b ” parameter 3.4698 Å, thus defining the conversion factor. The other distances were then measured, converted and compared to the other zone axes for a best possible fit, e.g. in Figure 4.12 if one assumes the longer spacing is 3.4698 Å, then by measuring the shorter spacing and converting from reciprocal space to real space, (Equation (2.14)), hypothetically one may obtain a value of 9.9655 Å. This is close to the 9.966 Å expected for the “ a ” unit cell parameter. The pattern can now be fully indexed to this structure as shown in Figure 4.12. Comparison of the measured spacings with calculated spacings for the monoclinic unit cell, (Equation (1.8)) gave a value for the error between the model and the SAED which could be used as a figure of merit for the unit cell model. Repeating the process for the best fit between all 3 indexed unit cell models (deduced by Dicvol from the PXD data), allowed the unit cell solutions to be quantitatively compared and the best structure chosen. The advantage of this method over using a calibration diffraction pattern is that the exact calibration of the diffractometer will drift minutely over short time periods. The only thing that is truly constant is the ratio of distances within a single diffraction pattern. This method therefore does not rely on calculations that may have associated systematic errors.

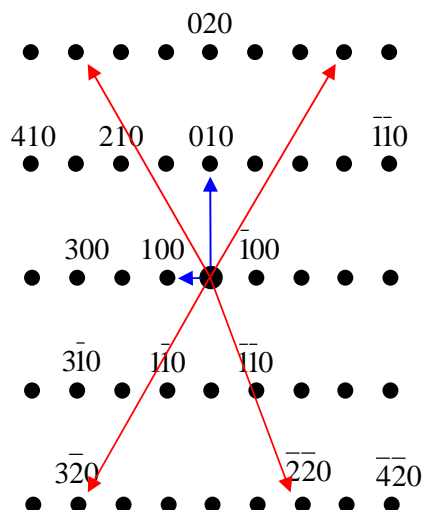


Figure 4.12: Schematic explaining how the SAED patterns were used to choose between the unit cell solutions from the PXD data towards the structure of the TaS₃ nanofibres.

The indexed unit cells showed a clear preference for the structure that has previously been referred to as m_i -TaS₃. The collective error over 40 measurements and 4 different SAED patterns was 0.04 Å. The other structures had a collective error over the same 40 spot measurements in the range 1.4 Å to 0.09 Å indicating that m_i -TaS₃ was indeed the best fit. m -TaS₃ was the next best fit with a collective error across the 40 spot measurements of 0.09 Å.

The diffraction pattern accompanying the image in Figure 4.11 shows spots in the 010 and 001 plane from the indexed monoclinic unit cell, m_i -TaS₃. Crucially the spacing of the diffraction spots is in no way relatable to the orthorhombic structure, adding weight to the earlier argument that the structure of the nanofibres was different to both that of the residual powders and the nanobelts found by Wu *et al.*⁵⁹

High resolution TEM imaging shows lattice fringes (Figure 4.13(a)) that can be measured to yield d-spacings ~9.9 Å, which is comparable to the 001 spacing of the m_i -TaS₃ unit cell. The nanowires had a high tendency to split along the direction of the lattice fringes (Figure 4.13(b)) indicating a cooperative growth mechanism which creates longitudinal weaknesses as the layered structure forms, one layer on top of the other. The splitting of the nanowires along the long axis of the wires and indeed the direction of the fringes in the high

resolution TEM (Figure 4.13(a)) suggests the wires have the 001 direction perpendicular to that of the long axis of the wire. As the angle between the $h00$ and $00l$ (β angle) is not 90° in the m_i -TaS₃ structure, it is possible to conclude that the long axis of the wire propagates either along the $0k0$ direction or at an angle to all three zone axes. The high-resolution TEM images also suggest that the fibres are solid with a flat cross section, indicating belts or ribbons (Section 1.1.3). These fibres are therefore probably not formed by the rolling of sheets as is often the case in pseudo-graphitic materials.

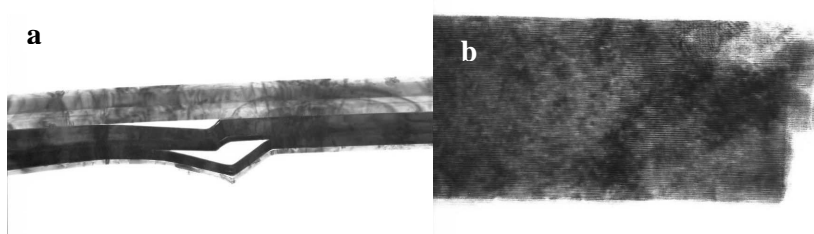


Figure 4.13: TEM images of TaS₃ nanowires showing (a) the high tendency of the wires to split along lattice fringes and (b) a high-resolution TEM image showing the lattice fringes at $\sim 9.9\text{\AA}$.

Two different zone axis SAED diffraction patterns are observed depending on the orientation of the nanobelts. The two different zone axis patterns show pairs of spacings corresponding to the 001 and the 010 axes at right angles in one and the 100 and 010 axes again at right angles in the other with respect to the m_i -TaS₃ structure. As both the zone axes show up the 010 direction, it follows that this direction is common to both planes within the nanofibres and therefore the direction of propagation of the crystal structure along the long axis of the nanofibre. The pictorial alignment of the nanofibre and diffraction pattern in Figure 4.11 also specifically shows the 010 direction is in line with the long axis of the fibre, (90° rotation between image and corresponding diffraction pattern Section 2.4.3.2).

The evidence above and the fringe spacing measurements suggest that the fibres propagate along the $0k0$ direction of the monoclinic structure which coincided with the direction in which the chains of tantalum atoms run through both the m -TaS₃ and m_{hp} -TaS₃ structures (Figure 4.1). Nanoribbons of the analogous NbSe₃ material were found by Hor *et*

al. to also propagate along the *b* direction of the unit cell with the 1-dimensional chains of atoms aligned with the length of the ribbons.⁵⁵ TiS_3 nanobelts, another stoichiometrically analogous system, have been seen with the 010 direction aligned parallel to the long axis of the nanobelts as well.¹⁰² The same concept has been seen in another low dimensional material that forms nanofibres Nb_3Te_4 .¹⁹³ However, in this case, the structure is hexagonal not monoclinic and the chains of metal atoms propagate parallel to the *c* axis rather than the *b* axis of the unit cell. The fibres are still crystallographically aligned so that the chains propagate down the lengths of the fibres. It is therefore not unprecedented for there to be crystallographic texture directed towards the chains of tantalum atoms that lead to the low dimensional properties in the bulk TaS_3 . The crystal structure remains ambiguous as refinement has been unsuccessful.

Although the crystal structure of $\text{m}_1\text{-TaS}_3$ is unknown it is likely to be similar to the other two known structures both of which have the same space group and therefore could possibly exhibit 1-dimensional electrical conductivity along their lengths, as a result of the crystal structure alignment. This possibility was investigated using AFM.

4.3.1.2.4 Electrical Measurements, Atomic Force Microscopy

The AFM work was carried out in collaboration with Prof. P. Moriarty and Mr. A. Stannard at the University of Nottingham to see if electrical conductance along the lengths of the nanofibres could be proven, following the indexing of the SAED patterns and the suggestion that the belts should conduct as a result of the crystal structure alignment within the nanowire crystallography.

Images of the surface of the silicon and the nanowires that were present after spin coating were obtained, as shown in Figure 4.14. The nanowires are seen to be $\sim 1\text{ }\mu\text{m}$ in diameter and longer than the $90\text{ }\mu\text{m}$ that the AFM can measure. The cross section of the nanofibres can be seen by a 3D plot of the AFM images and are seen to be either round or flat depending on the wire, with heights $\sim 200\text{-}300\text{ nm}$ in agreement with the TEM data presented.

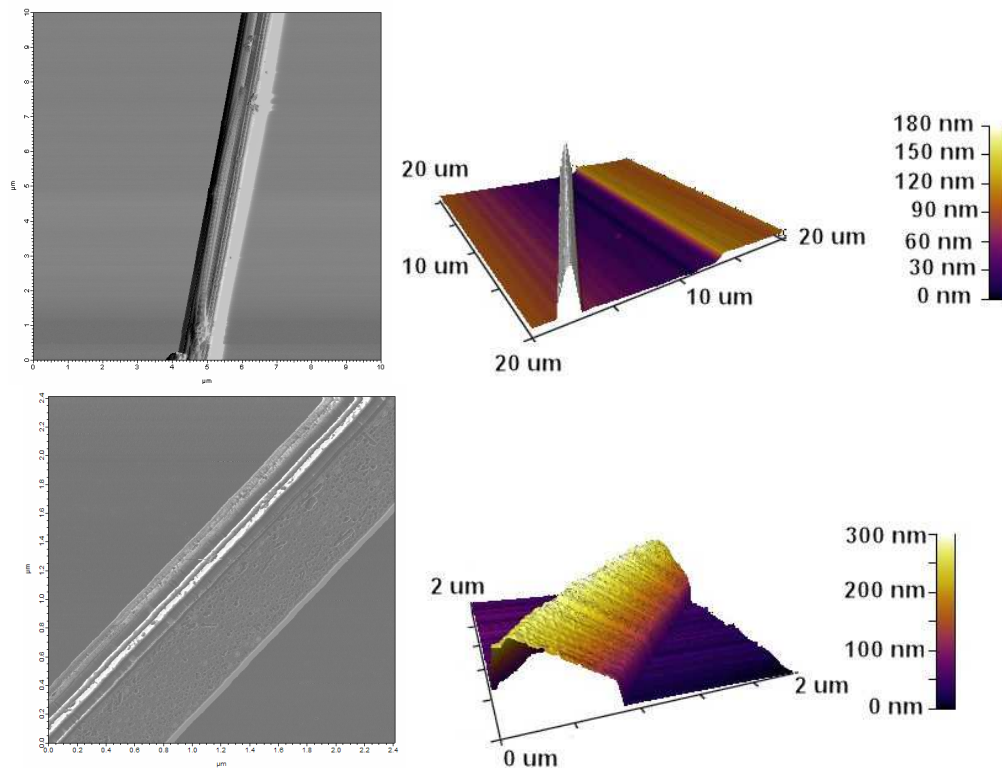


Figure 4.14: AFM images and 3D plots of TaS₃ nanowires on a SiO₂ surface.

Initial results for the electrical measurements showed that the nanowires were indeed conducting. Figure 4.15 shows a single TaS₃ nanowire, attached at one end to the gold electrode and crossing the SiO₂ surface. The current / time and voltage / time curves (Figure 4.15(b) and (c)) show 2 distinctly different responses. The first is that seen when the AFM tip is positioned for the measurement over the gold surface (Position 1). Here the current changes with time such that it mirrors the voltage change, indicating Ohmic behaviour (Ohms law is obeyed). The second is from the positioning of the AFM tip over the SiO₂ surface, (Position 3). The trace now looks just like background noise as the scales on the IV traces are different. In the trace on the left the scale is in nano-amps and on the right picoamps so there are 3 orders in magnitude difference between the two. The response from Position 2 on the diagram is identical to that of the response from Position 1, clearly indicating that the nanofibre is conducting along its length.

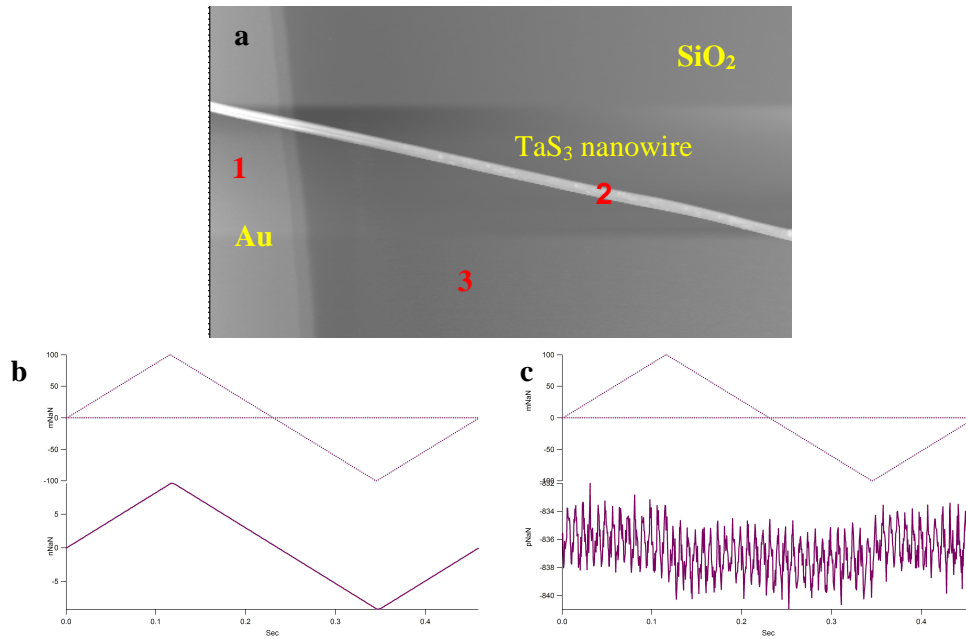


Figure 4.15: (a) Single TaS₃ nanowire connected to a gold electrode and the positions of the AFM IV curve measurements; (b) the IV trace from position 1 and 3 showing the potential vs. time and current vs. time plots that mirror each other and (c) IV trace showing the potential vs. time and current vs. time plots that show only background noise from position 3.

Ohm's law was utilised to calculate the resistance for the system as shown in Equation (4.1), giving a value of $\sim 10 \text{ M}\Omega$.

$$\frac{100\mu\text{V}}{10\text{nA}} = 10\text{M}\Omega \quad (4.1)$$

This was however the resistance of the resistor in series with the nanowires to prevent damage to the AFM from high currents. Removing the resistor yielded poor results as the contact resistance between the wire and the gold and the wire and the AFM tip was greater than the resistance of the wire over the short distance being measured $\sim \text{n}\Omega$.

TaS₃ in the bulk has a resistivity of $3 \times 10^{-4} \Omega\text{cm}$ at room temperature and experiences a metal-semiconductor transition at 270 K as a result of Peierls distortion.¹³⁶ The comparison of this measurement in the nanomorphology would have been of interest. The evidence above suggests that the nanofibres do indeed conduct electricity, and do so with low resistance.

The exact resistance of the nanowires cannot be calculated in this way. However over a distance of 100 nm a wire / crystal with cross sectional area 100 nm x 100 nm should have a resistance of $\sim 3 \times 10^{-5} \Omega$ (Calculated from the resistivity of the bulk material using Equation (4.2)).

$$\rho = \frac{RA}{\ell} \quad (4.2)$$

ρ = Resistivity

R = Resistance

A = Cross sectional area

ℓ = Length

A reliable alternative method of measuring the resistance of the nanowires is needed but equipment and time constraints have prevented such experiments from being carried out during the course of this project. The method used by Hor *et al.* to measure the charge-density-waves in the NbSe₃ system has been shown to yield accurate results. At the end of the project collaborations with the Electronic and Electrical Engineering department and the James Watt Nanofabrication Centre at the University of Glasgow were beginning.

The idea develops on the methods used at Nottingham and discussed above but the intention would be to spin coat the nanowires onto a insulating surface containing small square gold markers laid out in a grid of side ~ 3 mm in length. The grid of gold markers could be used to electronically map the surface allowing the position of nanowires to be reproducibly calculated. A removable insulating polymer would be applied to the surface on top of the nanowires to protect them and e-beam lithography used to cut channels into the polymer to be filled with gold, forming the electrodes. Finally the polymer could be removed and the measurements taken on a micro probing station. The advantages of this method are that the contacts will be placed over the nanowire rather than under them giving a much more secure fixing. Also 4 or indeed 5 terminal measurements can be use so as to avoid the measurement of contact resistance. Figure 4.16 shows a possible setup for the electrical

measurements on the probing station. The potential difference is applied through electrodes 1 and 2 with the flowing current measured across electrodes 3, 4 and 5. The distances between 3 and 4, 3 and 5 and indeed 4 and 5 should allow the accurate calculation of the resistivity of the nanowire from Ohm's Law and the equation of resistivity, Equation (4.2) the cross sectional area can be estimated by TEM.

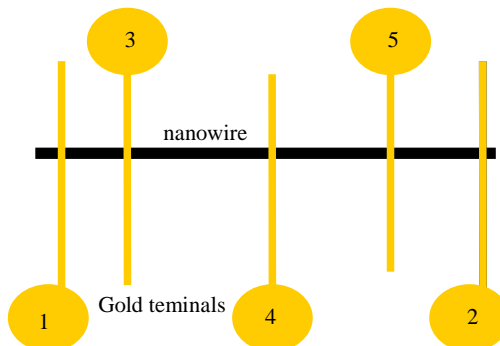


Figure 4.16: Schematic showing a 5 electrode measurement setup for the resistivity measurement on a single nanowire.

Conducting nanofibres have application in all fields of nano electronics as connecting wires with a 1-dimensional aspect to the conduction a serious advantage. Should these wires exhibit the low dimensional properties of the bulk and conduct significantly better along their lengths than across their widths then obvious advantages can be postulated. In macro scale electronics a 3-dimensional conductor (copper) is coated with insulating plastic to form what is essentially a 1-dimensional conductor to prevent shorting should wires cross, but the challenge associated with achieving this on the nanoscale are large. A 1-dimensional, (self insulating) conductor on the nanoscale would therefore be tantalising.

4.3.2 Effects of Temperature on Nanowire Formation

4.3.2.1 High Temperature Preparations

The ampoules from **TaS₃1100** showed no nanowire formation and a crystalline gold coloured powder with residual sulfur on the sides of the ampoule. The gold coloured crystals were

characteristic and suggestive of 1T-TaS₂ and were confirmed as such by PXD. The peaks were indexed to a hexagonal unit cell with cell parameters as shown in Table 4.3. The calculated cell parameters are in good agreement with those from 1T-TaS₂.

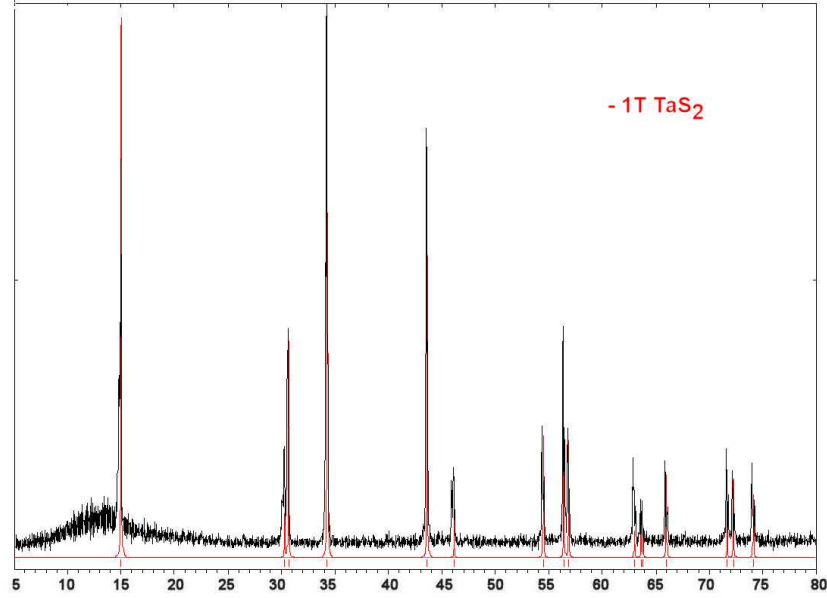


Figure 4.17: PXD analysis showing the match between the products of **TaS₃1100** and 1T-TaS₂. (D5000)

Phase	<i>a</i>	<i>c</i>
TaS₂1100_Std	3.371(4) Å	5.9032(4) Å
1T-TaS ₂	3.3649 Å	5.8971 Å

Table 4.3: Unit cell parameters from the indexed powder patterns of preparation **TaS₃1100** compared to the published values for 1T-TaS₂.¹¹²

This indicates that TaS₃ is unstable at high temperature in the bulk phase and decomposes to give 1T-TaS₂ (the high temperature phase of TaS₂) and sulfur. TaS₃ is known to decompose when heated under high vacuum ($\sim 10^{-7}$ Torr) at 650 °C into TaS₂ and sulfur so this is not surprising.¹²⁸ Wu *et al.*'s paper shows that the upper limit under 10^{-2} pa, (8×10^{-5} Torr) for TaS₃ to exist is less than 850 °C as at this temperature TaS₃ nanobelts were converted into TaS₂ nanobelts.⁵⁹

SEM showed smooth flat crystals as would be expected for the 1T polytype of TaS₂ and similar to those seen in the **TaS₂1100** reactions. The disk-like particles are 10-50 μm in

diameter and 5-10 μm thick. EDX shows an average ratio of 33:67, Ta:S, (± 2), indicating TaS_2 .

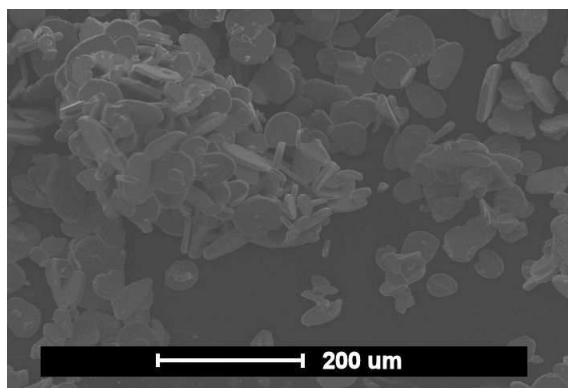


Figure 4.18: SEM micrograph showing the general morphology of products from **TaS₃1100**, (SEM #2).

4.3.2.2 Preparation TaS₃750

No fibrous material was observed in Region III and III' of the ampoules which contained a residual powder in Region I and I' of the ampoules. The residual powder was more crystalline and gold like in appearance than observed in the lower temperature preparations. In Region II and II', black crystals were observed along with large silver plate-like structures. These silver platelets grew off the walls of the ampoule anchored by a single vertex.

PXD of the residual powder shows peaks that match to both those expected for 1T- TaS_2 and 3R- TaS_2 , (Figure 4.19). The peaks associated with the 1T polytype were indexed to give unit cell parameters as shown in Table 4.4. These values match those of the 1T-polytype of TaS_2 .

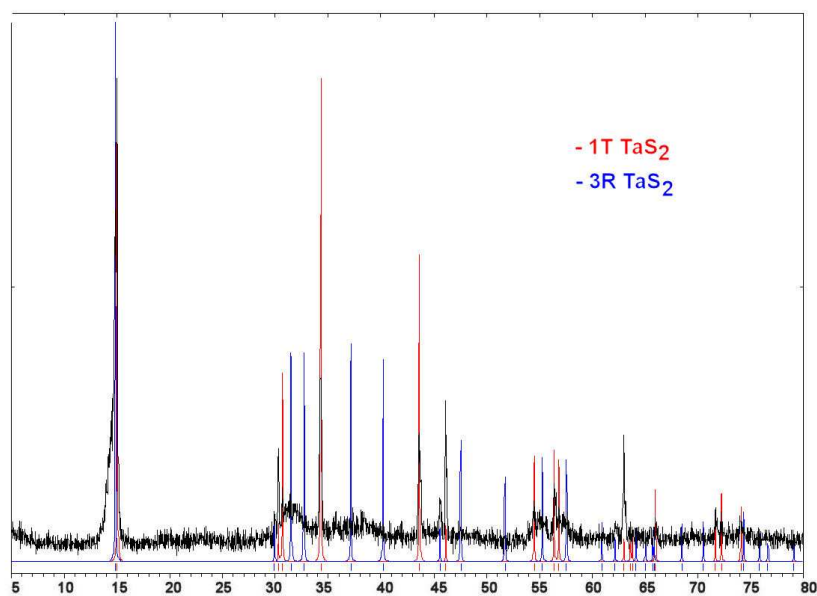


Figure 4.19: PXD pattern for **TaS₃750** showing a match to both 1T-TaS₂ and 3R-TaS₂.

Phase	<i>a</i>	<i>c</i>
TaS₃900	3.360(8) Å	5.8990(8) Å
1T-TaS ₂	3.3649 Å	5.8971 Å

Table 4.4: Unit cell parameters from the indexed powder patterns from **TaS₃750**, compared to the published values for 1T-TaS₂.¹¹²

SEM of the residual powders showed flat platelets as single particles of diameter between 20 and 100 μm and thickness in the range of 5 – 25 μm . These particles are different from those experienced in the higher temperature preparations as they are less smooth and clean and thicker. EDX still gives a ratio of 33: 67, Ta:S, (± 2).

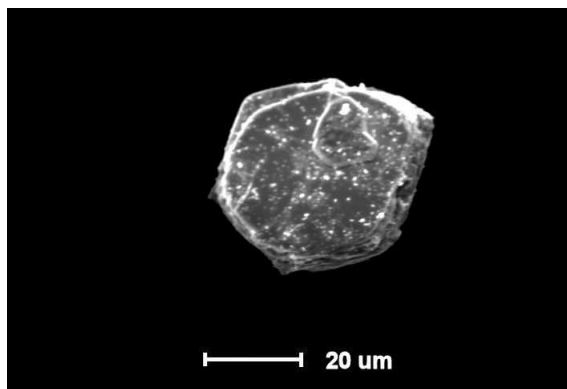


Figure 4.20: SEM micrograph of a particle from the residual powders from **TaS₃750**. (SEM #2)

The silver plate-like, structures were approximately 2.5 mm in length, hexagonal in shape and ~ 8-10 μm thick (Figure 4.21), EDX showed them to have ~ 1:2 ratio of Ta:S, (36:64, ± 2) indicating TaS_2 . In an attempt to determine the crystal structure of the silver platelets, they were submitted for single crystal X-ray analysis and found to be polycrystalline. All the crystallites were noted as being TaS_2 but polytypic analysis has been unsuccessful, though it was suggested that the structure was either the 2H or 1T polymorph, though being silver in colour are unlikely to be the 1T polymorph as this should be golden.

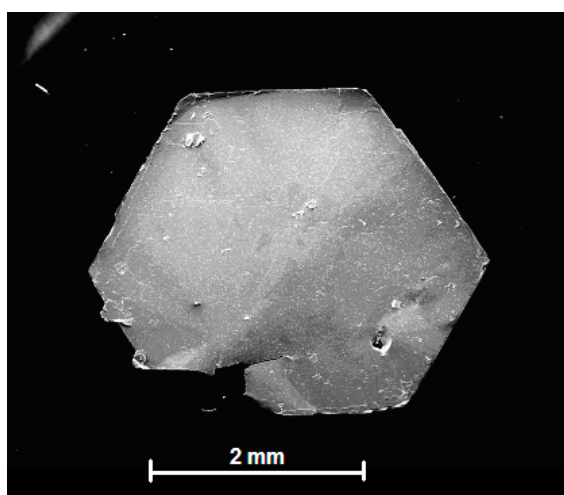


Figure 4.21: Hexagonal plate-like structure of TaS_2 from preparations **TaS₃750**, (SEM #4).

4.3.2.3 Low Temperature Preparations

4.3.2.3.1 Preparation TaS₃500_SAG

Upon removal from the furnace there was a residual powder in Region I' and a large yield of nanofibres noticed in Region III' with a similar consistency to those from **TaS₃650_SAG**. The PXD for the residual powder matched that of the o- TaS_3 polytype as discussed in **TaS₃650_SAG**. The PXD of the nanofibres utilising a carbon tab showed the m_i- TaS_3 . The PXD of the nanowires is shown in Figure 4.22 the powder pattern is shown matched to a

theoretical powder pattern generated from the m_i -TaS₃ unit cell. The discrepancy between the peak heights is due to the unrefined atom positions within the model of m_i -TaS₃.

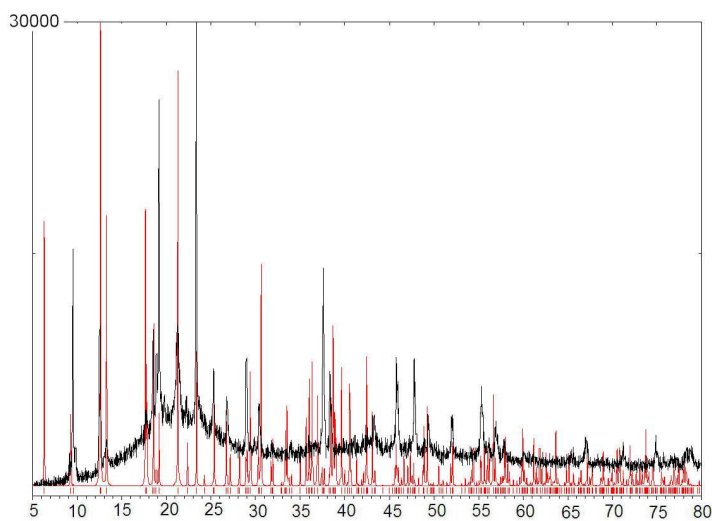


Figure 4.22: PXD data for the preparation **TaS₃500_SAG**, (D5000 diffractometer and a carbon tab).

The formation of nanostructures of TaS₃ is favoured by the lower temperatures as was noted in the TaS₂ nanofibre productions where at high temperature (**TaS₂1100**) the yields tended to zero and at low temperatures the fibres became ribbons of TaS₃, (**TaS₂500**). The yields were optimised at 650 °C for TaS₂; however, with TaS₃ a higher yield of formation occurs at 500 °C. At lower temperatures the fibrous yield falls again and the residual powders begin to contain much starting material. If the desired product is TaS₃ the optimum temperature is therefore 500 °C which is comparable to work achieved by Srivastava and Avasthi where it was found that single crystal formation of TaS₃ is best achieved at 500 – 550 °C using S₂Cl₂ as a transport agent in the presence of some excess sulfur.¹²⁸

SEM micrographs were taken of the nanowires which show fibrous masses of ribbons and belts that form together in bales and mats, similar to those seen in **TaS₃650_SAG**. The fibres are observed as multi-filament with very fine fibres making up the larger bundles. Aspect ratios outside of the clumps which appear to have broken off the foil surface are still

~20,000 with similar dimensions to those observed in **TaS₃650_SAG**, i.e. lengths in excess of 4 mm and widths up to 200 nm.

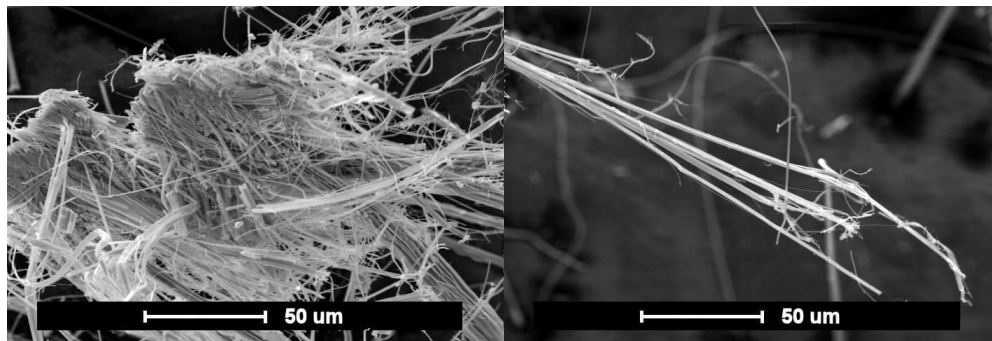


Figure 4.23: SEM micrographs of **TaS₃500_SAG**, (SEM#4)

Closer inspection of the foil surface showed the nanofibres growing off the surface in random directions. Growth is therefore nucleating on the surface and the crystal structure propagating in its preferred direction from the surface, (Figure 4.24(a)). In Figure 4.24(b), the surface is magnified showing that the TaS₃ nanofibres are not in fact growing directly from the tantalum surface but from a TaS₂ layer that is coating the Ta surface ~ 5 μm thick. A number of EDX measurements were taken with Figure 4.24(c) and the ratio of Ta:S calculated for different areas of the image and shows that the TaS₃ nanofibres are growing parallel to the TaS₂ surface and then curling upwards away from the surface to form the fibrous material observed (Figure 4.24(c)).

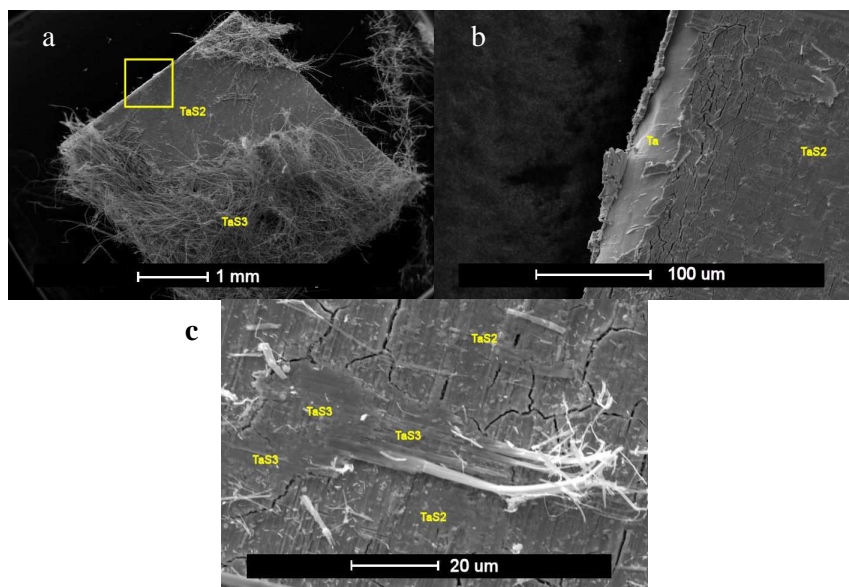


Figure 4.24: SEM micrographs showing; (a) the formation of TaS₃ nanofibres on a TaS₂ surface coating from preparation **TaS₃500_SAG** and (b) a close up of the surface from which the nanofibres are growing and (c) Nanofibres peeling back off the surface with spots measured by EDX with the ratio of Ta:S given, (SEM #4).

4.3.3 Conclusions

The crystal structure of the nanowires formed in **TaS₃650_Std** and **TaS₃650_SAG** were found to be monoclinic and indexed to a unit cell with space group $P12_1/m1$ and cell parameters $a = 9.966(1) \text{ \AA}$, $b = 3.4698(1) \text{ \AA}$ and $c = 14.631(3) \text{ \AA}$ and $\beta = 106.49(1)^\circ$ (m_i -TaS₃), in contrast to the o -TaS₃ structure nanobelts found by Wu *et al.*⁵⁹ The growth of the nanowires was noted as the direction of the shortest unit cell parameter which has been observed by other researchers working on other inorganic nanofibrous systems.^{55, 72, 152, 160, 193} Most notable in the context of this work is the formation of NbSe₃ nanowires and ribbons with a similar unit cell and space group to the m_i -TaS₃ structure discussed above.^{55, 164} These are also found to have the crystallographic b direction aligned to the long axis of the wire,⁵⁵ as are TiS₃ nanobelts.¹⁰² There is no mention of the crystal alignment within the nanobelts of TaS₃ by Wu.⁵⁹ Perhaps more importantly in these 1-dimensional materials is the concept that the crystal structure alignment corresponds with the direction of propagation of the chains of metal atoms rather than that the shortest unit cell parameter. Indeed it has been noted in

Nb₃Te₄ that the direction of propagation of the nanofibre also corresponds with the direction of the chains of metal atoms in a hexagonal system,¹⁹³ though again this could be down to preferential growth along the shortest unit cell parameter.

Unfortunately unlike the analogous systems, NbSe₃^{55, 164} and TiS₃,¹⁰² there is significant differences in crystal structure of the nanofibrous and bulk morphologies. Refinement of the nanofibre PXD data has been unsuccessful.

Early electrical measurements have been carried out and indicate that the fibres do indeed conduct electricity however 4-terminal measurements are needed to obtain a value for the resistance of the nanofibres.

Chapter 5: Tantalum Nitride and Tantalum Oxide

Nanofibres

5.1 Introduction

In this chapter, the potential for converting the sulfide nanofibres produced in Chapter 3 into other functional materials is investigated. The motivation behind this work was firstly to see if indeed it was possible to obtain a high level of morphological control over the desired products via the systematic control of the initial starting materials and secondly to set a precedent for the formation of otherwise unknown nanometric materials.

Tantalum nitride and tantalum oxide, although very different from the sulfide phases are highly desirable as they have potential use as photocatalysts and pigments.^{140, 146, 147, 216} Tantalum nitride nanofibres are as yet unknown while tantalum oxide nanofibres have been seen, either in a complicated hydrothermal synthesis that produced helical nanowire like structures³⁴ or in a very low yield of nanotubes produced by scrolling precursor sheets.¹⁷⁷ A simple preparation of both these phases from readily accessible sulfides with explicit control over morphology is therefore highly desirable. Figure 5.1 shows a schematic of the potential reactions that could allow for the inter-conversion of three independent and unique nanofibrous phases, investigated in this chapter.

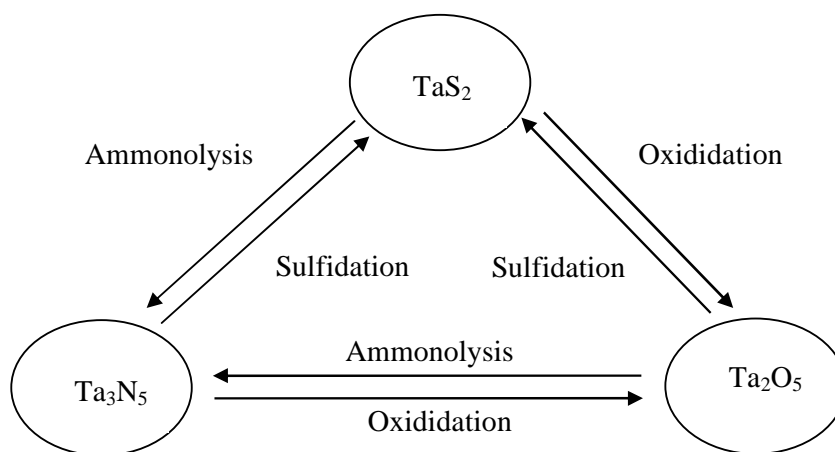


Figure 5.1: Schematic of the proposed reactions for pseudomorphic transformation and inter-conversion of three nanometric phases.

5.1.1 Precedent for Reversible Pseudomorphic Reactions

There are currently many methodologies for the formation of nanofibres, these include:

- i) Chemical reactions from elemental powders,^{59, 163} and seen in Chapters 3 and 4.
- ii) Chemical reaction from precursors, decompositions, reductions or reactions.^{41, 43, 50, 59, 152, 160}
- iii) Solvothermal methods.^{34, 156}
- iv) Mechanical methods.^{152, 159}
- v) Templating reactions.^{56, 75, 161, 165, 176}

All of these methods, with the exception of templating, utilise reaction conditions to obtain morphological control over the products and in many cases have limited control, i.e. only one type of morphology is possible.

So far, in the literature there are very few examples of preparations involving the conversion of, one nanofibrous phase into another, utilising simple solid-gas exchange reactions, though recently they have begun to appear more readily.^{68, 176} The pseudomorphic reactions discussed herein, offer a new direction in nanometric materials production, where, in theory, unprecedented control over morphology can be achieved by controlling the

morphology of the initial precursor without the need for a step where a templating agent is removed.

The concept of inter-conversion between sulfide, oxide and nitride phases in the bulk, utilising the three reactions suggested in Figure 5.1 have been widely applied and researched extensively for many decades, i.e. nitrides are commonly prepared by reacting oxide precursors with ammonia, sulfides by reacting oxide precursors with CS₂ and oxides by reacting many species, though rarely sulfides and nitrides, with oxygen.

Little, however, has yet been achieved on the study of the morphology of the products with respect to the reactant precursors in these types of exchange reactions, with very few papers concerned with the formation of nanoscale materials. Some of the more relevant examples are given here.

5.1.1.1 Solid-Gas Exchange Reaction Involving Nanometric Phases

Perhaps the most significant example, when trying to set a precedent for these types of reaction, was the conversion of TiO₂ micro-fibres into TiN micro-fibres back in 1987²¹⁷ using ammonia, again maintaining the morphology of the precursor. Surprisingly this was before the discovery of the first carbon nanotubes in 1991 by Iijima⁷ and would have suffered from predating many of the recent advances in electron microscopy that allow readily available characterisation of modern day nanomaterials.

Thin films of TiO₂ have been successfully reacted with ammonia to form TiN without significant disruption to the thin film.²¹⁸ Zhu, *et al.*, investigated the formation of tungsten oxy-nitride nanowires from tungsten oxide nanowires using ammonia, without significant loss of morphology.⁶⁸

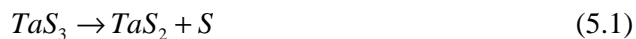
Henderson and Hector have described how Ta₃N₅ nanoparticles could be prepared from Ta₂O₅ powders at 950 °C in 4 hours using ammonia.²¹⁹ Lu *et al.* showed that by lowering the temperature to 850 °C and extending the reaction time to 15 hours a similar Ta₃N₅ product could be obtained from the same oxide precursor in a pseudomorphic

ammonolysis reaction.²²⁰ Ta_3N_5 thin films have been prepared from the ammonolysis of Ta_2O_5 thin films with little disruption to the morphology.²²¹

Cottam and Shaffer have shown the production of TiO_2 nanorods / nanowires from the oxidation of similar morphology TiC structures.¹⁷⁶ In this multi-step synthesis, easily produced CNT were reacted with $TiCl_4$ to form titanium carbide nanowires before being oxidised to form TiO_2 nanotubes.

In Section 1.9 of this thesis it was noted that many of the methods of formation for disulfide nanofibres, such as WS_2 and MoS_2 involve the sulfidation of oxide precursors using H_2S . e.g. WS_2 nanotubes were synthesised by Tenne *et al.* by the sulfidation of tungsten sub-oxide structures, produced in a fluidised bed reactor^{149,153} or produced by chemical methods as nanowhiskers.¹⁵⁴ Kroto and Zhu also have produced WS_2 nanotubes from the sulfidation of $WO_{2.7}$ nanorods, again using H_2S .¹⁰³ Although these reactions do not specifically involve pseudomorphic change, they do set a precedent in that they successfully interconvert between two phases, oxide and sulfide, with a general trend of forming nanotubes and relatively little alteration of morphology.

It has been shown that nanofibres of TaS_3 , in the form of nanobelts, can be converted into TaS_2 with little change to their morphology by a thermolysis reaction.⁵⁹ Although this reaction is not a sulfidation, there is a change in sulfur content without a significant change in morphology. The sulfur was removed from the lattice across a 100 °C temperature gradient from 850 °C under vacuum, where the stability of the disulfide exceeds that of the trisulfide and the decomposition reaction occurs as shown in Equation (5.1).



5.2 Experimental

5.2.1 Synthesis

There are three main reactions of concern to this chapter, all of which are similar to each other but very different to the reactions utilised in the previous chapters of this thesis. The experimental setups are outlined in the Section 2.3.2 with specific details given in this section.

Some of the following preparations require products from previously discussed preparations leading to issues with the intricate comparison of morphology. At the time of these experiments, many of the initial nanofibre preparations were still producing a range of products and the proportions of these different products did change with batch. Yields were too small to allow uniform use of a single batch of nanoprecursor for all of the following reactions so some alteration of morphology may be due to the different batches of nanowires used as precursors.

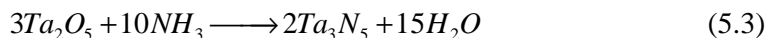
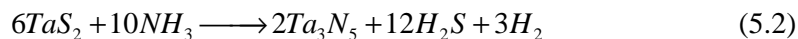
Due to the large number of different but similar preparations discussed in this section, the different preparations will be labelled for reference. A labelling method has been devised as follows.

(Precursor)-(Product)(Temperature)(nano/bulk)_(Time)

The initial letters, “S”, “N” or “O” indicate the precursor and product phases; “Sulfide”, “Nitride” or “Oxide” respectively. The number that follows represents the sintering temperature in °C and the final letter is either “b” to indicate that the *precursor* was of “bulk” origin or “n” indicating that the *precursor* was of “nanofibrous” origin. Finally, the sintering time in hours is given after the underscore. E.g. the preparation of nitride nanofibres from a sulfide nanofibrous precursor at 950 °C over a period of 4 hours carries the label “S-N950n_4h.” In a few cases where an extra notation is needed to indicate the specific starting phase these will be denoted as a second underscore and “a,b,c” etc. and the information given accordingly in the tables within the preparation sections.

5.2.1.1 Preparations by Ammonolysis Reactions

The preparations utilising the ammonolysis reaction should follow Equation (5.2) and Equation (5.3) depending on the initial precursor.



In order to balance Equation (5.2), we have to accept the loss of residual hydrogen.

These preparations were initially designed to see at which temperatures the ammonolysis reaction was possible under the experimental set up available and described in Section 2.3.2.1. Henderson and Hector have shown how Ta_3N_5 bulk powders can be prepared from Ta_2O_5 powders at 950 °C in 4 hours using ammonia.²¹⁹ Lu *et al.* showed that by lowering the temperature to 850 °C and extending the time to 15 hours a similar bulk product would be obtained in a transformation that was described as pseudomorphic from a bulk powdered precursor.²²⁰ Further, Zhang and Gao showed that a nano-precursor allowed the sintering temperature to be lowered, obtaining single crystals at 700 °C within 5 hours using a nanometric precursor.¹⁴¹ With this in mind, the initial preparation, **S-N950b_4h** was carried out at 950 °C and for 4 hours.

5.2.1.1.1 Preparations of Bulk Ta_3N_5

TaS_2 powders or Ta_2O_5 powder (99% Ta_2O_5 , Aldrich) were placed in an alumina boat and inserted into the tube furnace with the experimental setup shown in Section 2.3.2.1. The TaS_2 powder was the residual powders from the sulfide nanowire preparations (Section 3.3.1 and 3.3.2) and characterised as discussed in Section 3.3.1.1 and 3.3.2.1. In both preparations, ~1 g of starting material was used. In the case of the sulfide precursor, the work tube was purged with nitrogen for up to an hour to prevent pre-oxidation of the precursor prior to ammonolysis. The furnace was heated to the desired sintering temperature of 950 °C for 4

hours prior to cooling under the continuous flow of NH_3 (3 lmin^{-1} , BOC 99%). The experimental time and temperature variables are given in Table 5.1.

The TaS_2 used as a precursor in reaction **S-N950b_4h** was easily formed in large quantities and has been well characterised yielding a good comparison for the use of this reaction in pseudomorphic transformations.

Preparations Label	Sintering Temperature ($^{\circ}\text{C}$)	Sintering Time (hours)	Precursor
S-N950b_4h	950	4	TaS₂650
O-N950b_4h	950	4	Commercial Ta_2O_5

Table 5.1: Table showing the experimental parameters for the preparations of tantalum nitride from bulk precursors.

5.2.1.1.2 Preparations of Nanofibrous Ta_3N_5

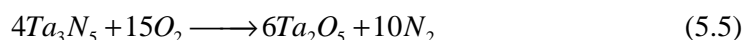
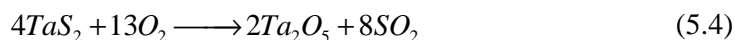
TaS_2 nanofibres prepared as discussed in Section 3.3.2 (**TaS₂650_SAG**) or Ta_2O_5 nanofibres as prepared in Section 5.2.1.2 were placed in an alumina boat inside a tube furnace with the experimental setup shown in Section 2.3.2.1. Nanofibrous yields from other reactions were fairly limited so only small amounts of nanofibrous precursor (~ 20 to 30 mg) were used in these preparations. In the case of the sulfide nanofibres, the work tube was purged with nitrogen for up to an hour to prevent pre-oxidation of the nanowires prior to ammonolysis. The furnace was set to heat to the desired temperature for the desired length of time prior to cooling under the continuous flow of NH_3 (0.3 lmin^{-1} BOC 99%). The preparation labels and variables are given in Table 5.2.

Preparation Label	Sintering Temperature ($^{\circ}\text{C}$)	Sintering Time (hours)	Precursor
S-N950n_4h	950	4	TaS₂650_SAG
S-N800n_4h	800	4	TaS₂650_SAG
S-N650n_4h	650	4	TaS₂650_SAG
O-N950n_4h	950	4	S-O800n_4h

Table 5.2: Table showing the experimental parameters for preparations of tantalum nitride from nanofibrous precursors.

5.2.1.2 Preparations by Oxidation Reactions

The preparations utilising the oxidation reaction should follow Equation (5.4) and Equation (5.5) depending on the initial precursor.



Equation (5.5), was proposed by Zhang and Gao.²¹⁶

5.2.1.2.1 Preparations of Bulk Ta₂O₅

TaS₂ powders, (prepared, Section 3.2.1.1 and discussed Section 3.3.1.1) or Ta₃N₅ powder, ((S-N950b_4h), prepared Section 5.2.1.1.1 and discussed Section 5.3.1.1) were placed in an alumina boat inside a tube furnace with the experimental setup shown in Section 2.3.2.3. In both sets of preparations, ~ 1 g of starting material was used. The furnace was set to heat to a desired temperature for set period of time, prior to cooling under the continuous flow of O₂, (BOC 99.9%), the flow rate was controlled by a cylinder regulator and set to a few bubbles per second through a paraffin oil bubbler. The preparation label and variables are given in Table 5.3.

Preparation Label	Sintering Temperature (°C)	Sintering Time (hours)	Precursor
S-O800b_4h	800	4	TaS₂650
S-O400b_4h	400	4	TaS₂650
S-O400b_16h	400	16	TaS₂650
N-O800b_4h	800	4	S-N950b_4h
N-O400b_4h	400	4	S-N950b_4h

Table 5.3: Table showing the experimental parameters for the preparations of tantalum oxide from bulk precursors.

5.2.1.2.2 Preparations of Nanofibrous Ta₂O₅

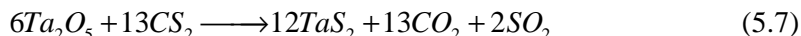
TaS₂ nanofibres prepared as discussed in Section 3.3.1 or Ta₃N₅ nanofibres as prepared in Section 5.2.1.1 were placed in an alumina boat inside a tube furnace with the experimental setup as shown in Section 2.3.2.3. Nanofibrous yields from other reactions were limited so ~ 20 to 30 mg was used in these preparations. The furnace was set to heat to the desired temperature for periods of 4 hours prior to cooling under a continuous flow of O₂, (BOC 99.9%). The flow rate was controlled by a cylinder regulator and set to a few bubbles per second through the paraffin oil bubbler. The preparation labels and variables are given in Table 5.4.

Preparation Label	Sintering Temperature (°C)	Sintering Time (hours)	Precursor
S-O800n_4h	800	4	TaS₂650
S-O400n_4h	400	4	TaS₂650
N-O800n_4h	800	4	S-N950n_4h
N-O400n_4h	400	4	S-N950n_4h

Table 5.4: Table showing the experimental parameters for the preparations of tantalum oxide from nanofibrous precursors.

5.2.1.3 Sulfidation Reactions

The preparations utilising the reaction with CS₂ should follow Equation (5.6) and Equation (5.7) depending on the initial precursor.



It is likely from Equation (5.6) that the reaction of CS₂ with Ta₃N₅ produces thiocyanate species and residual carbon and sulfur, though it is also possible to form other species such as C₂S₂²⁻.

5.2.1.3.1 Preparations of Bulk TaS₂

Ta₃N₅ powder as prepared in the high temperature reactions (**S-N950b_4h**) from Section 5.2.1.1.1 or Ta₂O₅ powder (99% Ta₂O₅ Aldrich) were placed in an alumina boat and inserted into the experimental setup as shown in Section 2.3.2.2. The furnace was set to heat to temperature for periods of time, prior to cooling under the continuous flow of CS₂/Ar (99% CS₂, Fisher Scientific, laboratory grade, 99.9% Ar from BOC gasses) the flow rate was controlled by the argon flow and set as a few bubbles per second through a paraffin oil bubbler. The preparation labels and variables are given in Table 5.5.

Preparation Label	Sintering Temperature (°C)	Sintering Time (hours)	Precursor
O-S850b_4h	850	4	Commercial oxide
N-S850b_4h	850	4	S-N950b_4h
O-S1000b_14h	1000	14	Commercial oxide

Table 5.5: Table showing the experimental parameters for the preparations of tantalum sulfide from bulk precursors.

5.2.1.3.2 Nanofibre Preparations of TaS₂

Ta₃N₅ nanofibres (as prepared in Section 5.2.1.1) and Ta₂O₅ nanofibres, (as prepared in Section 5.2.1.2) were placed in an alumina boat and inserted into the experimental setup as shown in Section 2.3.2.2. The furnace was set to heat to the desired temperature for set periods prior to cooling under the continuous flow of CS₂/Ar (99% CS₂, Fisher Scientific, laboratory grade, 99.9% Ar, BOC gasses) the flow rate was controlled by a gas tap and set to a few bubbles per second through the paraffin oil bubbler. The preparation label and variables are given in Table 5.6.

Preparation Label	Sintering Temperature (°C)	Sintering Time (hours)	Precursor
O-S850n_4h	850	4	S-O800n_4h
N-S850n_4h	850	4	S-N950n_4h

Table 5.6: Table showing the experimental parameters for the preparations of tantalum sulfide from nanofibrous precursors.

5.2.2 Characterisation

PXD was carried out with typical analysis running as a step scan between 5 and 80 ° 2 θ , with a step size of 0.02 ° utilising a speed that gave ~ 3 hour scans in flat plate mode. For the scans that were required for higher level analysis longer scans were carried out again over the same range but lasting for 15 hours. Different diffractometers have been used for the analysis as explained in Section 2.4.1.3. PXD slides were prepared for powders by smoothing the powder products over the indentation in the PXD slide to provide a flat uniform surface. Different methods of loading the PXD slide with nanofibres were attempted, as outlined in Section 2.4.1.2. The best results came from either adhering the nanofibres to the glass slide using a carbon tab, (Section 2.4.1.2.3.3) or dispersing the nanofibres in ethanol and dropping them into a hot glass slide (Section 2.4.1.2.3.4).

SEM was performed at 20 KV, in high vacuum mode, with a typical working distance of 10 mm and spot size 3 or 4. Samples were loaded onto aluminium slugs using a double-sided adhesive carbon tabs which provided enough conduction to prevent the need for a coating procedure. EDX was used in conjunction with the SEM to ascertain approximate elemental ratios. Different SEMs have been used for the SEM analysis as explained in Section 2.4.2.3.

TEM and electron diffraction was carried out using two different microscopes (Section 2.4.3.7), with typical samples loaded by dispersion of nanofibres onto a carbon holey grid (300 mesh Ni) using propan-2-ol.

TGA was achieved using a Netzsch STA. Powdered samples ~100 mg or nanofibrous samples ~5-10 mg were loaded into alumina crucibles and heated at a rate of 10 °C min⁻¹ over a temperature range of either RT-1000 °C or RT-1400 °C under a flow of air (60 mlmin⁻¹) and argon (20 mlmin⁻¹).

5.3 Results and Discussion

5.3.1 Ammonolysis Reactions

5.3.1.1 Preparation S-N950b_4h

Upon opening the tube furnace from preparation **S-N950b_4h**, a fine powder, wine red in colour was observed, as would be expected from Ta_3N_5 , (though Ta_3N_5 is known to change colour with particle size²¹⁹). The initial morphology appeared to contain a finer, less granular powder when compared to morphology of the flowing black TaS_2 . PXD analysis of this fine red powder matched the expected pattern generated for the structure of Ta_3N_5 ¹⁴⁸ (Figure 5.2).

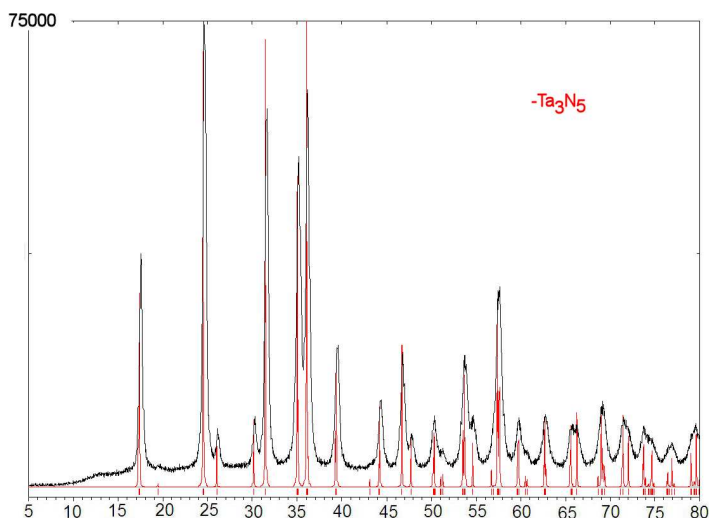


Figure 5.2: PXD pattern showing a match between the PXD peaks obtained from the products of preparation **S-N950b_4h** and those expected for the structure of Ta_3N_5 ¹⁴⁸ (D5000 diffractometer).

The pattern given in Figure 5.2 was indexed using Dicvol 6,¹⁸⁰ and refined to the best unit cell, using CELREF¹⁸¹ giving an orthorhombic unit cell as seen in Table 5.7. The cell parameters are a good match to those of the Ta_3N_5 structure, without any obvious expansion or contraction of unit cell parameters. The use of the Scherrer equation gives a value of ~27.7 nm for the thickness of the particles which is likely representative of the thickness of the disks, though is likely an over estimate as not all the disks will be aligned in the PXD slide.

Phase	<i>a</i>	<i>b</i>	<i>c</i>
S-N950b_4h	3.884(2) Å	10.208(4) Å	10.261(5) Å
Ta ₃ N ₅	3.8862 Å	10.2118 Å	10.2624 Å

Table 5.7: Unit cell parameters from the indexed powder patterns from **S-N950b_4h**, compared to the published values for Ta₃N₅.¹⁴⁸

SEM of **S-N950b_4h** shows the particles to consist of round plate-like particles (Figure 5.3(a)) and gave an average ratio of 38:62, Ta:N (± 2) by EDX, indicating close to Ta₃N₅ stoichiometry. When compared to the morphology of the sulfide precursor (Figure 5.3(b)) it was noted that the nitride particle shape was similar, in that they both consist of disk-like structures with lengths of ~40-100 μm and thicknesses of ~10 μm . It is the layered structure of the dichalcogenide materials that tends to promote the disk like structures seen in the SEM micrographs as the weakly bound layers can sheer easily. The structure of Ta₃N₅ is not layered and therefore does not promote the formation of disk-like platelets in this way. As the morphology of the nitride material seems to have changed very little when compared to the sulfide precursor, and the absence of crystallographic influence directing the formation of these disk-like structures, it is suggested that the precursor may have had some role in directing the formation of these nitride platelets. These results spurred interest in the ability to convert sulfide nanofibres into nitride nanofibres without affecting the morphology.

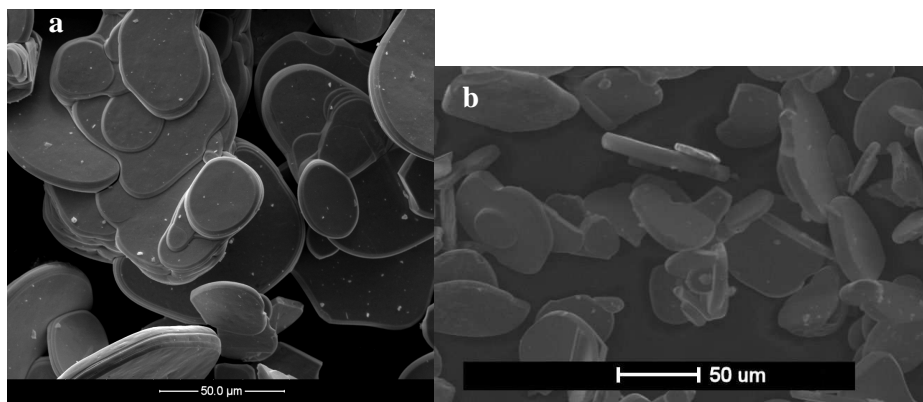


Figure 5.3: (a) SEM micrographs of typical Ta₃N₅ particles from **S-N950b_4h**, (SEM #3) and (b) SEM Micrograph of TaS₂ platelets, reproduced from Figure 3.3.

TG-DTA analysis was carried out as described in Section 2.4.4.3 and shows a trace that has been broken down into three distinct Regions, (A, B and C in Figure 5.4), suggesting that there are three separate processes happening as the temperature progresses from 20 to 1000 °C. Region A, is a loss in mass of less than 0.5 wt%, Region B, consists of a large gain in mass 8.25 wt% with exothermic nature (from DTA trace) running up to ~800 °C before Region C shows a small loss in mass ~0.5 wt% with the differential trace returning to the baseline. In Region A, the loss in mass is likely due to a small amount of water that is present in the sample having been stored in air for a short period. During Region B, the phase is oxidised to Ta₂O₅ hence the large exothermic DTA trace. This leaves the final part, Region C, which seems incomplete at 1000 °C. One possible explanation could be the loss of stoichiometric oxygen but it is hard to say without PXD analysis of the reactants at this temperature. High temperature (1000 °C) PXD was unobtainable.

As explained in Section 2.4.4.1, the likelihood of a predicted phase can be assessed by the comparison of the predicted mass change over a likely reaction with the actual mass change. It is reasonable to assume that at 1000 °C in flowing air the most stable tantalum phase and therefore the product is Ta₂O₅. This assumption is confirmed in Section 5.3.2 and shown in Figure 5.27. Equation (5.8) shows the predicted reaction of Ta₃N₅ with air giving a theoretical mass increase of 8.15 % (RFM Ta₃N₅ = 612.90, Ta₂O₅ = 441.90). The observed mass increase was 8.25 %, leading to the conclusion that the stoichiometry is extremely close to Ta₃N₅, though the small error could be due to systematic errors in the equipment or baseline calibration. Zhang and Gao noted that TGA of Ta₃N₅ powders gave a 8.28% mass increase when heated in air which corresponds well with the values obtained here.²¹⁶ The entrapment of nitrogen on the surface of the oxide during the TGA run was given as a reason for the difference between theoretical and actual mass change. They also proposed the change given in Equation (5.8). The transition occurred at ~450 °C as is expected and was completed

by 800 °C which gives a range that is comparably larger than found by Zhang and Gao.²¹⁶ The reason for this is likely the use of air / argon mix rather than air alone.

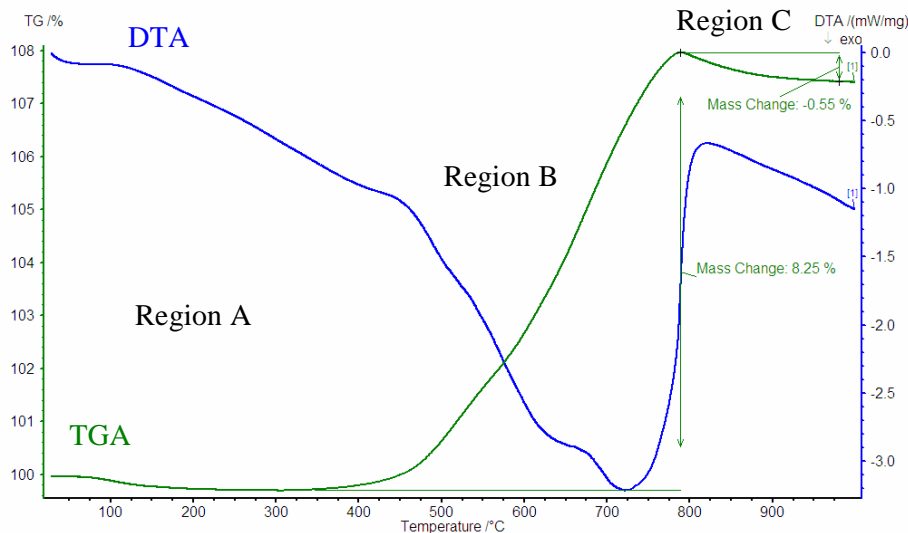
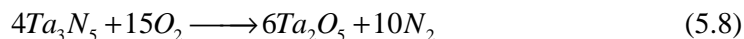


Figure 5.4: TGA data from the products from **S-N950b_4h**.

Ta₃N₅ has a theoretical absorption onset at 2.05 eV,¹³⁹ though the onset is known to alter as a result of crystallite size, specifically that a reduction in size morphology results in a blue shift. The band onset has been shown to occur between 2.00 and 2.08 eV^{140-143, 216, 219} leading to possible use as a photocatalyst and indeed Ta₃N₅ has shown promise as a water-splitting catalyst.^{219, 222} The wine red product **S-N950b_4h** was analysed by UV-vis DRS for its absorption onset, (Figure 5.5) and seen to have an onset at 2.04 eV which is within the range given above. The onset is measured as described in Section 2.4.6 and consists of extrapolating the steepest part of the curve to the base line value of the trace and reading off in nm, before converting to eV, (Equation (2.22)). The particle size has been measured by SEM, calculated by the Scherrer equation and is related to the BET surface area. The SEM indicates that the morphology is particulate with diameters in the range 40-100 µm and thickness 5-15 nm. The Scherrer equation calculated the average particle thickness at ~27.7 nm indicating a larger value than measured by SEM and BET analysis showed a surface area

of $1.38(4) \text{ m}^2\text{g}^{-1}$ as would be expected for a bulk powder and was carried out as a reference for other measurements. The band gap would therefore be expected to be somewhere mid range, but closer to the red boundary than the blue as $20 - 100 \text{ }\mu\text{m}$ is large when compared to the $18\text{-}40 \text{ nm}$ particles investigated by Zhang and Gao with a band gap of 2.08 eV .²¹⁶ 2.04 eV lies in the centre of the range given.

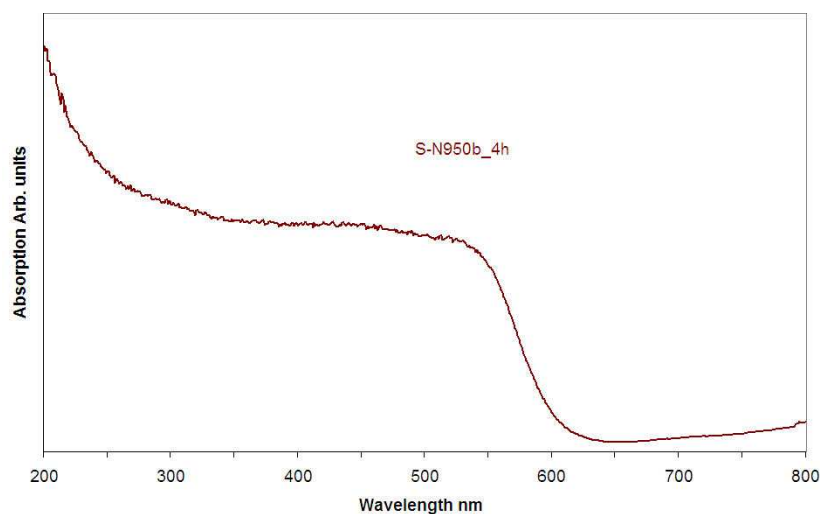


Figure 5.5: DRS spectra for the bulk Ta_3N_5 sample, **S-N950b_4h_a** showing the band gap at 2.04 eV .

5.3.1.2 Preparation O-N950b_4h

This preparation yielded a wine red flowing powder much the same as **S-N950b_4h** discussed in Section 5.3.1.1. PXD showed peaks that matched the position of those expected for the Ta_3N_5 phase as well as some peaks that matched the positions expected for the TaON phase. There is therefore some TaON ($\sim 20\%$ by calculated X-ray intensity as a fraction in PowderCell¹⁷⁹) contamination in this sample. It can be concluded that 4 h is not long enough to complete the reaction to Ta_3N_5 when the oxide starting material is used however complete reaction occurs for the same reaction conditions using a sulfide precursor. The nanomaterials should react faster as a result of higher surface area so this conclusion only holds for the bulk system. The peaks that correspond to the Ta_3N_5 phase were indexed and refined to give an orthorhombic unit cell with parameters shown in Table 5.8. These are compared to those

from **S-N950b_4h** and noted as being slightly larger in all directions, though still within the standard deviations to be effectively the same phase. The Scherrer equation yields an average particle thickness of $\sim 1.7 \mu\text{m}$ indicating that the particles are much thicker than those produced in **S-N950b_4h** though the non plate-like morphology will correspond to particle size rather than disk thickness as observed in SEM (Figure 5.7(a)).

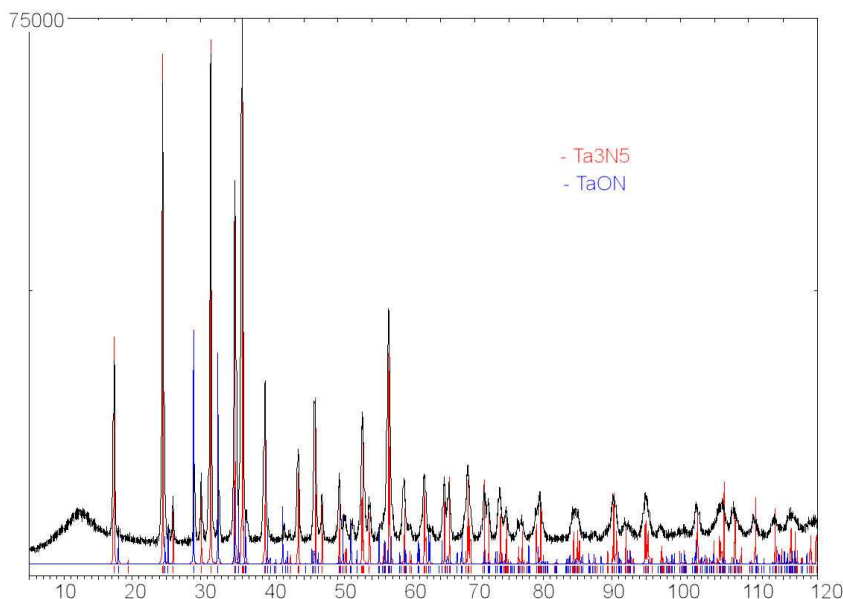


Figure 5.6: PXD data from **O-N950b_4h** showing a match to the peaks for both the Ta_3N_5 and TaON contamination, (D5000 diffractometer).

Phase	a	b	c
O-N950b_4h	3.893(9) Å	10.278(2) Å	10.278(5) Å
S-N950b_4h	3.884(2) Å	10.208(4) Å	10.261(5) Å
Ta_3N_5	3.8862 Å	10.2118 Å	10.2624 Å

Table 5.8: Unit cell parameters from the indexed powder patterns from **O-N950b_4h**, compared to the published values for Ta_3N_5 .¹⁴⁸

SEM analysis shows particles that are not flat plate-like disks as in Figure 5.3(a), but sharp angular particles. Figure 5.7(a). Figure 5.7(b) shows the morphology of the oxide precursor that was purchased commercially (99% Ta_2O_5 Aldrich). Both samples have a large distribution of particle sizes with the majority $\sim 10 \mu\text{m}$ in diameter and no plate-like appearance. EDX analysis again showed $\sim 3:5$ ratio, Ta:S but this time with a small tantalum deficit. It is clear from these micrographs and those in Figure 5.3, that the bulk reactions were

taking place with a large degree of retention of morphology, irrespective of whether the precursor is of oxide or sulfide origin.

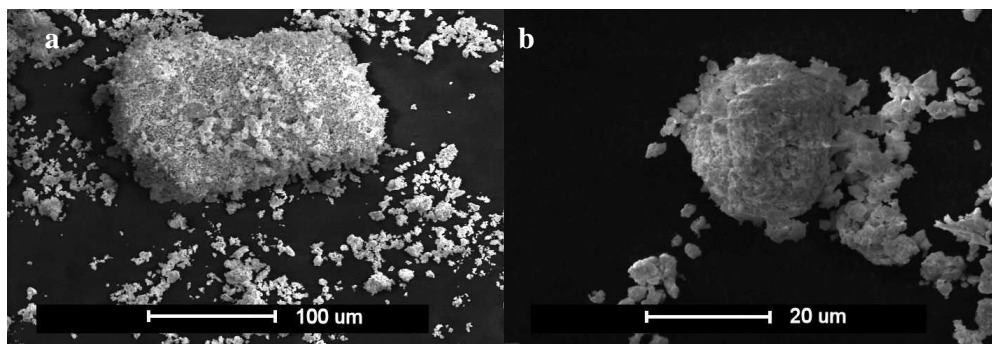


Figure 5.7: SEM micrographs showing: (a) general morphology from **O-N950b_4h** and (b) general morphology from the commercial oxide material that was used as a precursor, (SEM #4)

The UV-vis DRS spectrum is given in Figure 5.8 and shows the same band onset as 2.04 eV as observed with the products from **S-N950b_4h**. The band onset was calculated again by extrapolation of the steepest part of the curve to the base line. There is however no sign of the TaON in the DRS which would be expected to appear as a second onset at a higher eV (lower nm) value. The initial steep gradient occurs at too high an energy to be due to TaON which would have a predicted onset at ~520 nm (2.38 eV).¹⁴³ The change in particle size also has no effect on the band onset; though there is still a large range of particle sizes in the sample. The differences in band onset may be averaging out.

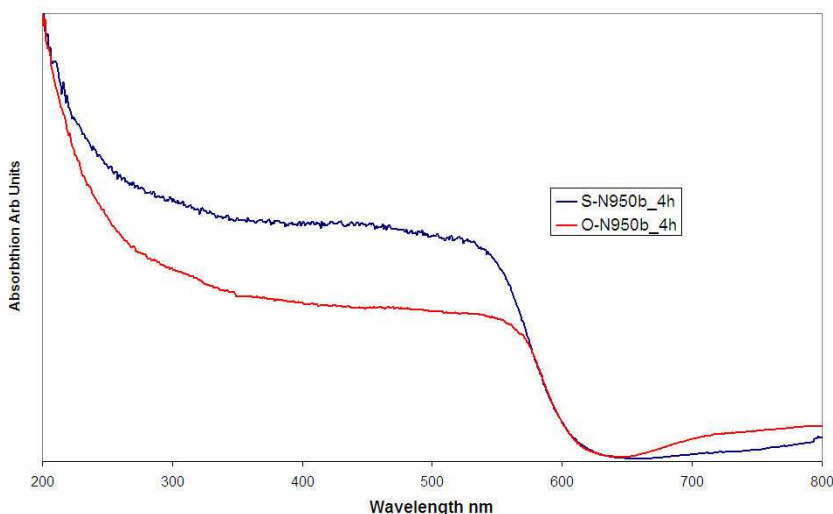


Figure 5.8: UV-vis DRS spectrum for the products of **O-N950b_4h** and **S-N950b_4h** showing a band onset at 2.04 eV.

5.3.1.3 Preparation S-N950n_4h

The fibrous materials recovered from **S-N950n_4h** were bright red in colour with some areas closer resembling wine red in colour.

PXD (Figure 5.9) showed only peaks in the correct positions to match those expected for the Ta_3N_5 structure, indicating that the sample was pure-phase. The peaks were indexed giving a good match to the published structure for Ta_3N_5 ¹⁴⁸ though with minimal expansion along the c parameter ($\sim 0.2\%$) as shown in Table 5.9. The peak width of the dominant peak led to a value of ~ 38 nm for the thickness of the fibres using the Scherrer equation which is approximately as expected for the thickness of the fibres from the TEM and SEM micrographs.

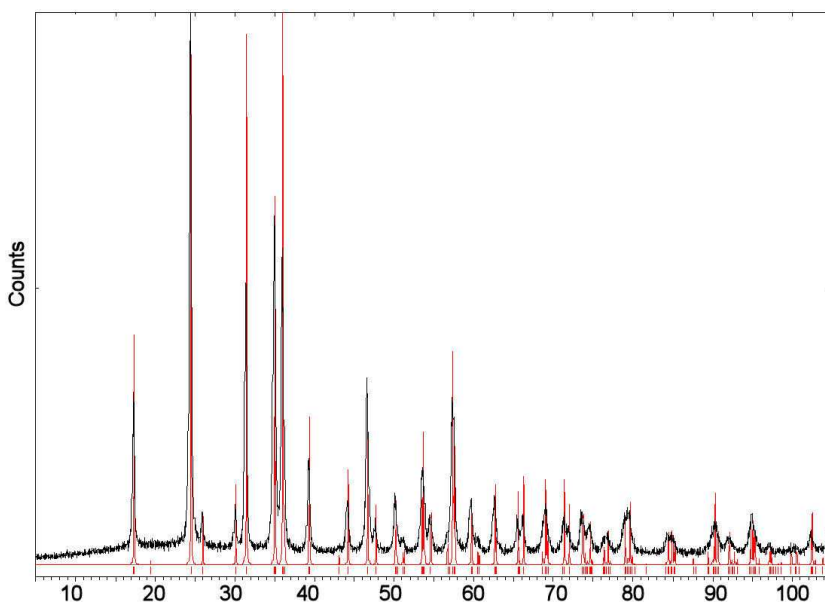


Figure 5.9: PXD pattern for the nanofibres from **S-N950n_4h** showing a match to the published structure of Ta_3N_5 ¹⁴⁸. Data collected using an adhesive carbon tab, (Section 2.4.1.2.3.3), (D5000 diffractometer).

Phase	a	b	c
S-N950b_4h	3.884(2) Å	10.208(4) Å	10.261(5) Å
S-N950n_4h	3.891(1) Å	10.234(2) Å	10.282(3) Å
Ta_3N_5	3.8862 Å	10.2118 Å	10.2624 Å

Table 5.9: Unit cell parameters from the indexed powder patterns of **S-N950b_4h** and **S-N950n_4h** compared to the published values for Ta_3N_5 ¹⁴⁸

SEM confirmed the fibrous nature of the products showing a 1-dimensional morphology with a range of aspect ratios. Typical fibres were 400 μm long and 100 nm wide giving aspect ratios of ~ 4000 . This morphology was similar to that of the nano-precursor as seen in Section 3.3.2. The TaS_2 nanofibres used as the precursor had longer lengths, in excess of 2.5 mm and generally wider widths 100 – 600 nm. The Ta_3N_5 fibres were again bundles of thinner fibrils. The precursor also consisted of cleaner fibres, Figure 5.10(b) shows particulates adhered to the surface of the fibres which were not so populous in the SEM images of the precursor, Figure 3.17. This may be due to fragmentation during the handling process or as the wires reduce in length. EDX showed an average elemental ratio of 38:62 (± 2) Ta:N which is within tolerance off a Ta_3N_5 stoichiometry, (37.5:62.5).

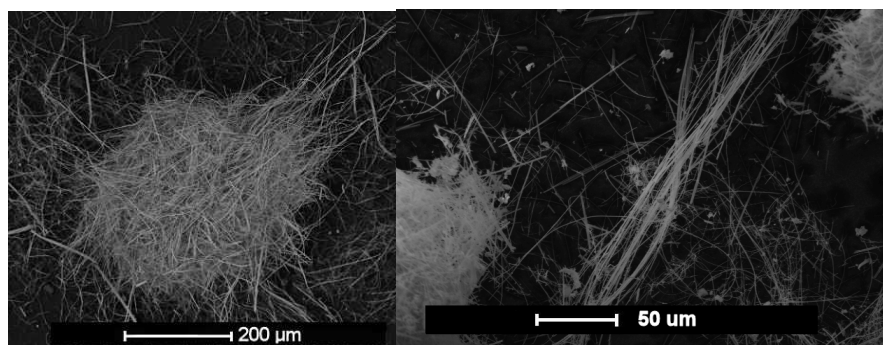


Figure 5.10: SEM micrographs showing the general morphology of the products from **S-N950n_4h**, (SEM #4).

TEM images showed that the fibres were in fact not single crystalline, with clear domains of about 20-30 nm in diameter. Figure 5.11 shows a typical Ta_3N_5 nanofibre with the corresponding SAED pattern inset. The polycrystalline fibres have a high degree of preferred orientation of the crystallites, towards the long axis of the wire known as texture. In a truly polycrystalline sample the crystallites will be oriented randomly leading to diffuse rings of diffraction pattern. As is seen in the inset of Figure 5.11, there are spots in the pattern similar to those of a single crystal while the image shows a polycrystalline material. The conclusion is that there is a high degree of cooperative growth between the crystal structure alignments of

all the crystallites leading to this texture in the SAED pattern. To conclude unambiguously that the contrast in the bright field image is due to slightly different alignments of the crystallites with respect to each other, dark field imaging is needed. Dark field imaging was carried out on this sample however; the results were not of sufficient quality for reproduction. Dark field imaging has been shown in the other preparations. The SAED pattern is oriented with a dominant axis at 90° to the direction of the long axis of the wire, pictorially, indicating that there is also cooperation between the crystal growth and the morphology of the material, (90° rotation between the SAED and the bright field images from the T20, Section 2.4.3.2). The pattern indexes well to the Cmc m space group of the Ta₃N₅ structure with the alternate spots seen clearest in the central line running diagonally top left to bottom right indicating one of the 2 glide planes associated with the Cmc m space group.

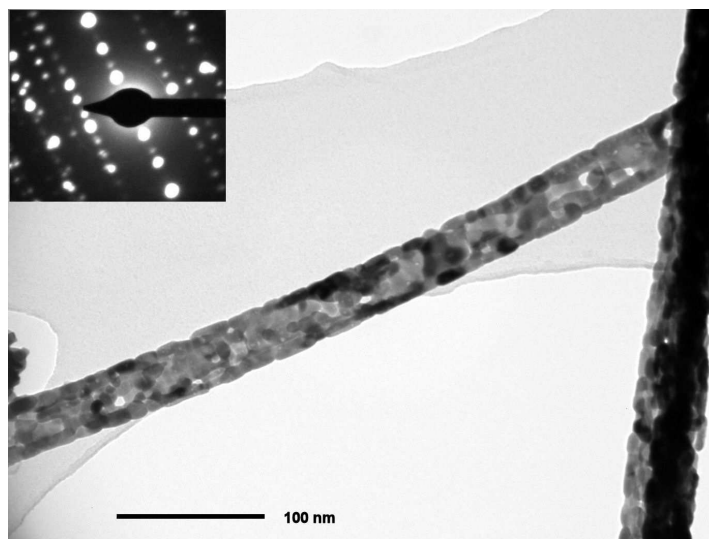


Figure 5.11: TEM micrographs showing a typical polycrystalline nanowire with SAED inset, (T20 microscope).

The inset diffraction pattern was indexed to the published structure for Ta₃N₅¹⁴⁸ with good agreement and the corresponding crystallographic directions determined (Figure 5.12). The two crystallographic directions at right angles to each other are noted as 001 and the 110. It is possible to conclude therefore that the direction of propagation of the wire is the 001 as this direction corresponds with the long axis in the TEM micrograph (Figure 5.11). This

conclusion is contrary to many publications where it has been noted that the maximum growth tends to occur along the shortest unit cell direction^{72, 152} though it should be noted that in all cases in the literature, the fibres were forming rather than converting which is likely to lead to crystallographic constraints as a result of the precursor. There is however no obvious correlation between the $\bar{2}110$ direction of the disulfide and the 001 of the nitride.

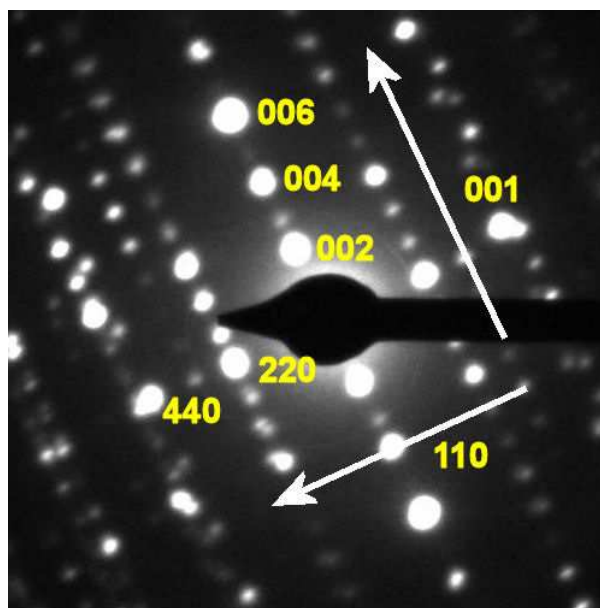


Figure 5.12: Typical SAED pattern for nanofibers from **S-N950n_4h** indexed to the published structure for Ta_3N_5 .¹⁴⁸

As the fibrous morphology is retained during the reaction from sulfide to nitride, it is reasonable to assume that the changing crystal structure from one phase to the other is responsible for the polycrystalline effect. The precursor consisted of single crystalline TaS_2 nanowires, which likely react with the ammonia during the synthesis relatively slowly, with nitrogen atoms diffusing in from the edges of the wire and sulfide atoms diffusing out. It appears that the anion exchange in the crystal structure occurs in isolated areas leading to the different contrast and appearance of grains. As two regions form side by side they grow in slightly different crystal alignments that lead to diffraction contrast in the TEM and are observed as the grain boundaries when they touch each other. Annealing at high temperature then sinters the crystallites together but cannot regain the single crystalline origins of the

initial precursor in the 4 hours given for the reaction leading to the micro-bead like structures. The time of reaction was shown to be a crucial aspect, with less than 8 hours at 900 °C leading to polycrystalline products by Henderson.²¹⁹ Lu *et al.* however, have shown that single crystalline particles can be made from Ta₂O₅ at 850 °C over a period of 15 hours.²²⁰

With a uniform anion exchange mechanism, as described above, the exchange should take place at about the same rate from all directions effectively turning the wire into a closed ended tube with a sulfide core, as the process occurs giving a very different expected morphology with less polycrystalline nature. Surface defects and imperfections in the TaS₂ nanowires may act as nucleation points for the crystal growth and anion exchange leading to faster growth and therefore a more grains and the appearance observed. Few surface constraints could possibly result in something like the TiO₂ beaded necklaces observed by Cottam and Shafer.¹⁷⁶ Many surface imperfections could lead to the grains observed in these samples, however, few surface defects were observed in TEM images of the nano-precursor, Section 3.3.2.

BET analysis shows that the nanowires have a specific surface area of 53.9(8) m²g⁻¹, which is in good agreement with the expected specific surface area for general nanofibrous materials. E.g. MoS₂ nanotubes investigated by Chen *et al.* have a specific surface area of 58 and 66 m²g⁻¹.¹⁸ This measurement can be compared to the observation from the bulk powder that showed a specific surface area of 1.38(4) m²g⁻¹. The nanofibres therefore have a 50 fold increase in specific surface area when compared to the bulk powder. Particles of Ta₃N₅ with higher surface area have been shown to be more catalytically active²¹⁶ so a 50 fold increase in surface area is desirable.

UV-vis DRS (Figure 5.13) shows a similar trace to that observed from **S-N950b_4h** (Figure 5.5). The onset point has now been blue shifted very slightly from 2.04 eV in the bulk to 2.05 eV in the nanofibrous morphology. Theoretical values for the bulk material calculated by de With *et al.* were 2.05 eV¹³⁹ which is in perfect agreement with these nanofibres. The

onset point of the absorption is dependant on the particle size with experiments showing that it can vary from 2.00 to 2.08 eV^{140-143, 216} for Ta₃N₅. The size dependence is generally seen as a blue shift occurring in the onset energy as particle size decreases.²¹⁶ This is observed in these results where there is a minimal blue shift from 2.04 to 2.05 eV as the morphology changes from bulk to nanofibre. The overall size dependence of the morphology is expected to be less in the case of bulk vs. nanowires rather than bulk vs. nanoparticles as individual nanoparticles will have nanoscale measurements in all three dimensions rather than just two in the case of the fibres, hence the smaller changes in band gap than reported for the nanoparticles. The change in size is apparent from comparing the SEM images of the bulk, (Figure 5.3(a)) and the nanofibrous (Figure 5.10) morphologies. The anisotropy of the platelets led to a value for the average particle size by PXD that is too low an estimate and is comparable with the widths of the nanowires observed in the nanomorphology reactions.

The DRS also shows the presence of a weak feature half way through the steep part of the curve at about 525 nm. This corresponds to a possible second onset point at very slightly higher energy, suggesting either a mixed morphology or an impure product phase. Given that the onset of TaON is 520 nm it is likely that this is the impurity.¹⁴³ The PXD shows that the phase is pure single phase Ta₃N₅ so it is also possible that the feature is due to the different morphologies of Ta₃N₅. In this case possibly the presence of nanoparticles in the sample of fibres

It has been reported that photocatalytic activity of Ta₃N₅ can be tuned within small ranges to a specific wavelength in the spectrum by changing the particle size,^{216, 219} however the increase in particle size is related to the morphology so it could therefore be possible to tune the photocatalytic activity of the photocatalyst by altering the morphology.²¹⁹ The nanowires have a larger surface area than the particles described by Zhang and Gao, 58 vs. 33 gm⁻² again potentially improving on photocatalytic activity as a direct result of the morphology.²¹⁶

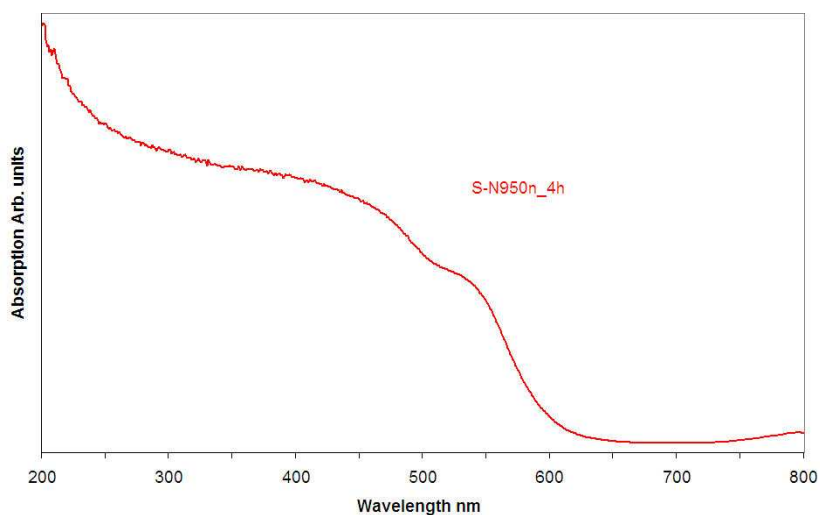


Figure 5.13: UV-vis DRS data for Ta₃N₅ nanowires prepared in **S-N950n_4h**.

Upon sonication it might be possible to form a nano particulate suspension of Ta₃N₅ particles with diameters in the region of 30 nm as seen in the fibrous TEM images, e.g. Figure 5.11. These could again have enhanced photocatalytic activity and indeed very different properties to particles produced by ball milling bulk material. The particles formed by this method should have lower energy at their boundaries as they have not been formed by grinding. The comparison of the UV-vis DRS spectrum between these particles and the nanofibres and indeed the bulk however showed minimal alteration in band onset. The band seems to have red shifted rather than blue shifted which is contrary to observation by other researchers, and now lies at 2.03 eV, which is still close to the predicted value and within the range of other researchers.^{140-143, 216} It is possible that there are quantum affects occurring (as the particle size is now considerably smaller than the wavelength of the radiation,) as well as the diameters of the particles that are influencing the band onset. As seen in Figure 5.14 the particles are much smaller in this sample than in **S-N950n_4h** before sonication but still a long way off the size of the grains in the fibres observed by TEM.

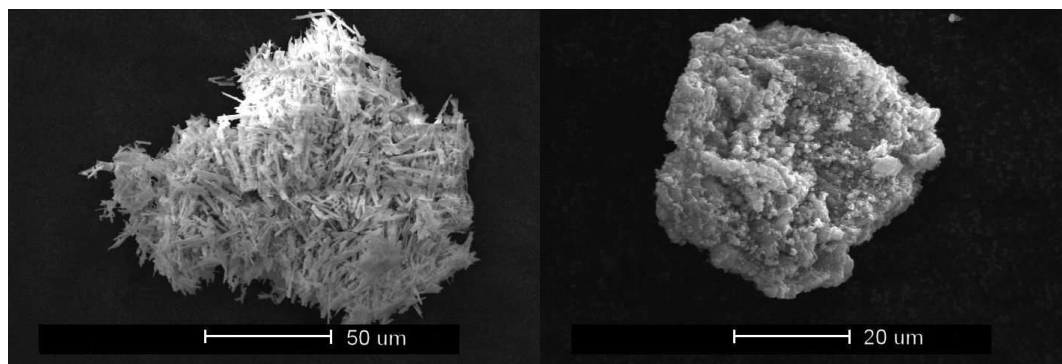


Figure 5.14: SEM micrographs of the sonicated nanofibres, (SEM #4).

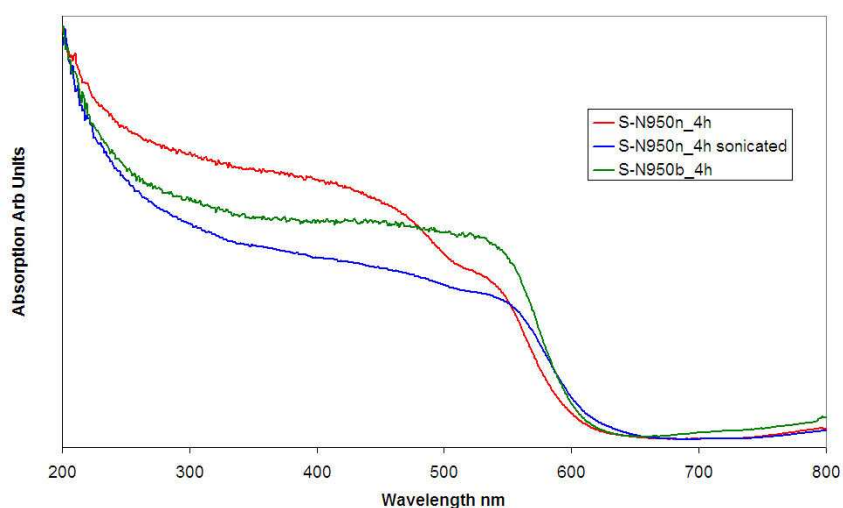


Figure 5.15: DRS spectrum comparing the results from **S-N950n_4h**, the sonicated particles and the bulk tantalum nitride from **S-N950b_4h**.

5.3.1.4 Preparation S-N800n_4h

S-N800n_4h and **S-N650n_4h** were to investigate the crystallinity of the nanowires at lower temperature. The fibres produced by **S-N800n_4h** were again bright red in colour with a PXD pattern indicating the presence of the Ta_3N_5 . A proportion of the underlying amorphous nature is likely from the adhesive carbon tab, (Section 2.4.1.2). The pattern, (Figure 5.16), has broader peaks than those observed for **S-N950n_4h** (Figure 5.9) suggesting a lower degree of crystallinity as the trends described above would indicate. The most resolved peaks were indexed and the refined unit cell parameters given in Table 5.10. In this sample, the Ta_3N_5

structure seems to have some general expansion in all of the unit cell directions when compared to the nanofibres formed at higher temperature.

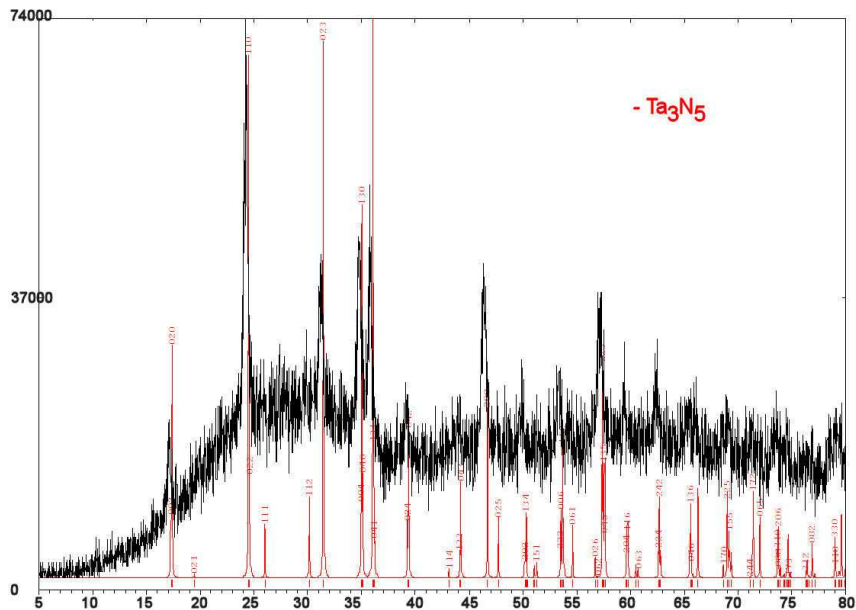


Figure 5.16: PXD pattern showing the match between the products from **S-N800n_4h** and the crystal structure for Ta_3N_5 . Data were collected from a sample adhered to an amorphous carbon tab (Section 2.4.1.2) using the D5000 diffractometer.

Phase	<i>a</i>	<i>b</i>	<i>c</i>
S-N800n_4h	3.897(2) Å	10.34(1) Å	10.31(1) Å
S-N950n_4h	3.891(1) Å	10.234(2) Å	10.282(3) Å
Ta_3N_5	3.8862 Å	10.2118 Å	10.2624 Å

Table 5.10: Unit cell parameters from the indexed powder patterns of **S-N800n_4h** and **S-N950n_4h**, compared to the published values for Ta_3N_5 .¹⁴⁸

SEM shows a more varied morphology than that observed in **S-N950n_4h**, though some of this could be due to the use of different batches of precursor. As stated in Section 5.2, the preparations for the precursor were not yielding identical results so some alteration in the morphology of the fibres may be due to the initial morphology of the precursor. The fibres appear to be broken into ~100 μm lengths and are flatter and more ribbon like, with a more brittle nature when compared to the fibres from **S-N950n_4h** they also have lower aspect ratios, with the average aspect ratio around 100, i.e. 100 μm length and 1 μm width. This is

evident from the number of occurrences of breaks in the fibres, probably from stress during the SEM sample loading procedure.

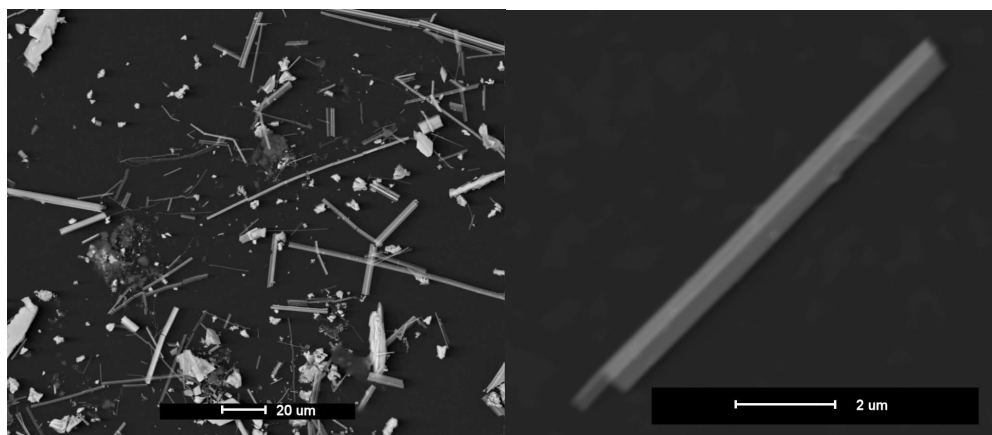


Figure 5.17: SEM micrographs showing the general morphology of fibres in the products of **S-N800n_4h**, (SEM #3).

TEM analysis shows the same polycrystalline nature as the **S-N950n_4h** sample. The crystallites appear to be much less ordered in these samples with respect to, **S-N950n_4h** as indicated by the less ordered inset SAED, Figure 5.18(a). There is however still much cooperation between the direction of growth and the long axis of the wire. The orientation of the spots in question (Figure 5.18(a)) run vertically up the page. Spots in the pattern align perpendicular to the long axis of the wire, which corresponds to a parallel direction to the long axis of the wire in real space, (Section 2.4.3.2). The aligned spots again show the correct spacing for the 002 direction of the Ta_3N_5 crystal structure, indicating that in these fibres the texture of the crystallites is aligned with the 002 direction running along the long axis of the wire, as is the case with the higher temperature reactions.

Nanodiffraction patterns were achieved (Figure 5.18(b)) by condensing the beam down to a spot of a diameter less than the grain size within the fibres. This pattern shows the SAED of the individual grains within the nanofibre structure and again was indexed to the structure of Ta_3N_5 with a clear indication of texture to the long axis of the wire (Figure 5.18(b)). The nanodiffraction inset has been corrected for the 90° rotation so the vertical alignment of the spots corresponds with the vertical alignment of the fibre. The alternate

spots of the 00l where the indices obey the $l = 2n$ rule outlined in the general conditions of reflections for the Cmc_m space group are observed running parallel to the long axis of the wire in agreement with the other higher temperature nanofibres.

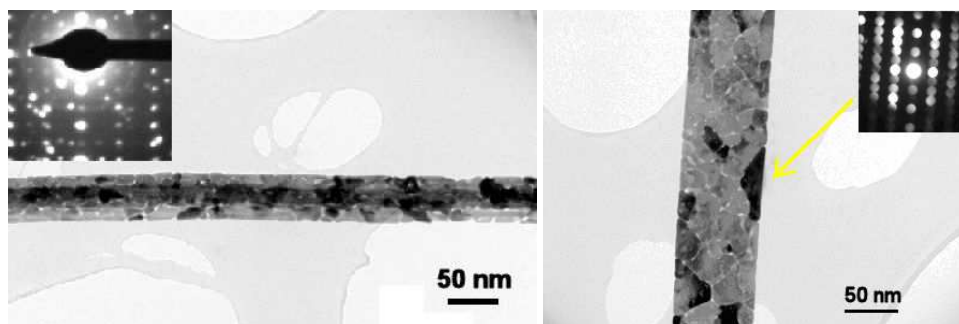


Figure 5.18: TEM micrographs of Ta₃N₅ nanowires from S-N800n_4h with inset diffraction patterns. The diffraction pattern in (b) was achieved by focussing the beam in on the individual crystal indicated and was indexed to the Ta₃N₅ structure, (T20 microscope).

Dark field imaging was achieved to show that the different crystallographic orientations of the particles within the nanocrystalline wires were responsible for the contrast in the bright field images. The set of 6 images in Figure 5.19 show the dark field imaging technique. Bright areas correspond to the regions of crystal that are responsible for the creation of the diffraction spot intensity in the diffraction pattern. Given the orientation of the five spots in the diffraction pattern, with respect to each other, three similar images would be expected from the 002, $00\bar{2}$ and $00\bar{4}$ spots and two different images from the $11\bar{2}$ and $11\bar{4}$ spots respectfully. Of these, two images should be almost identical as then originate from the most similar 002 and $00\bar{2}$ spots indexed in the inset diffraction pattern. This is indeed what is observed. Figure 5.19(b) and (d) are the almost identical images from the 002 and $00\bar{2}$ spots, Figure 5.19(c) is the image from the $00\bar{4}$ spot, similar to the first two while Figure 5.19(d) and (e) are from the $11\bar{2}$ and $11\bar{4}$ spots respectively. It can be concluded from this that the fibres are indeed polycrystalline and as such this is the cause of the contrast effect in the TEM that is producing the beadlike structure.

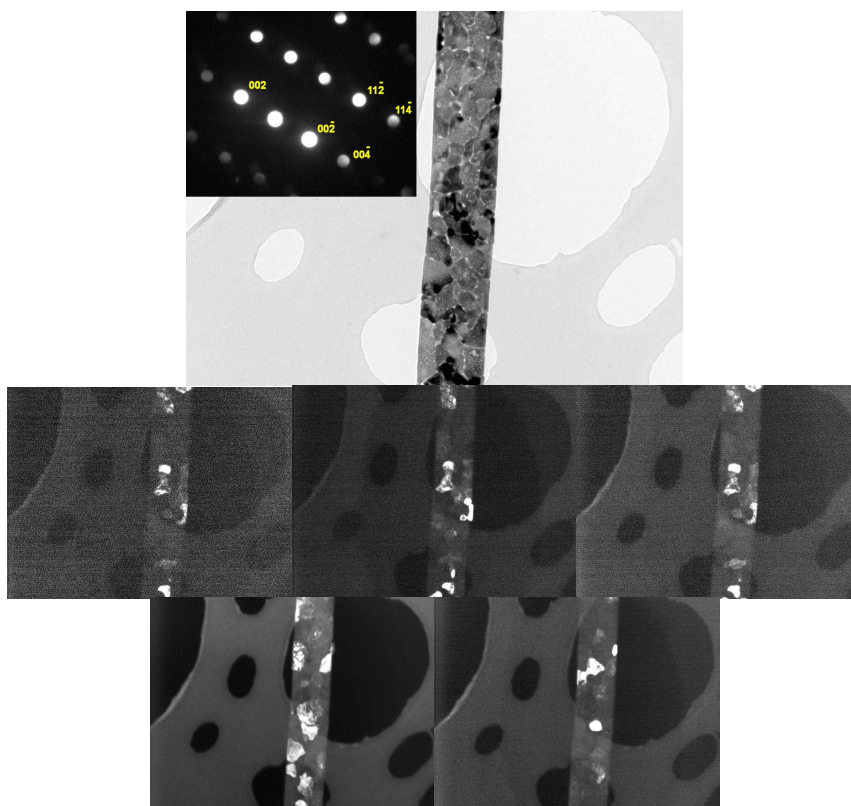


Figure 5.19: TEM micrographs showing: (a) Bright field image of the area in question with the indexed representative nanodiffraction pattern; (b-f) dark field images showing the different crystallographic orientations within the nanowire, (T20 microscope).

5.3.1.5 Preparation S-N650n 4h

The preparation at 650 °C produced nanofibres, with less crystalline nature than the **S-N800n_4h** sample, showing few resolved peaks by PXD that indexed to the Ta_3N_5 crystal structure. The amorphous nature of the PXD pattern (Figure 5.20) is shown by the board background from which few peaks are successfully resolved. It is likely that there is a mixture of phases containing both amorphous and crystalline Ta_3N_5 , with the few resolved peaks resulting from the crystalline material. Some of the underlying amorphous nature is likely due to the carbon tab but not enough to be significant, (Section 2.4.1.2.3.3). The powder pattern was indexed using the few best resolved peaks and cell parameters calculated and compared to the other sulfide \rightarrow nitride preparations as shown in Table 5.11. All the values for the cell parameters are in reasonable agreement and within the standard deviations of error to be

reliably the same phase. There is no obvious trend in the cell parameters as the sintering temperature decreases.

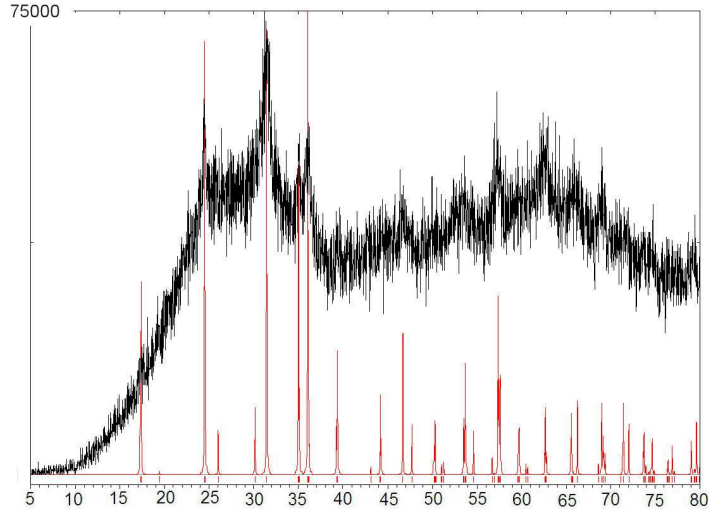


Figure 5.20: PXD showing the match to the crystal structure of Ta_3N_5 for the nitride nanowires formed in **S-N650n_4h**. Data were collected using an adhesive carbon tab (D5000 diffractometer).

Phase	a	b	c
S-N650n_4h	3.896(1) Å	10.20(4) Å	10.25(1) Å
S-N800n_4h	3.897(2) Å	10.34(1) Å	10.31(1) Å
S-N950n_4h	3.891(1) Å	10.234(2) Å	10.282(3) Å
Ta_3N_5	3.8862 Å	10.2118 Å	10.2624 Å

Table 5.11: Unit cell parameters from the indexed powder patterns of **S-N650n_4h**, **S-N800n_4h** and **S-N950n_4h**, compared to the published values for Ta_3N_5 .¹⁴⁸

SEM shows a ribbon-like morphology with aspect ratios in the region of 100. The fibres from **S-N650n_4h** are closer in appearance to those from **S-N800n_4h** than those from **S-N950n_4h** with the brittle nature of the products becoming more evident with a high proportion of ribbon fragments.

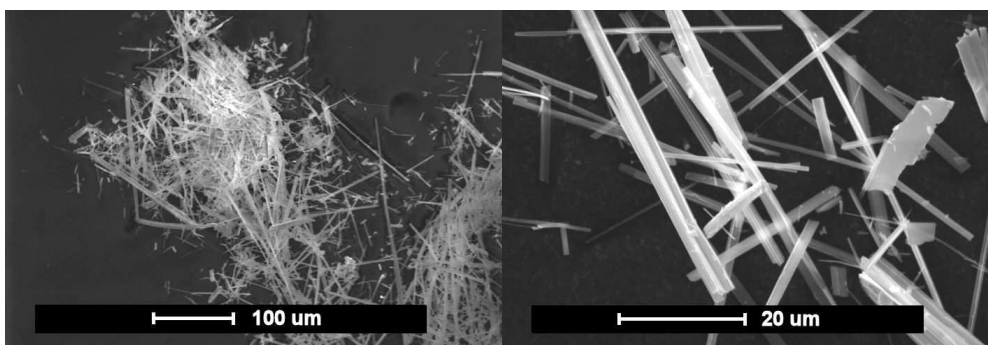


Figure 5.21: SEM micrographs showing the products of **S-N650n_4h**, (SEM #4).

TEM (Figure 5.22) shows nanowires of similar dimensions to those seen above but without the grain boundaries. It is possible that the anion exchange between sulfur and nitrogen as the crystal structure changes is much slower at 650 °C than at 950 °C preventing these large crystals from growing individually and meeting each other to form the grain boundaries. SAED was attempted but as expected for an amorphous material, no electron diffraction pattern was achieved for the nanofibres, concluding that the structure is amorphous.

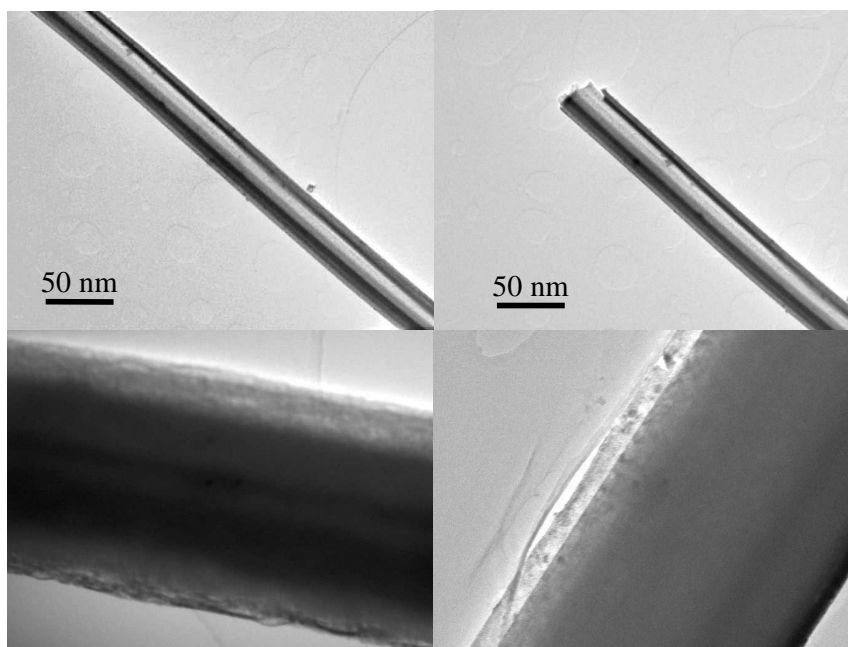


Figure 5.22: TEM micrograph showing the Ta_3N_5 nanowires from **S-N650n_4h**, (T20 microscope).

BET analysis showed a specific surface area of $17.5 \text{ m}^2\text{g}^{-1}$, indicating that these nanofibres had a considerably smaller surface area than the higher temperature preparations, but still an

order of magnitude above that of the bulk powders. Given the diffuseness of the peaks in the PXD the Scherrer equation can not be used to generate an average particle size for comparison.

5.3.1.6 Preparation O-N950n_4h

The nitride nanofibres produced at high temperature from the oxide nanofibrous precursor discussed in Section 5.3.2.2, yielded a red fibrous material visually identical to that produced from **S-N950n_4h**. PXD analysis was carried out with results (Figure 5.23) matching the peak positions of the published Ta_3N_5 phase.¹⁴⁸

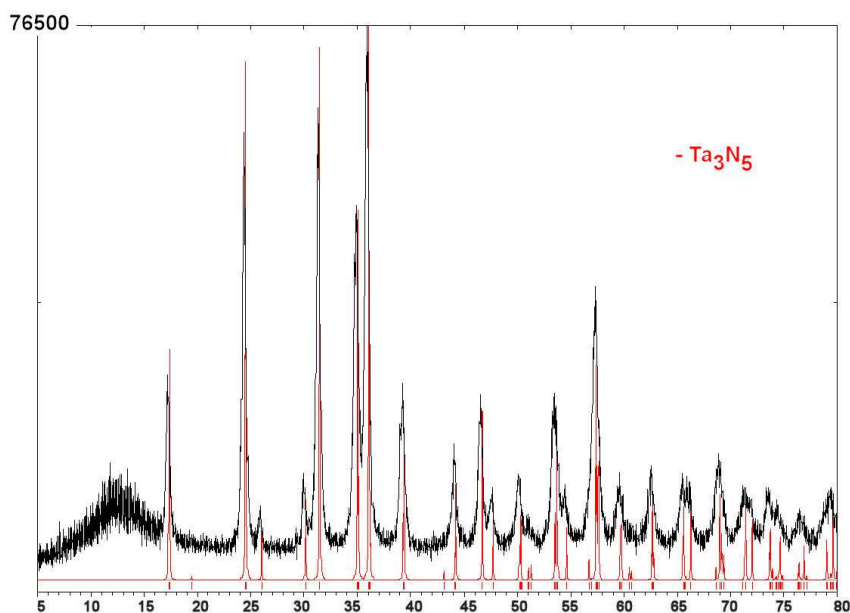


Figure 5.23: PXD data for **O-N950n_4h**.

The pattern given in Figure 5.23 was indexed using Dicvol 6,¹⁸⁰ and refined to the best unit cell, using CELREF¹⁸¹ giving an orthorhombic unit cell with parameters given in Table 5.12. The unit cell parameters are a reasonable match to those of the Ta_3N_5 structure, with some expansion, (0.04%) along the c parameter, when compared to the indexing of the **O-N950b_4h** products and the published structure for Ta_3N_5 . Other researchers have observed the expansion up to 3% along the c parameter when converting from bulk to nanophase morphology.⁵⁰

Phase	<i>a</i>	<i>b</i>	<i>c</i>
O-N950n_4h	3.898(1) Å	10.234(8) Å	10.686(4) Å
O-N950b_4h	3.893(9) Å	10.278(2) Å	10.278(5) Å
Ta ₃ N ₅	3.8862 Å	10.2118 Å	10.2624 Å

Table 5.12: Unit cell parameters from the indexed powder patterns of **O-N950n_4h** and **O-N950b_4h**, compared to the published values for Ta₃N₅.¹⁴⁸

There is no TaON observed in the PXD pattern when compared to that of **O-N950b_4h** indicating that the reaction achieves completion in the 4 hours with the nanophase precursor while not quite in the case of the bulk precursor.

SEM analysis shows a fibrous morphology that contains large bundles of fibres, (Figure 5.24). The individual bundles have aspect ratios of ~1000 (lengths ~1mm and widths of 1 µm). The fibres appear to be ribbon-like and were seen in some micrographs to curl much like the precursor (Figure 5.35), and have an elemental ratio of ~34:66, which is slightly less than the 37:63 that is expected for Ta₃N₅.

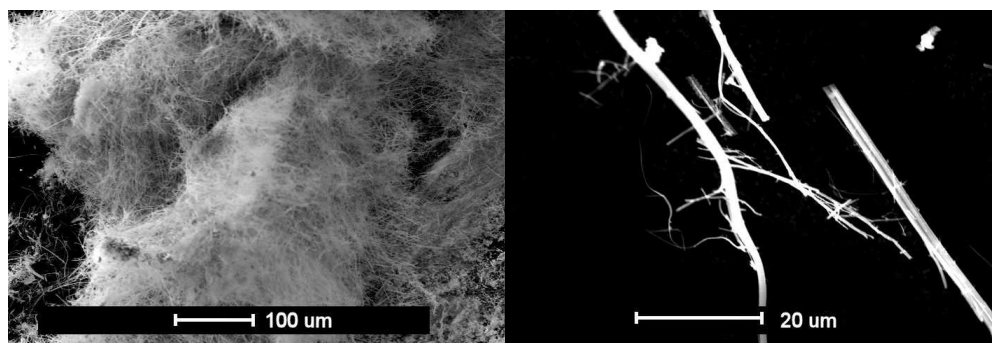


Figure 5.24: SEM micrographs showing the morphology of **O-N950n_4h**, (SEM #4).

The fibres have a similar contrast effect in the TEM micrographs (Figure 5.25) to that seen in the high temperature nitride preparations from a sulfide precursor.

Comparing the SAED pattern from **O-N950n_4h**, (Figure 5.25), and **S-N950n_4h**, (Figure 5.11); **O-N950n_4h** shows a distinct lack of texture, i.e. little alignment of the crystallites with respect to the long axis of the wires, when compared to **S-N950n_4h**. The beginnings of spot coalescence and polycrystalline ring formation, in the SAED indicate that the crystals are almost randomly orientated within the wire. The nitride nanofibres produced

from the oxide precursor have larger grain sizes and more of a layered effect than from the sulfide precursor. The layered effect can be seen in Figure 5.25 with the dark and light lines that run through the long axis of the structure.

The beaded effect in the contrast of the TEM does not resemble the starting material (Figure 5.36). Similar effects have been observed in the inter-conversion of other TiC nanotubes into TiO₂ by Cottam and Shaffer,¹⁷⁶ indicating that the beaded effect is not unique to the ammonolysis reaction.

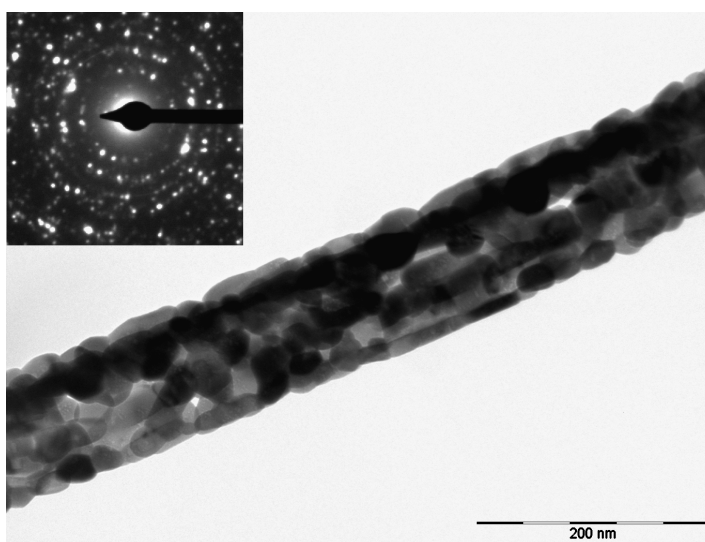


Figure 5.25: TEM micrograph of the nitride nanowires from preparation **O-N950n_4h**, (T20 microscope).

5.3.2 Preparations of Oxide Materials

5.3.2.1 Preparations S-O800b_4h

S-O800b_4h yielded a white powder, as would be expected for Ta₂O₅ and were similar in appearance to that purchased commercially (99% Ta₂O₅, Aldrich). The colour change; from black or red to white, was a good indicator that the phase had completely oxidised and the PXD pattern, (Figure 5.26), matched the peaks expected for a structure of Ta₂O₅ with space group Pccm and unit cell parameters $a = 6.2170$, $b = 3.6770$ and $c = 7.7940$ Å.²²³ Ta₂O₅ was

noted previously as the product of any of the preparations in Chapters 3 and 4 where the sealed tubes either failed to seal sufficiently or cracked during the heating process. The pattern given in Figure 5.26 was indexed using Dicvol 6,¹⁸⁰ and refined to the best unit cell, using CELREF¹⁸¹ giving an orthorhombic unit cell as seen in Table 5.13. The unit cell parameters match those of the published Ta₂O₅ structure.²²³

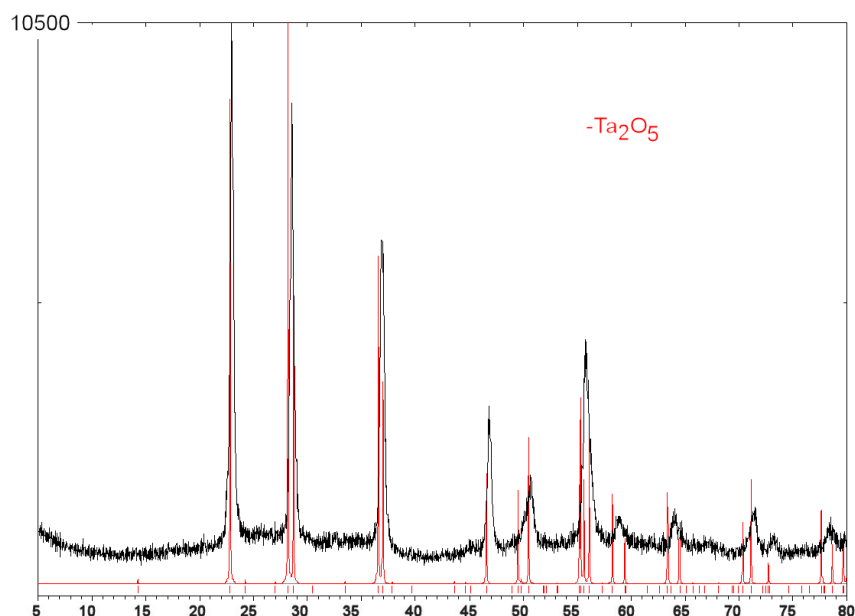


Figure 5.26: PXD pattern for the products of **S-O800b_4h**, showing a match to the Ta₂O₅ structure, (D5000 diffractometer).

Phase	<i>a</i>	<i>b</i>	<i>c</i>
S-O800b_4h	6.218(6) Å	3.664(9) Å	7.798(8) Å
Ta ₂ O ₅	6.2170 Å	3.6770 Å	7.7940 Å

Table 5.13: Unit cell parameters from the indexed powder patterns of **S-O800b_4h**, compared to the published values for Ta₂O₅.²²³

TG-DTA analysis was obtained for the powders produced in **S-O800b_4h** as in Section 2.4.4.3. The trace in Figure 5.27 shows very little alteration in mass as the sample is heated from 20 to 1000 °C in the presence of air. The data suggest firstly, that the stoichiometry of the oxide formed in the preparation is indeed stable and unchanging and secondly that the Ta₂O₅ phase (by PXD) is the dominant phase at 1000 °C and can therefore be used as a reference for the other TG-DTA data.

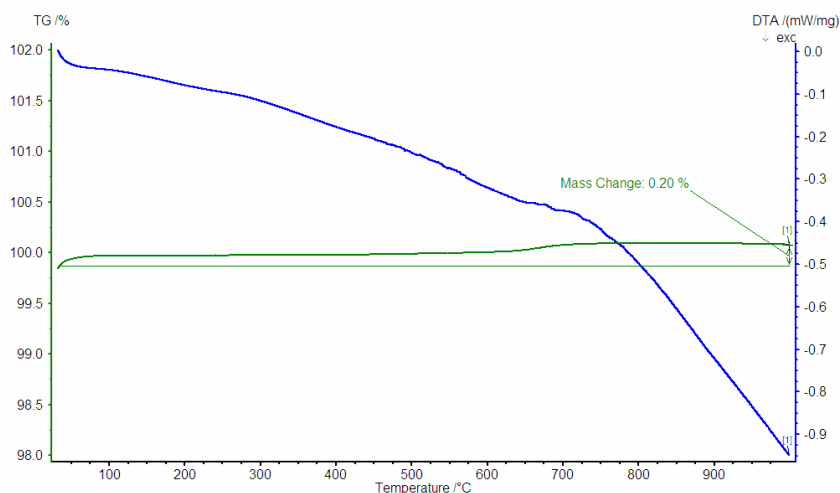


Figure 5.27: TG-DTA data from the bulk powders of Ta_2O_5 produced in **S-O800b_4h**.

SEM analysis shows the particulates of Ta_2O_5 with no plate-like morphology. It seems that the oxide does not maintain the plate-like morphology of the sulfide precursor.

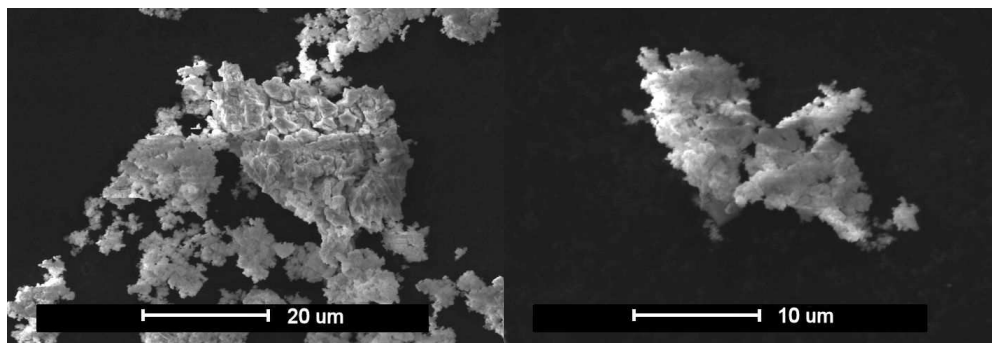


Figure 5.28: SEM micrographs showing the morphology from **S-O800b_4h**.

The Ta_2O_5 from **S-O800b_4h** was used as a reference for the UV-vis DRS measurements on the nanofibres. The UV-vis DRS data is shown in Figure 5.29 and shows a band gap onset, of 3.79 eV, (calculated as described in Section 2.4.6), which is in reasonable agreement with estimated values from other authors of 3.80 eV.¹³⁹⁻¹⁴³

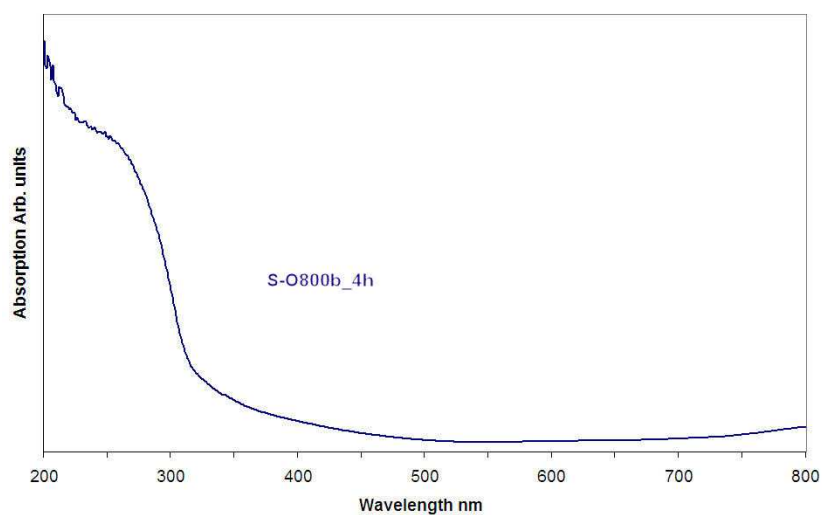


Figure 5.29: UV-vis DRS data for the Ta₂O₅ bulk powder produced in **S-O800b_4h**. The data show a band gap onset at 3.79 eV which is comparable to the 3.80 eV observed by other researchers.¹³⁹⁻¹⁴³

5.3.2.2 Preparation S-O400b_4h and S-O400b_16h

The reaction of TaS₂ powder and oxygen at 400 °C, (**S-O400b_4h**) did not go to completion. There was a mixture of white oxide and black sulfide phases. The white oxide was found on the surface of the product powder and sulfide beneath it in the alumina boat indicating that oxide diffusion within the Ta₂O₅ structure is limited and therefore a coating of oxide protected the underlying sulfide material. PXD confirms this by showing peak positions that match those expected for tantalum oxide and a number of the polytypes of tantalum sulfide.

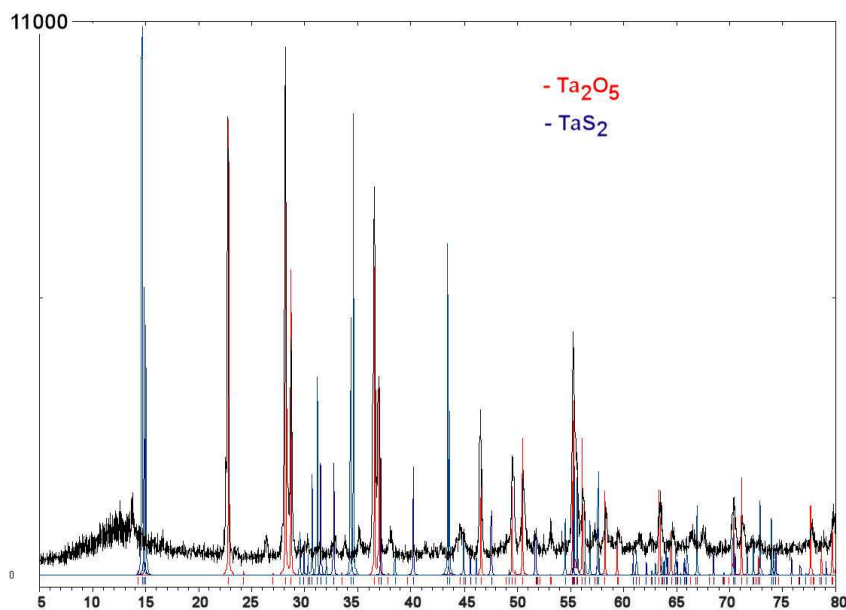


Figure 5.30: PXD analysis of the products from **S-O400b_4h**.

SEM shows a mixture of morphology with a high degree of angular sharp crystallites, (Figure 5.31). There is also the presence of some plate-like formations specifically seen in Figure 5.31(b). This indicated that at this temperature the transformation from sulfide to oxide fails to maintain the original morphology of disk-like structures and forms a crumbled powder instead.

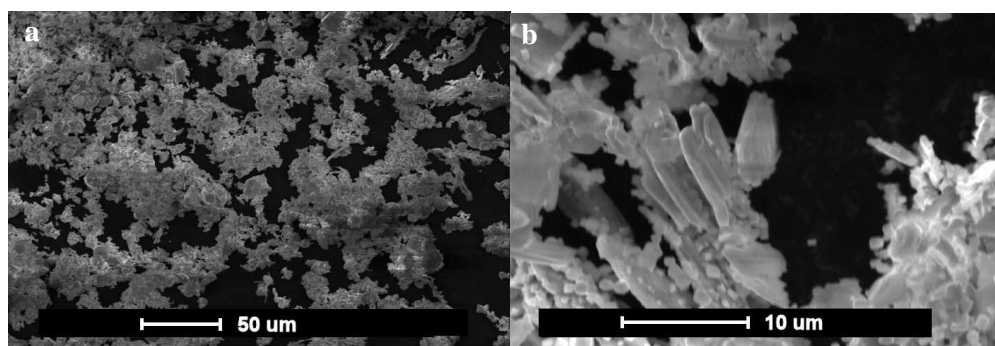
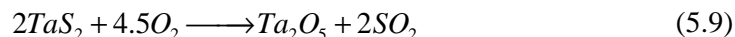


Figure 5.31: SEM micrographs from **S-O400b_4h** showing: (a) general morphology; (b) plate-like crystals, (SEM #4)

After 16 hours, (**S-O400b_16h**) the bulk materials appeared uniformly white in colour though with a slight greyish appearance. TG-DTA (Figure 5.32) was performed to see if the greyish appearance was due to small amounts of black TaS_2 being present. The initial loss in mass,

(Region A) is probably due to water coming off the sample. There is then an exothermic event that happens at 600 °C (Region B), resulting in the weight change of about +3.5 wt%. This weight change is very strange as any residual TaS₂ would lead to a weight loss of up to 9.8 % as a result of the molar ratio of 2:1 for the tantalum species as shown in Equation (5.9) and the loss of the heavy sulfur species. Ta₂O₅ would, as seen previously, have no change in mass on heating in air at these temperatures.



The increase in mass is indicating an increase in oxygen content so species with lower oxygen content than Ta₂O₅ were investigated. A theoretical transition as shown in Equation (5.10) would yield a theoretical weight change of +3.7% and is therefore a likely candidate for the reaction phase. This is suggesting that at 400 °C the reaction does indeed get close to completion but with TaO₂ as the majority phase in the product rather than Ta₂O₅.



It possible therefore that the nanofibres produced in this, (S-O400n_4h) will be of the TaO₂ structure rather than the Ta₂O₅.

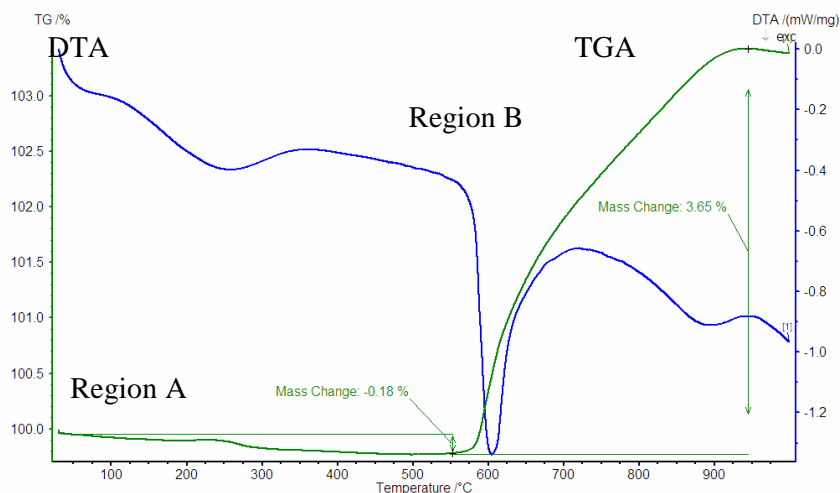


Figure 5.32: TG-DTA trace for S-O400b_16h.

5.3.2.3 Preparation N-O400b_4h

The products from this reaction were red in colour and appeared to have changed very little when compared to the starting material. PXD analysis however showed the presence of small amounts of Ta_2O_5 and TaON indicating that some reaction has taken place.

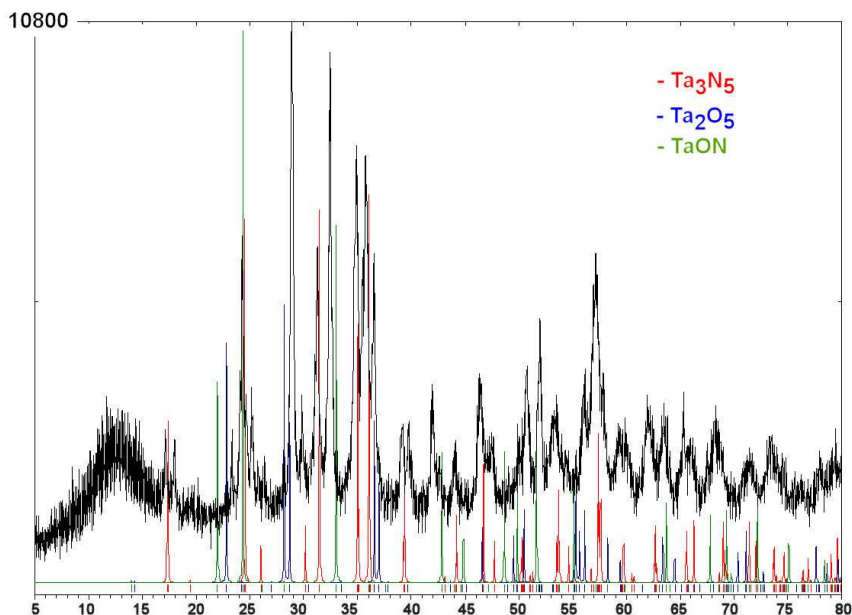


Figure 5.33: PXD analysis for N-O400b_4h.

5.3.2.4 Preparation S-O800n_4h

The reaction produced white fibrous material which was removed from the furnace and analysed by PXD and SEM. The PXD looks more crystalline (Figure 5.34) when compared to that observed for the low temperature (S-O400n_4h) (Figure 5.42(a)). The pattern given in Figure 5.34 was indexed using Dicvol 6,¹⁸⁰ and refined to the best unit cell, using CELREF¹⁸¹ giving an orthorhombic unit cell as seen in Table 5.12. The cell parameters are a reasonable match to those of the published Ta_2O_5 structure.²²³

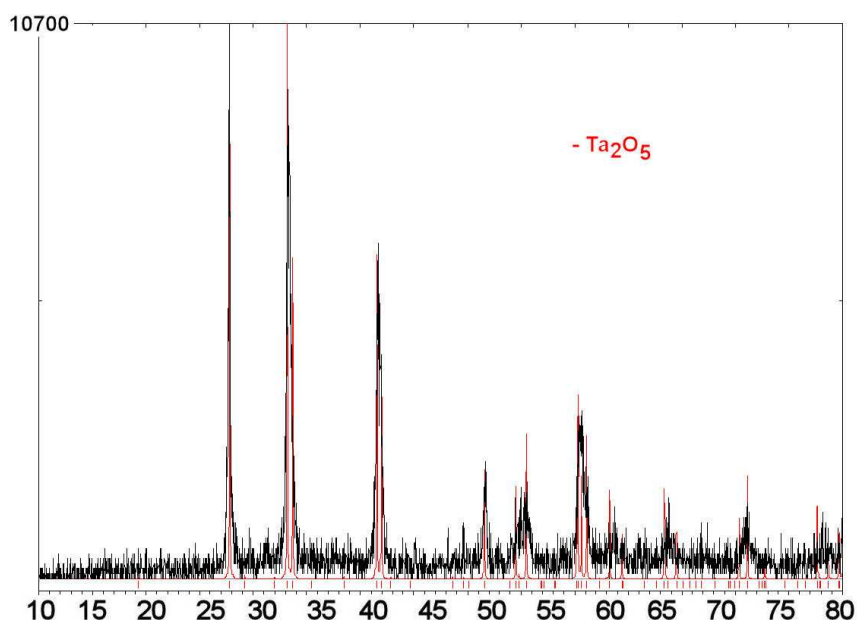


Figure 5.34: PXD data for the nanowires from **S-O800n_4h** showing a match to the structure for Ta_2O_5 , (D5000 diffractometer and double-sided adhesive carbon tab).

Phase	<i>a</i>	<i>b</i>	<i>c</i>
S-O800n_4h	6.21(1) Å	3.66(1) Å	7.778(1) Å
S-O800b_4h	6.218(6) Å	3.664(9) Å	7.798(8) Å
Ta_2O_5	6.2170 Å	3.6770 Å	7.7940 Å

Table 5.14: Unit cell parameters from the indexed powder patterns of preparation **S-O800n_4h**, compared to the published values for Ta_2O_5 .²²³

SEM Shows the presence of ribbons or belts, with a high tendency to curl up into scroll like formations or twist into ribbon-like curls, (Figure 5.35). The widths of the bundles ranged from a few microns to a few tens of nm, with aspect ratios of ~ 5000 , (lengths ~ 0.5 mm, Widths ~ 100 nm). These are similar in many respects to the sulfide fibres from which they were formed.

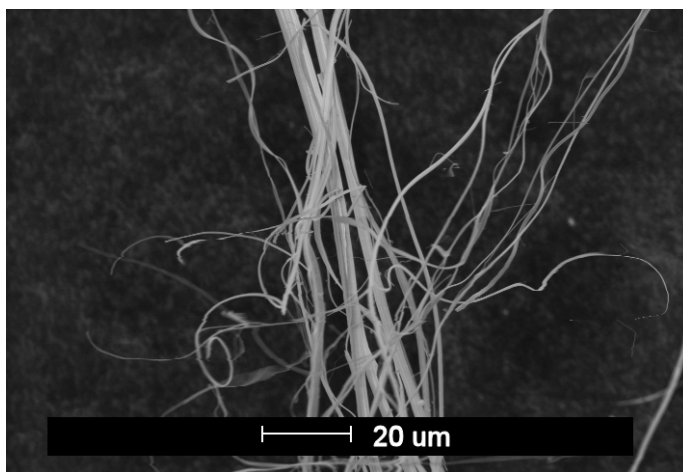


Figure 5.35: SEM micrograph showing the Ta_2O_5 ribbons from **S-O800n_4h**, (SEM #4).

TEM shows nanofibres with a high degree of crystallographic texture aligned towards the direction of propagation of the fibre. (Figure 5.36). The SAED inset has been indexed to the published structure of Ta_2O_5 and the directions of spots and corresponding hkl values have been marked. The direction of propagation of the long axis of the fibre corresponds with the 00l direction as has been found with the Ta_3N_5 nanofibres. The 110 direction is found to be perpendicular to the long axis of the fibre, again similar to the nitride nanofibres produced in **S-N950n_4h**, Section 5.3.1.3. The general reflection conditions for the space group indicate that the 00l should only show alternate spots as $l=2n$ which is indeed the case. There must be some cooperation between growth of the oxide / nitride crystal structure out of the sulfide structure that promotes growth along the 00l direction and prohibits growth along the 110 direction of the orthorhombic structure. The oxide fibres produced from single crystalline tantalum disulfide fibres do not have the clear granular effect in the bright field image that has been observed in the ammonolysis reactions. The diffraction contrast on the TEM micrograph in Figure 5.36 suggests more of a band type structure. However this is more likely due to bending strain caused by the minimal bending of the nanoribbon, similar to that noted by Hor *et al.* in NbSe_3 nanoribbons.⁵⁵

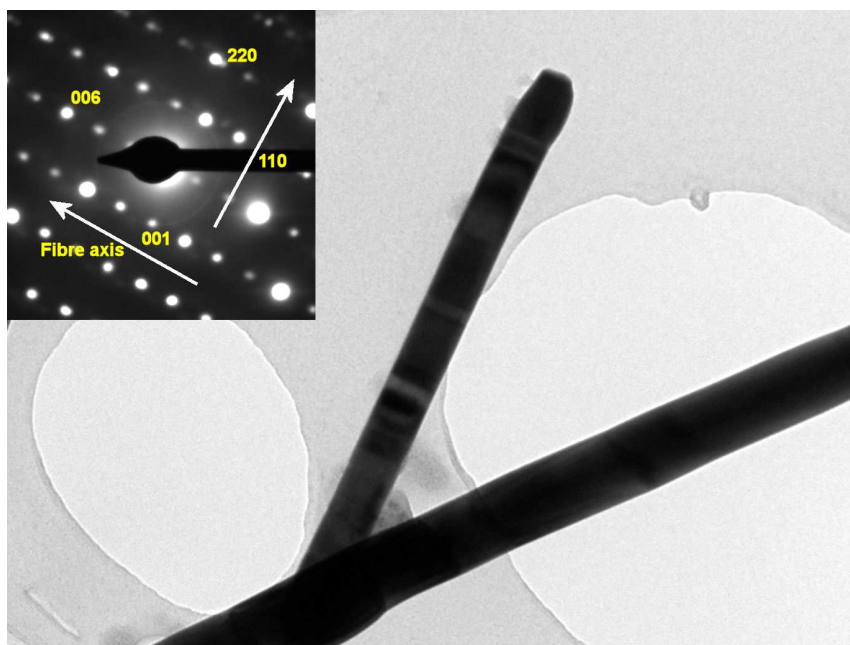


Figure 5.36: TEM micrograph with SAED inset showing typical Ta₂O₅ nanowires.

The UV-vis DRS (Figure 5.37) of Ta₂O₅ nanowires show a band gap of 3.81 eV in agreement with estimated values from other authors of 3.80 eV.¹³⁹⁻¹⁴³ A small blue shift is noticed that could be associated with the particle size relationship described above when the nanofibres are compared with the bulk materials from **S-O800b_4h** (Figure 5.29) with a band onset of 3.79 eV.

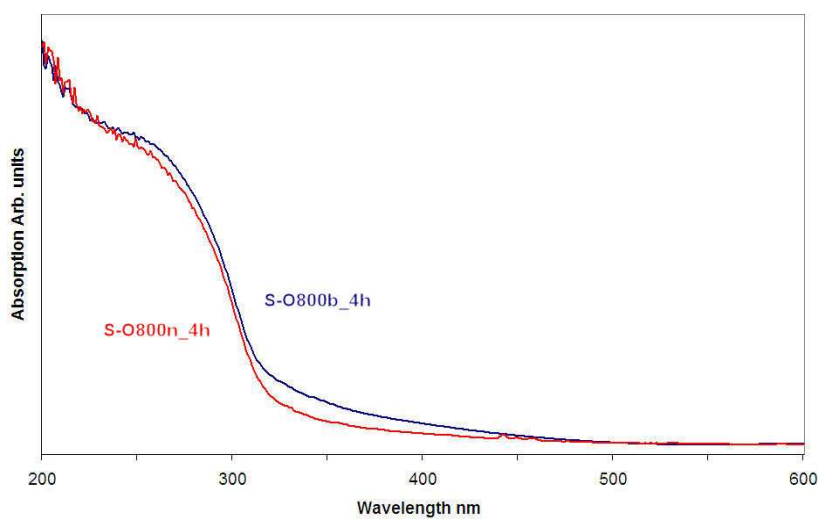


Figure 5.37: UV-vis DRS data collected for **S-O800n_4h**, showing a band gap onset at 3.81 eV for and **S-O800b_4h**, showing a band gap at 3.79 eV.

5.3.2.5 Preparation N-O800n_4h

The white fibrous material from **N-O800n_4h** was analysed by PXD showing a crystalline pattern that matches to the peaks expected from Ta_2O_5 . There also appears to be a minimal amount of Ta_3N_5 present, (Figure 5.38).

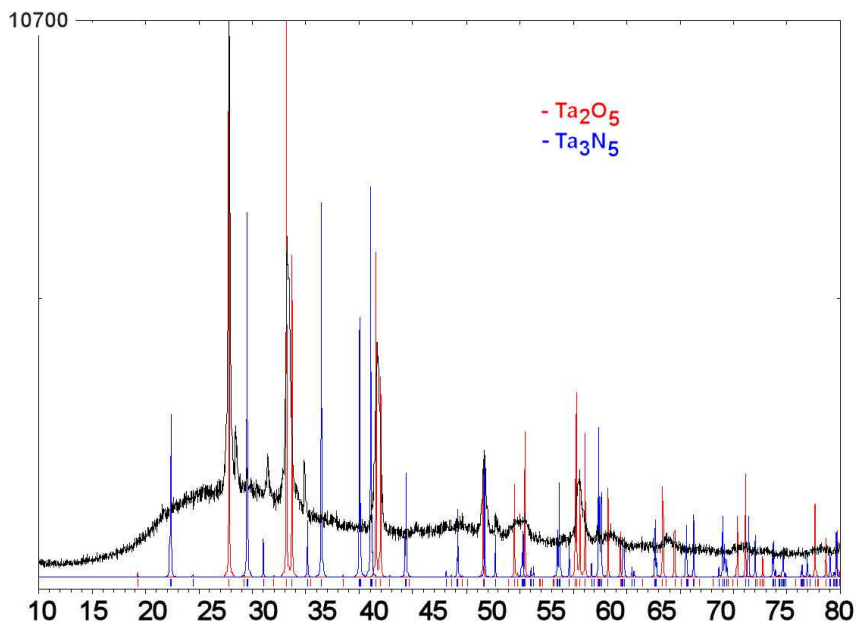


Figure 5.38: PXD analysis of products from **N-O800n_4h**.

The peaks from the main oxide phase were indexed and gave an orthorhombic unit cell with unit cell parameters given in Table 5.15. The values match with minimal contraction of the b and c unit cell directions showing that the phase is likely to be the Ta_2O_5 structure.

Phase	a	b	c
N-O800n_4h	6.25(1) Å	3.654(7) Å	7.782(6) Å
Ta_2O_5	6.2170 Å	3.6770 Å	7.7940 Å

Table 5.15: Unit cell parameters from the indexed powder patterns of **N-O800n_4h**, compared to the published values for Ta_2O_5 .²²³

SEM analysis shows the presence of a fibrous morphology with many similarities in appearance to those seen in the precursor, (Figure 5.10). Aspect ratios were recorded at less

than the 4000 from the precursor indicating that the fibres have been reduced in length during the synthesis. Typical aspect ratios were ~333 with lengths ~100 μm and widths ~300 nm.

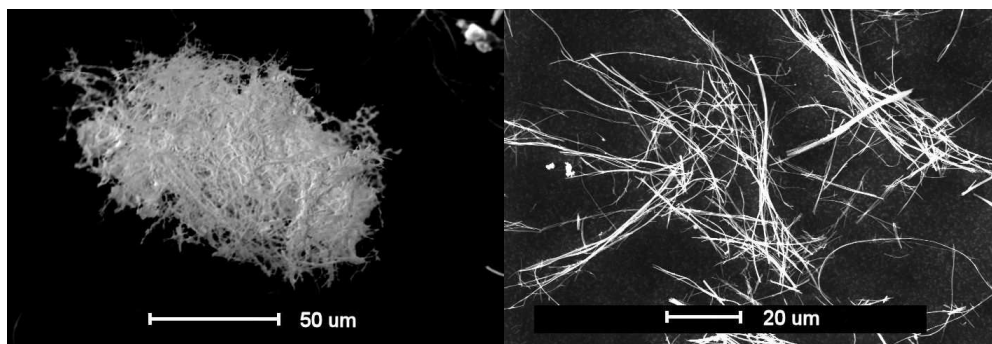


Figure 5.39: SEM micrographs from **N-O800n_4h**, (SEM #4).

The morphology of the oxide nanowires produced in **N-O800n_4h** is remarkably similar to that seen in the nitride precursor. The SAED data indicated that there is a reasonable degree of crystallinity to the wires with crystallographic texture observed running along the long axis of the wire though it is more subtle than that observed in the sulfide precursor reactions, (**S-O800n_4h**). The SAED pattern spots are more diffuse indicating that there are more crystals diffracting at slightly different angles spreading out the resolution of the spots. The pattern again indexes to the structure of Ta_2O_5 as in **S-O800n_4h** with the direction of propagation along the wire, being the 001 direction, as seen in Figure 5.40(b) running from position 1-2. The direction that is perpendicular to the long axis of the wire again is the 110 direction, (position 3-4). The positions 1-4 correspond to indexed spots of $00\bar{6}$, 006 , $\bar{1}10$ and 110 respectively.

BET analysis recorded a specific surface area of $42.42 \text{ m}^2\text{g}^{-1}$ which is comparable with the other values for nanofibrous materials discussed above. It is slightly lower than that of the nitride material but still a factor of 40 above that of the bulk.

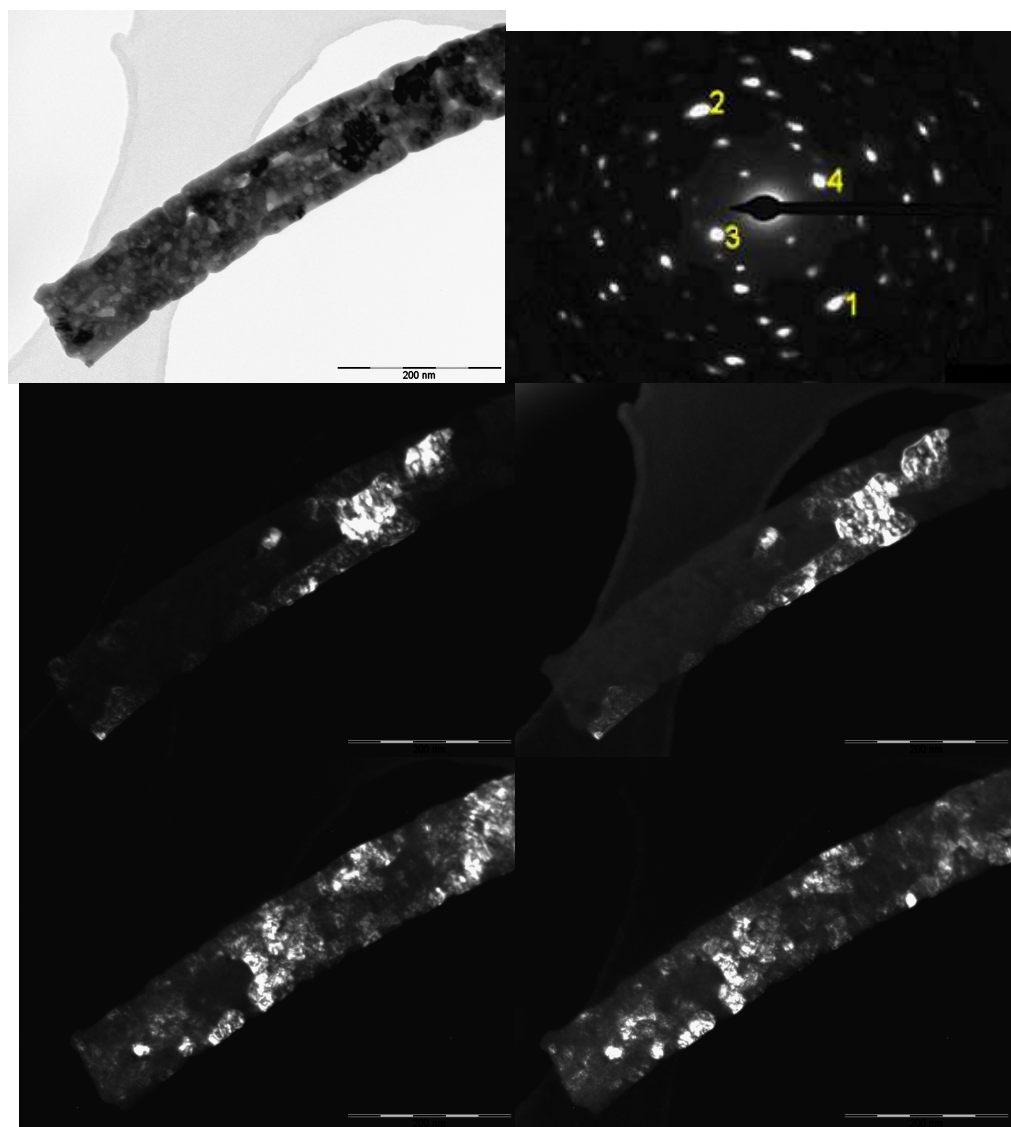


Figure 5.40: Bright field and corresponding dark field images of the products of **N-O800n_4h**, (T20 Microscope).

5.3.2.6 Preparation S-O400n 4h

Initial reactions at 400 °C showed an amorphous product as seen in Figure 5.42(a) by PXD. The positions of the diffuse peaks approximately match to those expected for both the Ta_2O_5 and TaO_2 structure, though resolution of the peaks does not allow for the determination of the likely underlying crystal structure or indeed the ratio of Ta:O within the amorphous mass.

TG data was recorded as in Section 2.4.4.3 but on samples of ~ 5-10 mg (Figure 5.41(b)) and shows a 6 % increase in mass as it is oxidised, indicating that the nanofibres are

not of Ta_2O_5 stoichiometry; however, the increase in mass is not attributable to any obvious stoichiometry, and therefore likely to be a mix of Ta_2O_5 and TaO_2 , as shown by the PXD. The increase in mass above 3.5 % will likely be due to the uptake of oxygen in the structure from other suboxides that may be present, e.g. TaO .

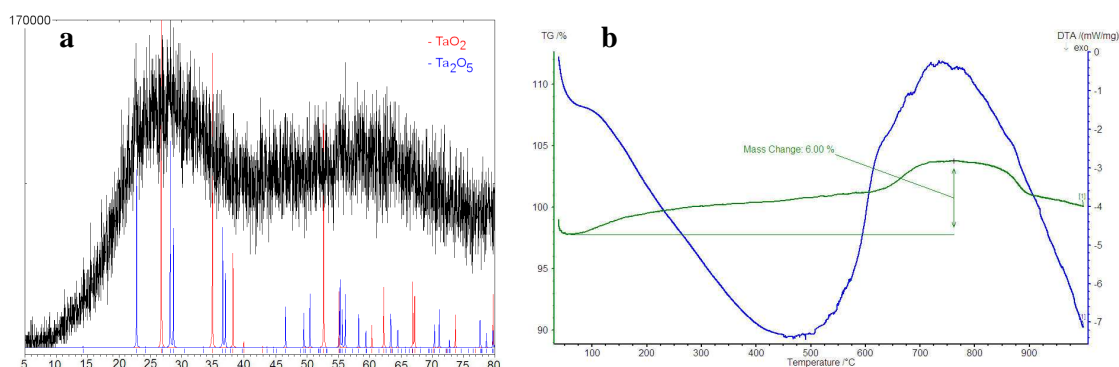


Figure 5.41: (a) PXD pattern showing oxide nanowires of amorphous nature, (D5000 diffractometer); (b) TG analysis showing a 6 % increase in mass on heating in Ar/air mixture;

SEM (Figure 5.42(a) and (b)) shows the presence of large brittle ribbons with other structures that have probably originated from splintering of ribbons during the sample preparation for SEM analysis. The aspect ratio of the fibres is ~ 60 , ($\sim 60 \mu\text{m}$ length, $1 \mu\text{m}$ width).

TEM shows the nanowires to be amorphous with regions of polycrystalline nature, indicated by the diffuse rings in the SAED pattern (Figure 5.42(c)).

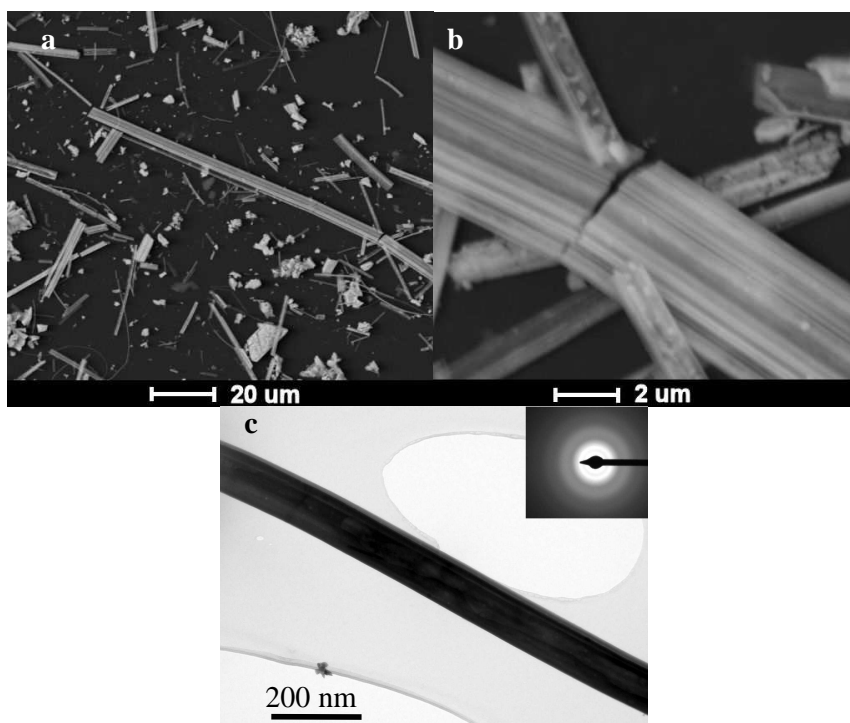


Figure 5.42: (a) SEM micrograph showing large ribbons, (S-O400n_4h); (b) SEM micrograph showing a fragmenting ribbon, (SEM #3) and (c) TEM micrograph showing a nanowire with the electron diffraction pattern inset, (S-O400n_4h), (T20 microscope).

5.3.2.7 Preparation N-O400n_4h

Initial reactions at 400 °C showed an amorphous product as seen with S-O400n_4h. PXD, (Figure 5.43) shows diffuse peaks approximately matching the position of those expected for both the Ta₂O₅ and TaO₂ structure, though resolution of the peaks does not allow for the determination of the likely underlying crystal structure or indeed the ratio of Ta:O within the amorphous mass. The fibres were red in colour indicating that unlike in the bulk form Ta₃N nanofibres do react with oxygen at these low temperatures. The thermal stability of the fibres is obviously an important property with higher temperature applications. In Figure 5.4 it was noted that the bulk nitride converts to oxide in the presence of air but not until the TG reaches temperatures above 450 °C.

TG data was recorded as in Section 2.4.4.3 but on samples of ~ 5-10 mg (Figure 5.41(b)) and shows a 5.69% increase in mass as it is oxidised, slightly less than for the sulfide

precursor, indicating that the nanofibres are not of Ta_2O_5 stoichiometry; however, the increase in mass is not attributable to any obvious stoichiometry.

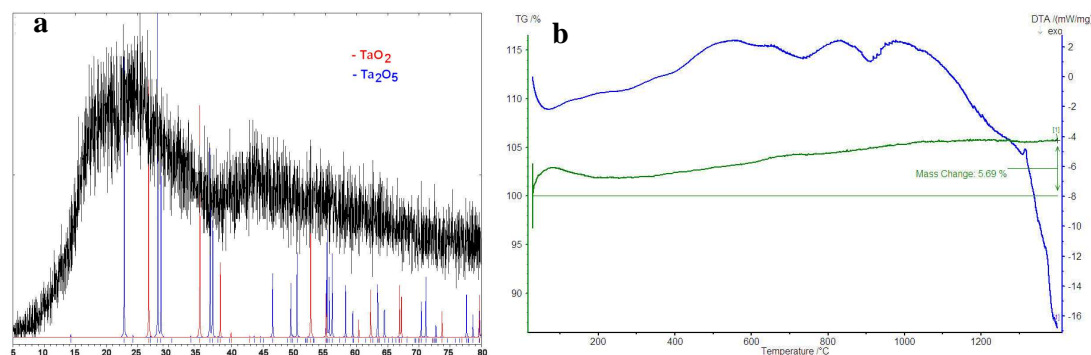


Figure 5.43: (a) PXD pattern showing oxide nanowires of amorphous nature, (D5000 diffractometer); (b) TG analysis showing a 6% increase in mass on heating in Ar/air mixture;

SEM (Figure 5.42(a) and (b)) shows the presence of large brittle ribbons with other structures that have probably originated from splintering of ribbons during the sample preparation for SEM analysis. The aspect ratio of the fibres in both cases is ~ 50 ($\sim 100 \mu\text{m}$ length, $\sim 2 \mu\text{m}$ width).

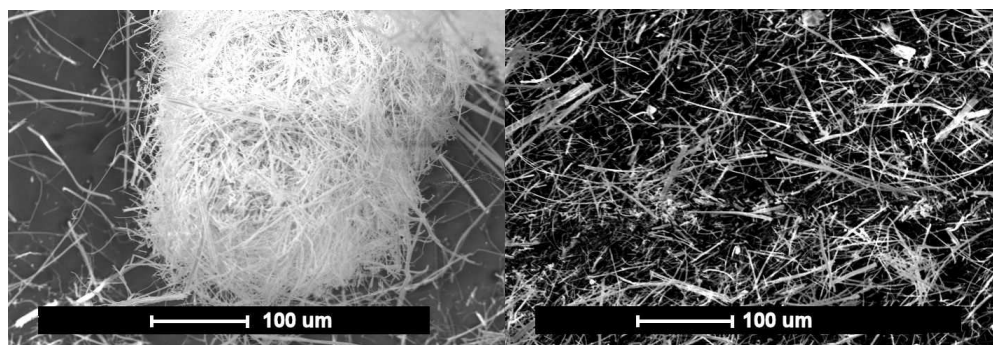


Figure 5.44: SEM micrograph showing large ribbons, (SEM #4).

5.3.3 Sulfidation Reactions

5.3.3.1 Preparations O-S1000b 14h

Upon opening the tube furnace and removing the alumina boat, it was noticed that there was a black powder and a small amount of black fibrous material on the edge of the boat. The products of the reaction were analysed and characterised.

PXD analysis of the residual powder showed the 3R polytype of TaS₂ as the dominant phase, as shown by Figure 5.45. A small amount (~ 2 % by peak intensity using PowderCell¹⁷⁹) of the 1T polytype is present in the pattern along with a small amount of starting material, indicating that the reaction did not go fully to completion; it is likely that the small quantity of Ta₂O₅ present was outside the flow of CS₂ and protected from reaction by the other reactants. This reaction used ~ 2 g of oxide precursor rather than the 1 g as in the other preparations. The presence of both 3R and 1T polytype is not unprecedented as at 1000 °C the 1T should be the dominant phase (as seen in Section 3.3.3.1 from the products of **TaS₂1000_Std**), however as the cooling was slow, the 1T-TaS₂ would likely convert to 3R-TaS₂ at around 600 °C. The peaks in the pattern were indexed and refined to give unit cell parameters in a hexagonal unit cell as shown in Table 5.16. The accuracy of the unit cell refinement is greater than that of the published values leading to the conclusion that the structure is the 3R-TaS₂. The use of the Scherrer equation on the primary peak yields a value of ~ 2 µm for the average particle size.

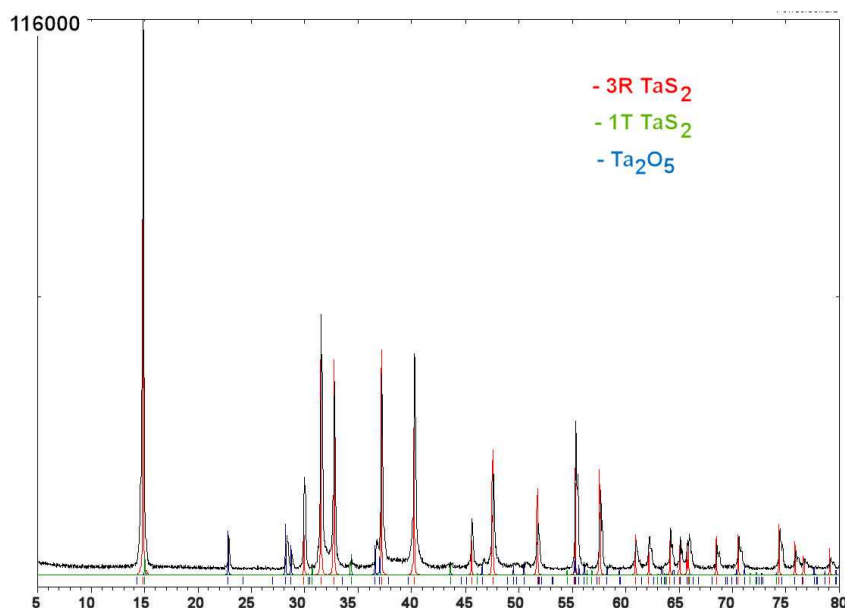


Figure 5.45: PXD pattern from the residual powder corresponding to the 3R and 1T phases of TaS₂, (D5000).

Phase	<i>a</i>	<i>c</i>
O-S1000n_14h	3.3180(8) Å	17.8969(2) Å
3R-TaS ₂	3.320 Å	17.90 Å

Table 5.16: Unit cell parameters from the indexed powder patterns of **O-S1000n_14h**, compared to the published values for 3R-TaS₂.¹¹²

SEM analysis of the low density fibrous material shows similar structures to those discussed in the silica ampoule experiments in Chapter 3. This was the only preparation in this section to start with a bulk precursor and finish with a nanophase product. The yield was however immeasurably small, reducing the potential of this preparation as a useful synthesis for TaS₂ nanofibres. The particles were seen to consist of blocks of TaS₂ and were present as contamination within the fibrous mass. Both morphologies had an average ratio of Ta:S of ~ 33:67 by EDX, (± 2).

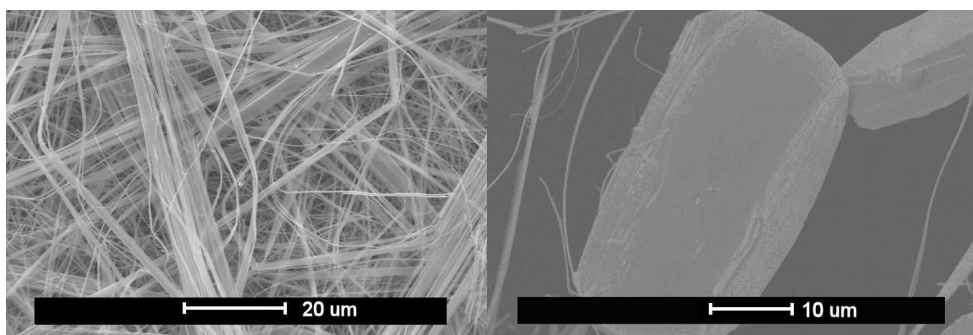


Figure 5.46: SEM micrographs showing the general morphology from **O-S1000b_14h**, (SEM #2)

5.3.3.2 Preparation O-S850b 4h and Preparation N-S850b 4h

A black powder was obtained from the alumina boat that was characterised to the 3R structure of TaS_2 with a small amount of oxide contamination. It appears that the reaction has not reached completion even though the material was uniformly black in colour. It is likely that a small amount of oxide material remained in the bottom of the alumina boat and was not reacted with the CS_2 . The pattern given in Figure 5.47 was indexed using Dicvol 6,¹⁸⁰ and refined to the best unit cell, using CELREF¹⁸¹ giving an hexagonal unit cell as seen in Table 5.17. The cell parameters are again a good match to those of the published 3R- TaS_2 structure,¹¹² as in the higher temperature synthesis.

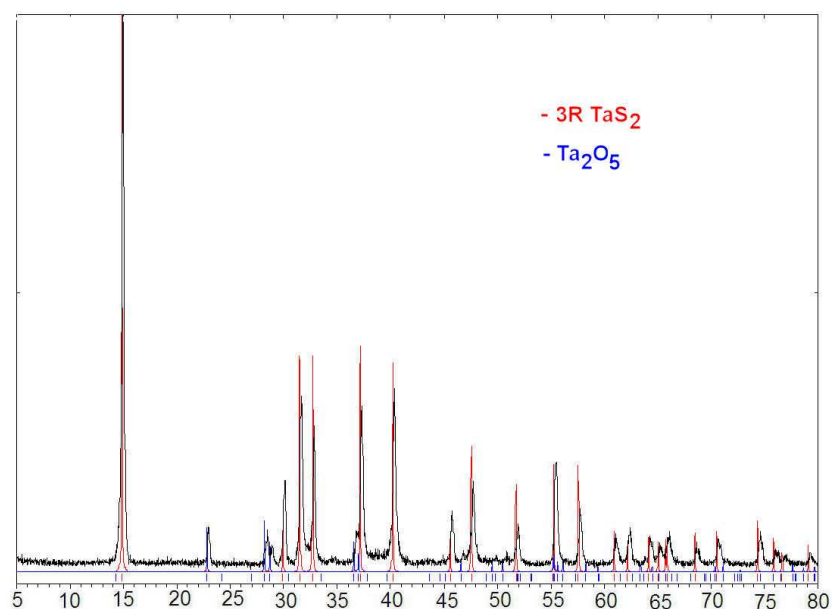


Figure 5.47: PXD for the products of **O-S850b_4h**, (D5000 diffractometer).

The pattern given in Figure 5.47 was indexed using Dicvol 6,¹⁸⁰ and refined to the best unit cell, using CELREF¹⁸¹ giving a hexagonal unit cell as seen in Table 5.17. The cell parameters are a good match to those of the 3R-TaS₂ structure, and have been compared to those from **O-S1000n_14h**.

Phase	<i>a</i>	<i>c</i>
O-S850b_4h	3.313(1) Å	17.8468(4) Å
O-S1000n_14h	3.3180(8) Å	17.8969(2) Å
3R-TaS ₂	3.320 Å	17.90 Å

Table 5.17: Unit cell parameters from the indexed powder patterns of **O-S850b_4h** and **O-S1000n_14h**, compared to the published values for 3R-TaS₂.¹¹²

SEM (Figure 5.48) shows sharp angular crystallites and a lack of round plate-like particles. The morphology is directly comparable with that in Figure 5.28, suggesting that the sulfidation reaction is pseudomorphic in nature. EDX again confirms the 1:2 ratio Ta:S indicating that the product is TaS₂.

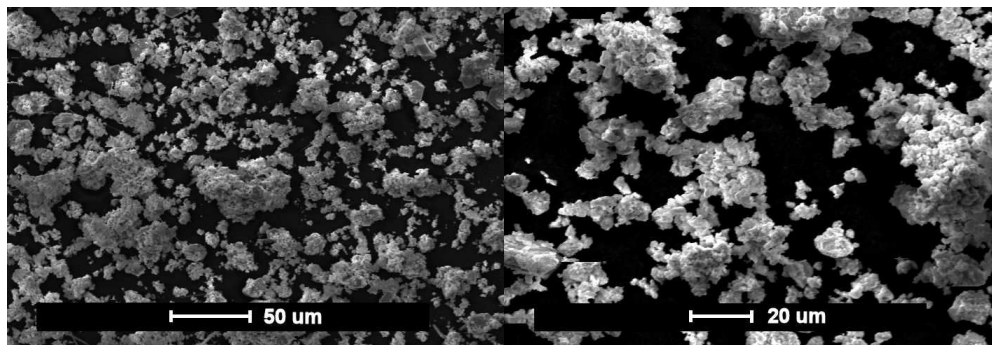


Figure 5.48: SEM micrograph showing the general morphology of the powders from **O-S850b_4h**, (SEM #4).

5.3.3.3 Preparation N-S850n_4h

A sample of black fibrous appearance was recovered from the alumina boat used in the preparation. The fibres were extremely similar to those seen in the precursor. Aspect ratios were recorded of ~ 4000, as observed in the nitride precursor. The fibres consist of ribbons and belts by conventional definitions (Section 1.1.3). These nanofibres have survived two

complete crystal structure changes from sulfide to nitride and back to sulfide without losing their 1-dimensional microstructure, or fragmenting along their lengths.

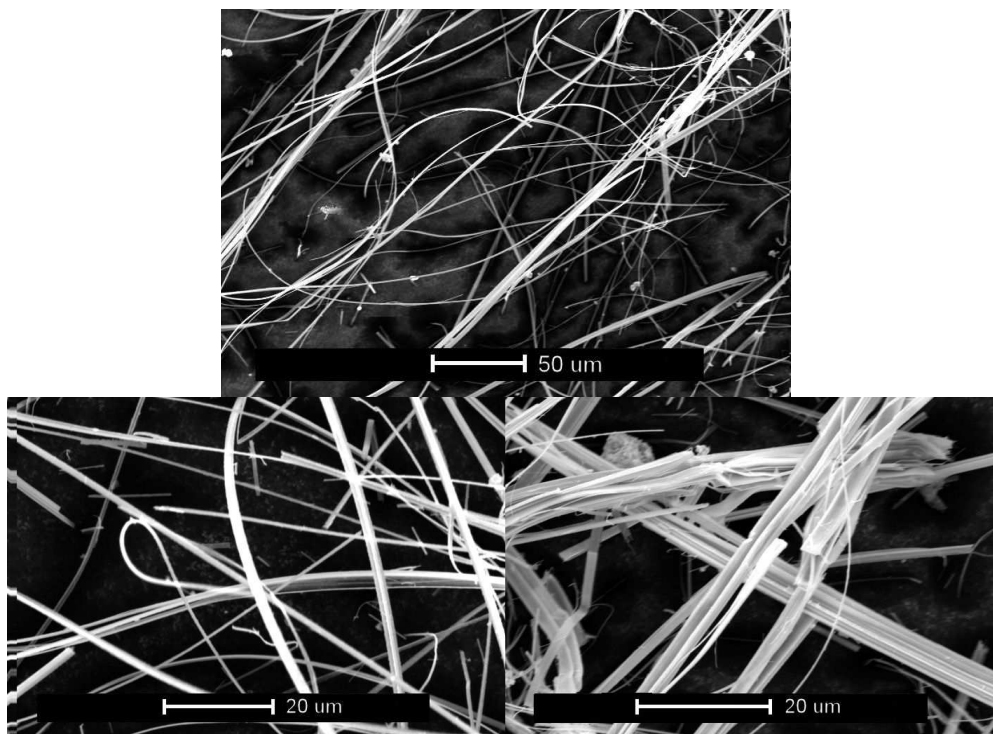


Figure 5.49: SEM micrograph of the products from **N-S850_4h**, (SEM #4).

Figure 5.50 shows the general morphology of the fibres in the three phases of the overall reaction. The fibres were initially in the form of TaS_2 from **TaS₂650_SAG** before being converted into Ta_3N_5 in **S-N950n_4h** and finally back into TaS_2 again after **N-S850n_4h**. The fibres have withstood their fibrous nature throughout the processes and are clearly intact with the 1-dimensional morphology characteristic of nanofibres. Aspect ratios have been maintained, though the fibres are no longer as clean and particulate free as in the initial sulfide phase.

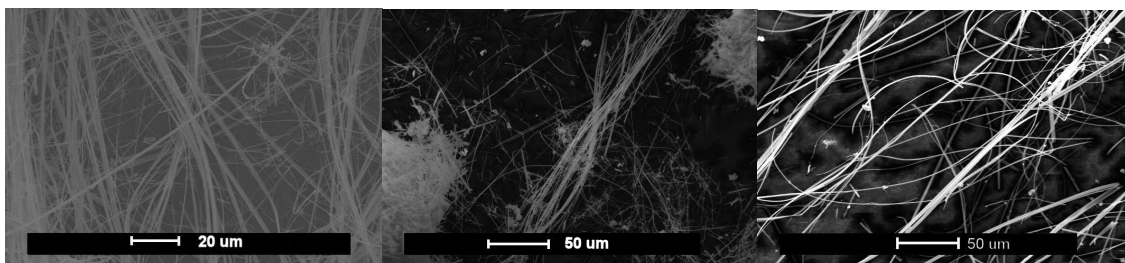


Figure 5.50: SEM micrographs showing the general morphology of : (a)TaS₂ fibres (Figure 3.17); (b) Ta₃N₅ nanofibres Figure 5.10 and (c) TaS₂ nanofibres (Figure 5.49) (SEM #4).

5.3.3.4 Preparation O-S850n 4h

The resultant nanofibres from the oxide precursor reaction were black in colour indicating that the formation of sulfide had been achieved. The PXD pattern (Figure 5.51) however showed significant amorphous character. This is unsurprising as there was some loss of crystallinity as the initial sulfide was converted into oxide (Section 5.3.2.3) There is one highly resolved peak at 14 ° 2θ which corresponds to the 001, 002 or 003 lattice planes of the 1T, 2H and 3R polytype structures respectfully. There is not resolution within the data to successfully differentiate between the different polytypes of TaS₂. The peak is not however, expected in the PXD pattern for the Ta₂O₅ structure indicating that the crystal structure has transforms and the sulfide has been formed. The few resolvable peaks do not match those expected for the any of the oxide phases described above.

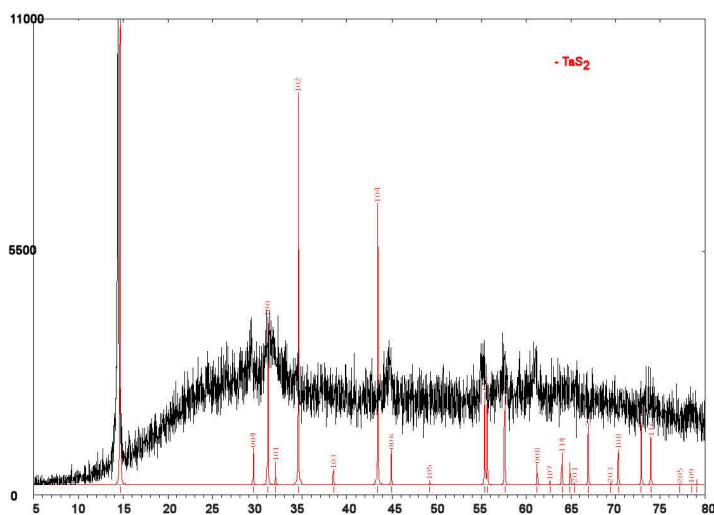


Figure 5.51: PXD showing the match between the products of S-O850n_4h, (D5000 diffractometer)

SEM shown in Figure 5.52 shows the morphology of the oxide nanofibres, Figure 5.35. Ribbons and belts are again observed as in **N-S850n_4h**, concluding that indeed the reaction back to TaS_2 nanofibres is possible with minimal change in morphology. The aspect ratio of 5000 is retained although these fibres appear to be straighter and less curly. Pictorially the products from **O-S850n_4h** appear half way between the straight long sulfide wires and the curly oxide wires, indicating that there is retention of morphology at each stage.

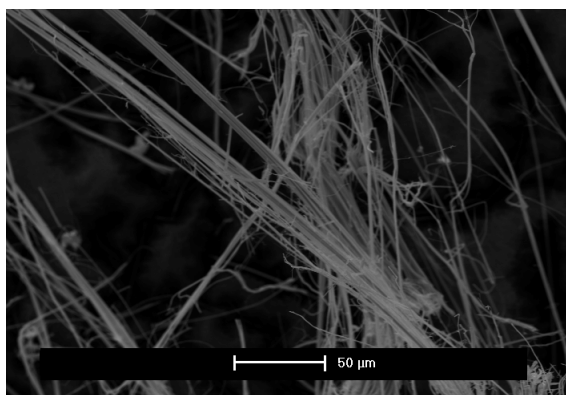


Figure 5.52: SEM micrograph showing the nanofibres obtained from **O-S850n_4h**, (SEM #4).

The pseudomorphic nature of the nanofibres is best shown with images of the different fibres side by side. The nanofibres obtained from **O-S850n_4h** originated as TaS_2 from **TaS₂650_SAG** Figure 5.53(a) before being converted into Ta_2O_5 in **S-O800n_4h** Figure 5.53(b) and then back into TaS_2 in **O-S850n_4h** Figure 5.53(c). The fibrous morphology is retained though there is a high degree in initial loss of aspect ratio in the first step of the process. The average aspect ratio of the initial sulfide precursor approximately halves with lengths approximately quartering during the oxidation process. The aspect ratio is then increases on conversion back into the sulfide material.

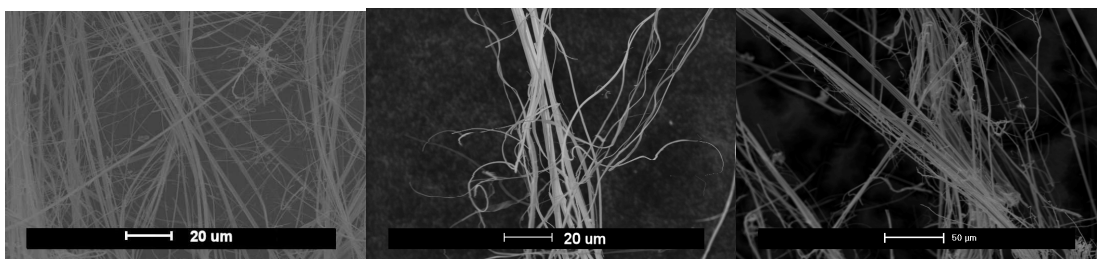


Figure 5.53: SEM micrographs showing the general morphology of : (a)TaS₂ fibres (Figure 3.17); (b) Ta₂O₅ Fibres (Figure 5.35) and (c) TaS₂ fibres (Figure 5.52), (SEM #4).

5.4 Conclusions

The pseudomorphic nature of these reactions is apparent from the retention of the fibrous morphology as can be seen from Figure 5.50 and Figure 5.53. A clear trend in crystallinity is observed between the products of the three preparations, **S-N950n_4h**, **S-N800n_4h**, and **S-N650n_4h**: the trend runs from most crystalline and least amorphous, at highest temperature (950 °C) to least crystalline and most amorphous, at the lower temperature (650 °C) as reported by Hector and Henderson.²¹⁹ The existence of single crystalline nanofibres of Ta₃N₅ remains unproven. There is however, a clear influence from the precursor crystallinity as the single crystal disulfide nanofibres once reacted with ammonia have more crystallographic texture than those originating from the less crystalline oxide precursor. The ramp rate of the heating step to obtain the sintering temperature may also have an effect on the crystallinity of the products and the size of the grains; however this has not been investigated.

Oxidation of the sulfide nanofibres did not lead to the beaded appearance observed in the nitride phases unless the beaded structure was already present, as is indicated by the similar reactions from sulfides to both the oxides and the nitrides. It is likely that the mechanism of oxidation is very different to that of the ammonolysis leading to the different structures or simply takes place in a slower and more uniform manner. The ammonolysis tends to form a beaded structure with differently ordered crystals while the oxidation forms amorphous or polycrystalline structures. In Shaffer's experiments however a large beaded effect was noted when converting from TiC to TiO₂.¹⁷⁶ It is therefore likely that the beaded

effect is more about the speed in which the chemical conversion occurs rather than the phases which are being converted. This is evident from the fact that in comparing the oxidation of TiC and TaS₂, one produced the beaded effect and the other does not, while the ammonolysis of TaS₂ again produces a beaded effect.

It is possible to convert the nitride and oxide species into sulfides using CS₂, however, it would be interesting to see if the formation of nanofibrous material could be facilitated by increasing the sintering temperature. It was observed in **O-S1000b_14h** that minimal nanofibres were formed from the bulk materials at high temperatures, (though the yield was immeasurably small). What therefore would happen if a preparation was attempted utilising a nanofibrous oxide precursor and reacting with CS₂ at 1000 °C for 14 hours? Would this indeed have a reducing effect on the size and morphology, as is the case with the reduction of trisulfide phases with H₂, used in the formation of many sulfide nanotubes where there is an apparent size and morphology reducing effect?^{43, 160} If so, would the reducing effect take place in all directions i.e. produce nanoparticulates or would it result in smaller nanofibres by reducing in an anisotropic manner?

The UV-vis DRS data shown in Figure 5.54 simultaneously show the comparisons between the bulk and nanofibrous phases of both the oxide and nitride. We observe a blue shift as the morphology changes from bulk to nanofibrous much the same as the shift associated with the reduction of particle size. It would be interesting to do the catalytic activity experiments and see if indeed the catalytic activity is improved as a result of the morphology as well as particle size. Differentiating between the two is likely to be difficult as the changing morphology will have an effect on the particle size.

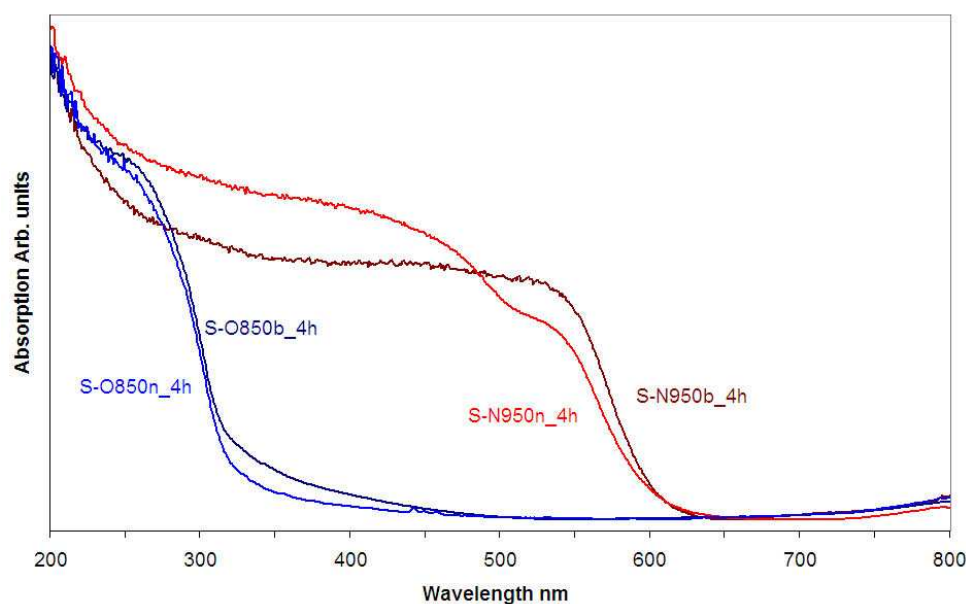


Figure 5.54: Diffuse reflectance data showing the superimposition of the 4 different phases described in this chapter on one set of axes.

The reactions described in this chapter also occur in a pseudomorphic way when starting with a trisulfide precursor (Chapter 4) potentially allowing unprecedented control over the yield and morphology of the products as a higher degree of initial control exists across both systems than for any one system. E.g. in Section 3.3.3.3 it was shown how nanoribbons of TaS_3 could be produced in a 1:2 ratio starting material at 500 °C.

The concept of “Pseudomorphic reactions to nanometric materials” has opened up a huge area of study. The examples listed in this section of this thesis barely scratch the surface of what is possible from the extension of this work. Tantalum nitride has many known structures the stable ones as calculated by Stampfl and Freeman, using density functional theory and include Ta_5N_6 and Ta_2N as well as Ta_3N_5 .²²⁴ There are then further meta-stable phases all of which could have interesting properties and potential uses in applications. Changing the preparative conditions could induce the formation or conversion to nanometric materials of all these phases. By changing the experimental parameters, e.g. sintering temperature, it should be possible to form independent nanometric phases outside the triangle shown in Figure 5.1. An example of this would be the formation of TaON , another

potentially useful photocatalyst,^{139, 141, 143, 220} by changing the ratio's of the gasses and temperature profiles or indeed by approaching the desired phase via a solely nitride or oxide phase. The chemistry and concepts of this chapter are far from limited to the tantalum system. The group at the University of Glasgow as a whole has had much recent success in the formation of the titanium analogues of the tantalum compounds discussed herein. This has resulted in the formation of other nanometric phases such as TiN and TiO₂. Extension still further opens an endless supply of potentially useful systems for which there is a single possible nanometric phase and the ability to form both nitrides, oxides, sulfides and indeed carbides. A possible example is the recent paper regarding ZnO nanospheres.²²⁵ These interesting spheres could, via the methods above, lead to the formation of nanospheres of zinc sulfide which has possible application in many of the currently used fields for zinc sulfide, e.g. IR optical materials and glow in the dark products.

Chapter 6: References

- 1 W. Yana, R. Wanga, Z. Xua, J. Xua, L. Lina, Z. Shena, and Y. Zhoua, *J. Molecular*
- 2 *Catalysis A*, 2006, **255**, 81.
- 3 S. Schimpf, M. Lucas, C. Mohra, U. Rodemerck, A. Brückner, J. Radnik, H.
- 4 Hofmeister, and P. Claus, *Catalysts Today*, 2002, **2592**, 1.
- 5 M. H. Rashid and T. K. Mandal, *J. Phys. Chem. C*, 2007, **45**, 16750.
- 6 B. L. V. Prasad, S. I. Stoeva, C. M. Sorensen, V. Zaikovski, and K. J. Klabunde, *J.*
- 7 *Am. Chem. Soc.*, 2003, **125**, 10488.
- 8 R. Feynman, in 'There's plenty of room at the bottom', 1959.
- 9 H. W. Kroto, J. R. Heath, S. C. O'Brien, R. F. Curl, and R. E. Smalley, *Nature*, 1985,
- 10 **318**, 14.
- 11 S. Iijima, *Nature*, 1991, **354**, 56.
- 12 R. Tenne, L. Margulis, M. Genut, and G. Hodes, *Nature*, 1992, **360**, 444.
- 13 R. R. Chianelli, E. Prestridge, T. Pecorano, and DeNeufville, *Science*, 1979, **203**,
- 14 1105.
- 15 L. V. Radushkevich and V. M. Lukyanovich, *Russ. J. Phys. Chem.*, 1952, **26**, 88.
- 16 J. Molera, C. Bayés, P. Roura, D. Crespo, and T. Pradell, *J. Am. Ceram. Soc.*, 2007,
- 17 **90**, 2245.
- 18 M. Reibold, P. Paufler, A. A. Levin, W. Kochmann, N. Pätzke, and D. C. Meyer,
- 19 *Nature*, 2006, **444**, 286.
- 20 <http://www.fibrils.com/index.htm>, Hyperion Catalysis FIBRILS.
- 21 L. Rapoport, Y. Bilik, Y. Fieldman, S. R. Cohen, M. Homyonfer, and R. Tenne,
- 22 *Nature*, 1997, **387**, 791.
- 23 S. Prasad and J. Zabinski, *Nature* 1997, **387**, 761
- 24 J. R. Kim, H. Oh, H. M. So, J. J. Kim, J. Kim, C. J. Lee, and S. C. Lyu,
- 25 *Nanotechnology*, 2000, **13**, 701.
- 26 J. Chen, S.-L. Li, Q. Xu, and K. Tanaka, *Chem. Commun.*, 2002, 1722.
- 27 J. Chen, N. Kuriyama, H. Yuan, Hiroyuki T. Takeshita, and T. Sakai, *J. Am. Chem.*
- 28 *Soc.*, 2001, **123**, 11813.
- 29 I. P. Parkin and R. G. Palgrave, *J. Mater. Chem.*, 2005, **15**, 1689
- 30 I. Ashiri, K. Gartsman, M. Cohen, and R. Tenne, *AIP Conf. Proc.* , 2003, **685**, 545.
- M. Remskar, *Adv. Mater.*, 2004, **16**, 1497.
- M. Nakamura and Y. Matsui, *J. Am. Chem. Soc.*, 1995, **117**, 2651.
- P. Hoyer, *Langmuir*, 1996, **12**, 1411.
- M. Spahr, P. Bitterli, R. Nesper, M. Muller, F. Krumeich, and H. Nissen, *Angew.*
- Chem. Int. Ed*, 1998, **37**, 1263.
- B. C. Satshkumar, A. Govindaraj, M. E. Vogl, L. Basumallick, and C. N. R. Rao, *J.*
- Mater. Res*, 1997, **12**, 604.
- B. W. Hu, Q. Y. Zhu, W. K. Hsu, B. H. Chang, M. Terrones, N. Grobert, H. Terrones,
- J. P. Hare, H. W. Kroto, and D. R. M. Walton, *Appl. Phys. A.*, 2000, **70**, 231.
- B. C. Satshkumar, A. Govindaraj, M. Nath, and C. N. R. Rao, *J. Mater. Chem.*, 2000,
- 10**, 2115.
- L. Pu, X. Bao, J. Zou, and D. Feng, *Angew. Chem. Int. Ed*, 2001, **40**, 1490.
- B. Cheng and E. T. Samulski, *J. Mater. Chem.*, 2001, **11**, 2901.
- J. Hu, Y. Bando, and Z. Liu, *Adv. Mater.*, 2003, **15**, 1000.

- 31 B. A. Hernandez, K. S. Chang, E. R. Fisher, and P. K. Dorhout, *Chem. Mater.*, 2002, **14**, 480.
- 32 M. Yada, M. Mihara, S. Mouri, M. Kuroki, and T. Kijima, *Adv. Mater.*, 2002, **14**, 309.
- 33 J. Wu, S. Liu, C. Wu, L. Chen, and K. Chen, *Appl. Phys. Letts.*, 2002, **81**, 1312.
- 34 S. Kobayashi, N. Hamasaki, M. Suzuki, M. Kimura, H. Shirai, and K. Hanabusa, *J. Am. Chem. Soc.*, 2002, **124**, 6550.
- 35 G. R. Patzke, F. Krumeich, and R. Nesper, *Angew. Chem. Int. Ed*, 2002, **41**, 2446.
- 36 C. Lu, L. Qi, J. Yang, D. Zhang, N. Wu, and J. Ma, *J. Phys. Chem. B*, 2004, **108**, 17825.
- 37 J. W. Wang and J. Lee, *J. Phys. Chem. B*, 2004, **108**, 17832.
- 38 R. S. Chen, Y. S. Haung, D. S. Tsai, S. Chattopadhyay, C. T. Wu, Z. H. Lan, and K. H. Chen, *Chem. Mater.*, 2004, **16**, 2457.
- 39 P. X. Huang, F. Wu, B. L. Zhu, X. P. Gao, H. Y. Zhu, T. Y. Yan, W. P. Huang, S. H. Wu, and D. Y. Song, *J. Phys. Chem. B*, 2005, **109**, 19169.
- 40 V. M. Bermudez and S. M. Prokes, *Langmuir*, 2007, **23**, 12566.
- 41 Y. Fieldman, E. Wasserman, D. J. Sorolovitz, and R. Tenne, *Science*, 1995, **267**, 222.
- 42 D. Galvan, J. Kim, M. Maple, M. Avlsos-Berja, and E. Adem, *Fullerene Science*, 2000, **8**, 143.
- 43 M. Nath and C. N. R. Rao, *J. Am. Chem. Soc.*, 2001, **123**, 4841.
- 44 C. N. R. Rao, A. Govindaraj, F. Deepak, and N. Gunari, *Isr. J. Chem*, 2001, **41**, 23.
- 45 C. N. R. Rao and A. K. Cheetham, *J. Mater. Chem.*, 2001, **11**, 2887.
- 46 L. Dloczik, R. Engelhardt, K. Ernst, S. Fiechter, I. Sieber, and R. Konenkamp, *Appl. Phys. Letts.*, 2001, **78**, 3687.
- 47 X. Ziang, Y. Xie, L. Zhu, W. He, and Y. Qian, *Adv. Mater.*, 2001, **13**, 1278.
- 48 M. Nath and C. N. R. Rao, *Chem. Commun.*, 2001, 2236.
- 49 J. Chen, S.-L. Li, Z.-L. Tao, and F. Gao, *Chem. Commun.*, 2003, 980.
- 50 M. Nath and C. N. R. Rao, *Angew. Chem. Int. Ed*, 2002, **41**, 3451.
- 51 M. Brorson, T. W. Hansen, and C. J. H. Jacobsen, *J. Am. Chem. Soc.*, 2002, **124**, 11582.
- 52 T. H. Larsen, M. B. Sigman, A. Ghezelbash, R. Christopher Doty, and B. A. Korgel, *J. Am. Chem. Soc.*, 2003, **125**, 5638.
- 53 X. Qiu, C. Burda, R. Fu, L. Pu, H. Chen, and J. Zhu, *J. Am. Chem. Soc.*, 2004, **126**, 16276.
- 54 Y. Wang, Z. Tang, S. Tan, and A. Kotov, *Nano Letts.*, 2005, **5**, 243.
- 55 S. Y. Hor, Z. L. Xiao, U. Welp, Y. Ito, J. F. Mitchell, R. E. Cook, W. K. Kwok, and G. W. Crabtree, *Nano Letts.*, 2005, **5**, 397.
- 56 X. Wen, Y. Xie, C. L. Choi, K. C. Wan, X.-Y. Li, and S. Yang, *Langmuir*, 2005, **21**, 4729.
- 57 K.-S. Cho, D. V. Talapin, W. Gaschler, and C. B. Murray, *J. Am. Chem. Soc.*, 2005, **127**, 7140.
- 58 X. Wen, S. Wang, Y. Xie, X.-Y. Li, and S. Yang, *J. Phys. Chem. B*, 2005, **109**, 10100.
- 59 X. Wu, Y. Tao, Y. Hu, Y. Song, Z. Hu, J. Zhu, and L. Dong, *Nanotechnology*, 2006, **17**, 201.
- 60 Y.-J. Hsu, C.-M. Hung, Y.-F. Lin, B.-J. Liaw, T. S. Lobana, S.-Y. Lu, and C. W. Liu, *Chem. Mater.*, 2006, **18**, 3323.
- 61 Y. Hochen, E. Grunbaum, R. Tenne, J. Sloan, and J. Hutchinson, *Nature*, 1998, **395**, 336.
- 62 R. Armstrong, J. Canales, and P. Bruce, *Angew. Chem. Int. Ed*, 2004, **43**, 4899.
- 63 O. Stephan, P. M. Ajayan, C. Colliex, P. Redlich, J. M. Lambert, P. Bernier, and P. Lefin, *Science*, 1994, **266**, 1683.
- 64 N. Chopra, R. Luyken, K. Cherrey, V. Crespi, M. Cohen, S. Louie, and A. Zettl, *Science*, 1995, **269**, 966.

- 65 Y. Zhang, J. Liu, R. He, Q. Zhang, X. Zhang, and J. Zhu, *Chem. Mater.*, 2001, **13**, 3899.
- 66 J. Li, X. Chen, Z. Qiao, Y. Cao, and H. Li, *J. Mater. Sci. Lett.*, 2001, **20**, 1987.
- 67 B. Schwenzer, L. Loeffler, R. Seshadri, S. Keller, F. F. Lange, S. P. DenBaars, and U. K. Mishra, *J. Mater. Chem.*, 2003, **14**, 637.
- 68 Y. M. Zhao, W. B. Hu, Y. D. Xia, E. F. Smith, Y. Q. Zhu, C. W. H. Dunnill, and D. H. Gregory, *J. Mater. Chem.*, 2007, **17**, 4436.
- 69 W. Yang, H. Wang, S. Liu, Z. Xie, and L. An, *J. Phys. Chem. B*, 2007, **111**, 4156.
- 70 D. Bernaerts, S. Amelincx, G. Van Tendeloo, and J. Van Landuyt, *J. Cryst. Growth*, 1997, **172**, 433.
- 71 W. K. Hsu, Y. Q. Zhu, C. B. Boothroyd, I. Kinloch, S. Trasobares, H. Terrones, N. Grobert, M. Terrones, R. Escudero, G. Z. Chen, C. Colliex, A. H. Windle, D. J. Fray, H. W. Kroto, and D. R. M. Walton, *Chem. Mater.*, 2000, **12**, 3541.
- 72 M. Remskar, Z. Skraba, P. Stadelmann, and F. Levy, *Adv. Mater.*, 2000, **12**, 814.
- 73 Y. Q. Zhu, W. K. Hsu, S. Firth, M. Terrones, R. J. H. Clark, H. W. Kroto, and D. R. M. Walton, *Chem. Phys. Letts.*, 2001, **342**, 15.
- 74 Y. Peng, Z. Meng, C. Zhong, J. Lu, L. Xu, S. Zhang, and Y. Qian, *New J. Chem.*, 2001, **25**, 1359.
- 75 R. L. D. Whitby, W. K. Hsu, T. H. Lee, C. B. Boothroyd, H. W. Kroto, and D. R. M. Walton, *Chem. Phys. Letts.*, 2002, **359**, 121.
- 76 M. Nath, K. Mukhopadhyay, and C. N. R. Rao, *Chem. Phys. Letts.*, 2002, **352**, 163.
- 77 Y. Q. Zhu, W. K. Hsu, H. W. Kroto, and D. R. M. Walton, *J. Phys. Chem. B*, 2002, **106**, 7623.
- 78 F. D. Morrison, L. Ramsay, and J. F. Scott, *J. Physics: Condensed Matter*, 2003, **15**, L527.
- 79 H. Li, C.-L. Xu, G.-Y. Zhao, and H.-L. Li, *J. Phys. Chem. B*, 2005, **109**, 3759.
- 80 H. Chen, J. Wang, H. Yu, H. Yang, S. Xie, and J. Li, *J. Phys. Chem. B*, 2005, **109**, 2573.
- 81 A. K. Sra, T. D. Ewers, and R. E. Schaak, *Chem. Mater.*, 2005, **17**, 758.
- 82 Y. Wang and H. Yang, *J. Am. Chem. Soc.*, 2004, **127**, 5316.
- 83 X. Qi and F. E. Osterloh, *J. Am. Chem. Soc.*, 2005, **127**, 7666.
- 84 S. Y. Bae, J. Lee, H. Jung, J. Park, and J.-P. Ahn, *J. Am. Chem. Soc.*, 2005, **127**, 10802.
- 85 B. Ha, H. C. Kim, S.-G. Kang, Y. H. Kim, J. Y. Lee, C. Y. Park, and L. C. Jin, *Chem. Mater.*, 2005, **17**, 5398.
- 86 H. Ogihara, M. Sadakane, Q. Wu, Y. Nodasaka, and W. Ueda, *Chem. Commun.*, 2007, 4047.
- 87 Y. Kim, H. J. Joyce, Q. Gao, H. H. Tan, C. Jagadish, M. Paladugu, Jin Zou, and A. A. Suvorova, *Nano Letts.*, 2006, **6**, 599.
- 88 J. Hulteen, K. Jirage, and C. Martin, *J. Am. Chem. Soc.*, 1998, **120**, 6603.
- 89 G. Tourillon, L. Pontonnier, J. Levy, and V. Langlais, *Electrochem. Solid-State Lett.*, 2000, **3**, 20.
- 90 Y. D. Li, J. W. Wang, Z. X. Deng, Y. Y. Wu, X. M. Sun, D. P. Yu, and P. D. Yang, *J. Am. Chem. Soc.*, 2001, **123**, 9904.
- 91 C. C. Han, M. Y. Bai, and J. T. Lee, *Chem. Mater.*, 2001, **13**, 4260.
- 92 B. Mayers and Y. Xia, *Adv. Mater.*, 2002, **14**, 279.
- 93 Y. W. Wang, B. Hong, Y. T. Lee, G. Kim, and K. S. Kim, *J. Phys. Chem. B*, 2004, **108**, 16723.
- 94 J. Sha, J. Niu, X. Ma, X. J. X. Zhang, Q. Yang, and D. Yang, *Adv. Mater.*, 2002, **14**, 1219.
- 95 G. Xi, Y. Peng, S. Wan, T. Li, W. Yu, and Y. Qian, *J. Phys. Chem. B*, 2004, **108**, 20102.

- 96 H. Zhang, Q. Zhang, J. Tang, and L.-C. Qin, *J. Am. Chem. Soc.*, 2004, **127**, 2862.
 97 D. S. Han, S. Bae, Y. H. W. Seo, Y. J. Kang, J. Park, G. Lee, J.-P. Ahn, S. Kim, and J.
 Chang, *J. Phys. Chem. B*, 2005, **109**, 9311.
 98 S. Shanmugam, D. S. Jacob, and A. Gedanken, *J. Phys. Chem. B*, 2005, **109**, 19056.
 99 K. A. Gregg, S. C. Perera, G. Lawes, S. Shinozaki, and S. L. Brock, *Chem. Mater.*,
 2006, **18**, 870.
 100 Y. Xiong, Y. Xie, Z. Li, X. Li, and S. Gao, *Chem. Eur. J.*, 2004, **10**, 654.
 101 J. McCarten, M. Maher, T. L. Adelman, and R. E. Thorne, *Phys. Rev. Letts.*, 1989, **63**,
 2841.
 102 J. Ma, X. Liu, X. Cao, S. Feng, and M. E. Fleet, *Eur. J. Inorg. Chem*, 2006, 519.
 103 Y. Q. Zhu, W. K. Hsu, N. Grobert, B. H. Chang, M. Terrones, H. Terrones, H. W.
 Kroto, and D. R. M. Walton, *Chem. Mater.*, 2000, **12**, 1190.
 104 R. E. Thorne, *Physics Today*, 1996, **May** 42.
 105 <http://www.princeton.edu/~npo/ChargeDensityWave.html>.
 106 G. Gruner, *Rev. Mod. Phys*, 1988, **60**, 1129.
 107 P. Weiss and H. K. Onnes, *J. Physique*, 1911, **9**, 555.
 108 J. G. Bednorz and K. A. Mueller, *Cond. Matter*, 1986, **64**, 189.
 109 C. T. Chu and B. Dunn, *J. Am. Ceram. Soc.*, 1987, **70**, C375.
 110 <http://www.worldofenergy.com.au>.
 111 J. Bardeen, L. N. Cooper, and J. R. Schrieffer, *Phys.Rev.*, 1957, **108**, 1175.
 112 F. Jellinek, *J. Less-Common Metals*, 1962, **4**, 9.
 113 F. J. DiSalvo, B. G. Bagley, J. M. Voorhoeve, and J. V. Waszczak, *J. Phys. Chem.*
Solids, 1973, **34**, 1357.
 114 R. G. Dickinson and L. Pauling, *J. Am. Chem. Soc.*, 1923, **45**, 1466.
 115 A. Meetsma, G. A. Wiegers, R. J. Haange, and J. L. De Boer, *Acta. Cryst*, 1990, **46**,
 1598.
 116 Y. Gotoh, J. Akimoto, and Y. Oosawa, *J. Alloys and Compounds*, 1998, **270**, 115.
 117 E. Figueroa, Y. K. Kuo, A. Olinger, M. A. Lloyd, L. D. Bastin, S. Petrosatos, Q. Chen,
 B. Dobbs, S. Dev, J. P. Selegue, L. E. DeLong, C. P. Brock, and J. W. Brill, *J. Solid*
State Chem., 1995, **114**, 486.
 118 J. A. Wilson and A. D. Yoffe, *Adv. Phys.*, 1969, **73**, 193.
 119 J. F. J. Revelli and W. A. Phillips, *J. Solid State Chem.*, 1974, **9**, 176.
 120 J. F. Revelli, *Inorg. Synth.*, 1979, **19**, 35.
 121 R. H. Friend and A. D. Yoffe, *Adv. Phys.*, 1987, **36**, 1.
 122 P. Blaha, *J. Physics: Condensed Matter*, 1991, **3**, 9381.
 123 A. Schlicht, M. Schwenker, W. Biberacher, and A. Lerf, *J. Phys. Chem. B*, 2001, **105**,
 4867.
 124 S. M. Whittingham, *Progress in Solid State Chemistry*, 1978, **12**, 41.
 125 F. R. Gamble, F. J. DiSalvo, R. A. Klemm, and T. H. Geballe, *Science*, 1970, **168**,
 568.
 126 M. H. Whangbo and E. Canadell, *J. Am. Chem. Soc.*, 1992, **114**, 9578.
 127 J. A. Wilson, F. J. DiSalvo, and S. Mahajan, *Adv. Phys.*, 2001, **50**, 1171.
 128 S. K. Srivastava and B. Avasthi, N, *J. Mater. Sci.*, 1992, **27**, 3693.
 129 A. Meerschaut, L. Guemas, and R. J. J., *J. Solid State Chem.*, 1981, **36**, 118.
 130 W. Biltz and A. Kocher, *Z. anorg. allgem. Chem.*, 1938, **238**, 81.
 131 G. A. Tsingdinos, 'Topics in Current Chemistry', Springer - Verlag, 1978.
 132 S. Kikkawa, N. Ogawa, M. Koizumi, and Y. Onuki, *J. Solid State Chem*, 1982, **41**,
 315.
 133 E. Bjerkelund and A. Kjekshus, *Zeitschrift Fur anorganische chimie*, 1964, **328**, 235.
 134 S. V. Smaalen, *Acta. Cryst*, 2005, **A61**, 51.
 135 K. Inagaki, T. Toshima, and S. Tanda, *J. Phys. Chem. Solids*, 2005, **66**, 1563.

- 136 T. Sambongi, K. Tsutsumi, Y. Shiozaki, M. Yamamoto, K. Yamaya, and Y. Abe,
Solid State Comms, 1977, **22**, 729.
- 137 A. J. Berlinsky, *Rep. Prog. Phys.*, 1979, **42**, 1243.
- 138 K. Lehovec, *J. Less-Common Metals*, 1964, **27**, 1037.
- 139 C. M. Fang, E. Orhan, G. A. de Wijs, H. T. Hintzen, R. A. de Groot, R. Manchand, J.
 Y. Saillard, and G. de With, *J. Mater. Chem.*, 2001, **11**, 1248.
- 140 G. Hitoki, A. Ishikawa, T. Takata, J. N. Kondo, M. Hara, and K. Domen, *Chem. Letts.*,
 2002, 736.
- 141 D. Yamasita, T. Takata, M. Hara, J. N. Kondo, and K. Domen, *Solid State Ionics*,
 2004, **172**, 591.
- 142 T. Takata, G. Hitoki, J. N. Kondo, S. Hara, H. Kobayashi, and K. Domen, *Res. Chem*
Intermed, 2007, **33**, 13.
- 143 W. J. Chun, A. Ishikawa, H. Fujisawa, T. Takata, J. N. Kondo, M. Hara, M. Kawai, Y.
 Matsumoto, and K. Domen, *J. Phys. Chem. B*, 2003, **107**, 1798.
- 144 M. Zhu, Z. Zhang, and W. Miao, *Appl. Phys. Letts.*, 2006, **89**, 021915.
- 145 J. Gatterer, G. Dufek, P. Ettmayer, and R. Kieffer, *Acta Cryst. A* 1975, **31**, 99.
- 146 G. Hitoki, T. Takata, J. N. Kondo, M. Hara, H. Kobayashi, and K. Domen, *Chem.*
Commun., 2002, 1698.
- 147 M. Hara, G. Hitoki, T. Tanaka, J. N. Hondo, H. Kobayashi, and K. Domen, *Catalysts*
Today, 2003, **78**, 555.
- 148 J. Straehle, *Zeitschrift Fur Anorganische Und Allgemeine Chemie*, 1973, **402**, 47.
- 149 A. Margolin, R. Rosentsveig, A. Albu-Yaron, R. Popovitz-Biro, and R. Tenne, *J.*
Mater. Chem., 2004, **14**, 617.
- 150 S. M. Szs, 'The physics of semiconductor devices', Wiley and Sons 1981.
- 151 Q. Li, J. T. Newberg, E. C. Walter, J. C. Hemminger, and R. M. Penner, *Nano Letts.*,
 2004, **4**, 277.
- 152 M. Remskar and A. Mrzel, *Vacuum*, 2003, **71**, 177.
- 153 A. Rothschild, G. L. Frey, M. Homyonfer, L. Rapoport, and R. Tenne, *Matter. Res.*
Inov., 1999, **3**, 145.
- 154 R. Tenne, *Colloids and Surfaces*, 2002, **208**, 83.
- 155 X. Liu, *Materials Chemistry and Physics*, 2005, **91**, 212.
- 156 N. Berntsen, T. Gutjahr, L. Loeffler, J. R. Gomm, R. Seshadri, and W. Tremel, *Chem.*
Mater., 2003, **15**, 4498.
- 157 X. Wu, Y. Tao, X. Ke, J. Zhu, and J. Hong, *Materials Research Buletin*, 2004, **39**,
 901.
- 158 Y. Z. Jin, W. K. Hsu, Y. L. Chueh, L. J. Chou, Q. Y. Zhu, K. Brigatti, H. W. Kroto,
 and D. R. M. Walton, *Angew. Chem. Int. Ed*, 2004, **43**, 5670.
- 159 M. Remskar, A. Mrzel, A. Jesih, and F. Levy, *Adv. Mater.*, 2002, **14**, 680.
- 160 M. Nath and C. N. R. Rao, *Pure Appl. Chem.*, 2002, **74**, 1545.
- 161 Y. Q. Zhu, W. K. Hsu, H. W. Kroto, and D. R. M. Walton, *Chem. Commun.*, 2001,
 2184.
- 162 M. Nath, S. Kar, A. K. Raychaudhum, and C. N. R. Rao, *Chem. Phys. Letts.*, 2003,
 690.
- 163 T. Tsuneta, T. Toshima, K. Inagaki, T. Shibayama, S. Tonda, S. Ilji, M. Ahlskog, P.
 Hakanen, and M. Paalanen, *Curr. Appl. Phys.*, 2003, **3**, 473.
- 164 Y. S. Hor, U. Welp, Y. Ito, Z. L. Xiao, U. Patel, J. F. Mitchell, W. K. Kwok, and G.
 W. Crabtree, *Appl. Phys. Letts.*, 2005, **87**, 142506.
- 165 B. Gates, B. Mayers, Y. Wu, Y. Sun, B. Cattle, P. Yang, and Y. Xia, *Adv. Funct.*
Mater., 2002, **12**, 679.
- 166 Y. Xiong, B. T. Mayers, and Y. Xia, *Chem. Commun.*, 2005, 5013.
- 167 S. Tanda, Taku Tsuneta, Yoshitoshi Okajima, Katsuhiko Inagaki, Kazuhiko Yamaya,
 and N. Hatakenaka, *Nature*, 2002, **417**, 397

- 168 E. Slot, M. A. Holst, H. S. J. van der Zant, and S. V. Zaitsev-Zotov, *Phys. Rev. Letts.*,
2004, **93**, 17602.
- 169 A. Loiseau, F. Williams, N. Demoncy, G. Hug, and H. Pascard, *Phys. Rev. Letts.*,
1996, **76**, 4737.
- 170 M. Terrones, W. K. Hsu, H. Terrones, J. P. Zhang, S. Ramos, J. P. Hare, R. Castillo,
K. Prassides, A. K. Cheetham, H. W. Kroto, and D. R. M. Walton, *Chem. Phys. Letts.*,
1996, **259**, 568.
- 171 D. Golberg, Y. Bando, M. Eremets, K. Takemura, K. Kurashima, and H. Yusa, *Appl.*
Phys. Letts., 1996, **69**, 2045.
- 172 T. Laude, Y. Matsui, A. Marraud, and B. Jouffrey, *Appl. Phys. Letts.*, 2000, **76**, 3239.
- 173 P. Ma, Y. Bando, and T. Sato, *Chem. Phys. Letts.*, 2001, **337**, 61.
- 174 O. R. Lourie, C. R. Jones, B. M. Bartlett, P. C. Gibson, R. S. Ruoff, and W. E. Buhro,
Chem. Mater., 2000, **12**, 1808.
- 175 Y. Chen, M. Conway, and J. S. Williams, *J. Mater. Res*, 2002, **17**, 1986.
- 176 B. F. Cottam and M. S. Shaffer, *Chem. Commun.*, 2007, 4378.
- 177 Y. Kobayashi, H. Hata, M. Salma, and T. E. Mallouk, *Nano Letts.*, 2007, **7**, 2142.
- 178 <http://www.icsd.ac.uk>.
- 179 http://users.omskreg.ru/~kolosov/bam/a_v/v_1/powder/e_cell.htm.
- 180 A. Boultif and D. Louer, *J. Appl. Cryst.*, 2004, **37**, 724.
- 181 Altermatt and B. E. Brown, *Acta. Cryst.*, 1987, **A34**, 125.
- 182 R. A. Young, 'The Rietveld Method', Oxford University Press, 1993.
- 183 B. H. Toby, *J. Appl. Cryst.*, 2001, **34**, 210.
- 184 D. B. Williams and B. C. Carter, 'Transmission Electron Microscopy: a Textbook for
Material Science.' Springer, 1996.
- 185 http://www.steve.gb.com/science/electron_microscopy.html.
- 186 <http://rsb.info.nih.gov/ij/>, in 'Image J'.
- 187 C. N. R. Rao and M. Nath, *Dalton Trans.*, 2003, 1.
- 188 C. W. H. Dunnill, H. K. Edwards, P. D. Brown, and D. H. Gregory, *Angew. Chem. Int.*
Ed, 2006, **45**, 7060.
- 189 J. Y. Raty, F. Gygi, and G. Galli, *Phys. Rev. Letts*, 2005, **95**, 096103.
- 190 Y. Homma, Y. Kobayashi, and T. Ogino, *J. Phys. Chem. B*, 2003, **107**, 12161.
- 191 Z. P. Huang, D. Z. Wang, J. G. Wen, M. Sennett, H. Gibson, and Z. F. Ren, *Appl.*
Phys. A., 2002, **74**, 387.
- 192 G. Haegg and N. Schoenberg, *Arkiv foer Kemi*, 1954, **7**, 371.
- 193 H. K. Edwards, P. A. Salyer, M. J. Roe, G. S. Walker, P. D. Brown, and D. H.
Gregory, *Angew. Chem. Int. Ed*, 2005, 2.
- 194 R. T. Webber, *Phys.Rev.*, 1947, **72**, 1241.
- 195 J. I. Budnick, *Phys.Rev.*, 1960, **119**, 1578.
- 196 M. Tian, J. Wang, N. Kumar, T. Han, Y. Kobayashi, Y. Liu, T. E. Mallouk, and M. H.
W. Chan, *Nano Letts.*, 2006, **6**, 2773.
- 197 V. V. Pokropivnyi, *Powder Metallurgy and Metal Ceramics*, 2002, **41**, 123.
- 198 X. Blase, J.-C. Charlier, A. De Vita, and R. Car, *Appl. Phys. Letts.*, 1997, **70**, 197.
- 199 M. Kociak, A. Y. Kasumov, and S. Gueron, *Phys. Rev. Letts*, 2001, **86**, 2416.
- 200 T. Matsuura, S. Tanda, K. Asada, Y. Sakai, T. Tsuneta, K. Inagaki, and K. Yamaya,
Physica B, 2003, 1550.
- 201 G. Yi and W. Schwarzacher, *Appl. Phys. Letts.*, 1999, **74**, 1746.
- 202 D. Vodolazov, F. M. Peeters, L. Piraux, S. Matefi-Tempfli, and S. Michotte, *Phys.*
Rev. Letts., 2003, **91**, 157001.
- 203 S. Michotte, S. Matefi-Tempfli, and L. Piraux, *Appl. Phys. Letts.*, 2003, **82**, 1620.
- 204 M. L. Tian, J. G. Wan, J. Snyder, J. Kurriz, Y. Liu, P. Schiffer, T. E. Mallouk, and H.
W. Chan, *Appl. Phys. Letts.*, 2003, **83**, 1620.
- 205 A. Rogachev and A. Berzryadin, *Appl. Phys. Letts.*, 2003, **83**, 512.

206 Y. L. Wang, X. C. Jiang, T. Herricks, and Y. N. Xia, *J. Phys. Chem. B*, 2004, **108**,
 8631.
 207 Z. L. Xiao, C. Y. Han, W. K. Kwok, H. W. Wang, U. Welp, J. Wang, and G. W.
 Crabtree, *J. Am. Chem. Soc.*, 2004, **126**, 2316.
 208 Y. Y. Wu, B. Messer, and P. D. Yang, *Adv. Mater.*, 2001, **13**, 1487.
 209 Q. Yang, J. Shu, X. Y. Ma, Y. J. Ji, and D. R. Yang, *Supercond. Sci. Technol*, 2004,
17, L31.
 210 A. Bezryadin, C. N. Lau, and M. Tinkham, *Nature*, 2000, **404**, 971.
 211 C. N. Lau, N. Markovic, M. Bockrath, A. Bezryadin, and M. Tinkham, *Phys. Rev.*
Letts., 2001, **87**, 217003.
 212 A. S. Mel'nikov and V. M. Vinokur, *Nature*, 2002, **415**, 60.
 213 M. Nath and C. N. R. Rao, *Chem. Commun.*, 2001, **21**, 2236.
 214 H. K. Edwards, P. A. Salyer, M. J. Roe, G. S. Walker, P. D. Brown, and D. H.
 Gregory, *Crystal Growth and Design*, 2005, **0**, 1.
 215 L. F. Matthes, *Phys. Rev. B*, 1973, **8**, 3719.
 216 Q. Zhang and L. Gao, *Langmiur*, 2004, **20**, 9821.
 217 K. Kamiya, T. Yoko, and M. Bessho, *J. Mater. Sci.*, 1987, **22**, 937.
 218 K. Kohno, *J. Mater. Sci.*, 1992, **27**, 658.
 219 S. J. Henderson and A. L. Hector, *J. Solid State Chem.*, 2006, **179** 3518.
 220 D. Lu, G. Hitoki, E. Katou, J. N. Kondo, M. Hara, and K. Domen, *Chem. Mater.*,
 2004, **16**, 1603.
 221 M. Kerlauer, O. Merdignac-Conanec, M. Guilloux-Viryb, and A. Perrinb, *Solid State*
Sciences, 2004, **6**, 101.
 222 Y. Lee, K. Nukumizu, T. Watanabe, T. Takata, M. Hara, M. Yoshimura, and K.
 Domen, *Chem. Letts.*, 2006, **35**, 352.
 223 L. A. Aleshina and S. V. Loginova, *Crystallography Reports*, 2002, **47**, 415.
 224 C. Stampfl and A. J. Freeman, *Phys. Rev. B*, 2005, **71**, 024111.
 225 J. Geng, B. Liu, L. Xu, F.-N. Hu, and J.-J. Zhu, *Langmiur*, 2007, **23**, 10286.